Czech Technical University in Prague
Faculty of Mechanical Engineering

Department of Technical Mathematics
Study Programme: Mechanical Engineering
Field of Study: Mathematical and Physical Engineering

Numerical Simulations of Turbine Blade Flutter

DOCTORAL THESIS

Author: Ing. Marek Pátý
Supervisor: doc. Ing. Jan Halama, Ph.D.
Year: 2022

Statutory declaration

I hereby declare that this thesis is my own work. Where other sources of information have been used, they have been acknowledged and referenced in the list of used literature and other sources.

I understand that my work relates to the rights and obligations under the Act No. 121/2000 Sb., the Copyright Act, as amended, in particular the fact that the Czech Technical University in Prague has the right to conclude a license agreement on the use of this work as a school work pursuant to Section 60 paragraph 1 of the Copyright Act.

In Prague .....

.....
Marek Pátý

Acknowledgement

I would like to thank my supervisor, Assoc. Prof. Jan Halama, for providing the research topic and for his further guidance. I especially appreciate his helpfulness in arranging my research stay at the von Karman Institute and his support for my travels to international conferences.

I gratefully acknowledge that this work was supported by the Grant Agency of CTU in Prague, namely grants No. SGS16/206/OHK2/3T/12 and No. SGS19/154/OHK2/3T/12, and by the Center of Advanced Aerospace Technology (CZ.02.1.01/0.0/0.0/16_019/0000826) in the framework of ESIF, EU Operational Programme Research, Development and Education.

Marek Pátý

Název: **Numerické simulace flutteru turbínové lopatky**
Autor: Ing. Marek Pátý
Obor: Matematické a fyzikální inženýrství
Druh práce: Disertační práce
Vedoucí práce: doc. Ing. Jan Halama, Ph.D.
Ústav technické matematiky, Fakulta strojní, České vysoké učení technické v Praze

Abstrakt: Pro zaručení dlouhé životnosti a bezpečného provozu lopatkového stroje je nezbytné, aby byl jeho návrh proveden s pečlivým zohledněním aeroelastických jevů. Mezi největší rizika patří samobuzené kmitání, zvané flutter. Pokud dojde k jeho vzniku, rychle se zvětšující výchylky kmitů mohou ve velmi krátkém čase vést ke katastrofickému selhání konstrukce. Tato práce se zabývá numerickou predikcí flutteru a zaměřuje se na okrajové podmínky zabraňující vzniku nežádoucích odrazů vln. Kompaktní prostorové uspořádání turbostrojů způsobuje, že perturbace vytvořené na vstupní či výstupní hranici oblasti přímo ovlivňují proudové pole okolo lopatek. Tento efekt nabývá na významu v souvislosti s trendem zvětšování průměru rotorů posledních stupňů parních turbín za účelem dosažení vyššího výkonu. Vstupní proudění může poblíž špičky lopatky přesáhnout rychlost zvuku a utvořit čelní rázovou vlnu, což klade zvýšené nároky na definici vstupní okrajové podmínky schopné zabránit vzniku nežádoucích odrazů.

Použitý aeroelastický model využívá především energetickou metodu s předepsaným harmonickým kmitáním lopatek. Řešení nestacionárního proudění je založené na Eulerových rovnicích ve dvou dimenzích, převedených do Arbitrary Lagrangian-Eulerian (ALE) formulace a diskretizovaných metodou konečných objemů. Nevazké toky jsou aproximované schématem AUSM$^+$-up a pro zvýšení prostorové přesnosti metody je použita rekonstrukce gradientů metodou vážených nejmenších čtverců s omezovačem toku. Integrace soustavy rovnic v čase je řešena pomocí implicitního schématu druhého řádu přesnosti za použití lokálního časového kroku a implicitního vyhlazování reziduí. Moderní spektrální bezodrazová okrajová podmínka (Spectral NRBC) je použita pro vstupní a výstupní hranici oblasti a porovnána s dalšími dvěma metodami. Numerický řešič byl od základu vyvinut a naprogramován autorem této práce v jazyce C++.

Výpočetní model je použit pro řešení aeroelastické stability osamoceného leteckého profilu NACA 0012 a tří lopatkových mříží se subsonickým (STCF10), transsonickým (STCF4) a supersonickým (M8) režimem proudění. Je ukázáno, že spektrální okrajová podmínka účinně zabraňuje nežádoucím odrazům vln a umožňuje tak přesné vyhodnocení aerodynamického tlumení i pro komplexní proudová pole. Přestože odrazy vln nejsou vždy zcela potlačeny kvůli použitému linearizovanému modelu, jejich intenzita je natolik nízká, že nemají významný vliv na proudové pole v okolí lopatek. Řešení se spektrální okrajovou podmínkou vykazuje velmi nízkou citlivost na velikost oblasti, což dovoluje zachovat přesnost výpočtu i při posunutí vstupní a výstupní hranice blízko k lopatkám. Oproti tomu použití okrajové podmínky s horšími bezodrazovými vlastnostmi může vést ke zcela nesprávnému vyhodnocení aeroelastické stability.

Klíčová slova: Flutter turbínových lopatek, Bezodrazové okrajové podmínky, Interakce proudění s elastickým tělesem, Metoda Arbitrary Lagrange-Euler, Výpočetní mechanika tekutin, Metoda konečných objemů

Title: **Numerical Simulations of Turbine Blade Flutter**

Author: Ing. Marek Pátý

Abstract: The design of a turbomachine needs to be executed with a careful consideration of aeroelastic effects in order to guarantee a long and safe operation. One of the greatest risks represent self-excited vibrations, called flutter. Once initiated, their rapidly increasing magnitude threatens to induce a catastrophic failure within a very short time. This thesis deals with numerical prediction of flutter and focuses on the treatment of boundary conditions for the prevention of spurious wave reflections. The compact spatial arrangement of turbomachines causes that any perturbation formed at the inlet or outlet boundary impacts directly the near-blade flow solution. The issue is exacerbated by the recent trend of increasing the diameter of last-stage steam turbine rotors in pursuit of a higher power output. As a consequence, supersonic inflow conditions may be encountered at higher spans. The upstream propagating bow shock, formed ahead of the blade leading edge, creates a particularly challenging environment for a reflection-free definition of inlet boundary conditions.

The present modelling approach is primarily based on the energy method with prescribed harmonic blade oscillations. The solution of unsteady aerodynamics adopts Euler equations in two dimensions, cast in the Arbitrary Lagrangian-Eulerian (ALE) formulation and discretised with a finite volume approach. The AUSM$^+$-up scheme is employed for the approximation of inviscid fluxes and spatial accuracy is enhanced by adopting a weighted least squares gradient reconstruction with flux limiting. The system of equations is integrated in time with a second order accurate implicit scheme with local time-stepping and implicit residual smoothing. The state-of-the-art Spectral non-reflecting boundary condition (NRBC) is employed for inflow and outflow and compared with two other formulations. The numerical solution procedure is realised with an in-house solver implemented by the author in C++.

The computational model is used to predict aeroelastic stability of an isolated airfoil NACA 0012 and of three blade cascades with a subsonic (STCF10), transonic (STCF4) and supersonic (M8) flow regime. The Spectral NRBC is shown to be highly successful in preventing the formation of spurious wave reflections and enables an accurate evaluation of aerodynamic damping even for complex flow-fields. Although the wave reflections are not always completely suppressed on account of the underlying linearised model, their magnitude is low enough to have only a minor effect on the near-blade flow field. Flow solution adopting the Spectral NRBC exhibits only a very mild sensitivity to the inflow and outflow positions, which allows employing highly truncated domains without compromising accuracy. The study further demonstrates that using a boundary condition that fails to suppress the spurious wave reflections can result in a fundamentally incorrect aeroelastic assessment.

Key words: Turbine blade flutter, Non-reflecting boundary conditions, Fluid-structure interaction, Arbitrary Lagrangian-Eulerian method, Computational fluid dynamics, Finite volume method

Dedicated to Lucy

for having turned my life upside down in the best way imaginable during the creation of this work

Contents

List of Figures

List of Tables

Nomenclature

Latin Symbols

a	Speed of sound
b	Blade span
b_y, b_ϕ	Damping in bending and in torsion
$\boldsymbol{c}$	Vector of characteristic variables
C	Chord
$\mathbb{C}$	Complex numbers
C_L	Lift coefficient
$\tilde{C}_p$	Coefficient of instantaneous pressure fluctuation: $\tilde{C}_p(\boldsymbol{x},t) = \frac{p(\boldsymbol{x},t)-\overline{p}(\boldsymbol{x})}{\Delta\alpha(p_{01}-p_2)}$ for a pitching mode, $\tilde{C}_p(\boldsymbol{x},t) = \frac{p(\boldsymbol{x},t)-\overline{p}(\boldsymbol{x})}{h/C(p_{01}-p_2)}$ for a general mode
C_p	Pressure coefficient: $C_p = \frac{p-p_1}{p_{01}-p_1}$ for airfoils, $C_p = \frac{p-p_2}{p_{01}-p_2}$ for blade cascades
$\hat{C}_{p(1)}$	First harmonic of $\tilde{C}_p$
c_p	Constant pressure specific heat
c_v	Constant volume specific heat
dS	Surface element
e	Internal energy
E_P, E_k	Potential and kinetic energy
e_0	Total energy
f	Frequency
F_x, F_y	x and y components of force
$\boldsymbol{F}$	Flux
h	Specific enthalpy; max. displacement
i	Complex unit
I	Identity matrix
I_ϕ	Inertial moment around elastic axis
Im	Imaginary part of a complex quantity
k	LSQ inverse distance weighting exponent; boundary-normal wavenumber
k_y, k_ϕ	Bending and torsional stiffness
l	Wavelength
$\boldsymbol{l}_j$	j-th left eigenvector
L	Limiter function; left eigenvector matrix of dispersion relation
L_{1d}	Transformation matrix from primitive to characteristic variables
L_s	Limit case of L for $\kappa \to \infty$
m	Weight; circumferential wavenumber

M	Mach number; torsional moment
$\boldsymbol{n}$	Normal vector
p	Pressure
$\hat{p}_{(1)}$	First pressure harmonic
P	Pitch (blade to blade spacing)
q	Vertex movement coefficient
$\boldsymbol{q}$	Vector of primitive variables
Q	Matrix of rotation
$\boldsymbol{Q}$	Source term
r	Radius; polar coordinate
$\boldsymbol{r}_j$	j-th right eigenvector
R	Specific gas constant; right eigenvector matrix of dispersion relation
$\mathbb{R}$	Real numbers
$\boldsymbol{R}$	Residual vector
R_{1d}	Transformation matrix from characteristic to primitive variables
Re	Real part of a complex quantity
s	Specific entropy
$\boldsymbol{s}$	Grid (ALE) velocity
S_ϕ	Static moment around elastic axis
t	Time
T	Period; temperature
u, v	Velocity vector components in x,y directions
$\boldsymbol{u}$	Velocity vector
V	Convection speed
w	LSQ weighting factor
w_{coeff}	Aerodynamic work coefficient
$\boldsymbol{W}$	Vector of conserved variables
W_{aero}	Work of aerodynamic forces
x, y	Coordinates

Greek Symbols

α	Angle of attack
α_i	Runge-Kutta scheme coefficients
β	Flow angle from axial direction
γ	Specific heat ratio
Γ	Circulation
δ	Blade stagger angle
ϵ	Residual smoothing coefficient
ζ	Limiter
η	Chord-normal coordinate
θ	Polar coordinate
κ	Ratio of circumferential wavenumber to angular frequency $\kappa = \frac{m}{\omega}$
λ	Eigenvalue
μ	Mass ratio

Ξ	Aerodynamic damping coefficient: $\Xi = \frac{-W_{aero}}{\pi b(\Delta\alpha C)^2(p_{01}-p_2)}$ for pitching oscillations, $\Xi = \frac{-W_{aero}}{\pi bh^2(p_{01}-p_2)}$ for a general mode
ρ	Density
σ	Interblade phase angle
τ	Pseudo-time
ϕ	Angle of airfoil rotation
$\phi_{p(1)}$	Phase of first pressure harmonic
χ	Natural mode shape
ψ	Convected vector in a flux
ω	Angular frequency
Ω	Control volume
$\tilde{\omega}$	Reduced frequency
ω_{rot}	Rotational speed
$d\Omega$	Volume element

Subscripts and Superscripts

bd	Boundary
FS	Freestream
int	Interior
ref	Reference
s	Surface
0	Total
v	Volume
is	Isentropic
$1, 2$	Inlet, outlet

Abbreviations and Acronyms

ALE	Arbitrary Lagrangian-Eulerian
AUSM	Advection upstream splitting method
BC	Boundary condition
CFD	Computational fluid dynamics
CFL	Courant-Friedrichs-Lewy
CSM	Computational structural mechanics
DFT	Discrete Fourier transform
DNS	Direct numerical simulation
EA	Elastic axis
EO	Engine order
FEM	Finite element method
FSI	Fluid-structure interaction
FVM	Finite volume method
GCD	Greatest common divisor

GCL	Geometric conservation law
GG	Green-Gauss method
HCF	High-cycle fatigue
IBPA	Interblade phase angle
LE	Leading edge
LES	Large eddy simulation
LPT	Low pressure turbine
LSQ	Least squares method
MLP	Multidimenisonal Limiting Process
MUSCL	Monotonic Upstream-centered Scheme for Conservation Laws
ND	Nodal diameter
NLH	Nonlinear harmonic method
NRBC	Non-reflecting boundary condition
ODE	Ordinary differential equations
RANS	Reynolds-Averaged Navier-Stokes
SLiQ	Steady linear quadratic
STCF	Standard configuration
TE	Trailing edge
TFI	Transfinite interpolation
TVD	Total variation diminishing
VAVL	van Albada-van Leer

Chapter 1

Introduction

Whether a turbomachine serves to propel an aircraft, generate electricity or carry a jetpack flier towards the skies, the fundamental working principle is always the same - to extract energy from a working fluid via a relative rotating motion of multiple blade-rows and convert it to a form that can be exploited further. Yet it is this continual blade passing, inherent to the operation of a turbomachine, that may eventually inflict its destruction. Blade-row interactions may induce high-cycle fatigue, leading to a preliminary termination of the operational life. Arguably an even more serious danger represent self-excited vibrations, known as flutter. Triggered by a small perturbation, their amplitude escalates quickly and threatens to cause an immediate structural failure. Unlike vibrations caused by blade-row interactions, self-excited oscillations are asynchronous and independent of engine orders, which complicates their prediction. The issue of blade vibration has been present since the outset of turbomachinery as an engineering discipline [170] and despite advances achieved in its understanding, it remains no less pressing nowadays. Failures continue to occur in final test phases or even during operation [170, 125], emphasising the need for further research.

This work deals with the development of a numerical model for the prediction of blade flutter and focuses on the treatment of boundary conditions. The compact spatial arrangement of turbomachines causes that any perturbation formed at the inlet or outlet boundary impacts directly the near-blade flow solution. The issue is exacerbated by the recent trend of increasing the diameter of last-stage steam turbine rotors in pursuit of a higher power output. As a consequence, supersonic inflow conditions may be encountered at higher spans. The upstream propagating bow shock, formed ahead of the blade leading edge, creates a particularly challenging environment for a reflection-free definition of inlet boundary conditions.

The present modelling approach is primarily based on the energy method with prescribed harmonic blade oscillations, but a fully coupled solution of fluid-structure interaction with two structural degrees of freedom is also provided. The solution of unsteady aerodynamics adopts Euler equations in two dimensions, cast in the Arbitrary Lagrangian-Eulerian (ALE) formulation and discretised with a finite volume approach. Three boundary condition formulations are implemented for inflow and outflow, including the state-of-the-art Spectral NRBC [158]. Their ability to sup-

press spurious wave reflections is extensively analysed on several demanding test cases, including a turbine cascade with a supersonic inflow. The numerical solution procedure is realised with an in-house solver written by the author in C++ and compatible with the universal format CGNS for the storage of mesh and solution.

The thesis is structured as follows. Chapter 1 opens with the introduction and Chapter 2 proceeds by outlining the most pressing aeroelastic problems in turbomachinery. The classification and brief description of each phenomenon is provided, together with an overview of relevant parameters driving the aeroelastic behaviour. This chapter further elaborates on computational methods for aeroelastic analysis, ranging from the original simplified analytical approaches to the state-of-the-art nonlinear fluid-structure coupled numerical simulations.

The objectives of this work are stated in Chapter 3.

Governing equations that form the core of the present computational model are described in Chapter 4. Unsteady aerodynamics is modelled with Euler equations that are derived in the Arbitrary Lagrangian-Eulerian reference frame in order to facilitate solution on domains with moving boundaries. Boundary conditions are discussed in a separate section, focusing mainly on the suppression of spurious wave reflections at inflow and outflow. Together with the classical Exact Steady NRBC of Giles [58], the novel Spectral NRBC of Schlüß et al. [158] for unsteady flows is elaborately described. Two strategies for the solution of fluid-structure interaction are presented, namely the energy method and a fully coupled model of an elastically mounted body with two degrees of freedom.

Chapter 5 elaborates on the numerical methods implemented in the solver. The description commences by presenting a grid motion algorithm for the case of an oscillating isolated airfoil and proceeds by proposing its extension to blade cascades. The main focus of this chapter is on the description of numerical techniques used for the solution of unsteady aerodynamics, comprising the ALE formulation of a finite volume method, strategies for flux approximation, gradient reconstruction and limiting and for temporal integration. The non-reflecting boundary conditions are described in a greater detail, as different paths can be taken at several points in their implementation. The last section of this chapter encompasses numerical techniques related to the structural part of the aeroelastic analysis, namely the approximation of a deforming elastic structure with a rigid body motion and the algorithm for a coupled solution of solid body motion and unsteady aerodynamics.

Chapter 6 discusses achieved results for four applications, presented in the order from trivial to complex. The motivation is to test and validate various features of the numerical model before proceeding to the most challenging test case, a supersonic turbine blade cascade.

The first application is a NACA 0012 airfoil in a freestream flow. The presence of a single solid body in the computational domain simplifies the grid deformation procedure and as the flow conditions are subsonic, no discontinuities need to be resolved by the finite volume scheme. Two configurations considered for the aeroelastic analysis are a harmonically oscillating airfoil and a fully coupled model of an elastically mounted airfoil with two degrees of freedom. The computational model

is validated by comparison with experimental data and with numerical solutions of other authors.

The second test case is a compressor cascade STCF10, known for being prone to artificial wave reflections from the inlet and outlet boundaries with a significant effect on the assessment of aeroelastic stability [146]. As such, it represents a suitable application for analysing the performance of non-reflecting boundary conditions. It is convenient that the flow conditions remain subsonic, detracting from the complexity of the flow solution and enabling to focus on the analysis of boundary conditions. More over, results obtained with the Spectral NRBC have already been published in [157] for this test case, providing the opportunity to verify that its present implementation is correct. Flutter analysis is performed for a prescribed pitching mode of oscillation.

The flow field complexity increases when proceeding to the transonic turbine cascade STCF4, featuring downstream propagating shockwaves. The accuracy and stability of the implemented gradient limiting strategies can thus be investigated. Aeroelastic predictions are performed for blades undergoing bending oscillations and compared with publicly available experimental data.

The last test case is a blade cascade M8, representing a near-tip section of a last-stage low-pressure steam turbine rotor. The inflow conditions are supersonic, causing a detached bow shock to form upstream of the blades and propagate towards the inlet. Shockwaves are thus encountered at both the inlet and outlet boundary and put the reflection properties of implemented boundary conditions to a demanding test. The blades oscillate in a coupled bending-torsion eigenmode.

The thesis finishes by summarising achieved results, drawing conclusions and presenting research outlook in Chapter 7.

Chapter 2

Aeroelasticity in Turbomachinery

The concept of aeroelasticity in the modern sense was established by Collar [27] in the 1940s. He defined it as an engineering discipline which studies the interaction between aerodynamic, elastic and inertial forces for a solid object submerged in a fluid flow. Up to that point, the individual subjects of aerodynamics and structural deformation were usually treated in isolation, but Collar emphasised that they are in fact inseparable and the matter of fluid-structure interaction (FSI) needs to be regarded as one interconnected whole. He placed the most pressing aeroelastic problems of that time within a triangle of forces, shown in Fig. 2.1. The depicted phenomena indicate that the research of that time concentrated primarily on the domain of aeronautics.

Aeroelastic problems have affected the development of airplanes since the early beginnings. Several days before the Wright brothers performed the first sustained flight of a heavier-than-air machine, Professor Samuel P. Langley tried to take off with his monoplane by being catapulted from a houseboat on the Potomac river near Washington on December 9, 1903. The wings dismounted and the machine was wrecked. Although there is some controversy regarding the cause of the accident, it is often ascribed to a torsional divergence of the wing, a problem that belongs to the area of static aeroelasticity [91]. The lack of structural rigidity was later resolved by the bi-plane design which became preferred during World War I. However, this solution had the adverse effect in that the connecting wires were susceptible to the dynamic aeroelastic phenomenon of flutter [93]. Comprehensive studies of aeroelastic effects concerning airplanes were commenced in the 1930s, namely by Cox, Pugsley, Duncan, Frazer and Collar (e.g. [28], [50]), and lead to a formation of stiffness criteria for aircraft wings and components [27]. In the same period, Theodorsen devised an analytical method for the prediction of wing and aileron flutter with three degrees of freedom (DOF), published in [177] and [178]. A re-evaluation of the procedure was recently presented by Perry [144].

Turbomachines have also encountered aeroelastic problems since their advent. Early steam turbines featured damping wires to mitigate blade vibration problems [93]. Srinivasan amusingly quotes a resolution of Glenn Warren from 1914 to make a gas turbine engine running without vibration before he quits [170]. Warren then remained with the turbine division of General Electric till the end of his professional

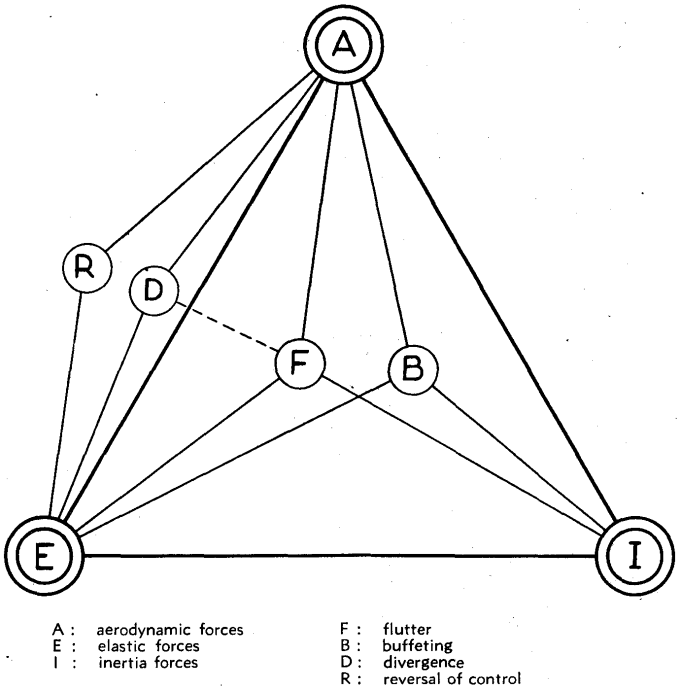

Figure 2.1: Triangle of forces and aeroelastic phenomena by Collar [27]

career. Jet engines have suffered from flutter problems since their early deployment during World War II. The most afflicted parts were the first compressors stages, open rotors, low-pressure turbines and later turbofans [39]. Particularly difficult-to-predict failures occurred due to high-cycle fatigue (HCF), caused by a large number of alternating stress cycles. The stress level is too small to induce any plastic deformation and the cracks propagate very rapidly [105]. HCF issues can account to between 10% and 40% of total development problems in gas turbine engines [198] and according to an estimation of the U.S. Air Force, they cause about 55% of fighter jet engine mishaps and 30% of jet engine maintenance [131]. According to an analysis presented by Sieg [161] in 2000, up to 46% of fighter aircrafts had been inoperative in certain periods during the previous decades as a result of HCF related problems. Srinivasan [170] mentions several incidents of jet engine failures which occurred during qualification tests or even once the production has begun. An illustrative example is the in-flight "primary failure" of a wide chord plane on the RB 211-524 G/H engine during a Cathay Pacific flight from Los Angeles. It was the first incident of that kind for a design that had successfully served over 12 million engine hours. Indeed, HCF problems are not exclusive to jet engines. A problem with steam turbine blade root cracking due to flutter was recently reported by Masserey et al. [125].

2.1 Aeroelastic Problems in Turbomachinery

Aeroelastic behaviour of turbomachines shares several important characteristics with aircrafts. Same as the wing of an airplane, the blade of a turbomachine is a slender

aerodynamic surface subjected to many conflicting requirements, such as performance, efficiency, low weight, reliability and structural integrity. Nevertheless, the engineering analysis of each requires a substantially different approach. The aircraft wing can be regarded as a self-standing elastic structure attached to a rigid fuselage and facing a largely uniform incoming flow with only minor distortions. This approach served as a basis for the aeroelastic theory of Theodorsen [177] and it is still applicable nowadays, at least for a preliminary analysis. In contrast, turbomachine blades are arranged with close spacing into a blade row and their mutual interactions are cardinal for the aeroelastic characteristics. In addition, strong aerodynamic and acoustic coupling effects exist also between multiple blade rows. The relative rotating motion is a source of a strong periodic forcing. Further non-uniformities in the flow-field may arise due to vortex shedding, in-passage shock movements, jet-engine burner outputs and combustion instabilities, impacts of cooling jets etc., all of which are convected throughout the machine.

The margin for engine optimization is becoming thinner, yet the pressure on improvements in efficiency, fuel consumption, environmental friendliness and cost reduction continues to grow. The boundaries of current designs are pushed and new radical ones emerge. Their aeroelastic behaviour is often driven by previously unencountered mechanisms, which further increases the complexity of the problem. One example of this trend is also addressed in the present work. In pursuit of a higher power output, blades in the aft stages of low-pressure steam turbines are becoming longer. Supersonic upstream conditions may thus be encountered in the near-tip region of a blade-row and the shockwave pattern is dramatically changed. Consequently, the empirical knowledge gained over long years of experience becomes largely inapplicable and the need for highly accurate predictive analytical tools is increased. Srinivasan [170] compiled a list of areas where advances are urgently needed for an accurate aeroelastic analysis:

- Assessment of flow defects at the location they originate and as they are transported along
- Unsteady aerodynamics of cascades under a wide variety of flow conditions expected in the operating range
- Structural vibration frequencies and modes of interest over the operating range
- Quantification of damping in the system due to non-aerodynamic sources
- Estimate of material properties (fatigue strength, ultimate strength, modulus of elasticity, etc.) for the configuration at the temperatures expected in the operating range, including the influence of processing, defects etc., leading to the calculation of structural integrity
- Identification of dissimilarities in aerodynamic parameters (gap/chord ratio, stagger, incidence, etc.) and structural parameters (frequencies, mode shapes and damping, etc.) and accounting for their influence in a statistical sense

Aeroelastic problems may be classified as either *static* or *dynamic*. Phenomena from both categories with the greatest relevance for turbomachinery are discussed in the remainder of this section.

2.1.1 Static Aeroelasticity

Static aeroelasticity is a category of fluid-structure interaction problems where the evolution in time is moderate enough to approximate the process as quasi-steady. Inertial forces are neglected and the problem is reduced to the interaction of aerodynamic and elastic forces. A typical example is the torsional divergence of aircraft wings. Aerodynamic forces deform the wing, which in turn increases the aerodynamic loading and induces further deformation. Structural stiffness of turbomachine blades is in general substantially higher than that of aircraft wings, hence the static aeroelastic phenomena do not pose a threat regarding the structural integrity. Nevertheless, they need to be taken into account for design and manufacturing. Turbomachine components are subjected to varying operating conditions in terms of rotational speeds and flow parameters. This is especially significant for jet engines whose mode of operation changes substantially for take-off, climb, cruise, descent and landing. Each phase of flight is characterised by different aerodynamic and centrifugal loads that act on the blade and cause it to deform from the manufactured shape. The deformation mainly occurs in a torsional mode, but a bending displacement can also be present for higher aspect ratio blades. The elastic deformation of the loaded blade needs to be considered when the manufactured (*cold*) shape is being retrieved from the targeted in-operation geometry by a procedure called *unrunning* [150].

2.1.2 Dynamic Aeroelasticity

Dynamic aeroelasticity is a discipline studying the complex interactions between vibrating structures and the surrounding flow. All three forces defining the Collar's triangle are involved: aerodynamic, elastic and inertial. The behaviour of the system can be further affected by the presence of mechanical or material damping. The most relevant dynamic aeroelastic phenomena in turbomachinery are forced response and flutter.

Forced Response

Flow conditions in a turbine or a compressor are inherently non-uniform both in space and time. The spatial variations in the stationary reference frame are experienced as unsteady distortions by a rotating blade row. The blades are subjected to periodic fluctuations in pressure, velocity, temperature and flow angle. Further excitations may be caused by the motion of shocks in blade passages, vortex shedding or due to a number of mechanical sources [170]. All of these flow-field non-uniformities act as an external periodic forcing on the blade at a frequency corresponding to

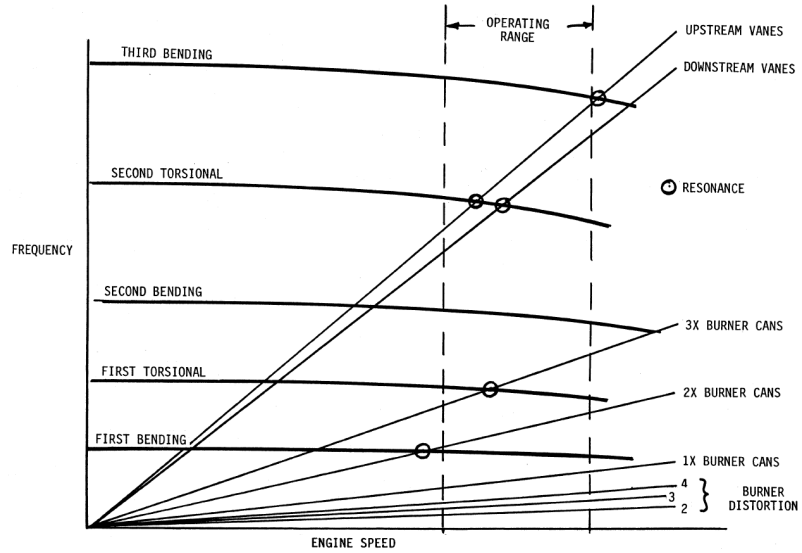

Figure 2.2: Example of a Campbell diagram from [104]

engine orders (EO), multiples of the rotational frequency. A common tool for the assessment of risks related to forced response vibrations is the Campbell diagram, devised in 1924 by Wilfred Campbell [17] and still in use today.

An example of the diagram for a turbine rotor is shown in Fig. 2.2. One set of lines represents natural frequencies corresponding to different modes of deformation in function of the rotational speed. Typically for a turbine, a slight decrease in eigenfrequencies occurs for higher rotational speeds, as the increased temperature causes a reduction in modulus [131]. An opposite trend would be experienced for fans and compressors, where the effect of centrifugal stiffening prevails and increases the natural frequencies especially for bending modes [150]. Another set of lines, characterised by a constant slope, marks the frequencies of various sources of excitation. In the example, the distortions due to adjacent blade rows and burner cans are included. Further flow-field non-uniformities may arise for example due to a rotating stall, cooling jets and wakes from wings or pylons [105]. Mechanical sources such as gear meshing or blade rubbing could also be relevant [170]. The crossings between the two sets of lines identify the conditions where resonant response could potentially occur. The excitations could induce sustained vibrations, imposing alternating stress levels on the blades and leading eventually to a HCF. In order for the resonance to occur, the excited mode shape of the structure must match the circumferential and local excitation patterns [105]. Therefore only some crossings are marked as resonant conditions.

While the effort must be to keep the potentially risky crossings out of the operation range, it is impossible to do so for every one of them, especially for jet engines operating in a wide range of speeds and often undergoing transient procedures. A common design rule is to keep the first bending mode above the first or second EO at top speed and to separate the first and second bending modes [170]. For the other resonant conditions it has to be ensured that sufficient damping is present in the system.

Flutter

Flutter is an aeroelastic instability of a structure surrounded by fluid-flow, for which a small perturbation can trigger self-sustained vibrations. A displacement of a blade modifies the unsteady flow-field, which in turn alters the aerodynamic loading acting on the blade. In the case that the energy absorbed during one cycle of oscillation is greater than the energy dissipated by material or mechanical damping, the amplitude of the motion may grow exponentially until it causes a structural failure. Flutter is regarded as perhaps the most serious danger for blade failures [170], in particular for two reasons. Firstly, the escalation of stresses leading to a failure may be very rapid and usually cannot be stopped once initiated. And secondly, the oscillations are asynchronous and independent of engine orders, which makes them harder to predict in comparison with forced response.

Turbomachine blades bear a geometrical similarity to aircraft wings, but their flutter mechanisms are substantially different. They are characterised by a significantly higher mass ratio, a parameter that compares the mass of an airfoil cross-section with that of a fluid contained in a circumcircle. Therefore, the blades may flutter in a single mode as opposed to aircraft wings whose modes often coalesce [191]. The aeroelastic behaviour of blades arranged on a wheel is also influenced by both a mechanical and an aerodynamic coupling. The former is realized by shrouds located at part-span or connecting the blade tips, either via an interlocking system or by welding the blades together. The purpose of the structural constraints is to increase mechanical stiffness and restrict the range of relative motion for neighbouring blades, helping thus to suppress their susceptibility to flutter [190]. An adverse effect may occur for the so-called *blisks*. They are manufactured from a single piece of material, which removes mechanical damping from the system and leads to an increase of oscillation amplitudes [131].

The aerodynamic coupling effects between the neighbouring blades cause the aeroelastic behaviour of the blade row to be different from that of an isolated blade. The motion of each blade influences the surrounding instantaneous flow field and affects directly the loads acting on its neighbours. The whole blade-row thus forms an aerodynamically interconnected system. Studies have indicated that the stability of an isolated blade and the coupling effects are equally important for flutter characteristics of a blade-row [176]. It has been shown that a blade which is aeroelastically stable in isolation might become unstable when arranged in a cascade [190].

Flutter problems in aircraft engines and power turbines are most likely to occur in the front and aft parts of the machine [105], [190], [191]. Fans and low-pressure compressors as well as low pressure turbines feature relatively long and slender blades subjected to a high loading, which entails an unfavourable ratio of aerodynamic forces and structural stiffness. Similarly, in steam turbines the rear low-pressure stages are the ones most prone to flutter. The self-excited instabilities in compressors are generally classified into 4 categories: subsonic/transonic stall flutter, choke flutter, supersonic stall flutter and unstalled supersonic flutter [170]. The boundaries of the flutter regions are depicted in Fig. 2.3, showing a typical axial-flow compressor map where an operating point is defined by pressure ratio and mass-flow. Additional

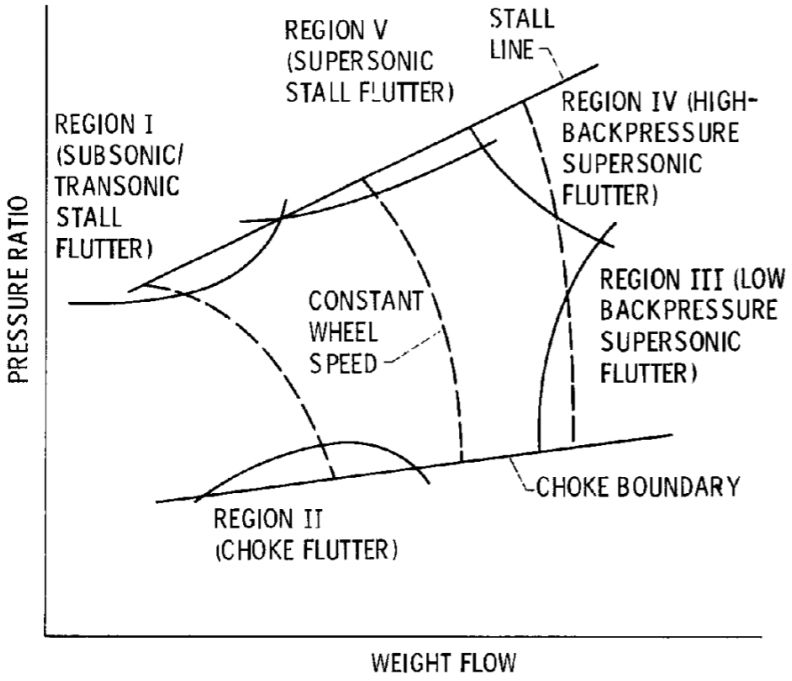

Figure 2.3: Compressor map with flutter boundaries [123]

types of flutter are sometimes considered, such as the acoustic flutter [150].

Subsonic/Transonic Stall Flutter is one of the most common instabilities and occurs at part-speed operation near the surge limit [93]. The angle of incidence is increased, until large separations emerge on the blade suction side. The instability may affect fan blades [170] and up to the first three compressor stages [37]. It is typically encountered for a commercial aircraft flying at subsonic speeds, but with a relative inlet Mach number at fan blades reaching supersonic conditions [131]. The deformations may occur in bending or torsional modes with a sudden onset of coupled modes [170].

Choke Flutter also occurs at a part-speed operation, but for negative incidence angles inducing a choked flow. The region is located below the operation line in the compressor map and the instability is typically encountered for the mid and aft stages of compressors [170]. Strong compressibility effects are presumed to drive the flutter mechanisms, as the in-passage shocks with the associated separation change the effective throat location in time [37].

Supersonic Stall Flutter (high back pressure) may be encountered in fans [170] during the operation at near 100% design speed with high angles of incidence. The region is found above the operation line and it is characterised by a high pressure-ratio, high positive angles of incidence and a strong blade loading. The inlet flow conditions at blade tips are supersonic with a detached bow shock forming at the entrance of each passage [37]. Stalling of the flow together with the shock motion is assumed to influence the aeroelastic stability.

Supersonic Unstalled Flutter (low back pressure) is regarded as perhaps the most serious one because its boundary crosses the operation line near a design point

for the take-off power conditions. Hence it may impose a limit on the over-speed capability of the engine [93]. The instability concerns fan blades with supersonic relative flow speeds in the near-tip region. The rotation speed for the flutter onset changes in function of the blade loading, which is ascribed to the stabilizing or destabilizing effects of the shockwave structure inside the blade passage [37].

Acoustic Flutter describes a special condition when the acoustic waves generated by the vibrating blade are reflected back onto the blade and further enhance the instability of the system [150]. This behaviour can be encountered e.g. due to the interaction between the fan blades and the engine intake.

The unsteady aerodynamics of low-pressure turbines is relatively simpler, as their flow is comparatively cleaner and to a larger extent linear and two-dimensional [191]. Historically, most of the flutter investigations have been targeted at compressors [99] and there is no universally accepted classification of flutter for turbines. A definition of several types of flutter is given by [93]. Potential flutter is experienced for small angles of incidence at a pressure ratio of ≈ 1.5. The oscillations are sustained due to a phase lag between the blade motion and the integral aerodynamic force. Shock flutter is encountered for a higher pressure ratio ≈ 2.0 and the mechanism is presumed to be a separation induced by the shock boundary layer interaction. And finally, for a choked turbine at a pressure ratio above ≈ 3.0 a supersonic flutter may occur.

2.2 Blade Vibration Characteristics and Parameters

Blade vibration and interaction with the surrounding flow is a complex phenomenon, driven by a combination of structural, aerodynamic, and in some cases also acoustic aspects. Srinivasan [170] gives an exhaustive list of 20 parameters influencing the aeroelastic behaviour. In order to gain a deeper understanding of flutter and forced vibrations, the investigation must concentrate on the selection of the most important ones. At the same time, no relevant aspect may be omitted. This section offers an overview of characteristics, parameters and effects influencing blade vibrations and a discussion of their relevance.

2.2.1 Mass Ratio

The relevance of the ratio of wing mass to the mass of the surrounding air was recognised early in the investigation of aircraft wing flutter [190]. The mass ratio μ compares the mass of a wing in cross-section to that of a fluid contained within a circumcircle:

$$\mu = \frac{4m}{\pi \rho_{air} C^2}, \tag{2.1}$$

with m denoting mass per unit of blade span, ρ_{air} fluid density and C blade chord. A graphical representation of the mass ratio is provided in Fig. 2.4. Turbomachine blades are characterised by a substantially higher value of μ, hence the unsteady

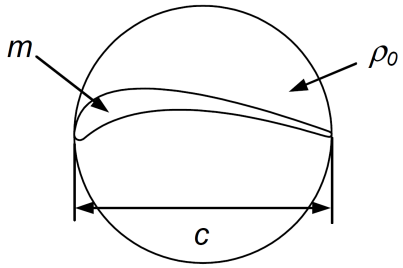

Figure 2.4: Graphical representation of mass ratio [190]

aerodynamic loading has a diminished influence on the structural modes and frequencies. The aeroelastic analysis often goes as far as to neglect this influence entirely and decouple the structural and aerodynamic analysis. In the *energy method*, the eigenmodes and eigenfrequencies are determined in advance by considering the centrifugal loading but not the aerodynamic forces. These *in-vacuo* characteristics are then employed to prescribe the blade motion for an unsteady aerodynamic analysis, whose primary goal is to evaluate the energy transfer between the blade and the surrounding fluid. The work done during one vibration cycle is then expressed in terms of an aerodynamic damping coefficient, whose value is positive in the case that the flow has a stabilizing effect on the blade motion and negative otherwise. It has been argued in the past that the underlying assumption of fluid-structure decoupling may not always hold. Nevertheless, this approach is still popular to date for its favourably low computational requirements and rapidity of evaluation [39]. It needs to be stressed that the coupling effects may become non-negligible for modern composite blades whose mass ratio is typically several times lower compared to a common titanium blade [131].

2.2.2 Reduced Frequency

The reduced frequency $\tilde{\omega}$ is an important parameter for characterising the unsteadiness of the flow. Considering blade oscillations at an angular frequency ω, the time-scale of the induced flow disturbance is $1/\omega$. A second time-scale is defined to express the time taken by the flow perturbation to be convected past the blade. Using a blade semichord [170] as a length-scale, this time-scale is given by $C/(2V)$. The inlet relative velocity is commonly used as the convection speed in the case of compressors, whereas for turbines the exit relative velocity is preferred [191]. The ratio of these two time-scales yields the reduced frequency:

$$\tilde{\omega} = \frac{\omega C}{2V} = \frac{Convection\,time}{Disturbance\,period} \tag{2.2}$$

Another, equivalent interpretation [170] relates the chord length C to the wavelength of a sinusoidal wake formed by the blade oscillations, $l = VT = 2\pi V/\omega$ (Fig. 2.5). The ratio of these two length scales yields $C/l = \tilde{\omega}/\pi$.

In either interpretation, high values of reduced frequency ($\tilde{\omega} \gg 1$) imply that multiple blade oscillations occur as a particle passes along the blade, i.e. the flow varies in

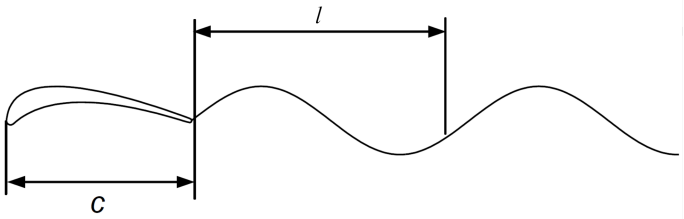

Figure 2.5: Graphical representation of reduced frequency [190]

time very quickly and it needs to be regarded as unsteady. On the other hand, when the disturbance period is significantly longer then the convection time ($\tilde{\omega} \ll 1$), the temporal flow-field changes during the particle passing are negligible and the flow becomes quasi-steady.

Critical reduced frequencies for turbomachine blades lie in the range 0.1 to 1.0 ([170],[190],[99]), for which both the unsteady and the quasi-steady effects play an important role. In general, blades characterised by lower reduced frequencies have a higher tendency to self-excited oscillations [191], [131]. This needs to be considered especially for the aft low-pressure turbine stages operating at high transonic or supersonic flow regimes which yield particularly low values of $\tilde{\omega}$. The current trends in turbomachinery design further promote this issue, as the manufactures of aircraft engines try to maximize the power-to-weight ratio in the endeavour to achieve a better efficiency and fuel economy. Lighter blades with a reduced chord and blade thickness have a lower natural frequency and thus also a decreased reduced frequency. A similar shift of $\tilde{\omega}$ occurs in the case of steam turbines, whose blade length and relative flow velocity are increased in pursuit of higher power output.

2.2.3 Mode Shape

A turbomachine rotor is formed of individual blades mounted on a supporting structure, such as a hub or a disk. The dynamic behaviour of the assembly is a superposition of blade-dominated and disk-dominated modes [190]. The former describe the behaviour of a blade in isolation, whereas the latter characterise the rotor itself with blades attached as passive masses.

Flutter usually occurs in the first few natural blade modes with lowest frequencies [191], such as flexing modes, torsion modes, edgewise bending modes and plate modes [105]. The deformation often happens in a coupled mode, comprising the contents of multiple elementary modes [170]. The three-dimensional modes can be approximated in two-dimensional cuts as a superposition of three fundamental rigid body mode shapes: two orthogonal translations and a rotation with a spanwise-varying amplitude. A systematic investigation of the mode shape relation to the critical reduced frequency was performed by Panovsky and Kielb, who devised a preliminary design tool called the *Tie-Dye* plot [140]. The fundamental idea is to determine for each mode shape the critical frequency $\tilde{\omega}_{crit}$ that corresponds to a neutral aerodynamic damping.

Figure 2.6 gives an example of the Tie-Dye plot. An arbitrary rigid body motion of a

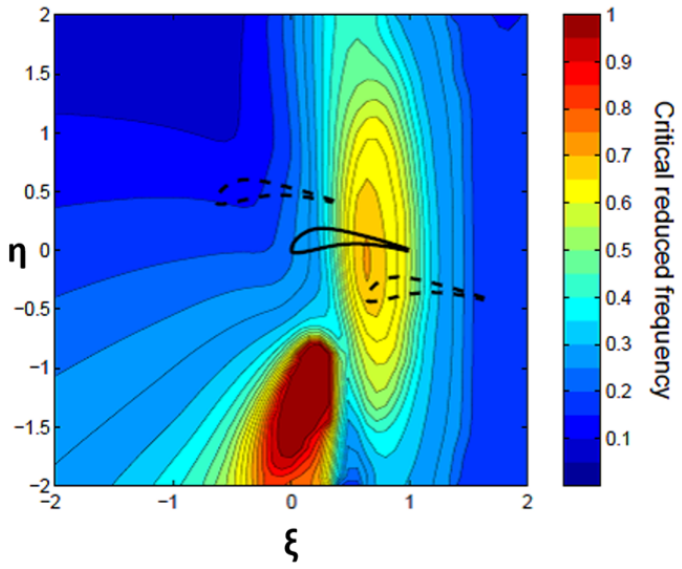

Figure 2.6: An example of the Panovsky-Kielb Tie-Dye plot [191]. Contours of critical reduced frequency in function of the blade torsion axis

2D section can be expressed as a single rotation with an appropriate axis of the pitching motion. The coordinate system is based on two orthogonal, chord-normalized axes: the ξ-coordinate is parallel with the chord-line, the η-coordinate is perpendicular to it and the origin of the coordinate system is at the blade leading edge. For example, the axis position $(\xi, \eta) = (0, 0)$ would represent pitching about leading edge, whereas a bending perpendicular to the chord-line would be characterised by $(\xi, \eta) = (\infty, 0)$. The contours show the value of the critical reduced frequency in function of the torsion axis location, i.e. of the mode shape. In the case that the reduced frequency drops below $\tilde{\omega}_{crit}$ for the given position of torsion axis, the system is aerodynamically unstable and there is a danger of flutter occurring.

Some regions in the plot are characterised by steep gradients of critical reduced frequency, marking a dangerous zone where a slight shift of the torsion axis impacts greatly the flutter boundary. This also illustrates the strong correlation between the mode shape and aerodynamic stability. It has been demonstrated that the Tie-Dye plots are qualitatively similar for different types of turbine geometries, which makes them a useful tool for preliminary design before a more comprehensive but time-consuming aeroelastic analysis is performed [190].

The significance of disk-dominated modes depends on the level of coupling in the assembly. Mechanical coupling is realized via connection to the supporting hub or disk and potentially also by the presence of shrouds. The blades might be tied together to blade packages or over the whole circumference to increase mechanical stiffness. Moreover, the relative motion of neighbouring blades is restricted to a few interblade phase angles [190]. The bladed disk vibrates in assembly modes which may exhibit circumferential variations of displacement amplitudes and thus form a pattern. These modes may represent a standing wave, or a wave travelling in the forward or backward direction relatively to the rotation speed. In the case that this wave travels backwards exactly at the rotation speed, it is identified as a stationary

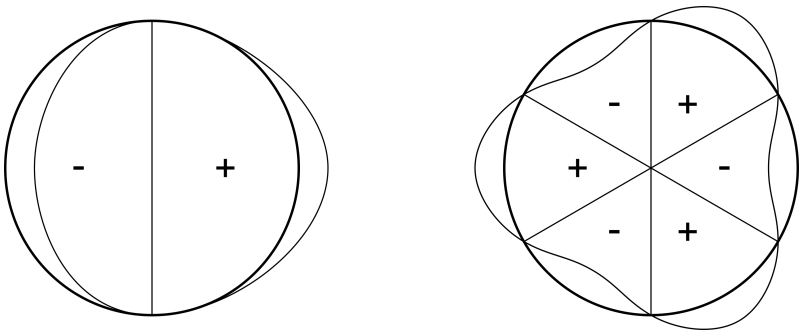

Figure 2.7: Nodal diameter representation: $ND = 1$ (left) and $ND = 3$ (right)

wave and the corresponding rotor speed is denoted as resonant speed [170].

2.2.4 IBPA

One of the most common aeroelastic formulations for blade-row motion is the travelling wave mode. Assuming that all blades are manufactured identically (a perfectly tuned rotor), they will all oscillate with the same mode shape, frequency and amplitude, but with a constant phase-lag between each two neighbours. The concept was first introduced by Lane [111] and used in the aerodynamic theory of Whitehead [195]. The phase-shift is called the interblade phase angle (IBPA, denoted σ) and due to a circumferential periodicity, it can only attain discrete values. The set of *allowable* IBPAs is determined in function of the number of blades included in the blade-row, N_b:

$$\sigma = \frac{2\pi \cdot \mathrm{ND}}{N_b}, \quad \mathrm{ND} = 1, 2, 3, ...N_b \tag{2.3}$$

The nodal diameter (ND) represents the number of diametrical lines that can be drawn to connect blades with zero displacements [150]. In other words, it is the wave-number of the travelling wave [170], as illustrated in Fig. 2.7. According to a convention, the IBPA is positive for a wave travelling in the direction of rotation and negative in the opposite case.

The concept of the travelling wave with phase-shifted, identically oscillating blades allows a great simplification of computational model. This representation is adopted by frequency domain methods and it also enables reducing the computational domain of time-marching methods to a single blade passage. However, the validity of the model always needs to be carefully considered, because real blades are never perfectly identical due to manufacturing tolerances and uneven wear in operation. Some level of mistuning is therefore always present and the extent to which the circumferential periodicity is disturbed needs to be assessed.

2.2.5 Mechanical Damping

The classical technique for the assessment of flutter stability, the energy method, evaluates aerodynamic damping during one cycle of oscillation. Even if the aerodynamic damping is negative, it does not necessarily imply that the system becomes aeroelastically unstable, as the present mechanical damping may be sufficient to suppress the aerodynamic excitation. The level of mechanical damping is also essential to control forced response oscillations amplitude and prevent high cycle fatigue.

Inherent to the bladed disk assembly are material and friction damping. The former describes the dissipation of energy to heat due to material deformation. Its magnitude is proportional to the square of frequency [105], but the contribution to the overall mechanical damping is usually negligible even for higher frequency modes, given the materials typically used for blade manufacturing (titanium and nickel based alloys) [170]. Material damping is therefore usually omitted in aeroelastic models. The major part of mechanical damping is due to friction occurring at the root structure attaching the blade to the disk, and at part-span or tip shrouds. The rubbing at the interfaces is a complex, nonlinear phenomenon, difficult to include in the computational model [170], [37]. The matter is further complicated by the wearing-out of the material due to the friction contact, causing the characteristics to change over time. Additional damping can be introduced into the system by adding blade dampers, installed usually at the blade root. They do not disturb the flow field, unlike shrouds, and they can be applied to *blisks*, characterised otherwise by a lack of mechanical damping due to the absence of rubbing interfaces.

2.2.6 Mistuning

Mistuning describes the measure of deviation of aerodynamic and structural properties from the designed reference values [170]. Although most aeroelastic studies consider an idealised model of a perfectly tuned rotor with identical blades, in reality some level of mistuning always occurs. The causes comprise any circumferential asymmetry, whether dynamic (variation in eigenmodes and eigenfrequencies) or aerodynamic (incoming flow disturbance, operational wear of aerodynamic surfaces). While its presence introduces further complexity into the system, this phenomenon can also be exploited to improve the aeroelastic properties.

Several researchers have investigated alternate frequency mistuning, in which the blade row comprises two sets of blades with distinct eigenfrequencies, arranged in an alternating pattern. Such an arrangement is simple to both analyse and to implement in praxis. Kielb and Kaza [108] show that the locus of the system eigenvalues, characterising the frequency and damping for different IBPAs, develops a waist and breaks into two separate loci when the frequency difference between the two blade sets is increased. Nowinski and Panovsky [139] demonstrated that alternate mistuning can help to reduce susceptibility to flutter in a low pressure turbine. Similar conclusions were reached by Silkowski et al. [162], who have found that any level of alternate stiffness mistuning is beneficial for flutter suppression. Crawley and Hall [29] developed a design procedure to find an *optimum* pattern of structural mis-

tuning and concluded that it resembled an alternate pattern, but broken down at several locations around the rotor. While it offered superior damping compared to the alternate pattern, it was also more sensitive to the level of mistuning and therefore less suitable for practical implementation. The authors also pointed out that unless the blade in isolation is self-damped, no mistuning can achieve aerodynamic stability.

A successful application of deliberate mistuning was performed by the turbine manufacturer Alstom to resolve a flutter instability causing root cracking of last stage steam turbine blades [125]. The potential to aid flutter stability has also been demonstrated for aerodynamic mistuning. Hoyniak and Fleeter [96] presented a model for the analysis of a finite blade cascade with circumferentially alternating blade spacing and found that the region of stability can be enhanced with this type of mistuning.

Overall, mistuning has beneficial effects on the suppression of self-excited vibrations. A flutter analysis using a tuned cascade model is conservative, as any unanticipated mistuning that will inevitably be present in the system will further promote the flutter stability. However, contrary effects have been reported for forced response vibrations. Miyakozawa [131] found that frequency mistuning can amplify the blade vibrations due to structural coupling effects at small nodal diameters. Aerodynamic mistuning also amplified the forced response of a single blade, but the inclusion of structural coupling largely suppressed this effect.

2.2.7 Steady Loading Parameters

Steady loading conditions play a just as prominent role as reduced frequency or mode shape in driving the flutter stability. The parameters that seem to have the most dominant effect are the incidence angle, pressure difference across the blade, flow separation and shock location. Indeed, it is difficult to observe the contributions of individual parameters in isolation, as they are mutually interconnected. A change in the incidence angle modifies the blade loading, affects the shock structure and may induce flow separation. A review of the past research in this area was presented by Vogt [190] and more recently by Waite [191].

The angle of attack, directly influencing the mean loading, was shown to affect negatively the aerodynamic damping of a linear subsonic compressor by Carta and St. Hilaire [21]. Szechenyi [176] observed a reduction of aerodynamic self-damping with the increase of incidence for a compressor blade in subsonic to transonic flow. The coupling coefficients were on the other hand less affected. An increase of the angle of attack can also induce flow separation on the leading edge. He [82] found that the separation bubble has a destabilizing effect on the blade, which is however largely counteracted by a stabilizing influence in the region downstream of the reattachment point. Experimental investigation of LPT flutter, performed by Nowinski and Panovski [139], didn't show the stability to be significantly affected by angle of incidence. Instead, the blade loading was identified as the most influential steady flow condition. An interesting conclusion regarding the influence of steady loading on LPT flutter stability was drawn by Waite [191]. An increase of loading would

have a beneficial effect for some modes, whereas for others it would contribute to a destabilization of the system. The targeted loading might therefore dictate the *allowable* mode shapes for the turbine designer. Passage shock formation was identified as the key factor that drives the mode-dependent flutter sensitivity to loading. A study of the influence of shock pattern on transonic fan flutter was performed by Srivastava [171]. The presence of a normal shock may have both a stabilizing and a destabilizing effect on the blade row stability, depending on the shock location and interblade phase angle.

2.2.8 Acoustic Resonance

Acoustic resonance describes a limit state for which the acoustic waves generated by blade oscillations are on the verge of propagating throughout the domain. The energy transfer due to pressure waves in axial direction affects forced response, whereas the circumferential waves are important for self-excited oscillations [39]. Whitehead [196] divides flutter into three regions based on the axial acoustic wave propagation:

1. Subcritical flutter - no acoustic waves can propagate
2. Acoustic resonance flutter - a pair of acoustic waves is on the verge of propagating
3. Supercritical flutter - at least one pair of acoustic waves can propagate

The plot of aerodynamic damping vs. IBPA is in general a nearly sinusoidal curve. In fact, when only the blade-on-itself damping and the contributions due to the two neighbouring blades are considered, it takes on the shape of an exact sinusoid [140]. In the case that the acoustic resonance conditions occur, this sinusoid is distorted by a sharp and narrow peak, referred to as the *flutter bite*. Its effect on flutter stability may be either beneficial or detrimental. Given that the flutter stability is determined by the minimum aerodynamic damping over the set of allowable IBPAs, the presence of the flutter bite can affect significantly the overall aeroelastic behaviour. Sharp reductions of flutter stability margin were reported by Wu et al. [199] for a jet engine fan. The authors ascribed the occurrence of the flutter bites to the aeroacoustic interaction of the fan with the intake duct.

Lane and Friedman [111] studied the propagation of acoustic waves in a 2D flat plate cascade and derived analytically the acoustic resonant condition. An equivalent formulation may be obtained by setting the time of circumferential propagation of a disturbance equal to an integral number of oscillations plus the phase lag corresponding to the interblade phase angle [39]. The resonant IBPAs are calculated using the relation:

$$\sigma_r = \left(M_\eta \pm \sqrt{1 - M_\xi^2}\right) \frac{M\tilde{\omega}P}{(1 - M^2)C}, \tag{2.4}$$

where M_ξ and M_η are the axial and tangential Mach numbers respectively, $\tilde{\omega}$ is the reduced frequency, P the blade-to-blade spacing and C the chord. Using either the inlet or the outlet Mach number and reduced frequency, we obtain two pairs of resonant IBPAs. Although the flat plate cascade model used in the derivation is strongly simplified and doesn't account for the flow non-uniformity, actual blade geometry or viscous effects, it has been shown to give predictions matching reasonably well with CFD [191].

2.2.9 3D Effects

Three-dimensional flow effects in low-pressure turbines (LPT) are of a lesser importance than in compressors. Past LPT flutter studies have commonly used planar models and also the most extensive publicly available database of flutter measurements, the Standard Configurations of EPFL, contains 2D flutter data [16]. Since approximately the 2000s, the potential relevance of three-dimensionality for aeroelastic stability has started to gain attention.

Sanders et al. [154] investigated numerically and experimentally the flutter stability of a transonic fan. They found the tip clearance to affect significantly both the magnitude and the phase angle of unsteady surface pressure distribution in the tip region, although the effect on time-averaged loading was small. Huang [99] discovered a strong three-dimensionality in the unsteady behaviour of flow in an oscillating linear turbine cascade. In contrast, the tip clearance value exhibited a negligible effect on the aeroelastic stability. An extensive analysis of 3D flutter mechanisms in a LPT was presented by Vogt [190]. Oscillations in bending modes manifested spanwise variations in response magnitude, while the hub and casing proximity effects were observed in a torsion mode. The latter resulted in distinct variations in local stability behaviour. A comparison of 2D and 3D calculations showed a fair agreement in aeroelastic response magnitude, but greater discrepancies were found in terms of phase. McBean et al. [128] validated the results of two-dimensional, three-dimensional, viscous and inviscid simulations against experimental data for a transonic turbine cascade. He concluded that only the 3D Navier-Stoke computations captured correctly the phase angle of unsteady surface pressure distributions, essential for an accurate evaluation of aerodynamic damping. The presented results, however, do not entirely support this conclusion. More recently, a three-dimensional viscous flow flutter analysis for a turbine cascade was presented by Micallef et al. [129]. The investigation concentrated primarily on the evaluation and validation of the performance of two numerical solvers, but a brief assessment of a tip clearance influence on aeroelastic stability was also included. It was found to have a very small effect on the steady aerodynamics at midspan and to be nearly negligible for the aerodynamic damping evaluation.

2.2.10 Multirow Effects

Although flutter stability is often investigated for an isolated blade cascade, in a real turbomachine the interactions with adjacent blade rows may become important. The

unsteadiness induced by the relative blade row motion is superimposed with the flow disturbances generated by the self-excited vibrations, diffusing thus the boundary between flutter and forced response. More over, the pressure waves generated by the oscillating motion of blades may be partially reflected back onto the cascade and influence the flutter stability.

The combined effect of a gust and flutter was investigated by Frey and Fleeter [51] for a three-stage axial flow research compressor. The interaction of the two phenomena depended strongly on the gust-blade motion phase angle, affecting the unsteady lift and moment magnitudes either in a constructive or in a destructive manner. An approach for an efficient capturing of the blade-row interactions was developed by Hall and Silkowski [71]. The unsteady aerodynamic interactions were modelled by pressure and vorticity waves of different circumferential wave numbers and frequencies, denoted *spinning modes*. Reflection and transmission coefficients were then calculated for each mode in each blade row and the individual modes were coupled at the row interfaces. The coupling effects were found to affect significantly the aerodynamic damping and to depend strongly on the axial spacing. A similar observation was made by Li and He [116], who used a three-dimensional time-marching Navier Stokes solver to study the multirow coupling effects on the aeroelastic behaviour of a vibrating compressor rotor. The aerodynamic damping showed a non-monotonic dependence on the axial gap, suggesting the existence of an optimum gap size for flutter stability.

Hall and Ekici [74] employed the method of spinning modes to analyse multistage coupling effects for a flat plate cascade and for a three-stage compressor. They concluded that only the two nearest neighbours had a profound influence on the aerodynamic response of a vibrating blade row. This behaviour was confirmed by Saiz [150], who employed a time-linearised computational model to analyse the multirow coupling effects in a turbine. The blade-row interactions changed the aerodynamic damping by more then 100% for some modal diameters and they were found to have an overall stabilizing effect. Huang [99] studied the influence of upstream stator blades on aeroelastic stability of a low pressure steam turbine rotor. A two-dimensional analysis showed a strong variation of the rotor aerodynamic damping in function of the axial gap. The presence of the upstream stator changed the rotor aerodynamic damping by 35% according to a three-dimensional study.

2.3 Computational Methods - State of the Art

2.3.1 Analytical Approaches

The earliest attempts to solve aeroelastic problems employed analytical methods, based typically on a linearised potential flow theory. Given the complexity of the phenomenon, major simplifications needed to be undertaken to obtain an analytical or semi-analytical solution. The structure was usually represented as a flat plate with zero thickness, facing an inviscid, uniform, incompressible flow either in the subsonic or in the supersonic regime. One may ask whether such simplified models

remain relevant for the modern turbomachines, characterised by a high blade loading, non-uniform three-dimensional flow-field, inherent unsteadiness and complex shock structures. In these conditions, the analytical approaches cannot be expected to yield accurate predictions of aeroelastic instability. However, their computational efficiency allows one to perform large parametrization studies in a short time, which may help to gain insight into the effect of individual parameters. They may also serve to verify novel numerical approaches on basic test-cases.

One of the earliest comprehensive analytical models is Theodorsen's theory [177] which describes flutter onset for an aircraft wing with aileron. The aerodynamic formulation is based on a linearised unsteady potential flow. The theory assumes a sinusoidal motion with infinitely small amplitudes about the position of equilibrium, considering up to three degrees of freedom for the wing-aileron system. Only primary effects are of interest and any secondary effects are neglected (finite wing span, section shape and deviations from potential flow, twisting and bending of actual wing instead of pure torsion and deflection, friction). The aim of the theory is to determine the borderline case for loss of stability, i.e. unstable equilibrium. Theodorsen determines the velocity potentials due to position and velocity of the individual parts in the wing-aileron system, from which the pressure distribution, forces and moments acting on the airfoil and aileron are obtained. The aerodynamic forces and moments are then set into differential equations of motion with the assumption of a purely sinusoidal translation and rotation. The resulting set of equations can be used to calculate the velocity at which the loss of stability occurs. The original report of Theodorsen contains some unclarities and numerical errors, not surprisingly given the complexity of the theory and the limited computational resources at the time of creation. A comprehensive review of the report with newly recomputed results was published by Perry [144].

Several authors later extended Theodorsen's theory for application on blade cascades. Among the most prominent works are that of Lane and Friedman [111] and Whitehead [195]. Strong simplifications remained regarding the representation of both the geometry and the flow. Blades were modelled as flat plates with zero thickness and zero mean incidence, oscillating in a harmonic motion of infinitesimal amplitude. The flow was approximated as inviscid, irrotational and isentropic.

Further development ensued to expand the applicability of the method. The effect of a non-zero mean flow deflection was included by Whitehead [194], while Attasi and Akkai [7, 5] accounted for the actual geometry of the airfoils and the cascade parameters. Both models were, however, based on the assumption of an incompressible flow. Whitehead [196] later adapted the model to compressible flows, although with the restriction of zero mean flow deflection. He showed the increase of Mach number in the subsonic regime to suppress the tendency to flutter predicted by the incompressible theory. A model allowing to investigate the compressibility effect in combination with a non-zero flow deflection was devised by Namba [136].

The need to analyse the aeroelastic behaviour for tips of low-pressure compressor blades motivated a formulation for supersonic flows. Typically, the axial flow is subsonic in turbomachinery flows even with supersonic relative Mach numbers, which complicates the solution. Another difficulty arises in devising a solution for an infinite

cascade [37]. The first model to overcome these complications was developed by Verdon and McCune [188], employing the assumption of an inviscid, two-dimensional, linearised flow-field and neglecting the blade thickness, camber and flow deflection. A similar method was proposed by Nagashima and Whitehead [133], who employed the pressure potential instead of the velocity potential in order to simplify the mathematical formulation. The agreement between the two approaches was shown to be very close. Both works assumed a supersonic underlying flow. However, as pointed out by Goldstein et al. [62], the in-passage shocks in modern compressor and fan tip sections may be strong enough to violate the assumption of an approximately uniform supersonic flow. Hence they introduced an approach treating separately the subsonic and supersonic regions and employing the Rankine-Hugoniot condition across the interface. Unlike the theory for a completely supersonic flow, this model was able to predict the occurrence of a supersonic bending flutter. Another model combining different formulations for subsonic and supersonic regions was introduced by Imregun [102], employing respectively the linearised cascade theories of Smith [167] and of Nagashima and Whitehead [133]. Flutter stability was evaluated with aeroelastic frequency response functions that were obtained by inverting the dynamic stiffness matrix of the aeroelastic system.

The models discussed up to this point operated with the assumption of a two-dimensional flow. Namba and Ishikawa [135] analysed the importance of three-dimensional effects in fan and compressor stages, where the flow varies from subsonic at the hub to supersonic at the tip. They used a lifting surface theory to develop a model applicable to unsteady three-dimensional flows in rotating subsonic, transonic and supersonic annular cascades. They concluded that although the strip theory predicts aerodynamic forces with a good accuracy in supersonic cascades, near the sonic span the three-dimensional effects become substantial. Further development of the approach brought the inclusion of multiple blade-rows, enabling to study the effect of neighbouring blade-rows on flutter characteristics [134].

2.3.2 Frequency Domain Time-Linearised Methods

In spite of the considerable progress in classical methods, even the most advanced ones adopt simplifications that are too restricting to accurately predict aeroelastic behaviour in modern turbomachines. The need to include the effects of the steady blade loading, flow nonlinearity and nonuniformity, viscosity and three-dimensionality yields the search for an analytical or at least semi-analytical solution fruitless. The need for models providing more reliable predictions was felt urgently at a time when performing a discrete non-linear time-marching computation was out of the question due to a lack of computational resources. And to a considerable extent, this limitation still persists today, at least in the industrial sphere which requires running many simulations in as short a time as possible.

The time-linearised models represent the next logical step from the classical theories, as they enable improving the model fidelity while retaining reasonably low computational requirements. An illustrative description of the method is provided e.g. in [37] or [150]. The fundamental concept of flow linearisation in time is shared

with the classical methods. The instantaneous flow-field is represented as a superposition of a steady-state flow and a small unsteady perturbation. Importantly, the underlying flow field may be modelled as nonlinear and nonuniform, enabling to account for geometry effects and transonic shockwave patterns. The superimposed perturbation is assumed as periodic in time, hence it can be expressed as a sum of Fourier modes proportional to $e^{\mathrm{i}\omega_n t}$. By inserting this representation into the flow equations, the time derivative $\frac{\partial}{\partial t}$ is replaced by $\mathrm{i}\omega_n$ and one obtains an additional set of equations for each harmonic. These become mathematically steady and they can be solved with conventional numerical methods, such as finite differences, finite volumes or finite elements. The blade eigenmodes and eigenfrequencies serve as an input for the computation and they need to be obtained a priori from a structural analysis. Aeroelastic stability is then evaluated using the energy method.

The time-linearised formulation offers considerable benefits in terms of computational requirements. The assumption of a chorochronic (temporal and spatial) periodicity allows restricting the domain to a single blade passage for an arbitrary number of blades on the wheel and an arbitrary IBPA. The well-tried acceleration techniques for steady-state computations are applicable, such as preconditioning, local time-stepping and multigrid [150]. The demands on computational resources are thus significantly lower compared to the nonlinear time-marching unsteady simulations, although still much higher than those of the classical methods.

The time-linearised approach may be applied to various aerodynamic theories of different complexity, ranging from a planar potential flow to three-dimensional Navier-Stokes equations. The mean solution may thus account for complex flow characteristics, such as the formation of shocks, boundary layers or turbulence effects. However, the basic assumption of small perturbations superimposed to a steady-state solution remains, regardless of how sophisticated the aerodynamic theory may be. This simplification seems justified for the analysis of flutter onset, but its application to forced response and limit cycle oscillations is more questionable [105]. Moreover, the method does not consider any influence of the unsteady perturbations on the mean flow, hence the time-average of the solution is in fact equal to the steady-state flow. This assumption may yield inaccurate results in the case that strong nonlinearities are present, such as a flow separation or a shock-boundary layer interaction [37].

Linearised Potential Flow Solvers

Potential methods assume that there exists a scalar function ψ such that the flow velocity can be defined as $\boldsymbol{u} = \nabla\psi$. The flow is inviscid, irrotational and isentropic [150]. The latter assumption makes the model unsuitable for computations of transonic flows, as in reality entropy changes across a shock according to the Rankine-Hugoniot relations. An error whose magnitude depends on the strength of the shock is thus introduced into the solution. Moreover, the actual position of the shock is ambiguous since it is not determined by the entropy condition.

Among the first applications of the time-linearised potential flow solvers were the works of Verdon and Caspar [187] and of Whitehead [193]. They studied flutter in torsional and bending modes with a two-dimesional model. Verdon and Caspar used

shock-fitting techniques with supersonic regions embedded on a subsonic flow field and discretised the potential flow equations with an implicit finite difference approximation. The model of Whitehead relied instead on a shock capturing strategy, using the finite element method for discretisation. The effect of entropic, vortical and acoustic gusts on the aerodynamic response of a subsonic cascade was studied by Hall and Verdon [76]. Although linearised Euler methods had already begun to gain popularity at that time, they argued that the potential flow approach is more efficient. Nevertheless, the need to model three-dimensional, rotational flows with strong shocks was never satisfied with the potential methods and caused a shift towards models based on Euler equations.

Linearised Euler Solvers

Techniques based on Euler equations enable capturing accurately shock positions and to resolve correctly the jumps in flow variables across the discontinuity. Therefore, they are much more suitable for the simulation of transonic flows than potential methods. However, the application of time-linearised Euler solvers to unsteady flows with shocks is still problematic due to the assumption of small perturbations. Even a small shift of the shock position induces local jumps in flow variables which cannot be regarded as small relatively to the steady-state flow.

One of the pioneering works on time-linearised Euler-based solvers was performed by Ni and Sisto [137]. Using the assumption of a homentropic flow, they studied unsteady aerodynamics of two-dimensional flat plate cascades in both subsonic and supersonic regimes. Although the presented test-case was rather basic, the method was directly extendable to real geometries and nonuniform inlet flows. Hall and Crawley [73] based their code on Euler equations for a general flow and analysed gust response and self-excited vibrations of a turbine cascade with a realistic blade geometry. The authors used a shock fitting technique requiring that the shock be aligned with a computational grid line on a logically rectangular grid. While this method ensured a good resolution of discontinuities even on a fairly coarse grid, it prevented the applicability to transonic flows on staggered cascades.

A shock capturing scheme would provide a greater flexibility and easier implementation, but its viability in conjunction with the time-linearised methods first needed to be verified. Lindquist and Giles [119] demonstrated the equivalence of the shock fitting and shock capturing approaches for conservative schemes on a shock tube problem and on a variable-area duct. An application of the shock capturing technique to more complex cases was presented by Hall et al. [69], who analysed two- and three-dimensional unsteady transonic flows in cascades. They stressed the requirement of scheme conservativity and observed that the time-linearised solutions were in an excellent agreement with non-linear time-accurate methods. An improvement in accuracy was brought by performing the calculations on deforming grids, such that the grid points on the blade surface moved together with the blade. This procedure was employed by Holmes and Chuang [94] and by Hall and Lorence [70] in order to eliminate the error in extrapolation of flow variables from the grid boundary to the instantaneous airfoil position. Multiple works on turbomachine aeroelasticity

using a three-dimensional time-linearised Euler method with moving grid have since been published, for example the paper of Marshal and Giles [124].

Linearised Navier-Stokes Solvers

Euler-based methods cannot account for viscous effects such as wakes, boundary layers, flow separation and stall, secondary flows, etc. For this reason, some time-linearised solvers incorporated the Reynolds-Averaged Navier-Stokes equations (RANS). Among the first was the two-dimensional model of Clark and Hall [26], based on RANS equations with the Spalart-Allmaras turbulence model. Their paper presented an analysis of flutter stability for a fan at design point and at an off-design condition with high-incidence stall. They validated the model by comparison with experimental data and with the results of a nonlinear time-domain Navier-Stokes solver and observed a satisfactory agreement, in spite of the limitations coming from the two-dimensionality of the model. A three-dimensional study was performed by Sbardella and Imregun [155], who discussed the correct approach for the linearisation of the turbulence model and wall functions. Campobasso and Giles encountered a numerical instability using preconditioned multigrid iteration in their time-linearised NS solver and evaluated the behaviour of complex stabilization algorithms in a series of papers [19, 18, 20]. A more recent example of aeroelastic analysis using a time-linearised Navier-Stokes code was shown by Petrie-Repar et al. [145]. They performed flutter computations of a last-stage steam turbine blade in 3D, employing the Spalart-Allmaras turbulence model, an equilibrium wet-steam gas model and a three-dimensional non-reflecting boundary condition.

2.3.3 Nonlinear Frequency-Domain Methods

The time-linearised methods offer great benefits in computational costs compared to time-domain approaches. Casting the equations into the frequency domain allows one to limit the computational domain to a single blade passage and to apply acceleration techniques developed for steady state solvers. However, the nonlinear interactions between the unsteady perturbations and the mean flow are completely neglected. It is assumed that the time-averaged flow-field is exactly the same as the steady-state one. Therefore, the technique is limited to small-disturbance flows, for example flutter onset. Cases with large unsteady displacements, such as limit-cycle oscillations, cannot be simulated with this approach. Further research concentrated on techniques which would exploit the advantages of frequency-domain methods while capturing the nonlinear unsteady interactions. An illustrative review of the most popular approaches is provided by Saiz [150].

SLIQ Approach

Among the first efforts to incorporate nonlinear unsteady effects in the time-averaged solution was the SLiQ (Steady Linear Quadratic) method of Giles [57], based on an

earlier work by Adamczyk [4]. In contrast with the traditional time-linearised approach, the expansion series of the flow variables includes also the quadratic term. The time-average of this term is non-zero, therefore the mean-flow solution is no longer identical to the steady state flow. The method requires that three sets of equations are solved. The steady-state flow and the first order unsteadiness are calculated analogically to the time-linearised methods and an additional set of equations is used to determine the second order term. Finally, the time-average of the quadratic term serves to correct the solution of the mean flow.

An essential drawback of the SLiQ approach is that the loop is not closed and there is no feedback from the corrected time-averaged flow onto the unsteady flow perturbations. The implications are twofold. Firstly, the corrections to the steady-state flow due to unsteadiness are based solely on the steady-state solution and the linearised perturbations, although the assumption of their inadequacy is the actual reason for choosing this method over the traditional time-linearised approach. Secondly, application of this technique does not affect the linearised unsteady terms, hence it does not offer any benefits over the time-linearised methods for an aeroelastic analysis. Instead, it is rather suited for unsteady multistage flow calculations it was originally developed for.

In spite of these drawbacks, the method still enjoys some popularity to this day thanks to the low computational costs. Jocker [105] employed the SLiQ approach for the unsteady flow analysis of a transonic high-pressure turbine stage with a prescribed incoming gust. One of the more recent applications was shown by Torkaman et al. [181] regarding a flutter analysis of the 4^{th} stage of an industrial gas turbine.

Nonlinear Harmonics

Aiming to address the shortcomings of the time-linearised techniques and of the SLiQ approach, Ning and He [138] developed the nonlinear harmonic method (NLH). The harmonic series approximating the unsteady flow is expanded around the time-averaged flow rather than the steady-state one. Similarly to the time-linearised approach, one obtains equations for the mean flow and for the individual harmonics. However, extra terms are generated in the momentum and energy equations for the mean flow, in the same manner that Reynolds stress terms appear in RANS equations. These terms are referred to as *deterministic stresses* [150] and they convey the effect of flow unsteadiness on the time-averaged solution. The equations are closely coupled and they need to be solved interactively, preferably via a simultaneous pseudo-time marching procedure.

The NLH technique retains most of the advantages of the time-linearised methods in terms of computational costs. The equations are mathematically steady, hence the traditional acceleration techniques for steady flow solvers are applicable, such as multigrid or local time-stepping. Moreover, the domain can be limited to a single blade passage even for multistage computations with arbitrary blade counts. Although the CPU time increases by about 60% compared to the time-linearised harmonic methods [138], it is still much lower than in the case of nonlinear time-marching solvers. Depending on the number of included harmonics, the reduction of computational

time may account up to one or two orders of magnitude [189, 192].

In their original publication, Ning and He [138] demonstrated the benefits of the NLH approach on the case of a supersonic compressor cascade with oscillating blades. The results were compared with a time-linearised method and with a nonlinear time-marching computation. A substantial improvement in accuracy over the time-linearised approach was shown, as the unsteady blade-pressure distributions achieved a much closer agreement with the time-marching solution.

The method was originally developed as a single blade-row model, but it was soon extended to multirow calculations. Chen et al. [24] employed NLH to study a three-dimensional stator/rotor compressor stage and found a good agreement with the results of a nonlinear time-marching computation. Compared to a steady-state computation, NLH was able to recover 90% of the interface mixing loss generated when the first two harmonics were included. He et al. [86] showed that the method can be successfully employed for the analysis of a circumferential aperiodicity in multi-stage simulations. The authors evaluated clocking effects in a two-and-a-half-stage transonic compressor, concluding that the rotor-rotor interaction is much stronger than the stator-stator one. The interference between upstream rotor wakes and downstream rotor passage shockwaves was proposed as the possible mechanism behind this behaviour.

Thanks to its advantageous combination of low computational demands and capability of capturing nonlinear unsteady effects, the method became widely used also outside of the academic environment. Vilmin et al. [189] presented the implementation of NLH into the commercial RANS solver Numeca FINE/Turbo. They provided several analytical examples for validation as well as two more complex industrial applications of a radial turbine and a 4-stage transonic compressor. The method was shown to improve substantially the time-averaged flow predictions and to resolve unsteadiness accurately, providing that a sufficient number of harmonics was included. The FINE/Turbo package was also used by Wang and Liu [192] to study a counter-rotating research compressor, comprising the inlet guide vane, two rotors and the outlet guide vane. The results of the NLH computations were validated by comparison with experimental data and with time-domain simulations. The performance of the compressor was analysed at the design point and at off-design conditions. The authors concluded that the NLH predictions achieved a good accuracy especially for the design point, while reducing the computational demands considerably compared to the time-domain approach.

Harmonic Balance Method

The nonlinear harmonic method offers a substantial improvement in fidelity compared to the time-linearised approach. It accounts for nonlinear unsteady effects and treats accurately cases with large displacements. However, a certain limitation persists in that there is no direct interaction between unsteady phenomena of different frequencies. The only connection between different temporal harmonics is via the time-averaged flow. This shortcoming is addressed by the harmonic balance (HB) method of Hall [75] which accounts for the nonlinear interaction between several

harmonics at the same time.

The approach exploits the assumption of temporal periodicity to represent the flow variables with a temporal Fourier series whose coefficients vary spatially. The straightforward approach would be to substitute this representation into the flow equations and obtain a harmonic balance form for the unknown vector of Fourier series coefficients. Although the method can be applied in this form and produces accurate flow solutions, it has some major drawbacks. The calculation of harmonic fluxes is difficult and computationally expensive, requiring N^3 operations (N being the number of harmonics included in the Fourier series). Moreover, the approach is not applicable to complex turbulence models [72].

The authors proposed an alternative technique. The Fourier coefficients can be reconstructed from the knowledge of the temporal behaviour of conserved variables and fluxes at $2N + 1$ equally spaced points over one temporal period. The solution procedure starts with generating grids for $2N + 1$ time levels. On each of these grids, the solution is calculated conventionally by pseudo-time marching to a steady state condition. The solutions on the different time levels are coupled via a spectral derivative term and via periodic boundary conditions. A notable drawback of this approach is that the need to compute $2N+1$ steady-state solutions increases significantly the CPU cost compared to the time-linearised techniques. The computational demands are thus brought closer to the nonlinear time-marching methods. Another potential limitation is found in the number of harmonics that can be included in the solution. Hall et al. [75] performed tests with 1, 3, 5 and 7 harmonics and experienced a failure to converge for the case $N = 7$. They concluded that this did not represent a serious problem, as a lower number of harmonics is sufficient to capture accurately the zeroth and the first harmonic components of the unsteady flow.

The harmonic balance method achieves a significant improvement in fidelity compared to the conventional harmonic time-linearised techniques. The nonlinear interactions are modelled not only between the time-averaged solution and the harmonic unsteady perturbations, but also between the different temporal harmonics. No assumption is made about the size of the unsteadiness, which enables treating phenomena characterized by large displacements, such as limit cycle oscillations. As Hall et al. [75] point out, the method bears some similarities to the dual time stepping method. However, thanks to using the spectral time derivative instead of a finite difference scheme, the number of time levels per period may be reduced significantly.

The approach has been successfully applied for example to the simulation of a transonic front stage compressor with oscillating blades [75], a study of nonlinear effects in relation to flutter onset and limit cycle oscillations of a transonic airfoil [179] and a multirow computation of an axial turbine with 1.5 stages [32]. The authors of the latter paper performed the simulations with an implementation of the harmonic balance method in the commercial solver Star-CCM$^+$. Overall, the studies demonstrate that the harmonic balance method yields results in close agreement with the time-marching techniques. In spite of the increased computational demands in comparison with the time-linearised techniques, the method still achieves a considerable CPU time reduction relatively to the time-domain simulations. Depending on the

test-case configuration, the computational cost may be decreased by more than one order of magnitude [32].

2.3.4 Nonlinear Time Marching Methods

The most comprehensive approach for the simulation of unsteady flows is represented by the nonlinear time-marching methods. No assumptions are made regarding the size of unsteadiness, which enables performing large-displacement aeroelastic computations with all types of nonlinear effects included. While the state-of-the-art frequency domain techniques can also be employed successfully for such simulations, the time-marching approach in addition permits to calculate transient phases and to account for aperiodic phenomena. The major drawback of this high-fidelity approach is in the increased computational costs, especially in the case of three-dimensional, viscous multi blade-row simulations. Even nowadays, it is prohibitively expensive for a routine application in the industry.

The use of the Direct Numerical Simulation (DNS) or Large Eddy Simulation (LES) for aeroelastic analysis is usually too costly even in the academic environment. The flow equations are therefore typically solved with the RANS approach, employing various turbulence models. The governing equations are integrated in time, starting from initial conditions, until a periodic flow pattern is established. The computational time depends on the number of iterations and thus on the timestep size. Its selection is limited by the requirements to retain numerical stability and to achieve the desired temporal accuracy. Time is a meaningful physical quantity in unsteady simulations, which rules out the application of local time-stepping, commonly used for the acceleration of steady-state computations. The maximum allowable timestep for the traditional explicit time integration schemes is thus determined by the stability limit of the finest cells. In the case of viscous simulations, these are found in the near-wall regions and they need to be very thin in order to resolve the boundary layers. The timestep thus becomes too small for practical use. Moreover, the global time-stepping also yields the multigrid acceleration technique ineffective [97]. Several techniques have therefore been proposed to accelerate the computations. He [81] devised a time-consistent scheme, employing two meshes. The motivation was to achieve spatial accuracy corresponding to a basic fine mesh, while a coarse mesh was applied locally in the near-wall regions to increase the allowable timestep length. This method is not fully time-accurate and it has been shown to produce some discrepancies in modelling the time-resolved skin friction and pressure distribution on stator and rotor blades [97]. An alternative strategy is the fully implicit dual time-stepping method of Jameson [103]. The integration in physical time is realized via external Newton iterations, while a pseudo-time is introduced to drive the solution to convergence within each external iteration. The pseudo-time integration enables using acceleration techniques developed for steady state flows and the physical timestep restriction is relaxed thanks to the implicit outer iterations.

An important issue related to the time-domain aeroelastic computations is accounting for the time-varying computational domain due to the movement and deformation of solid bodies. Traditionally, fluid dynamics solutions employ Eulerian repres-

entation where the mesh is fixed in space and the fluid particles travel from one cell to another. On the other hand, Lagrangian formulations with cell vertices following the motion of associated material points are usually used in solid dynamics. In order to account for the deforming fluid-domain boundaries while preserving the independence of particle and mesh motion, the Arbitrary Lagrangian Eulerian (ALE) technique was devised [92]. It allows one to choose arbitrarily the motion of the grid vertices in a way deemed suitable for the particular problem. In the case of an aeroelastic analysis, the grid vertices on the solid surface typically follow its motion in a Lagrangian fashion and the inlet and outlet boundaries remain fixed in space analogically to an Eulerian representation. The motion of the inner mesh vertices represents an additional problem to the investigated fluid-structure interaction. The remeshing algorithm needs to be fast as the vertex movement is performed in every iteration. It also needs to be robust and fully automatic, without requiring any user input throughout the run of the simulation. And finally, good cell quality has to be ensured in order to maintain satisfactory solution accuracy and avoid solver divergence.

Various strategies have been devised in the past to address the problem of mesh movement due to domain deformation. Batina [9] developed a linear spring analogy algorithm for unstructured grids, modelling each edge of a tetrahedron as a spring with stiffness inversely proportional to the edge length. In each step, the mesh motion was realized by an iterative predictor-corrector algorithm. This method was successfully applied to computations of oscillating wings and airfoils with relatively small displacements [46, 30], but it was prone to produce invalid triangulations in the case that significant deformations were involved. Degand and Farhat therefore proposed a more robust torsional spring method, designed to prevent a vertex from crossing an edge or a face of an element [33]. Structured grid movement on a single-block domain may also be realized by a transfinite interpolation (TFI) [44]. Hybrid strategies have been used for multiblock meshes, employing the TFI within each block and the spring analogy [77] or a master/slave strategy [107] to move the block boundary vertices. A popular approach is based on treating the mesh as an elastic solid body and solving partial differential equations to obtain an updated configuration in each iteration. The desired characteristics of the mesh movement can be achieved by selectively adjusting the stiffness of individual elements based on their shape and volume changes [173]. An optimization step may also be included in order to improve the cell quality or to cluster cells in regions with large solution gradients [151, 98]. If the domain deformation becomes too large, it may no longer be possible to achieve satisfactory cell quality only by the movement of nodes. In that case it may be necessary to remesh the region completely and interpolate the solution from the original mesh onto the new one.

We have outlined in the Sec. 2.3.2 that the frequency domain methods have progressed from employing a simple flow representation, such as potential equations for planar flow, to complex flow models accounting for three-dimensional geometries, compressible effects, blade-row interactions and viscous phenomena. A similar historical development can be observed also for the nonlinear time-marching calculations. The pioneering time-domain analyses of aeroelastic effects employed two-dimensional Euler equations, such as the work of Fransson and Pandolfi [48]

on vibrating cascades with thin blades in a subsonic compressible flow. Extensions to quasi three-dimensional models were soon presented for example by Gerolymos [55] and by He [80] and a fully three-dimensional analysis of vibrating transonic compressor cascades ensued [54]. These early works relied on the generally accepted assumption that viscous effects are not relevant for aeroelastic investigations, except in the stall and choke flutter problems [11]. Later research showed that they may significantly affect aerodynamic damping in some cases, driving its value in either direction. Grüber and Carstens [64] identified the underlying mechanism as the viscous shock - boundary layer interaction. In order to reduce the increase of computational demands due to the inclusion of viscous effects, simplified formulations were initially used before proceeding to full Navier-Stokes equations. He and Denton modelled viscous effects by coupling integral boundary layer equations with inviscid Euler equations [83, 84] or by neglecting the viscous term in the energy equation and employing the thin-layer assumption for the viscous terms in the momentum equations [85]. One of the first time-domain aeroelastic models based on RANS equations was developed by Huff [101], who computed two-dimensional transonic flow over isolated and cascaded airfoils using the Baldwin-Lomax turbulence model. Further progress in turbulence modelling and the increase of computational power enabled capturing the viscous effects with ever-increasing fidelity and three-dimensional RANS computations have since become widely used in aeroelastic analysis [162, 156].

While the evolution of the aerodynamic model bears similarity with the frequency domain techniques, an aspect specific to the time-domain methods concerns the efforts to alleviate the CPU demands by reducing the computational domain. The most straightforward approach is to employ a whole-annulus model containing the complete blade-rows in the computational domain. However, this technique is too costly for most applications, which stimulated the development of more efficient models exploiting the inherent chorochronic periodicity of turbomachinery flows. The core of the solution strategy, such as spatial discretisation and temporal integration, is adopted from the whole-annulus model. However, the formulation of special boundary conditions allows one to reduce the domain extent to a single passage per blade row in some cases.

Whole Annulus Model

The whole-annulus representation is the most comprehensive and enables capturing complex unsteady flow fields inclusive of aperiodic phenomena. However, the high modelling fidelity comes at the cost of increased computational requirements, especially in the case of multi blade-row simulations. A common practice is therefore to find periodically repeating sectors and to reduce the computational domain to a single one of them, applying direct periodicity boundary conditions. For example, in the case of a single-stage computation with 46 stator blades and 69 rotor blades, the highest common factor is 23 and the domain can be truncated to just 2 stator and 3 rotor blade-passages. This approach has some notable limitations. Firstly, one forsakes modelling of aperiodic effects, occurring for example in multirow computations with more than 2 stages [150]. For the same reason, the method cannot

be used for an aeroelastic analysis of mistuned blades. Perhaps more importantly, the domain truncation often cannot be applied to real turbomachines, as the blade counts typically have no high common dividing factors.

In order to resolve the latter issue, a domain scaling technique became widely used in the industry. The blade counts are altered, such that the greatest common factor is increased and the computational domain can be reduced more substantially. This modification inevitably results in a change of the stage geometrical properties, such as the pitch to throat ratio, pitch to chord ratio, blade curvature or trailing edge thickness. The blades are either restaggered, reskewed or scaled, depending on which parameters are chosen to be preserved [159]. However, strong evidence has been produced that although this approach achieves reasonable accuracy for the time-averaged results, the unsteady flow field may be predicted incorrectly in terms of the magnitude and phase of the unsteadiness [25]. The domain scaling approach is therefore not at all suitable for aeroelastic computations where the accurate prediction of unsteady blade pressure phase and magnitude is of essence.

The remarkable rise in computational power has only recently allowed three-dimensional, viscous flow flutter studies on whole-annulus domains to be performed. Peng [143] investigated the effect of tip clearance on compressor rotor flutter induced by tip vortices. He first computed a steady-state solution with a multirow single-passage model and used it to prescribe the initial and boundary conditions for a whole-annulus single-blade-row flutter computation. Salles and Vahdati [152] analysed the effects of mistuning on fan flutter. They performed whole-annulus time marching computations to validate their aerodynamic influence coefficient method developed for rapid aeroelastic evaluations.

Single Blade-Passage Model

The efforts to reduce the computational domain to a single blade passage per blade-row can be traced back to the earliest unsteady nonlinear time-marching computations. The approach first appeared in the work of Erdos [43], who calculated a 2D inviscid unsteady flow in a transonic fan stage. He formulated phase-shifted boundary conditions using the inherent chorochronic periodicity. In the case of steady-state flows, or unsteady flows with an equal stator and rotor pitch P, the periodic boundary condition simply expresses that the solution at one periodic boundary is equal to the solution at the other periodic boundary:

$$\phi(x, y, t) = \phi(x, y + P, t) \tag{2.5}$$

If we consider an arbitrary pitch ratio, a relation between the two periodic boundaries still exists, but now it needs to take into account the time lag Δt given by:

$$\Delta t = \frac{P_s - P_r}{\omega_{rot} r}, \tag{2.6}$$

where P_s and P_r are the stator and rotor pitches respectively, ω_{rot} is the rotational

speed and r radius. The lagged periodic boundary condition for the rotor is then expressed as [60]:

$$\phi(x, y, t) = \phi(x, y + P_r, t + \Delta t) \tag{2.7}$$

Although the phase-shifted boundary conditions were derived to calculate unsteady blade-row interactions, they are just as well applicable to flutter computations using the travelling wave mode with a constant interblade phase angle. The implementation of Erdos required storing the solution history at both periodic boundaries over the course of the last period and reintroducing it later to update the solution. This technique, which became known as the direct store method, offered a substantial reduction of CPU time compared to whole-annulus simulations. On the other hand, the necessity to store the solution histories imposed large requirements on computer memory.

An alternative method for reducing the domain extent to a single blade passage, called time-inclination or time-tilting, was introduced by Giles [60]. The motivation behind this approach is to enable imposing a simple spatial periodicity condition to unsteady flows, just as it is possible in the steady-state case. Instead of considering all points in the computational domain to be at the same physical time-level in the given iteration, the computational plane is sloped in time. If a point at one periodic boundary is at a time t, the corresponding point at the other boundary is at a time $t + \Delta t$, with Δt being the time lag given by Eq. 2.6. In mathematical terms, the idea is to perform a coordinate transformation:

$$\tilde{x} = x, \quad \tilde{y} = y, \quad \tilde{t} = t - \left(\frac{\Delta t}{P_r}\right) y \tag{2.8}$$

The computational plane at each iteration is now given by $\tilde{t} = const$ and simple periodic boundary conditions can be applied, disposing of the large memory requirements characteristic for the direct store method. However, there exists a limitation on the slope of the time-inclination, given by the characteristics of the governing equations. For stator-rotor interaction computations with single blade passage per blade-row, the pitch ratio must not exceed the value of 1.5. This also imposes a significant restriction for the application range of IBPA in flutter simulations.

Another formulation of the phase-shifted boundary conditions for single-passage computations was proposed by He [80] as a *shape-correction* method. In order to dispose of the excessive memory load required by the direct store method of Erdos, the temporal evolution of the variables at periodic boundaries is represented by a Fourier series. Only the first few Fourier coefficients are stored as opposed to the entire solution history over the last period. The memory saving is thus comparable to the time-tilted approach of Giles without the limitations on blade count ratio or IBPA. Moreover, the shape-correction method was later updated to include multiple perturbations [87]. Its applicability hence extends to computations with multiple rotating blade-rows that are not possible with the other two methods.

Each perturbation is assumed to have its own phase-shifted periodicity, character-

ised by a spatial wavelength and a constant circumferential travelling speed. The unsteady change of flow variables induced by the i-th perturbation can be approximated by Fourier series according to the following relation:

$$\phi_i(x,y,z,t) = \sum_{n=1}^{N_{fou}} \left[A_{ni}(x,y,z) sin(n\omega_i t) + B_{ni}(x,y,z) cos(n\omega_i t) \right], \tag{2.9}$$

where ω_i is the disturbance frequency and N_{fou} is the number of included harmonics. The unsteady flow at any point of the periodic boundary can be expressed by adding a time-averaged part ϕ_0 to the sum of all considered disturbances:

$$\phi(x,y,z,t) = \phi_0 + \sum_{i=1}^{N_{dst}} \phi_i(x,y,z,t) \tag{2.10}$$

In a typical flutter computation based on the travelling wave formulation with a constant IBPA, the number of disturbances N_{dst} would be equal to one. In the cases where there are multiple phenomena of different frequencies present, such as flutter under distortion or multirow interactions, one needs to consider carefully the number of disturbances. If the nonlinear interactions between the fundamental perturbations are strong, it may be necessary to include not only the fundamental frequencies, but also their combinations [87].

The shape-correction method was applied successfully to investigate oscillating blades subjected to inlet and outlet perturbations [87, 86] or intra-row interactions in a one-and-a-half stage transonic compressor [117]. Both applications required the treatment of multiple perturbations with different frequencies and wavelengths, which is not possible with the direct-store and time-tilting techniques. Moreover, the shape-correction method does not impose excessive memory requirements unlike the direct-store technique. In spite of the extra effort related to the boundary condition treatment, a reduction of computational time by the factor of 5-10 was observed in comparison with whole annulus simulations [86]. At the same time, it achieves a comparable accuracy, providing that each perturbation can be represented by a constant frequency and interblade phase angle. This may not be the case for multi blade-row simulations with more than two rows. It has been shown that a three blade-row simulation includes some aperiodicity generated by the unsteady interaction between the first and the last blade-row, hence the shape-correction is not completely accurate for such applications [150].

Non-Reflecting Boundary Conditions

The compact spatial arrangement of turbomachines requires that the inlet and outlet boundaries are placed close to the blades. Any perturbation formed at the boundary thus directly impacts the near-blade flow solution. Great attention therefore needs to be paid to the formulation of boundary conditions, such that the contamination of flow solution with spurious wave reflections is prevented. Most often, the issue is

addressed either by adding a buffer layer to absorb the propagating waves, or by adopting a boundary condition designed to suppress the wave reflections.

The first approach, involving a modification of the computational grid or the governing flow equations, is found for example in the works of Hayder et al. [79] or Zhang et al. [201]. The latter strategy typically builds upon the theory of non-reflecting boundary conditions formulated by Giles [58, 61, 59]. The theoretical foundations for his research stem from the work of Kreis [110] who examined the well-posedness of initial boundary value problems for hyperbolic systems. A physical interpretation in terms of wave propagation was subsequently provided by Higdon [89]. Engquist and Majda [42] introduced a hierarchy of non-reflecting boundary conditions for multi-dimensional problems.

A majority of the previously published literature on non-reflecting boundary conditions had been written by mathematicians for mathematicians, which reduced its accessibility to those with an engineering background. Giles' major contribution is in formulating the theory such that its understanding doesn't require the knowledge of a complex mathematical apparatus and in presenting an application to Euler equations. His work reached wide popularity and gave impulse to further research on non-reflecting boundary conditions.

The methodology of Giles is based on linearised Euler equations and the assumption of wave-like perturbations around a mean flow state. An eigenvalue problem solution allows one to distinguish between the waves entering and leaving the domain for each spatial and temporal perturbation mode. The boundary condition can thus be defined such that undesired incoming perturbations are avoided. The general formulation is non-local both in time and space, which lead Giles to propose several simplified definitions. The *2D Exact Steady NRBC* considers only spatial perturbations and disposes of the necessity to perform the temporal decomposition. For unsteady flows, a *2D Approximate Unsteady NRBC* is suggested, local both in time and space and based on a second-order Taylor series expansion about a 1D boundary condition. However, its non-reflecting properties are compromised for the sake of well-posedness, and spurious reflections may be produced for modes with large circumferential wave numbers [61]. A higher-order approximation was introduced by Hagstrom [67] and shown by Henninger et al. [88] to achieve superior non-reflecting properties compared to the original formulation of Giles.

Chassaing and Gerolymos [23] presented an implementation of *Spectral boundary conditions* in a time-domain solver. The method is exact for linearised Euler equations and involves two-dimensional space-time Fourier transforms. The authors tested its behaviour on the propagation of acoustic waves in a uniform mean flow, where it exhibited superior reflection properties to Giles' approximate condition, albeit at the cost of slower convergence. Schlüß et al. [158] and Schlüß and Frey [156, 157] reimplemented the Spectral boundary condition with the purpose of enhancing its applicability by taking into account the specifics of time-domain solvers. They applied the Spectral NRBC to a flutter computation of a steam turbine stage and highlighted its favourable non-reflecting properties. While the method required about twice as many steps to converge as the one-dimensional boundary condition, no stability issues were encountered in contrast to previous implementations.

Moreover, the results showed little sensitivity to boundary position, allowing one to use a truncated domain and reduce the computational effort per step thanks to a lower number of cells. Sivel [163] exploited the possibility to decrease the computational requirements of the Spectral NRBC by reducing the set of temporal harmonics employed in the modal decomposition.

2.3.5 Fluid-Structure Coupled Methods

Uncoupled approaches, such as the energy method, are widely used for aeroelastic analysis in turbomachinery. It is assumed that the effect of aerodynamic forces on the change of structural dynamics can be neglected thanks to the large density ratio between fluid and structure. The analysis is performed only for one mode and frequency at a time, ignoring thus any potential mode coupling. While the underlying assumptions may hold for conventional turbomachinery blades with high mass ratio and stiffness, their validity has been questioned for modern lightweight designs with long and slender blades, fabricated possibly from composite materials. For such applications, it may be necessary to include the full fluid-structure coupling in order to obtain realistic results.

Several studies have been published on the validity of uncoupled methods for modern blade designs. Li and Sheng [118] combined unsteady potential flow solution with a two DOF structural model to investigate the stall flutter of a transonic fan. They emphasized the importance of bending and torsion coupling effects which cannot be modelled with the single-mode energy method. A similar conclusion was reached by Srivastava and Reddy [172] in their study comparing three flutter prediction methods. Moyroud et al. [132] investigated the limitations of the energy method in relation to the fan blade material. Significant discrepancies appeared in the predictions obtained with the coupled and uncoupled approaches. The errors associated with the natural frequency assumption and with the single-mode assumption were of a similar gravity. A shift in the blade vibration frequency from its natural frequency was observed also by Sadeghi and Liu [149], the effect being more pronounced for lower mass-ratio configurations. Chahine et al. [22] investigated the discrepancy between coupled and uncoupled flutter predictions by a parametric variation of mass ratio and blade stiffness. The two approaches showed a very good agreement in the case that only one parameter in isolation was varied from the baseline full titanium blade. However, a combined variation of both parameters magnified the coupling effects and caused a substantial decline in accuracy of the energy method.

In order to capture the fluid-structure coupled problems in all its complexity, one needs to resort to discrete time-marching methods. Flow is represented by a nonlinear model based on the Euler or Navier-Stokes equations, while the structural dynamics is usually sufficiently approximated by a linear elastic model. The dynamic equation of the body motion is given by [22]:

$$M\ddot{\boldsymbol{x}} + B\dot{\boldsymbol{x}} + K\boldsymbol{x} = \boldsymbol{F} \tag{2.11}$$

Here the mass matrix M, the structural damping matrix B and the stiffness matrix

K characterize the structure, while the aerodynamic force $\boldsymbol{F}$, corresponding to the nodal displacement vector $\boldsymbol{x}$, is obtained from the flow solution. This formulation allows a certain flexibility in selecting a particular model for the approximation of either part. For example, the structural models can range from solid blade sections to 3D finite elements and the aerodynamic solution may vary from a 2D potential flow model to 3D RANS equations. An important part of the solution procedure is the exchange of information between the structural and aerodynamic domains. Based on the degree of coupling, the aeroelastic models can be generally classified as directly or weakly coupled.

Directly Coupled Methods

The governing equations for fluid and structure are solved simultaneously within an interconnected time-marching procedure. A full two-way coupling is ensured throughout the computation by transferring the aerodynamic loads onto the structure and by using the instantaneous surface displacements to deform the flow solution domain. In order to eliminate any error during the transfer of information across the interface, it is beneficial to employ the same discretisation techniques for both domains. However, the separate historical development of computational fluid dynamics (CFD) and computational structural mechanics (CSM) has lead to the formation of specific techniques for each discipline, differing in both the discretisation and the solution methods.

Solid mechanics problems are formulated in a Lagrangian representation, expressing the deformations as a function of the initial configuration and time. The equations are usually discretised with high-order finite element (FE) methods. Although iterative solvers are popular, the assembled system of equations may also be solved directly [164]. Flow problems, on the other hand, are traditionally treated in an Eulerian representation. The stiffness of the associated matrices is therefore by orders of magnitude lower compared to structural problems [66]. The discretisation is most often performed with the finite volume (FV) methods, whose spatial accuracy is typically limited to second order. Structured meshes are employed where possible and the solution procedure is iterative. Due to the rather disparate solution procedures for CSM and CFD, the development of directly coupled fluid-structure interaction solvers has split into two separate paths.

One group of researchers has strived to achieve compatibility of the existing solution methods by employing a suitable interfacing technique for the transfer of data from one mesh to another. Guruswamy and Byun [66] coupled finite difference solution of Euler equations to a shell FE structural discretisation. The transfer of aerodynamic loads onto the structure was realized either by a simple bilinear interpolation or by a virtual surface treatment, capable of preserving the work done by aerodynamic forces due to structural deformations. The authors presented an application of the model to the flutter analysis of a fighter-type wing. Garcia and Guruswamy [53] combined nonlinear models for both structure and aerodynamics in their 3D aeroelastic analysis of a transonic wing under large deformations. Nonlinear beam elements were used to model the wing and a finite difference discretisation of thin-layer RANS was

employed for the flow solution.

The second option is to employ a unified discretisation technique for the complete multiphysics problem, avoiding thus the issue of interpolation on the interface. This requires that either finite volumes are adapted for structural computations, or finite elements for flow solution. The former approach was pursued by Slone et al. [165, 164], who developed a single FV discretisation strategy for flow and solid mechanics problems on unstructured meshes. They presented a computational example of a three-dimensional cantilever surrounded by flow, with the ultimate goal of applying the code to flutter analysis of turbines and aircraft wings. The FE discretisation strategy was, on the other hand, chosen by Sanches and Coda [153]. They coupled a flow solver in an arbitrary Lagrangian-Eulerian formulation to a Lagrangian shell solver for geometric nonlinear dynamics. In spite of both problems being solved via a FE formulation, a coupling procedure was implemented to allow for the use of meshes with non-matching nodes as well as different time steps in each domain. The computational method was successfully tested on the aeroelastic behaviour of a vertical plate exposed to shock and of a rocket nozzle at start-up.

The direct coupling enables modelling the fluid-structure interaction accurately, but it comes with the downside of higher computational costs. The equation of motion (Eq. 2.11) represents a coupled system of nonlinear equations, whose size is equal to the number of degrees of freedom given by the system discretisation. In the state-of-the-art turbomachinery simulations, it is not rare for this number to reach tens of millions. The cost of solving the full system of equations makes it often prohibitively expensive for routine computations in the industrial environment, and less demanding approaches are taken instead.

Weakly Coupled Methods

In the classification of fluid-structure coupled techniques where the closest coupling is achieved with the directly coupled methods, the opposite end of the spectrum is occupied by the weakly coupled approaches. Rather than developing a single code for a simultaneous solution of flow and structure equations, the computations are performed with a set of already existing solvers, connected via an interfacing technique. A multidisciplinary computing environment is formed, comprising different modules that can be suitably combined for the particular multiphysics problem. The benefit of this approach is in the use of highly efficient and extensively validated codes. Additionally, the programming effort required for the implementation of an interfacing technique is marginal compared to the development of a bespoke fluid-structure interaction solver. However, the use of completely independent solvers may lead to problems regarding their compatibility on the interface and a subsequent loss of accuracy in the communication procedure. The exchange of information is typically realized only after a partial or complete convergence, hence the coupling effects may not be captured in their full extent. The weakly coupled approach is therefore suitable mainly for small perturbations and problems with a moderate nonlinearity [107].

An example of combining independent codes into a multiphysics computing envir-

onment for the purpose of aeroelastic simulations was presented by Harrand et al. [106]. They coupled a computational fluid dynamics module CFD-FASTRAN with a finite element/modal analysis module FEMSTRESS. They compared several different interfacing techniques and performed a flutter analysis of the AGARD 445 wing. Doi and Alonso [38] applied a similar approach to predict the aeroelastic response of the NASA Rotor 67. The flow was resolved with a three-dimensional Navier-Stokes code TFLO, while the structural analysis was performed with a finite-element package MSC/NASTRAN. The two modules were connected via an interfacing strategy capable of conserving loads and energy. The authors concluded that their approach was able to predict successfully the time history of blade displacements in function of operating conditions.

Coupled Eigenmode Methods

The eigenmode approach offers a way to decrease greatly the computational costs associated with the directly coupled methods while maintaining a strong fluid-structure coupling. Providing that the structural dynamics model is linear, such as given by Eq. 2.11, the system of structural equations can be decoupled by transformation into a modal eigenspace. Only a few low order modes need to be retained to capture the structural dynamics of turbomachinery blades with sufficient accuracy [22]. The number of equations can therefore be reduced substantially.

The derivation of modal equations can be found for example in [148], [202] or [22]. The first step is to obtain the matrix of in-vacuo natural mode shapes $\chi = [\boldsymbol{\chi}_1, \boldsymbol{\chi}_2, ..., \boldsymbol{\chi}_N]$ with a conventional FE analysis. The blade displacement can be written as a linear combination of the mode shapes:

$$\boldsymbol{x} = \chi \boldsymbol{q}, \tag{2.12}$$

where $\boldsymbol{q}$ is the modal displacement vector. The eigenvectors are orthogonal with respect to the stiffness matrix K and mass matrix M, and assuming that the damping matrix D can be expressed as a linear combination of M and K (e.g. Rayleigh damping), the corresponding modal matrices are diagonal:

$$\chi^T M \chi = diag(\boldsymbol{m}), \qquad \chi^T D \chi = diag(\boldsymbol{d}), \qquad \chi^T K \chi = diag(\boldsymbol{k}) \tag{2.13}$$

The modeshapes are usually scaled to obtain a unity modal mass matrix, $diag(\boldsymbol{m}) = I$. Consequently, the elements of $\boldsymbol{k}$ are equal to the square of natural frequency, $k_i = \omega_i^2$. After substituting Eq. 2.12 to Eq. 2.11, premultiplied by χ^T, we obtain the following set of decoupled equations:

$$\ddot{q}_i + d_i \dot{q}_i + \omega_i^2 q_i = f_i, \qquad i = 1, 2, ..., N, \tag{2.14}$$

where $f_i = \boldsymbol{\chi}_i^T \boldsymbol{F}$ is the modal aerodynamic force. Up to this point, the derivation was performed for the full set of N natural shapes. However, as only the first $\tilde{N}$ most influential eigenmodes need to be included ($\tilde{N} \ll N$), and thanks to the decoupling, the number of equations may be reduced significantly.

In the simplest implementation of the eigenmode approach, the blades are modelled in 2D or quasi-3D as solids with two degrees of freedom allowing for torsion and bending. This approach was employed by Sadeghi and Liu [149] in their study on the influence of coupling, viscosity and nonlinearity on turbomachinery cascade flutter. Although they introduced a structural model with two degrees of freedom, the analysis of the coupling effects was limited to the torsional DOF. Sváček et al. [174] investigated the aeroelastic stability of the NACA 63_2 - 415 airfoil. The flow solution was based on laminar Navier-Stokes equations discretised with a FE method, while the airfoil was modelled as a solid structure with two DOF.

In general, the eigenmode technique may be applied applied to 3D computations with an arbitrary number of natural shapes included in the analysis. Vahdati and Imregun [183] were among the first to use this approach for a full 3D viscous investigation of fan flutter. The flow solver was based on a FE discretisation of Navier-Stokes equations and the first five modes were included in the structural model. The trends predicted by the flutter analysis of NASA Rotor 67 matched expectations, although no experimental data were available for validation. An overview of computational methods for fluid-structure coupled simulations was presented by Kamakoti and Shyy, concentrating on grid movement techniques, interfacing procedures and integration schemes [107]. They presented a computational example of the AGARD 445.6 wing, using a 3D multiblock RANS solver within the coupled eigenmode technique. Sadeghi and Liu [148] strived to decrease the computational costs by implementing a variety of acceleration techniques, such as implicit dual-time integration, multigrid discretisation and parallelisation. They investigated the aeroelastic behaviour of NASA Rotor 67 and their assertion of its stability matched the conclusions drawn by Vahdati and Imregun [183]. Vahdati et al. [184] employed the eigenmode approach for the investigation of combined effects of stall and acoustic fan flutter. Acoustic flutter was suppressed by blade-only damping when occurring on its own, without a flow separation. However, the presence of acoustic reflections from intake was shown to amplify stall flutter. A computational study regarding forced response and flutter boundary of a transonic compressor rotor was published by Zhang et al. [200]. They discovered the self-excited instability to be initiated by tip leakage vortex shedding. The effect of the tip clearance on flutter changed from destabilizing to stabilizing with an increase of the gap size. All blades were found to vibrate at the same mode and frequency, conforming approximately to a travelling wave mode. However, the vibration pattern showed circumferential asymmetry in terms of a varying oscillation amplitude and IBPA.

Chapter 3

Aims of the Thesis

This work elaborates on the numerical solution of self-excited vibrations in turbomachinery blade cascades. The targeted applications include supersonic flow regimes, characterised by shockwaves propagating both upstream and downstream. Great attention therefore needs to be paid to the use of non-reflecting boundary conditions. The analysis of their ability to suppress spurious wave reflections in complex flow conditions and to produce an accurate assessment of aeroelastic stability even on truncated domains forms a primary goal of this study.

The subtasks defined for reaching the main objective are arranged in two groups. The first one concerns the implementation of a numerical solver for the simulation of turbine blade flutter, while the second one involves analysis of non-reflecting boundary conditions in application to several flutter test-cases. This study focuses primarily on the unsteady aerodynamic part of the aeroelastic problem, hence the solution strategy adopts the energy method with prescribed harmonic blade oscillations. This choice is also motivated by the use of Spectral non-reflecting boundary conditions (NRBC) that require temporal periodicity of the flow. Transonic and supersonic flows on blade cascades are strongly nonlinear due to the presence of shockwaves, therefore the computational model is based on nonlinear flow equations solved with a time-marching strategy. With this approach, a high number of simulated oscillation cycles may be required to reach convergence. In order to maintain low computational costs enabling an extensive study with a large number of evaluations, a two-dimensional inviscid flow model is adopted. The following objectives are related to the implementation of the flow solver:

- **Devise a mesh motion strategy for flow solution on deforming domains.** The time-marching solution procedure requires the mesh to be updated in each time step, therefore the mesh motion strategy needs to be computationally efficient. At the same time, it is crucial to maintain high mesh quality even for large blade displacements, in order to guarantee stability and accuracy of the solution.
- **Analyse techniques for gradient reconstruction and limiting.** The method employed for the extrapolation of cell-center variables to cell faces

affects substantially the stability of numerical solution and the sharpness of resolved discontinuities. The goal is to analyse and compare available approaches and select the one most suited for the present applications.

- **Implement non-reflecting boundary conditions.** Spurious wave reflections on inflow and outflow boundaries can entail an inaccurate assessment of aeroelastic stability. This issue is exacerbated on blade cascades with a supersonic inflow, as they are typically highly sensitive to inlet conditions and feature upstream propagating shockwaves. Boundary conditions capable of minimizing spurious wave reflections in unsteady turbomachinery flows need to be implemented in the solver.

- **Validate the computational model.** Comparison of obtained results with available experimental and numerical data is necessary to gain confidence in the fidelity of the computational model.

In the second part, the performance of non-reflecting boundary conditions is investigated on several flutter test-cases. The applications are chosen such that they cover a wide range of flow conditions and modes of blade oscillation. Importantly, a turbine blade cascade with a supersonic inflow is among the selected test-cases. Several subtasks are formulated for this part:

- **Analyse the performance of the Spectral NRBC in nonlinear flows.** The Spectral NRBC of Schlüß et al. [158] represents a state-of-the-art method for the prevention of spurious wave reflections in unsteady flows. However, the approach is based on the linearised form of governing flow equations, which requires that its applicability to the strongly nonlinear flow conditions of the present test cases is verified.

- **Quantify the impact of unsuppressed wave reflections on aeroelastic assessments.** The Spectral NRBC is compared with two boundary conditions with a limited ability to suppress wave reflections, namely the Simple Turbomachinery BC and the Exact Steady NRBC. The purpose is to establish how the failure to prevent wave reflections affects the evaluation of aeroelastic stability.

- **Analyse the sensitivity of flutter predictions to domain extent.** The inlet and outlet boundaries are typically placed in a close vicinity of the blade row, whether to reflect the compact design of the turbomachine or to decrease computational requirements by reducing the mesh size and accelerating convergence. This can affect the accuracy of a numerical solution, especially if wave reflections are formed on the boundaries. This investigation aims to determine how close the boundaries can be placed without compromising the accuracy of aeroelastic assessments.

Chapter 4

Mathematical Model

This chapter describes the governing equations that form the foundation of the computational model. The focus is predominantly on the modelling of unsteady aerodynamics, including the specifics of flow solution on deforming domains. A separate section is dedicated to the formulation of boundary conditions with emphasis on the suppression of spurious wave reflections at inflow and outflow. A description of two approaches for flutter analysis concludes the chapter.

4.1 Flow Model

Steam and gas turbine flows are generally characterized by high Mach numbers associated with strong compressibility effects. Transonic or supersonic regimes are common, hence the aerodynamic model needs to account for the transition from subsonic to supersonic conditions and for the possible occurrence of shockwaves. The mathematical formulation is based on Euler equations in two dimensions in order to achieve lower computational costs compared to a three-dimensional viscous flow model. Although inviscid mechanisms are predominant in most aeroelastic problems [11], a future inclusion of turbulence modelling could further enhance the fidelity of the aerodynamic model.

4.1.1 Euler Equations

The system of Euler equations is derived by considering the conservation of mass, momentum and energy. The derivation can be found in numerous fluid dynamics textbooks, e.g. [90, 14]. It is assumed that the fluid has a high enough particle number density to justify its approximation as a continuum. Any infinitesimally small element is supposed to contain a sufficient number of particles to allow the specification of a mean velocity and a mean kinetic energy. The formulation of Euler equations will be given in an integral form which has the desirable property of remaining valid in the presence of flow field discontinuities, such as shockwaves or contact discontinuities. Moreover, the integral formulation is a starting point for the

derivation of the finite volume method.

Starting with the derivation of a scalar conservation law, we define an arbitrary control volume Ω, fixed in space and bounded by a closed surface $\partial\Omega$. A surface element of $\partial\Omega$ will be denoted as dS and the associated outward normal vector as $\boldsymbol{n} = [n_x, n_y]^T$. The temporal variation of the total amount of a scalar quantity ϕ within Ω is expressed as

$$\frac{\partial}{\partial t}\int_\Omega \phi d\Omega. \tag{4.1}$$

and it is equal to the sum of contributions due to fluxes through the control volume boundary and due to volume and surface sources. There are two types of fluxes, the convective and the diffusive flux. However, since we are dealing with an inviscid fluid, we consider only the convective flux expressing the amount of ϕ entering the control volume through its boundary at the velocity $\boldsymbol{u} = [u, v]^T$. The flux is defined by $\boldsymbol{F}_c = \phi\boldsymbol{u}$, hence its contribution to the change of ϕ is obtained as

$$-\oint_{\partial\Omega} \boldsymbol{F}_c \cdot \boldsymbol{n} dS = -\oint_{\partial\Omega} \phi\boldsymbol{u} \cdot \boldsymbol{n} dS, \tag{4.2}$$

The second contribution is due to the volume and surface sources, Q_v and $\boldsymbol{Q}_s$:

$$\int_\Omega Q_v d\Omega + \oint_{\partial\Omega} \boldsymbol{Q}_s \cdot \boldsymbol{n} dS. \tag{4.3}$$

The sum of all contributions yields the general form of the scalar conservation law for an inviscid fluid:

$$\frac{\partial}{\partial t}\int_\Omega \phi d\Omega + \oint_{\partial\Omega} \boldsymbol{F}_c \cdot \boldsymbol{n} dS = \int_\Omega Q_v d\Omega + \oint_{\partial\Omega} \boldsymbol{Q}_s \cdot \boldsymbol{n} dS. \tag{4.4}$$

The conservation law can also be formulated for a vector quantity $\boldsymbol{\phi}$ by considering the scalar form for each of its components. The result is formally equal to the scalar law, except that the convective flux is now a tensor $\overline{\overline{F}}_c = \boldsymbol{\phi} \otimes \boldsymbol{u}$ and the volume and surface fluxes are a vector and a tensor respectively. The vector form of the conservation law is hence given by:

$$\frac{\partial}{\partial t}\int_\Omega \boldsymbol{\phi} d\Omega + \oint_{\partial\Omega} \overline{\overline{F}}_c \cdot \boldsymbol{n} dS = \int_\Omega \boldsymbol{Q}_v d\Omega + \oint_{\partial\Omega} \overline{\overline{Q}}_s \cdot \boldsymbol{n} dS. \tag{4.5}$$

The system of Euler equations is obtained by writing the conservation laws for mass, momentum and energy.

Mass conservation. The mass conservation law, also referred to as the continuity equation, expresses the fact that mass can neither disappear nor be created. The quantity ϕ is substituted by the fluid density ρ and the convective flux is given

by $\boldsymbol{F_c} = \rho\boldsymbol{u}$. There are no surface or volume sources of mass. Using the scalar conservation law, we obtain the continuity equation

$$\frac{\partial}{\partial t}\int_\Omega \rho d\Omega + \oint_{\partial\Omega} \rho\boldsymbol{u}\cdot\boldsymbol{n}dS = 0. \tag{4.6}$$

Momentum conservation. The conservation of momentum is obtained by applying Newton's second law, stating that the change of momentum corresponds to the sum of forces acting on the mass element. The conserved quantity is momentum $\rho\boldsymbol{u}$, and the corresponding convective flux $\overline{\overline{F_c}} = \rho\boldsymbol{u}\otimes\boldsymbol{u}$. Volume sources, such as the gravitational, buoyancy, Coriolis, electromagnetic or centrifugal forces, may be considered. The total contribution due to external forces will be summarized in the term $\boldsymbol{Q}_v = \rho\boldsymbol{f}_e$. In the present case of an inviscid fluid, the surface source term is limited to the contribution of pressure $\overline{\overline{Q}}_s = -p\overline{\overline{I}}$. Substituting all the terms in the vector conservation law yields

$$\frac{\partial}{\partial t}\int_\Omega \rho\boldsymbol{u}d\Omega + \oint_{\partial\Omega} \rho\boldsymbol{u}(\boldsymbol{u}\cdot\boldsymbol{n})dS = \int_\Omega \rho\boldsymbol{f}_e d\Omega - \oint_{\partial\Omega} p\boldsymbol{n}dS. \tag{4.7}$$

Energy conservation. The first law of thermodynamics states that the variation of total energy inside a volume is equal to the sum of the work of forces acting on the volume and of the heat transmitted to the volume. Total energy per unit mass, e_0, is composed of internal and kinetic energy:

$$e_0 = e + \frac{||\boldsymbol{u}||^2}{2}. \tag{4.8}$$

The conserved quantity is total energy per unit volume, ρe_0, with the inviscid flux defined as $\boldsymbol{F}_c = \rho e_0\boldsymbol{u}$. Since the Euler equations describe an inviscid fluid, there is no diffusive flux, otherwise representing the diffusion of heat due to molecular thermal conduction. The volume sources account for the rate of work done by body forces and, if present, also for the volumetric heating due to radiation or chemical reactions. Together, they are expressed as $Q_v = \rho\boldsymbol{f}_e\cdot\boldsymbol{u} + \dot{q}_h$. As there are no shear stresses in an inviscid fluid and no heat conduction is considered, the surface source term comprises only the rate of work done by pressure:

$$\boldsymbol{Q}_s = -p\boldsymbol{u} \tag{4.9}$$

Summing all the contributions, we obtain the energy conservation equation:

$$\frac{\partial}{\partial t}\int_\Omega \rho e_0 d\Omega + \oint_{\partial\Omega} \rho e_0(\boldsymbol{u}\cdot\boldsymbol{n})dS = \int_\Omega (\rho\boldsymbol{f}_e\cdot\boldsymbol{u} + \dot{q}_h)d\Omega - \oint_{\partial\Omega} p(\boldsymbol{u}\cdot\boldsymbol{n})dS. \tag{4.10}$$

It is often advantageous to write the Euler equations in a more compact vector form. Density, momentum and total energy are encompassed in the vector of conserved

variables, denoted $\boldsymbol{W}$. The momentum and energy conservation laws include pressure source terms, but it is a common practice to include them in the flux vector $\boldsymbol{F}$ together with the actual convective flux terms. Further, $\boldsymbol{F}$ in the following represents the flux normal to the volume boundary, i.e. it is obtained by performing the scalar product of the original flux with the unit normal $\boldsymbol{n}$. Lastly, we define a volume source term $\boldsymbol{Q}$, comprising all contributions due to body forces and volumetric heating. Using these definitions together with the general vector conservation law (Eq. 4.5) and the conservation laws for mass (Eq. 4.6), momentum (Eq. 4.7) and energy (Eq. 4.10), we arrive at the vector form of Euler equations

$$\frac{\partial}{\partial t}\int_{\Omega} \boldsymbol{W} d\Omega + \oint_{\partial\Omega} \boldsymbol{F} dS = \int_{\Omega} \boldsymbol{Q}, \tag{4.11}$$

where the vector of conserved variables $\boldsymbol{W}$, the flux vector $\boldsymbol{F}$ and the volume source term $\boldsymbol{Q}$ are respectively given by:

$$\boldsymbol{W} = \begin{bmatrix} \rho \\ \rho \boldsymbol{u} \\ \rho e_0 \end{bmatrix}, \quad \boldsymbol{F} = (\boldsymbol{u} \cdot \boldsymbol{n}) \begin{bmatrix} \rho \\ \rho \boldsymbol{u} \\ \rho e_0 + p \end{bmatrix} + \begin{bmatrix} 0 \\ p\boldsymbol{n} \\ 0 \end{bmatrix}, \quad \boldsymbol{Q} = \begin{bmatrix} 0 \\ \rho \boldsymbol{f}_e \\ \rho \boldsymbol{f}_e \cdot \boldsymbol{u} + \dot{q}_h \end{bmatrix}. \tag{4.12}$$

We will not consider any source terms in the present model, hence the right-hand side of Eq. 4.11 will be equal to zero.

4.1.2 Arbitrary Lagrangian-Eulerian Formulation

The governing equations for fluid dynamics problems are typically formulated in the Eulerian reference frame, as is also the case of Euler equations derived in Sec. 4.1.1. The quantities of interest are defined as functions of coordinates fixed in space and the computational domain does not vary in time. This approach allows particles to enter and leave arbitrarily without distorting the domain, hence it is convenient for flow solutions. Structural problems, on the other hand, typically feature relatively small displacements, making it more appropriate to cast the equations in the Lagrangian reference frame. The motion of each particle is followed and the quantities are defined in material coordinates with respect to a reference configuration.

Neither of these approaches is, however, particularly suitable for the solution of unsteady aerodynamics in fluid-structure interaction problems, characterised by deforming domains. The Eulerian reference frame does not allow for a straightforward implementation of moving boundaries, while the Lagrangian approach would very quickly lead to excessive domain and mesh distortions. The desired flexibility is provided by the Arbitrary Lagrangian Eulerian (ALE) method (See e.g. [92, 113, 166, 95]). The grid vertices are neither fixed nor they follow material points and their motion may be chosen arbitrarily, at least to some extent. Both the Eulerian and the Lagrangian representations can be obtained as a particular case of the general ALE formulation.

Let Ω_t be the computational domain occupied by fluid at a time $t \in \langle 0, T \rangle$. A reference configuration Ω_{ref} is considered, taken for example as the initial configuration $\Omega_{ref} = \Omega_{t=0}$. An ALE mapping from the reference configuration onto the current configuration is introduced:

$$\mathcal{A}_t : \Omega_{ref} \to \Omega_t, \quad \boldsymbol{X} \to \boldsymbol{x}(\boldsymbol{X}, t) = \mathcal{A}_t(\boldsymbol{X}), \tag{4.13}$$

describing the time-dependent position $\boldsymbol{x} \in \Omega_t$ of a point from the reference domain $\boldsymbol{X} \in \Omega_{ref}$. The ALE mapping should be continuous and bijective on the closure of Ω_{ref} [95]. The points $\boldsymbol{x} = \mathcal{A}_t(\boldsymbol{X})$, comprising the grid vertices of a discretised domain, move with the ALE velocity defined as:

$$\boldsymbol{s}(\boldsymbol{x}, t) = \frac{\partial}{\partial t}\boldsymbol{x}(\boldsymbol{X}, t) = \frac{\partial}{\partial t}\mathcal{A}_t(\boldsymbol{X}), \quad t \in \langle 0, T \rangle, \quad \boldsymbol{X} \in \Omega_{ref} \tag{4.14}$$

The set of Euler equations recast in the ALE formulation formally corresponds to the original Eulerian representation [166]:

$$\frac{\partial}{\partial t}\int_{\Omega(t)} \boldsymbol{W} d\Omega + \oint_{\partial\Omega(t)} \boldsymbol{F}^{ALE} dS = 0. \tag{4.15}$$

However, the flux vector $\boldsymbol{F}^{ALE}$ is now modified to account for the change of convective terms due to the motion of the control volume boundary:

$$\boldsymbol{F}^{ALE} = \boldsymbol{F} - (\boldsymbol{s} \cdot \boldsymbol{n})\boldsymbol{W} = (\boldsymbol{u} - \boldsymbol{s}) \cdot \boldsymbol{n} \begin{bmatrix} \rho \\ \rho\boldsymbol{u} \\ \rho e_0 + p \end{bmatrix} + \begin{bmatrix} 0 \\ p\boldsymbol{n} \\ p\boldsymbol{s} \cdot \boldsymbol{n} \end{bmatrix}. \tag{4.16}$$

4.1.3 Ideal Gas Law

The system of Euler equations for planar flows comprises one equation for mass conservation, two equations for momentum conservation in x and y directions, and one equation for energy conservation. Hence we have four equations, but five unknowns: density, two components of the velocity vector, total energy and static pressure. In order to obtain a unique solution, we need to introduce an additional equation defining the relation between the state variables.

For the applications presented in this work, the working fluid can be approximated with sufficient accuracy as an ideal gas. The relation between static pressure p, density ρ and static temperature T is expressed by the perfect gas law, or thermal equation of state [112]:

$$p = \rho R T, \tag{4.17}$$

where R denotes the specific gas constant that is unique for each gas. A fluid satisfying the perfect gas law is referred to as thermally perfect, while for calorically perfect gases the caloric equation of state is valid:

$$e = c_v T, \tag{4.18}$$

where c_v is the constant volume specific heat, or alternatively

$$h = c_p T, \tag{4.19}$$

with h denoting enthalpy and c_p the constant pressure specific heat. A fluid which satisfies both the thermal and the caloric equations of state is called an ideal gas.

For the purpose of flow computations, it is advantageous to combine the above relations into a single formula, expressed in terms of the state variables appearing in the Euler equations (Eq. 4.15). Hence we introduce the ratio of specific heats

$$\gamma = \frac{c_p}{c_v} \tag{4.20}$$

and Mayer's formula:

$$c_p = c_v + R \tag{4.21}$$

and use these two relations in combination with the caloric equation of state (Eq. 4.18) to express the specific internal energy as:

$$e = \frac{R}{\gamma - 1} T \tag{4.22}$$

Substituting T from Eq. 4.22 into the thermal equation of state (Eq. 4.17) and recalling the definition of specific total energy (Eq. 4.8) yields:

$$p = (\gamma - 1)\rho e = (\gamma - 1)\left[\rho e_0 - \frac{1}{2}\rho\left(u^2 + v^2\right)\right] \tag{4.23}$$

The perfect gas model also allows for a simple evaluation of the speed of sound, defined as follows:

$$a = \sqrt{\gamma R T} = \sqrt{\frac{\gamma p}{\rho}}. \tag{4.24}$$

4.2 Boundary Conditions

The governing equations must be supplemented by a set of boundary conditions (BC) in order to obtain a correctly defined problem with a unique solution. The computational domain is truncated at a finite distance from the blade rows, creating thus artificial inlet and outlet boundaries that do not exist in the physical domain. Only one or several blade channels are usually included in the simulations, instead of the whole annulus, which requires that some form of periodicity is imposed. The computational domain is also naturally bounded by the solid walls of blades and other components exposed to the flow. A sketch of 2D computational domains for turbomachinery and for external aerodynamics is provided in Fig 4.1.

The correct definition of boundary conditions depends on the mathematical nature of the governing equations. The present solution procedure is based on marching the

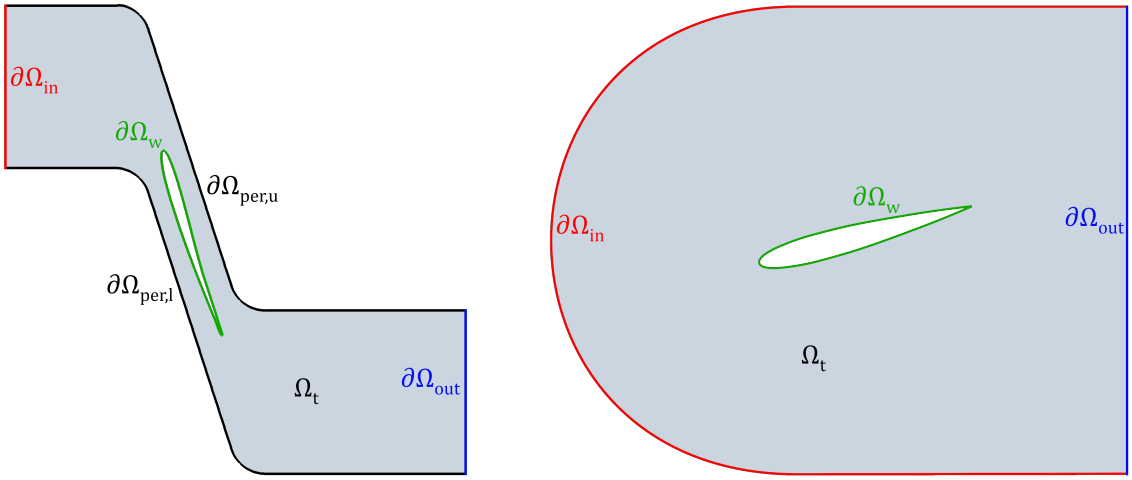

Figure 4.1: Examples of computational domains for a blade channel (left) and an airfoil (right)

unsteady Euler equations in time, with either the converged steady-state solution or the unsteady flow behaviour being of interest. The governing equations are therefore always hyperbolic, regardless of whether the flow is locally subsonic or supersonic [14]. There are four dependent variables that need to be determined at the inlet and outlet boundaries, either by extrapolation from inside the domain, or by specifying their value. The theory of characteristics shows that the number of quantities that need to be prescribed explicitly is equal to the number of characteristics entering the domain. The direction of propagation is determined by the sign of eigenvalues of the convective flux Jacobians (for more detail see e.g. [90, 14]). For the system of Euler equations in two dimensions, the eigenvalues are:

$$\lambda_1 = \lambda_2 = \boldsymbol{u} \cdot \boldsymbol{n}, \quad \lambda_3 = \boldsymbol{u} \cdot \boldsymbol{n} + a, \quad \lambda_4 = \boldsymbol{u} \cdot \boldsymbol{n} - a, \tag{4.25}$$

where $\boldsymbol{n}$ is a unit vector normal to the boundary, pointing inside the domain. The number of variables imposed at the boundary is given by the number of positive eigenvalues.

The formulation of boundary conditions requires a particular care in the case of the artificial inflow and outflow boundaries, since they are typically placed in a close vicinity of the analysed blade-rows. Any flow perturbations propagating from inside the domain are therefore likely to reach these boundaries with a nearly undiminished magnitude. Unless a special treatment is applied to the inlet and outlet boundary conditions, unphysical reflections of the perturbations may occur and introduce an error into the solution. Simulations of low-pressure turbine near-tip sections are especially challenging in this regard, as the inlet flow may be supersonic. Additionally to the downstream propagating in-passage shock, typical for transonic turbine flows, a detached shock forms upstream of the blade leading edge and propagates towards the inlet.

Different boundary conditions are considered for the artificial boundaries in simulations of external aerodynamics and of internal turbomachinery flows. In the former case, either the freestream or the farfield boundary condition with an optional vortex

correction is applied. Blade cascade simulations are performed either with the Simple Turbomachinery BC, or with one of the two implemented non-reflecting boundary conditions (NRBC) based on linearised Euler equations.

4.2.1 Solid Wall

No flow may penetrate the wall, therefore only λ_3 is positive and only one physical condition is imposed. The relative velocity normal to the wall is required to be zero, which for simulations on fixed domains simply reads:

$$\boldsymbol{u} \cdot \boldsymbol{n} \,|_{\partial\Omega_{wall}} = 0 \tag{4.26}$$

If we are dealing with simulations on deforming domains, the velocity of wall motion $\boldsymbol{s}$ needs to be taken into account:

$$(\boldsymbol{u} - \boldsymbol{s}) \cdot \boldsymbol{n} \,|_{\partial\Omega_{wall}} = 0 \tag{4.27}$$

The tangential component of flow velocity is extrapolated from the domain interior together with state variables, therefore the boundary condition is called *free-slip*. Enforcing the free-slip boundary condition in fact translates into setting the convective flux to zero. The only remaining contributions to flux are the pressure terms found in the momentum equation, and in the case of a deforming domain also in the energy equation.

4.2.2 Periodicity

The need to reduce computational requirements motivates the effort to limit the computational domain to as few blade channels per blade row as possible. The restriction to a single blade passage is straightforward in steady computations, where the inherent flow periodicity is exploited by applying direct periodic boundary conditions between the lower and upper boundaries:

$$\boldsymbol{W} \,\big|_{\partial\Omega_{per,l}} = \boldsymbol{W} \,\big|_{\partial\Omega_{per,u}} \tag{4.28}$$

Unsteady computations are in the present work performed with the travelling wave approach. The concept of direct periodicity is still applicable, but it requires the inclusion of multiple blade passages in the computational domain in function of the IBPA value. The number of blade passages to be included is calculated as follows:

$$N_{passages} = \frac{360^\circ}{\mathrm{GCD}(\sigma, 360^\circ)}, \tag{4.29}$$

where σ denotes the IBPA and GCD() is the greatest common divisor.

4.2.3 Farfield Boundary for External Flows

In simulations of external aerodynamics, the investigated body is typically placed in a uniform flow-field denoted the freestream. The artificial domain boundaries are located as close to the body as possible in pursuit of low computational demands. Therefore, the body-induced perturbation of the freestream flow needs to be considered and a farfield boundary condition is imposed. The number of incoming characteristics depends on the flow direction relatively to the boundary and on the local Mach number. Altogether, we have four possible combinations: a subsonic inflow, a supersonic inflow, a subsonic outflow and a supersonic outflow. The computations of external aerodynamics in the present work are limited to subsonic flows, therefore only two of these cases need to be treated.

Subsonic Inflow

The fourth eigenvalue is negative and the other three are positive, hence we need to prescribe three boundary conditions. According to the theory of characteristics, entropy and vorticity perturbations are convected with the flow, together with one acoustic mode. The farfield boundary conditions for inlet are given as [6]:

$$\begin{aligned} &\Delta p - \rho_{ref} a_{ref} \Delta(\boldsymbol{u} \cdot \boldsymbol{n}) = 0 \\ &\Delta p - a_{ref}^2 \Delta \rho = 0 \\ &\Delta(\boldsymbol{u} \cdot \boldsymbol{t}) = 0, \end{aligned} \tag{4.30}$$

where Δ is a difference between the freestream flow and the local state, the subscript $_{ref}$ denotes a reference quantity evaluated either in freestream or at the local state, and the unit vectors $\boldsymbol{n}$ and $\boldsymbol{t}$ point respectively in the outward normal and tangential directions relatively to the boundary.

Primitive variables at the boundary can be calculated with the use of the following formulas [14]:

$$\begin{aligned} p_{bd} &= \frac{1}{2}\left[p_{FS} + p_{int} - \rho_{FS} a_{FS} (\boldsymbol{u}_{FS} - \boldsymbol{u}_{int}) \cdot \boldsymbol{n}\right] \\ \rho_{bd} &= \rho_{FS} + (p_{bd} - p_{FS})/a_{FS}^2 \\ \boldsymbol{u}_{bd} &= \boldsymbol{u}_{FS} + (p_{bd} - p_{FS})\boldsymbol{n}/(\rho_{FS} a_{FS}), \end{aligned} \tag{4.31}$$

where the subscript $_{FS}$ denotes the freestream state and the subscript $_{int}$ quantities extrapolated from the domain interior.

Subsonic Outflow

The three eigenvalues λ_1, λ_2 and λ_3 are positive and only one acoustic mode is transported into the domain. A single boundary condition is required, obtained from the theory of characteristics as follows [6]:

$$\Delta p - \rho_{ref} a_{ref} \Delta(\boldsymbol{u} \cdot \boldsymbol{n}) = 0 \tag{4.32}$$

The formulas for the outlet boundary state are then given by [14]:

$$\begin{aligned} p_{bd} &= p_{FS} \\ \rho_{bd} &= \rho_{int} + (p_{bd} - p_{int})/a_{FS}^2 \\ \boldsymbol{u}_{bd} &= \boldsymbol{u}_{int} - (p_{bd} - p_{int})\boldsymbol{n}/(\rho_{FS} a_{FS}). \end{aligned} \tag{4.33}$$

Vortex Correction

The farfield definition in Eqs. 4.31 and 4.33 operated directly with the uniform freestream flow. However, a uniform flow-field is characterised by zero circulation, which is incorrect for a lifting body in a subsonic flow [14]. In order to obtain accurate results without having to extend the domain very far from the body, a vortex correction must be implemented. The vortex is assumed to be centered on the airfoil chord, usually at one quarter from the leading edge, and its strength is proportional to the produced lift.

We employ the approach introduced by Usab and Murman [197]. First, the airfoil lift coefficient needs to be determined:

$$C_L = \frac{F_y}{\frac{1}{2}\rho_{FS}||\boldsymbol{u}_{FS}||^2 C}, \tag{4.34}$$

where F_y is the lift force obtained by integrating pressure along the airfoil surface, C is the airfoil chord and the subscript $_{FS}$ denotes freestream quantities. Using the Kutta-Joukowsky theorem, we obtain circulation:

$$\Gamma = \frac{1}{2} C_L C ||\boldsymbol{u}_{FS}|| = \frac{F_y}{\rho_{FS}||\boldsymbol{u}_{FS}||}. \tag{4.35}$$

The corrected freestream state is then calculated using the following relations:

$$\begin{aligned} \tilde{u}_{FS} &= u_{FS} + \left(\frac{\Gamma\sqrt{1-M_{FS}^2}}{2\pi r}\right) \frac{1}{1 - M_{FS}^2 \sin^2(\theta - \alpha)} \sin\theta \\ \tilde{v}_{FS} &= v_{FS} - \left(\frac{\Gamma\sqrt{1-M_{FS}^2}}{2\pi r}\right) \frac{1}{1 - M_{FS}^2 \sin^2(\theta - \alpha)} \cos\theta \\ \tilde{p}_{FS} &= \left[p_{FS}^{(\gamma-1)/\gamma} + \left(\frac{\gamma-1}{\gamma}\right) \frac{\rho_{FS}(||\boldsymbol{u}_{FS}||^2 - ||\tilde{\boldsymbol{u}}_{FS}||^2)}{2 p_{FS}^{1/\gamma}}\right]^{\gamma/(\gamma-1)} \\ \tilde{\rho}_{FS} &= \rho_{FS}\left(\frac{\tilde{p}_{FS}}{p_{FS}}\right)^{1/\gamma} \end{aligned} \tag{4.36}$$

where $[r, \theta]$ are polar coordinates with origin at the vortex center and α is the angle of attack.

4.2.4 Simple Turbomachinery Boundary Conditions

The definition of boundary conditions in turbine simulations is alike to an experimental setup. At the inlet we have a reservoir with a known total temperature and total pressure, while at the outlet is an environment characterised by the ambient static pressure. The number of imposed conditions is based on the characteristic theory, hence we need to distinguish between inflow/outflow and axially subsonic/supersonic flow. Only axially subsonic cases are considered here, as flows with a supersonic axial component are not common in turbomachinery.

A rather straightforward definition of subsonic inlet boundary conditions may be obtained by assuming that the fluid undergoes an isentropic state change between the reservoir and the inflow. At the outlet, the average static pressure value is imposed.

Subsonic Inlet

The theory of characteristics dictates that three conditions are imposed and one quantity is extrapolated from the domain interior. The total state provides two conditions, the total pressure p_0 and the total temperature T_0, while the third one is defined by fixing the inlet flow angle β. We choose the Mach number M_{int} to be extrapolated from the domain interior and assume an isentropic expansion from total conditions to the inlet flow state. Using the ideal gas model, the following relations can be derived for the calculation of inflow variables [68]:

$$\begin{aligned}
\rho_{bd} &= \left(1 + \frac{\gamma - 1}{2} M_{int}^2\right)^{\frac{1}{1-\gamma}} \rho_0 \\
(\rho u)_{bd} &= \left(1 + \frac{\gamma - 1}{2} M_{int}^2\right)^{\frac{1}{1-\gamma} - \frac{1}{2}} M_{int} \rho_0 a_0 \cos\beta \\
(\rho v)_{bd} &= \left(1 + \frac{\gamma - 1}{2} M_{int}^2\right)^{\frac{1}{1-\gamma} - \frac{1}{2}} M_{int} \rho_0 a_0 \sin\beta \\
(\rho e_0)_{bd} &= \left(1 + \frac{\gamma - 1}{2} M_{int}^2\right)^{\frac{1}{1-\gamma}} \left(\frac{1}{\gamma(\gamma - 1)} + \frac{M_{int}^2}{2}\right) \rho_0 a_0^2,
\end{aligned} \tag{4.37}$$

Subsonic Outlet

The outlet static pressure p_{out} represents the single boundary condition needed for the axially subsonic outflow. Using the ideal gas equation 4.23, the specified static pressure is employed to correct the value of total energy:

$$(\rho e_0)_{bd} = \frac{p_{out}}{\gamma - 1} + \frac{1}{2} \rho_{int} (u_{int}^2 + v_{int}^2), \tag{4.38}$$

where quantities subscripted with $_{int}$ are extrapolated from the domain interior.

However, imposing a uniform static pressure profile may lead to spurious wave reflections if the flow field downstream of a blade row features significant pressure gradients. The boundary condition formulation is therefore altered to impose only the average value and to allow for variations of static pressure along the boundary. The static pressure profile $p_{int}(\xi)$, extrapolated from the domain interior, is scaled to match the average value $\bar{p}_{int}$ with the prescribed outlet pressure p_{out}:

$$\bar{p}_{int} = \frac{1}{\Xi}\int_0^{\Xi} p_{int}(\xi)d\xi, \qquad \tilde{p}_{out}(\xi) = p_{int}(\xi)\frac{p_{out}}{\bar{p}_{int}}, \tag{4.39}$$

where $\xi \in \langle 0; \Xi \rangle$ is a coordinate along the boundary $\partial\Omega_{out}$. This scaled profile is then substituted into Eq. 4.38:

$$(\rho e_0)_{bd}(\xi) = \frac{\tilde{p}_{out}(\xi)}{\gamma - 1} + \frac{1}{2}\rho_{int}(u_{int}^2 + v_{int}^2), \tag{4.40}$$

The other conserved variables are simply extrapolated from the domain interior.

4.2.5 Non-Reflecting Boundary Conditions for Turbomachinery

The simple inlet and outlet boundary conditions described in Sec. 4.2.4 may produce spurious wave reflections that contaminate the flow solution. This issue can be addressed by using suitable non-reflecting boundary conditions. Two such formulations are implemented in the present computational model: the Exact Steady NRBC of Giles [58] and the Spectral NRBC of Schlüß et al. [158]. Both methods are derived from Giles' theory of NRBC, presented in the papers [58, 61, 59]. The Spectral NRBC for time-domain solvers was devised by Chassaing and Gerolymos [23] and the presently used updated version was recently published by Schlüß et al. [158, 156, 157]. This section provides a brief overview of the theory of NRBC described in the aforementioned papers of Giles and Schlüß et al. Specific details of the present implementation are given in Sec. 5.2.6.

General Approach

The boundary flow-field, varying both in time and space, is approximated by a superposition of a mean state and perturbations. The perturbation amplitude is assumed to be sufficiently small to allow for linearisation of the governing equations. Without loss of generality, we consider a coordinate system aligned such that the axis x is normal to the boundary and oriented in the flow direction (i.e. it points in the inward normal direction at the inlet, outward normal at the outlet) and the axis y is oriented along the boundary in the pitchwise direction. We denote the vector of perturbations in primitive variables $\boldsymbol{q} = [\rho, u, v, p]^T$, where u and v are respectively the $x-$ and $y-$components of the velocity vector. The set of linearised Euler equations reads:

$$\frac{\partial \boldsymbol{q}}{\partial t} + A\frac{\partial \boldsymbol{q}}{\partial x} + B\frac{\partial \boldsymbol{q}}{\partial y} = 0, \tag{4.41}$$

where the matrices A, B are functions of the mean state only:

$$A = \begin{bmatrix} \bar{u} & \bar{\rho} & 0 & 0 \\ 0 & \bar{u} & 0 & 1/\bar{\rho} \\ 0 & 0 & \bar{u} & 0 \\ 0 & \gamma\bar{p} & 0 & \bar{u} \end{bmatrix}, \quad B = \begin{bmatrix} \bar{v} & 0 & \bar{\rho} & 0 \\ 0 & \bar{v} & 0 & 0 \\ 0 & 0 & \bar{v} & 1/\bar{\rho} \\ 0 & 0 & \gamma\bar{p} & \bar{v} \end{bmatrix} \tag{4.42}$$

The mean flow $\overline{\boldsymbol{q}} = [\overline{\rho}, \overline{u}, \overline{v}, \overline{p}]^T$ represents a spatial (along the boundary) as well as temporal average. Within the linearised theory, any flow state may be constructed as a superposition of wave-like perturbations

$$\boldsymbol{q} = \mathrm{Re}(\hat{\boldsymbol{q}} e^{\mathrm{i}(kx+my+\omega t)}) \tag{4.43}$$

and the mean flow $\overline{\boldsymbol{q}}$. Here k and m are wave numbers along x and y respectively and ω denotes angular frequency. Note that ω in 4.43 is sometimes considered with an opposite sign [58, 158], i.e.:

$$\boldsymbol{q} = \mathrm{Re}(\hat{\boldsymbol{q}} e^{\mathrm{i}(kx+my-\omega t)}). \tag{4.44}$$

However, for the purpose of implementing a discrete Fourier transform in the solver, the form 4.43 is more convenient. Substituting the perturbation $\boldsymbol{q}$ into linearised Euler equations 4.41, we obtain:

$$(\omega I + kA + mB)\hat{\boldsymbol{q}} = 0, \tag{4.45}$$

which for non-trivial solutions yields the dispersion relation

$$\det(\omega I + kA + mB) = 0, \tag{4.46}$$

or equivalently

$$\det(\omega A^{-1} + kI + mA^{-1}B) = 0. \tag{4.47}$$

The dispersion relation is a polynomial equation of degree four in each of ω, k, and m. We are interested in the roots k_j for a fixed ω and m. Equation 4.47 can be interpreted as an eigenvalue problem

$$(\omega A^{-1} + mA^{-1}B)\boldsymbol{r}_j = -k_j \boldsymbol{r}_j \tag{4.48}$$

with eigenvalues $-k$ and right eigenvectors $\boldsymbol{r}_j$. Analogously, the eigenvalue problem can be defined using left eigenvectors $\boldsymbol{l}_j$:

$$\boldsymbol{l}_j(\omega A^{-1} + mA^{-1}B) = -k_j \boldsymbol{l}_j. \tag{4.49}$$

The purpose of performing the eigenvalue analysis is to distinguish between the waves entering and leaving the domain. The flow solution at the boundary is decomposed into a sum of Fourier modes $\hat{\boldsymbol{q}}$ with distinct values of ω and m. Each of these modes comprises a set of four fundamental waves, one for each k_j. As the wave numbers k correspond to waves normal to the boundary, they may be used to determine whether the wave propagates into or out of the domain.

The dispersion relation for two-dimensional linearised Euler equations yields the following eigenvalues:

$$k_{1,2} = -\frac{\omega + m\bar{v}}{\bar{u}}, \quad k_3 = \frac{(\omega + m\bar{v})(-\bar{a}\psi + \bar{u})}{\bar{a}^2 - \bar{u}^2}, \quad k_4 = \frac{(\omega + m\bar{v})(\bar{a}\psi + \bar{u})}{\bar{a}^2 - \bar{u}^2}, \tag{4.50}$$

with

$$\psi = \begin{cases} \sqrt{\Delta} & \text{if } \Delta > 0 \\ -\mathrm{i}\,\mathrm{sign}(\omega + m\bar{v})\sqrt{-\Delta} & \text{if } \Delta < 0 \end{cases}, \tag{4.51}$$

and

$$\Delta = 1 - \frac{(\bar{a}^2 - \bar{u}^2)m^2}{(\omega + m\bar{v})^2} \tag{4.52}$$

The first two eigenvalues correspond to perturbations propagating convectively in the flow direction and they represent incoming waves at inflow and outgoing waves at outflow. For the third and fourth wave, it needs to be distinguished between flows with a subsonic and with a supersonic velocity component normal to the boundary. In the case of normally subsonic flows, providing that $\Delta \neq 0$, the third wave propagates also with the flow direction, but the fourth one travels upstream. Note that Eq. 4.51 is in the original paper of Schlüß, Frey and Ashcroft [158] incorrectly given with an opposite sign for $\Delta < 0$. In this case, ψ is complex, hence the sign needs to be chosen such that k_3 is the root with a positive imaginary component in order to uphold the convention that k_3 corresponds to a downstream-running wave and k_4 to an upstream running wave [61].

Acoustic resonance occurs for $\Delta = 0$ and represents additional challenges for the construction of boundary conditions. This case is, however, not considered here. Neither are considered axially supersonic flows with all four waves propagating downstream, due to their rarity in turbomachinery applications.

Since the first two eigenvalues are identical, the determination of corresponding eigenvectors is not unique. A convenient choice is to define $\boldsymbol{r}_1$ as an entropy perturbation and $\boldsymbol{r}_2$ as a vorticity wave, which fulfils the required orthogonality. The third and fourth eigenvectors represent downstream and upstream running acoustic

waves. Defining $\kappa = \frac{m}{\omega}$, the matrix of right eigenvectors $R = \begin{bmatrix} \boldsymbol{r}_1 & \boldsymbol{r}_2 & \boldsymbol{r}_3 & \boldsymbol{r}_4 \end{bmatrix}$ reads [158]

$$R = \begin{bmatrix} -\bar{\rho} & 0 & \frac{\bar{\rho}(1-(1+\bar{v}\kappa)M_x\psi)}{2(1-M_x)} & \frac{\bar{\rho}(1+(1+\bar{v}\kappa)M_x\psi)}{2(1+M_x)} \\ 0 & -\bar{a}\bar{u}\kappa & \frac{\bar{a}(1+\bar{v}\kappa)(\psi-M_x)}{2(1-M_x)} & \frac{-\bar{a}(1+\bar{v}\kappa)(\psi+M_x)}{2(1+M_x)} \\ 0 & \bar{a}(1+\bar{v}\kappa) & -\frac{\bar{a}^2(1-M_x^2)\kappa}{2(1-M_x)} & -\frac{\bar{a}^2(1-M_x^2)\kappa}{2(1+M_x)} \\ 0 & 0 & \frac{\bar{\rho}\bar{a}^2(1-(1+\bar{v}\kappa)M_x\psi)}{2(1-M_x)} & \frac{\bar{\rho}\bar{a}^2(1+(1+\bar{v}\kappa)M_x\psi)}{2(1+M_x)} \end{bmatrix}, \tag{4.53}$$

where $M_x = \frac{\bar{u}}{\bar{a}}$ is the boundary-normal Mach number. The left eigenvector matrix may be obtained by inverting R:

$$L = \begin{bmatrix} \boldsymbol{l}_1 \\ \boldsymbol{l}_2 \\ \boldsymbol{l}_3 \\ \boldsymbol{l}_4 \end{bmatrix} = R^{-1} = \begin{bmatrix} -\frac{1}{\bar{\rho}} & 0 & 0 & \frac{1}{\bar{\rho}\bar{a}^2} \\ 0 & \frac{\bar{u}\kappa}{\bar{a}} & \frac{1+\bar{v}\kappa}{\bar{a}} & \frac{\kappa}{\bar{\rho}\bar{a}} \\ 0 & \frac{1+\bar{v}\kappa}{\bar{a}} & -\frac{\bar{u}\kappa}{\bar{a}} & \frac{(1+\bar{v}\kappa)\psi}{\bar{\rho}\bar{a}^2} \\ 0 & -\frac{1+\bar{v}\kappa}{\bar{a}} & \frac{\bar{u}\kappa}{\bar{a}} & \frac{(1+\bar{v}\kappa)\psi}{\bar{\rho}\bar{a}^2} \end{bmatrix}, \tag{4.54}$$

The right eigenvectors form a set of linearly independent basis vectors. Every perturbation from a mean state can thus be expressed as a linear combination of right eigenvectors with weights α_j:

$$\boldsymbol{q} = \mathrm{Re}\left(\left[\sum_{j=1}^{4} \alpha_j \boldsymbol{r}_j e^{\mathrm{i}k_j x} \right] e^{\mathrm{i}(my+\omega t)} \right) \tag{4.55}$$

The left and right eigenvectors are constructed such that $l_j r_k = 0$ for $j \neq k$. Therefore, the left eigenvectors represent the share of their corresponding right vector in any arbitrary perturbation and the weight of the right eigenvector is $\alpha_j = \boldsymbol{l}_j \hat{\boldsymbol{q}}$. In order to achieve a non-reflecting behaviour, the weight of the right eigenvector has to be zero for all incoming waves. The non-reflecting boundary condition is finally expressed by the requirement that, for any combination of m and ω, for each $\boldsymbol{l}_j$ representing an incoming wave

$$\boldsymbol{l}_{(\omega,m)j} \cdot \hat{\boldsymbol{q}}_{(\omega,m)} = 0. \tag{4.56}$$

Transformation to characteristic variables

For the considered case of a normally subsonic flow, there are both outgoing and incoming waves at the boundary. The outgoing perturbations therefore need to be extrapolated to the boundary faces from the domain interior [158]. One-dimensional characteristic variables $\boldsymbol{c} = [c_1, c_2, c_3, c_4]^T$ are introduced for this purpose. By definition, these characteristics coincide with the weights α_j in Eq. 4.55 for planar waves

propagating in the direction normal to the boundary ($\kappa = 0$). The forward and backward transforms are given by

$$\boldsymbol{c} = L_{1d}\boldsymbol{q}, \qquad \boldsymbol{q} = R_{1d}\boldsymbol{c} \tag{4.57}$$

respectively, with the transformation matrices defined as

$$L_{1d} = L(\kappa = 0) = \begin{bmatrix} -\frac{1}{\bar{\rho}} & 0 & 0 & \frac{1}{\bar{\rho}\bar{a}^2} \\ 0 & 0 & \frac{1}{\bar{a}} & 0 \\ 0 & \frac{1}{\bar{a}} & 0 & \frac{1}{\bar{\rho}\bar{a}^2} \\ 0 & -\frac{1}{\bar{a}} & 0 & \frac{1}{\bar{\rho}\bar{a}^2} \end{bmatrix} \tag{4.58}$$

$$R_{1d} = R(\kappa = 0) = \begin{bmatrix} -\bar{\rho} & 0 & \frac{\bar{\rho}}{2} & \frac{\bar{\rho}}{2} \\ 0 & 0 & \frac{\bar{a}}{2} & -\frac{\bar{a}}{2} \\ 0 & \bar{a} & 0 & 0 \\ 0 & 0 & \frac{\bar{\rho}\bar{a}^2}{2} & \frac{\bar{\rho}\bar{a}^2}{2} \end{bmatrix} \tag{4.59}$$

We further introduce notation distinguishing between the incoming and outgoing characteristics, which will allow us to define the inflow and outflow boundary conditions in a unified compact form. At a normally subsonic inlet boundary, three waves enter the domain and one exits:

$$\left[\begin{array}{c} L^{in} \\ \hline L^{out} \end{array}\right] = \left[\begin{array}{c} \boldsymbol{l}_1 \\ \boldsymbol{l}_2 \\ \boldsymbol{l}_3 \\ \hline \boldsymbol{l}_4 \end{array}\right], \quad \left[\begin{array}{c} \boldsymbol{c}^{in} \\ \hline \boldsymbol{c}^{out} \end{array}\right] = \left[\begin{array}{c} c_1 \\ c_2 \\ c_3 \\ \hline c_4 \end{array}\right], \quad [R^{in}|R^{out}] = \left[\begin{array}{ccc|c} \boldsymbol{r}_1 & \boldsymbol{r}_2 & \boldsymbol{r}_3 & \boldsymbol{r}_4 \end{array}\right] \tag{4.60}$$

At a normally subsonic outlet boundary, in contrast, there are three outgoing waves and one incoming:

$$\left[\begin{array}{c} L^{out} \\ \hline L^{in} \end{array}\right] = \left[\begin{array}{c} \boldsymbol{l}_1 \\ \boldsymbol{l}_2 \\ \boldsymbol{l}_3 \\ \hline \boldsymbol{l}_4 \end{array}\right], \quad \left[\begin{array}{c} \boldsymbol{c}^{out} \\ \hline \boldsymbol{c}^{in} \end{array}\right] = \left[\begin{array}{c} c_1 \\ c_2 \\ c_3 \\ \hline c_4 \end{array}\right], \quad [R^{out}|R^{in}] = \left[\begin{array}{ccc|c} \boldsymbol{r}_1 & \boldsymbol{r}_2 & \boldsymbol{r}_3 & \boldsymbol{r}_4 \end{array}\right] \tag{4.61}$$

Spectral NRBC

The Spectral NRBC is given by Eq. 4.56. Expressed in characteristic variables, the condition becomes

$$L^{in}_{(\omega,m)}\hat{\boldsymbol{q}}_{(\omega,m)} = L^{in}_{(\omega,m)}\left(R^{in}_{1d}\hat{\boldsymbol{c}}^{in}_{(\omega,m),target} + R^{out}_{1d}\hat{\boldsymbol{c}}^{out}_{(\omega,m)}\right) = 0. \tag{4.62}$$

The outgoing characteristics $\hat{\boldsymbol{c}}^{out}_{(\omega,m)}$ are extrapolated from the domain interior. Hence the *target* values of the incoming characteristics for achieving a non-reflecting behaviour are the only unknowns. Rearranging Eq. 4.62 yields the formula

$$\hat{\boldsymbol{c}}^{in}_{(\omega,m),target} = -\left(L^{in}_{(\omega,m)}R^{in}_{1D}\right)^{-1} L^{in}_{(\omega,m)}R^{out}_{1D}\hat{\boldsymbol{c}}^{out}_{(\omega,m)}. \tag{4.63}$$

This equation serves to obtain the Fourier coefficients of incoming characteristics for every combination of ω and m. The only exception is the mode $\omega = 0$, $m = 0$, representing the temporally and spatially mean value. This mode is treated differently in order to uphold the user-prescribed values at the boundary. A description of this procedure is given in Sec. 4.2.5.

Equation 4.63 provides a unified compact formulation of the Spectral NRBC for both the inflow and the outflow boundary. Substituting for the respective matrices for incoming and outgoing waves from Eqs. 4.60, 4.61 yields the following expanded formulations.

Inlet Spectral NRBC:

$$\begin{bmatrix} \hat{c}_1 \\ \hat{c}_2 \\ \hat{c}_3 \end{bmatrix}^{in}_{target} = \begin{bmatrix} 0 \\ \frac{\kappa(\kappa\overline{v}+1)(\psi\overline{u}-\overline{a})}{(\psi+1)(\kappa\overline{v}+1)^2+\kappa^2\overline{u}(\overline{a}+\overline{u})}\hat{c}_4 \\ -\frac{(\psi-1)(\kappa\overline{v}+1)^2+\kappa^2\overline{u}(\overline{a}-\overline{u})}{(\psi+1)(\kappa\overline{v}+1)^2+\kappa^2\overline{u}(\overline{a}+\overline{u})}\hat{c}_4 \end{bmatrix} \tag{4.64}$$

Outlet Spectral NRBC:

$$\hat{c}^{in}_{4,target} = -\frac{2\kappa\overline{u}}{(\psi+1)(\kappa\overline{v}+1)}\hat{c}_2 - \frac{\psi-1}{\psi+1}\hat{c}_3 \tag{4.65}$$

Exact Steady NRBC

The original Exact Steady NRBC of Giles [58] is derived by considering only spatial modes with $m \neq 0, \omega = 0$. The left eigenvector matrix for steady state flows becomes

$$L_s = \lim_{\kappa\to\infty} L(\kappa) = \begin{bmatrix} -\frac{1}{\overline{\rho}} & 0 & 0 & \frac{1}{\overline{\rho}\overline{a}^2} \\ 0 & -\frac{\overline{u}}{\overline{a}^2} & -\frac{\overline{v}}{\overline{a}^2} & -\frac{1}{\overline{\rho}\overline{a}^2} \\ 0 & -\frac{\overline{v}}{\overline{a}^2} & \frac{\overline{u}}{\overline{a}^2} & \frac{\beta}{\overline{\rho}\overline{a}^3} \\ 0 & \frac{\overline{v}}{\overline{a}^2} & -\frac{\overline{u}}{\overline{a}^2} & \frac{\beta}{\overline{\rho}\overline{a}^3} \end{bmatrix} \tag{4.66}$$

with

$$\beta = \begin{cases} -\text{sign}(\overline{v})\sqrt{(\overline{u}^2+\overline{v}^2)-\overline{a}^2} & \text{for } \overline{u}^2+\overline{v}^2 > \overline{a}^2 \\ \text{i}\,\text{sign}(m)\sqrt{\overline{a}^2-(\overline{u}^2+\overline{v}^2)} & \text{for } \overline{u}^2+\overline{v}^2 < \overline{a}^2 \end{cases}. \tag{4.67}$$

Analogously to the Spectral NRBC, the Exact Steady NRBC is given in a unified compact form for both the inlet and outlet boundaries:

$$\hat{\boldsymbol{c}}^{in}_{(m),target} = -\left(L^{in}_{s(m)}R^{in}_{1D}\right)^{-1} L^{in}_{s(m)}R^{out}_{1D}\hat{\boldsymbol{c}}^{out}_{(m)} \tag{4.68}$$

The expanded formulations of Exact Steady NRBC for each boundary are given below.

Inlet Exact Steady NRBC:

$$\begin{bmatrix} \hat{c}_1 \\ \hat{c}_2 \\ \hat{c}_3 \end{bmatrix}^{in}_{target} = \begin{bmatrix} 0 \\ -\frac{\beta+\overline{v}}{\overline{a}+\overline{u}}\hat{c}_4 \\ \left(\frac{\beta+\overline{v}}{\overline{a}+\overline{u}}\right)^2\hat{c}_4 \end{bmatrix} \tag{4.69}$$

Outlet Exact Steady NRBC:

$$\hat{c}^{in}_{4,target} = \frac{2\overline{u}}{\beta-\overline{v}}\hat{c}_2 - \frac{\beta+\overline{v}}{\beta-\overline{v}}\hat{c}_3 \tag{4.70}$$

Mean Flow Treatment

The mode $\omega = 0$, $m = 0$ is treated separately from all other modes to ensure that the user-prescribed values at the boundary are respected. The procedure is nearly identical for the Spectral and Exact Steady NRBC. The only difference is in the definition of mean value, which is obtained by averaging either only spatially (Exact Steady NRBC), or both spatially and temporally (Spectral NRBC).

The deviation of the average boundary state from the prescribed values is expressed by the residual vector $\boldsymbol{\mathfrak{R}}$:

$$\boldsymbol{\mathfrak{R}}|_{inlet} = \begin{bmatrix} \bar{p}(\bar{s}-s_{bd}) \\ \bar{\rho}\bar{a}(\bar{v}-\bar{u}\tan(\beta_{bd})) \\ \bar{\rho}(\bar{h}_t-\bar{h}_{t,bd}) \end{bmatrix}, \qquad \boldsymbol{\mathfrak{R}}|_{outlet} = \bar{p}-p_{bd}, \tag{4.71}$$

where s is specific entropy, h_0 specific total enthalpy and β is flow angle relatively to the axial downstream direction. Averaged quantities at the boundary are denoted with a bar and prescribed values with a subscript *bd*.

The residuals are driven to zero using a single step of Newton-Raphson iteration procedure:

$$\boldsymbol{\mathfrak{R}} + \frac{\partial\boldsymbol{\mathfrak{R}}}{\partial\boldsymbol{c}^{in}}\delta\overline{\boldsymbol{c}^{in}} = 0. \tag{4.72}$$

The Jacobian matrix may be written as a product of two matrices

$$\frac{\partial \mathfrak{R}}{\partial \boldsymbol{c}^{in}} = \frac{\partial \mathfrak{R}}{\partial \boldsymbol{q}} \frac{\partial \boldsymbol{q}}{\partial \boldsymbol{c}^{in}} = \frac{\partial \mathfrak{R}}{\partial \boldsymbol{q}} R_{1d}^{in}, \tag{4.73}$$

which yields

$$\mathfrak{R} + \frac{\partial \mathfrak{R}}{\partial \boldsymbol{q}} R_{1d}^{in} \delta \overline{\boldsymbol{c}^{in}} = 0. \tag{4.74}$$

It remains to determine the matrices $\frac{\partial \mathfrak{R}}{\partial \boldsymbol{q}}$ for both boundary conditions. The terms proportional to the residual may be neglected, as they are zero in the converged limit [59]. Hence we obtain for the inflow boundary

$$\left.\frac{\partial \mathfrak{R}}{\partial \boldsymbol{q}}\right|_{inlet} = \begin{bmatrix} p \left.\dfrac{\partial s}{\partial \rho}\right|_{p} & 0 & 0 & p \left.\dfrac{\partial s}{\partial p}\right|_{\rho} \\ 0 & -\rho a \tan(\beta_{bd}) & \rho a & 0 \\ \rho \left.\dfrac{\partial h_0}{\partial \rho}\right|_{u,v,p} & \rho u & \rho v & \rho \left.\dfrac{\partial h_0}{\partial p}\right|_{\rho,u,v} \end{bmatrix}. \tag{4.75}$$

Given that the fluid is represented by an ideal gas model, the partial derivatives of entropy and total enthalpy may be easily expressed, yielding

$$\left.\frac{\partial \mathfrak{R}}{\partial \boldsymbol{q}}\right|_{inlet} = \begin{bmatrix} -c_v a^2 & 0 & 0 & c_v \\ 0 & -\rho a \tan(\beta_{bd}) & \rho a & 0 \\ -\dfrac{a^2}{\gamma - 1} & \rho u & \rho v & \dfrac{\gamma}{\gamma - 1} \end{bmatrix}. \tag{4.76}$$

Analogically, we obtain for the outlet

$$\left.\frac{\partial \mathfrak{R}}{\partial \boldsymbol{q}}\right|_{outlet} = \begin{bmatrix} 0 & 0 & 0 & 1 \end{bmatrix}. \tag{4.77}$$

4.3 Aeroelastic Analysis

The three-dimensional deformation of an elastic body needs to be represented with the two-dimensional computational model. The fundamental eigenmodes of flexing, torsion and edgewise bending are in the two-dimensional section expressed with two orthogonal translations and a rotation. The airfoil or blade profile is modelled as a rigid body with no distortion.

4.3.1 Energy Method

The energy method is based on the assumption that the effect of aerodynamic forces on the change of structural dynamic properties can be neglected. The necessary prerequisite for the validity of this assumption is a large density ratio between fluid and structure, which is usually fulfilled in turbomachines.

The eigenmodes and eigenfrequencies of a blade are determined in advance with a structural solver and serve to prescribe its motion as a boundary condition for an unsteady fluid dynamics solver. It is further assumed that all blades in the blade row are perfectly identical and thus they are subjected to the same motion, only with a constant phase shift between each two neighbouring blades (IBPA). The energy transfer between fluid and structure during one cycle of oscillation is quantified by the aerodynamic damping coefficient Ξ. We are adopting two different definitions, depending on the type of blade motion. In the case of a torsion mode where the blade undergoes pitching oscillations, the following formula is used [157]:

$$\Xi = \frac{-W_{aero}}{\pi b(\Delta\alpha C)^2(p_{01} - p_2)} \tag{4.78}$$

Here W_{aero} is the work of aerodynamic forces, b and C are the blade span and chord respectively, $\Delta\alpha$ is the pitching magnitude in radians, p_{01} denotes the inlet total pressure and p_2 the outlet static pressure. On the other hand, if the blade vibrates in a bending mode or in a general coupled mode, the damping coefficient is defined as follows [156]:

$$\Xi = \frac{-W_{aero}}{\pi b h^2(p_{01} - p_2)}, \tag{4.79}$$

where h is the maximum displacement of all points on blade surface during the oscillation cycle and reduces simply to the translatory motion amplitude in the case of a bending mode. A positive value of Ξ indicates a stable flutter behaviour. Out of the set of all admissible IBPAs, the one with the lowest value of Ξ determines the overall aeroelastic stability.

4.3.2 Elastically Mounted Solid Body

The fluid-structure coupled computations consider an elastically mounted solid body with two degrees of freedom. The body may be vertically translated in representation of a flexing mode, or rotated about the elastic axis (EA) to express torsion. A sketch of the body in the reference and displaced configurations is provided in Fig. 4.2. The translatory motion is defined by the EA displacement Δy_{EA}, while the angle of rotation is denoted ϕ . The elastic axis is located at ξ_{EA} and the center of gravity (CG) at ξ_{CG}, measured along the chord C from the leading edge (LE). The pressure exerted on the airfoil surface $\partial\Omega_w$ by the surrounding flow-field results into a horizontal drag force F_x, vertical lift force F_y and torsional moment M acting on the body:

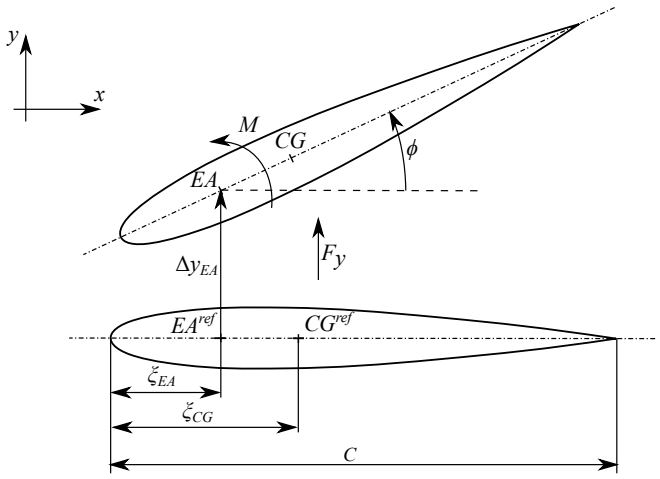

Figure 4.2: Solid body with two degrees of freedom

$$F_y = \oint_{\partial\Omega_w} -p\, n_y dS, \quad F_x = \oint_{\partial\Omega_w} -p\, n_x dS, \quad M = \oint_{\partial\Omega_w} \begin{bmatrix} x_{EA} - x \\ y - y_{EA} \end{bmatrix} \cdot \boldsymbol{n} p\, dS, \tag{4.80}$$

where $[x, y]^T$ are the surface coordinates, $[x_{EA}, y_{EA}]^T$ is the instantaneous position of the EA and $\boldsymbol{n} = [n_x, n_y]^T$ is the unit outward normal to the surface.

Equations of motion can be derived for the solid body from the Lagrange equations of second kind [95]:

$$\frac{d}{dt}\frac{\partial E_K}{\partial \dot{q}_j} - \frac{\partial E_K}{\partial q_j} + \frac{\partial E_P}{\partial q_j} = Q_j, \qquad j = 1, 2 \tag{4.81}$$

where q_j are the generalized coordinates, in this case $q_1 = \Delta y_{EA}$ and $q_2 = \phi$, and Q_j are the generalized forces, $Q_1 = F_y$ and $Q_2 = M$. The potential energy E_P is defined as

$$E_P = \frac{1}{2} k_y \Delta y_{EA}^2 + \frac{1}{2} k_\phi \phi^2, \tag{4.82}$$

where k_y is the bending stiffness and k_ϕ is the torsional stiffness of the supporting springs. Denoting $\rho_l(\xi)$ the linear density of the body, such that its total mass is given by

$$m = \int_0^C \rho_l(\xi) d\xi, \tag{4.83}$$

we can define the static (S_ϕ) and inertia (I_ϕ) moments around EA:

$$S_\phi = \int_0^C (\xi - \xi_{EA}) \rho_l(\xi) d\xi, \qquad I_\phi = \int_0^C (\xi - \xi_{EA})^2 \rho_l(\xi) d\xi. \tag{4.84}$$

Hence the kinetic energy E_K can be expressed as [95]

$$E_K = \frac{1}{2}\Delta\dot{y}_{EA}^2 m + \Delta\dot{y}_{EA}\dot{\phi}\cos\phi S_\phi + \frac{1}{2}\dot{\phi}^2 I_\phi. \tag{4.85}$$

Substituting E_P from Eq. 4.82 and E_K from Eq. 4.85 into Eq. 4.81, we obtain a set of two nonlinear ordinary differential equations describing the motion of a body with two degrees of freedom:

$$\begin{aligned} m\Delta\ddot{y}_{EA} + S_\phi\ddot{\phi}\cos\phi - S_\phi\dot{\phi}^2\sin\phi + k_y\Delta y_{EA} &= F_y \\ S_\phi\Delta\ddot{y}_{EA}\cos\phi + I_\phi\ddot{\phi} + k_\phi\phi &= M. \end{aligned} \tag{4.86}$$

Additionally, structural damping may be considered, yielding the following set of equations:

$$\begin{aligned} m\Delta\ddot{y}_{EA} + S_\phi\ddot{\phi}\cos\phi - S_\phi\dot{\phi}^2\sin\phi + k_y\Delta y_{EA} + b_y\Delta\dot{y}_{EA} &= F_y \\ S_\phi\Delta\ddot{y}_{EA}\cos\phi + I_\phi\ddot{\phi} + k_\phi\phi + b_\phi\dot{\phi} &= M, \end{aligned} \tag{4.87}$$

with the coefficients of structural damping in bending and in torsion denoted b_y, b_ϕ respectively.

The equations of motion can be linearised under the assumption of small angular displacements. As shown in author's paper [1], linearisation has a nearly negligible effect on the predicted temporal evolution of airfoil displacement in the applications considered in this work. However, since the equations of motion are solved numerically, there is no benefit in using the linearised version.

Chapter 5

Numerical Solution

Numerical results presented in this thesis were obtained with a finite volume code written in C++ by the author. This chapter provides a description of numerical methods implemented in the solver. First, a grid motion algorithm for computations with oscillating bodies is presented. The core of the computational model is the solution of unsteady aerodynamics. A brief account of the finite volume method is given, followed by a description of schemes used for spatial and temporal discretisation. Aeroelastic evaluations use either the energy method, or a fluid-structure coupled model with elastically mounted solid bodies. A description of the numerical solution of body motion and its coupling with flow solver in the time-stepping procedure concludes the chapter.

5.1 Domain Discretisation and Grid Motion

All computations were performed on two-dimensional unstructured grids generated with ANSYS® ICEM 19.1. The grids used for the simulation of external aerodynamics were created as C-type structured, but converted to unstructured representation before being loaded by the solver. The domain discretisation was performed with either triangular elements, quadrilateral elements, or a combination of both. The universal CGNS format was used for storing the grid as well as the flow solution and convergence history. Functions of the CGNS mid-level library [147] were employed for reading and exporting the data.

Aeroelastic computations are performed on domains with moving boundaries, requiring the positions of grid nodes to be updated accordingly in each iteration. The procedure for calculating the node coordinates needs to be highly efficient, in order not to extend the computational time notably. At the same time, a satisfactory mesh quality needs to be guaranteed even for large domain deformations. The implemented algorithm exploits the representation of the oscillating structure as a rigid body and interpolates its motion onto the mesh vertices within the domain.

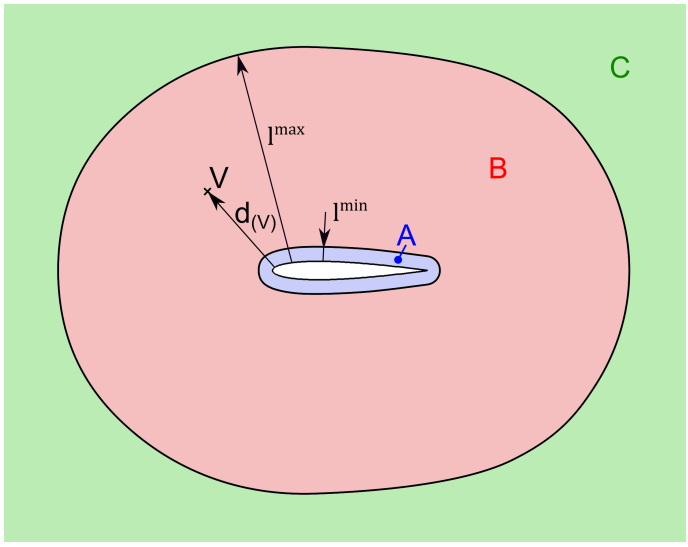

Figure 5.1: Mesh movement subdomains, isolated airfoil

5.1.1 Isolated Airfoil

Let us first consider the case of an isolated airfoil. The computational domain is divided into three subdomains labelled A, B and C, as shown in Fig. 5.1. The depicted position of the airfoil will be considered as a reference configuration. Grid vertices inside the subdomain A move together with the airfoil as a rigid body, vertices in C remain at their reference position, and the motion of vertices in B is obtained by interpolating between A and C. The borders between A, B and between B, C are formed by curves equidistant to the airfoil surface, at a distance defined by the lower (l^{min}) and upper (l^{max}) movement limits respectively.

The instantaneous position of the airfoil is defined by the translation $\Delta\boldsymbol{x}_{EA} = [\Delta x_{EA}, \Delta y_{EA}]^T$ of elastic axis (EA) and by the angle of rotation about EA, denoted ϕ. The displacement of a vertex V on the airfoil surface, with respect to its position in the reference configuration $\boldsymbol{x}_V^{ref}$, is calculated as

$$\Delta\boldsymbol{x}_V^{rigid} = \boldsymbol{x}_V - \boldsymbol{x}_V^{ref} = \boldsymbol{x}_{EA}^{ref} + \Delta\boldsymbol{x}_{EA} + Q(\boldsymbol{x}_V^{ref} - \boldsymbol{x}_{EA}^{ref}) - \boldsymbol{x}_V^{ref}, \tag{5.1}$$

where Q is a matrix of rotation by angle ϕ:

$$Q = \begin{bmatrix} \cos\phi & -\sin\phi \\ \sin\phi & \cos\phi \end{bmatrix}. \tag{5.2}$$

In order to obtain the displacement of the mesh vertices inside the domain, the rigid body motion given by Eq. 5.1 is multiplied with a coefficient q_V, whose value is equal to 1 in the subdomain A and equal to 0 in the subdomain C. In the subdomain B, it is varied linearly in function of the vertex distance from airfoil surface d_V:

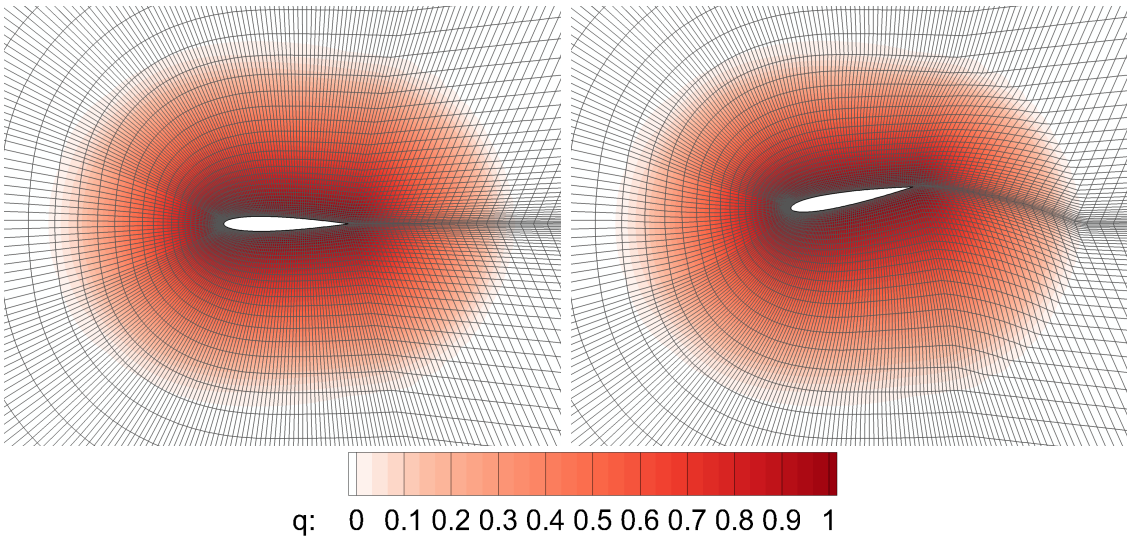

Figure 5.2: Isolated airfoil mesh and q distribution in reference (left) and displaced (right) configurations

$$q_V = \begin{cases} 1 & \text{for } d_V \leq l^{min}, & \text{i.e. } V \in A \\ \dfrac{d_V - l^{min}}{l^{max} - l^{min}} & \text{for } l^{min} < d_V < l^{max}, & \text{i.e. } V \in B \\ 0 & \text{for } d_V \geq l^{max}, & \text{i.e. } V \in C \end{cases} \tag{5.3}$$

The distance d_V needs to be known for each grid vertex. Its calculation is computationally expensive on large meshes, but since it is performed only once during initialization, it impacts negligibly the overall computational time. A formula for the instantaneous position of an arbitrary vertex in any of the three subdomains then reads:

$$\boldsymbol{x}_V = \boldsymbol{x}_V^{ref} + q_V \Delta \boldsymbol{x}_V^{rigid} = \boldsymbol{x}_V^{ref} + q_V \left[\boldsymbol{x}_{EA}^{ref} + \Delta \boldsymbol{x}_{EA} + Q(\boldsymbol{x}_V^{ref} - \boldsymbol{x}_{EA}^{ref}) - \boldsymbol{x}_V^{ref} \right] \tag{5.4}$$

5.1.2 Blade Cascade

The mesh motion algorithm for a single airfoil, described in Sec. 5.1.1, can be extended to blade cascades with an arbitrary number of blades in a relatively straightforward manner. The instantaneous position of a mesh vertex V is obtained by adding the contributions due to individual blade movements to its reference position:

$$\boldsymbol{x}_V = \boldsymbol{x}_V^{ref} + \sum_{j=1}^{N_b} \Delta \boldsymbol{x}_{V,j}, \tag{5.5}$$

where N_b is the number of blades in the cascade and the contribution due to a blade j reads

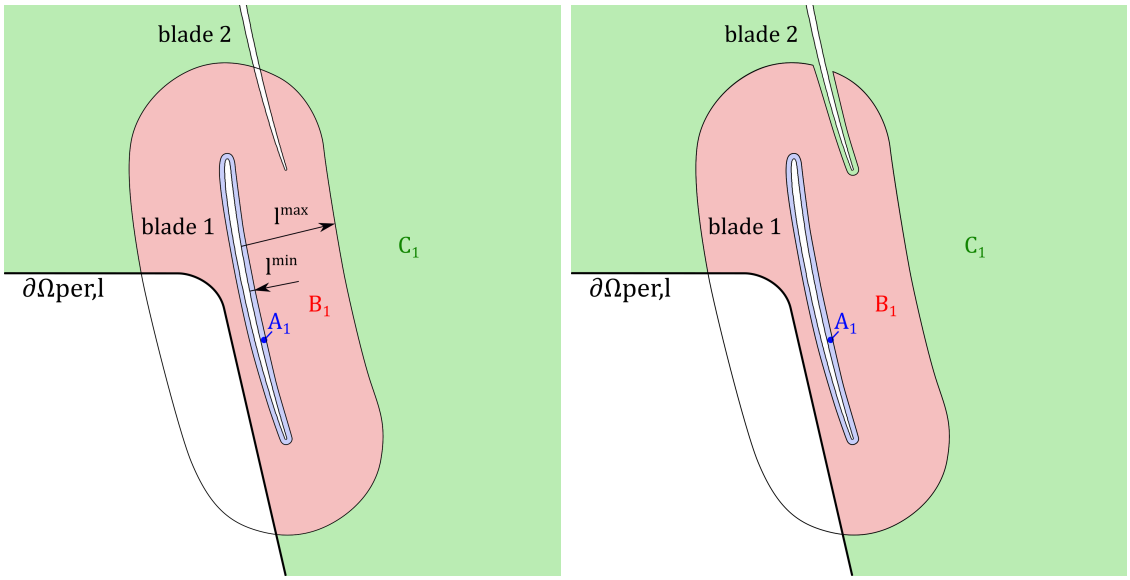

Figure 5.3: Mesh movement subdomains of *blade 1*. Original (left) and modified (right) definition of subdomain boundaries

$$\Delta \boldsymbol{x}_{V,j} = q_{V,j} \left[\boldsymbol{x}^{ref}_{EA,j} + \Delta \boldsymbol{x}_{EA,j} + Q_j(\boldsymbol{x}^{ref}_{V} - \boldsymbol{x}^{ref}_{EA,j}) - \boldsymbol{x}^{ref}_{V} \right]. \tag{5.6}$$

It only remains to establish the coefficients $q_{V,j}$. The fundamental idea of decomposing the computational domain into the three subdomains A_j, B_j and C_j for each blade j is retained. However, the subdomain borders cannot be constructed simply as curves equidistant to the blade surface, as shown in Fig. 5.3 left. The subdomain B_1 includes a part of the *blade 2* surface as well as a part of the lower periodic boundary $\partial\Omega_{per,l}$. Since the coefficient $q_{V,1}$ is non-zero in B_1, a movement of *blade 1* would shift some of the points forming the *blade 2* surface and thus deform its shape. Moreover, a part of the lower periodic boundary would also be displaced, whereas its upper counterpart $\partial\Omega_{per,u}$ would remain unaffected, resulting in a loss of spatial periodicity at the boundaries.

A trivial solution would be to choose d_1^{max} sufficiently low, such that that there is no intersection of the subdomain B_1 with either a blade surface or a domain boundary. However, this would prevent from spreading the mesh deformation sufficiently far throughout the domain and the resulting mesh quality would be compromised, with a possible occurrence of negative cell volumes.

The intersections of the subdomains B_j with other blades are addressed by defining the upper movement limit as a function of the vertex distance to the nearest blade instead of taking a constant value. The modified upper movement limit at a vertex V, used to evaluate the movement coefficient $q_{V,j}$, is defined as:

$$\tilde{l}^{max}_{V,j} = \min\{l^{max}, d_{V,j} + \min_{k \neq j}(d_{V,k}) - l^{min}\}, \tag{5.7}$$

where l^{max} is the user-defined upper movement limit, $d_{V,k}$ is a distance of the vertex

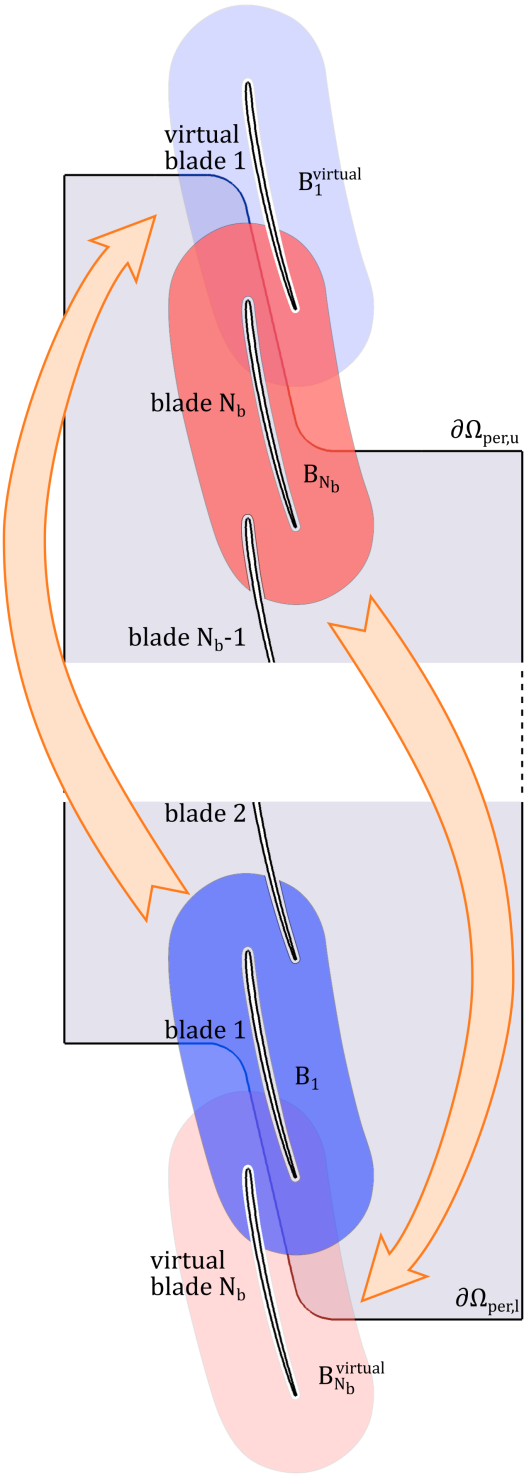

Figure 5.4: Virtual blades for mesh movement

V to the surface of a blade k, and l^{min} is the lower movement limit. The coefficient $q_{V,j}$ is then calculated with the following formula:

$$q_{V,j} = \begin{cases} 1 & \text{for } d_{V,j} \leq l^{min}, & \text{i.e. } V \in A_j \\ \dfrac{d_{V,j} - l^{min}}{\tilde{l}^{max}_{V,j} - l^{min}} & \text{for } l^{min} < d_{V,j} < \tilde{l}^{max}_{V,j}, & \text{i.e. } V \in B_j \\ 0 & \text{for } d_{V,j} \geq \tilde{l}^{max}_{V,j}, & \text{i.e. } V \in C_j \end{cases} \tag{5.8}$$

This definition guarantees that if a vertex V is located in the inner subdomain A_j of a blade j, i.e. $d_{V,j} \leq l^{min}$, then all the movement coefficients of other blades $q_{k(V)}$, $k \neq j$, are set to zero. Hence all the vertices inside A_j are displaced only when the blade j itself moves, including those forming the blade surface. The *blade 1* movement subdomains constructed with the modified definition are shown in Fig. 5.3 right.

The loss of spatial periodicity due to the periodic boundary deformation is resolved by the addition of *virtual blades*. These are copies of the blades physically present in the computational domain and they undergo the same motion, but their axes are shifted vertically by the domain pitch. Let us consider a cascade featuring N_b blades, visualised in Fig 5.4. The *virtual blade* N_b has the same instantaneous displacement and rotation angle as *blade* N_b, but the reference position of its elastic axis is defined as

$$\begin{bmatrix} x^{ref}_{EA,N_b,virtual} \\ y^{ref}_{EA,N_b,virtual} \end{bmatrix} = \begin{bmatrix} x^{ref}_{EA,N_b} \\ y^{ref}_{EA,N_b} - N_b \cdot P \end{bmatrix}, \tag{5.9}$$

where P is the pitch of a single blade passage. Analogically, the elastic axis of the *virtual blade 1* is in the reference configuration located at:

$$\begin{bmatrix} x^{ref}_{EA,1,virtual} \\ y^{ref}_{EA,1,virtual} \end{bmatrix} = \begin{bmatrix} x^{ref}_{EA,1} \\ y^{ref}_{EA,1} + N_b \cdot P \end{bmatrix}. \tag{5.10}$$

By including the contribution due to the virtual blades to the total displacement of grid vertices in Eq. 5.5, it is ensured that the corresponding points at periodic boundaries undergo exactly the same motion and the spatial periodicity is thus preserved. An example of a deformed mesh for a blade cascade featuring 6 blades is shown in Fig. 5.5.

5.2 Unsteady Aerodynamics

5.2.1 Finite Volume Method

The system of Euler equations in two dimensions is discretised with a cell-centered finite volume method (FVM) in ALE formulation. The governing equations are

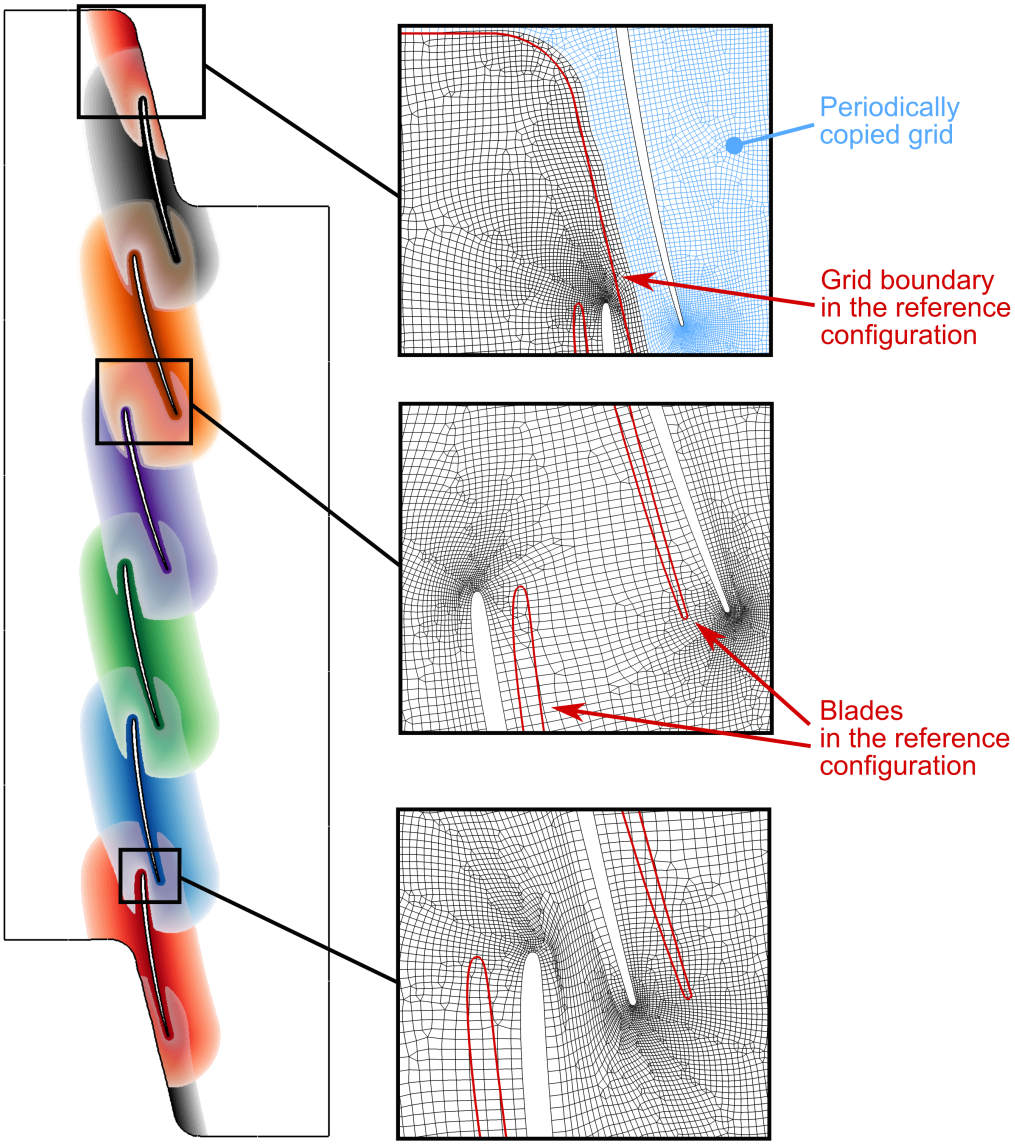

Figure 5.5: Deformed mesh of a blade cascade. Contours of the q coefficient, differentiated for individual blades by color, on the left (darker hue marks higher value of q on the scale from 0 to 1). Details of the displaced mesh on the right

written in the integral form

$$\frac{\partial}{\partial t}\int_{\Omega(t)} \boldsymbol{W} d\Omega + \oint_{\partial\Omega(t)} \boldsymbol{F}^{ALE} dS = 0, \tag{5.11}$$

with the definitions of the vector of conserved variables $\boldsymbol{W}$ and of the inviscid flux vector $\boldsymbol{F}^{ALE}$ given in Eq. 4.16. The computational domain Ω is divided into a set of non-overlapping subsets Ω_i (finite volumes or cells) which must cover it completely. The integral conservation law 5.11 has to be satisfied in each finite volume cell. Let us denote $\boldsymbol{W}_i$ the average of $\boldsymbol{W}$ over a cell Ω_i:

$$\boldsymbol{W}_i(t) = \frac{1}{|\Omega_i|}\int_{\Omega_i(t)} \boldsymbol{W}(\boldsymbol{x}, t) d\Omega, \tag{5.12}$$

where $|\Omega_i|$ is the volume of the cell Ω_i. Surface integral of the inviscid flux $\boldsymbol{F}^{ALE}$ may be written as a sum of fluxes crossing the faces $\partial\Omega_{ij}$ of the cell Ω_i:

$$\oint_{\partial\Omega_i(t)} \boldsymbol{F}^{ALE}(\boldsymbol{x}, t) dS = \sum_{j=1}^{N_F} \int_{\partial\Omega_{ij}(t)} \boldsymbol{F}^{ALE}(\boldsymbol{x}, t) dS, \tag{5.13}$$

where N_F is the number of cell faces. Next, we perform spatial discretisation and approximate the flux $\boldsymbol{F}^{ALE}$ as a function of the states $\boldsymbol{W}_i$, $\boldsymbol{W}_j$ in the cells Ω_i, Ω_j adjacent to the face $\partial\Omega_{ij}$:

$$\int_{\partial\Omega_{ij}(t)} \boldsymbol{F}^{ALE}(\boldsymbol{x}, t) dS \approx \boldsymbol{\mathcal{F}}_{ij}^{ALE}(\boldsymbol{W}_i(t), \boldsymbol{W}_j(t)) \Delta S_{ij}(t) \tag{5.14}$$

The numerical flux is required to be conservative, consistent with the conservation laws and Lipschitz continuous (for details see e.g. [114]). Substituting from Eqs. 5.12, 5.13 and 5.14 into the system of Euler equations 5.11, we obtain a semi-discrete form of the FVM:

$$\frac{d}{dt}\left(\boldsymbol{W}_i |\Omega_i|\right) = -\sum_{j=1}^{N_F} \boldsymbol{\mathcal{F}}_{ij}^{ALE} \Delta S_{ij} = -\boldsymbol{R}_i, \tag{5.15}$$

where $\boldsymbol{R}_i$ denotes a residual vector. In order to obtain a fully discrete FVM scheme, the temporal derivative needs to be discretised and a suitable approximation has to be selected for the inviscid fluxes. This approach of discretising the governing equations separately in space and time is referred to as a *method of lines* [14]. For a more comprehensive description of the FVM, the reader is referred e.g. to [114], [90] or [14].

5.2.2 Flux Approximation

The inviscid fluxes on cell interfaces are approximated with a numerical scheme from the family of advection upstream splitting methods (AUSM), first introduced

by Liou and Steffen [122]. The choice of the scheme is motivated by its ability to capture sharply shockwaves and contact discontinuities. A modified version called AUSM$^+$ was published by Liou [121], boasting improved accuracy in comparison with the original formulation. However, one notable deficiency persisted also in the newer version, in that it was found to produce pressure oscillations in a grid direction with a very small velocity component. The phenomenon occurs for example in the direction normal to a boundary layer and it is amplified in regions of low speed flow. This behaviour motivated Liou [120] to develop the AUSM$^+$-up variant of the scheme which prevents the formation of pressure oscillations from the outset and is applicable to all speed regimes. The improved formulation was shown to address the issue of pressure oscillations also in author's publication [1] and it is implemented in the present computational model.

The pivotal idea of the AUSM schemes is to decompose the inviscid flux vector into a purely convective term and a pressure term:

$$\boldsymbol{\mathcal{F}}^{ALE} = \boldsymbol{\mathcal{F}}_c + \boldsymbol{\mathcal{P}}_{1/2} = M_{1/2} a_{1/2} \boldsymbol{\psi}_{L/R} + \boldsymbol{\mathcal{P}}_{1/2}. \tag{5.16}$$

The two parts are physically distinct, hence the approaches taken for their discretisation differ. The first term expresses convection of the vector

$$\boldsymbol{\psi} = \begin{bmatrix} \rho \\ \rho u \\ \rho v \\ \rho e_t + p \end{bmatrix} \tag{5.17}$$

across the cell interface. Depending on the flow direction, either the state in the left (L) or in the right (R) face-adjacent cell is considered, in a purely upwind manner:

$$\boldsymbol{\psi}_{\mathrm{L/R}} = \begin{cases} \boldsymbol{\psi}_L & \text{if } M_{1/2} > 0, \\ \boldsymbol{\psi}_R & \text{otherwise.} \end{cases} \tag{5.18}$$

The pressure term [166]

$$\boldsymbol{\mathcal{P}}_{1/2} = \begin{bmatrix} 0 \\ p_{1/2} n_x \\ p_{1/2} n_y \\ p_{1/2} \boldsymbol{s} \cdot \boldsymbol{n} \end{bmatrix}, \tag{5.19}$$

on the other hand, is governed by the acoustic wave speed. It depends on both states in the subsonic case, becoming fully upwind only for a supersonic flow [14]. Note that the definition of $\boldsymbol{\mathcal{P}}_{1/2}$ in ALE reference frame differs from an Eulerian formulation in the fourth component, $p_{1/2} \boldsymbol{s} \cdot \boldsymbol{n}$. On a stationary grid, this term becomes zero and the Eulerian formulation is recovered. The vector $\boldsymbol{n} = [n_x, n_y]^T$ is a unit normal vector to the interface, pointing towards the right cell.

The interface speed of sound is given by

$$a_{1/2} = \min(\hat{a}_{\mathrm{L}}, \hat{a}_{\mathrm{R}}), \tag{5.20}$$

where

$$\hat{a}_{\mathrm{L}} = a^{*^2}/\max(a^*, u^n_{\mathrm{L}}), \qquad \hat{a}_{\mathrm{R}} = a^{*^2}/\max(a^*, -u^n_{\mathrm{R}}) \tag{5.21}$$

and a^* is the critical speed of sound, evaluated when the local Mach number is unity:

$$a^{*^2} = \frac{2(\gamma-1)}{\gamma+1} h_t. \tag{5.22}$$

The contravariant velocity $u^n_{\mathrm{L/R}}$ is obtained by projecting the flow velocity relative to the local grid velocity in the face-normal direction:

$$u^n_{\mathrm{L/R}} = (\boldsymbol{u}_{\mathrm{L/R}} - \boldsymbol{s}) \cdot \boldsymbol{n}. \tag{5.23}$$

In conjunction with the interface speed of sound, it serves to define the local Mach number in the face-adjacent cells:

$$M_{\mathrm{L/R}} = \frac{u^n_{\mathrm{L/R}}}{a_{1/2}}, \tag{5.24}$$

The interface Mach number is given by the following formula:

$$M_{1/2} = \mathscr{M}^{+}_{(4)}(M_{\mathrm{L}}) + \mathscr{M}^{-}_{(4)}(M_{\mathrm{R}}) - \frac{K_p}{f_a}\max(1-\sigma\bar{M}^2, 0)\frac{p_{\mathrm{R}} - p_{\mathrm{L}}}{\rho_{1/2} a^2_{1/2}}, \tag{5.25}$$

where the split Mach numbers $\mathscr{M}^{\pm}_{(4)}(M)$ are polynomial functions of M and the third term represents pressure diffusion, introduced to enhance calculations in low Mach number regions. The formula for the split Mach number reads

$$\mathscr{M}^{\pm}_{(4)}(M) = \begin{cases} \mathscr{M}^{\pm}_{(1)} & \text{if } |M| \geq 1, \\ \mathscr{M}^{\pm}_{(2)}(1 \mp 16\beta \mathscr{M}^{\mp}_{(2)}) & \text{otherwise,} \end{cases} \tag{5.26}$$

with

$$\mathscr{M}^{\pm}_{(1)}(M) = \tfrac{1}{2}(M + |M|) \quad \text{and} \quad \mathscr{M}^{\pm}_{(2)}(M) = \pm\tfrac{1}{4}(M \pm 1)^2. \tag{5.27}$$

The pressure diffusion term requires evaluating the mean local Mach number $\bar{M}$:

$$\bar{M}^2 = \frac{u^2_{\mathrm{L}} + u^2_{\mathrm{R}}}{2a^2_{1/2}}, \tag{5.28}$$

and the scaling function f_a together with the reference Mach number M_o:

$$f_a(M_o) = M_o(2 - M_o), \qquad M_o^2 = \min\left(1, \max(\bar{M}^2, M^2_\infty)\right), \tag{5.29}$$

where M_∞ denotes the freestream Mach number. The interface density is defined simply as

$$\rho_{1/2} = (\rho_\mathrm{L} + \rho_\mathrm{R})/2. \tag{5.30}$$

The interface pressure $p_{1/2}$ is defined in a similar manner as the interface Mach number:

$$p_{1/2} = \mathscr{P}^+_{(5)}(M_\mathrm{L})p_\mathrm{L} + \mathscr{P}^-_{(5)}(M_\mathrm{R})p_\mathrm{R} - K_u \mathscr{P}^+_{(5)}\mathscr{P}^-_{(5)}(\rho_\mathrm{L} + \rho_\mathrm{R})(f_a a_{1/2})(u_\mathrm{R} - u_\mathrm{L}). \tag{5.31}$$

The fifth-degree polynomials $\mathscr{P}^\pm_{(5)}$ are again expressed in terms of split Mach number functions:

$$\mathscr{P}^\pm_{(5)}(M) = \begin{cases} \frac{1}{M}\mathscr{M}^\pm_{(1)} & \text{if } |M| \geq 1, \\ \mathscr{M}^\pm_{(2)}\left[(\pm 2 - M) \mp 16\alpha M \mathscr{M}^\mp_{(2)}\right] & \end{cases} \tag{5.32}$$

and the third term in 5.31 represents velocity diffusion.

There are five constants whose values need to be prescribed. The constants α, β that appear already in the previous AUSM$^+$ scheme are now set to

$$\alpha = \frac{3}{16}(-4 + 5f_a^2), \qquad \beta = \frac{1}{8}. \tag{5.33}$$

The remaining three constants are bounded by the following inequalities:

$$0 \leq K_p \leq 1, \qquad 0 \leq K_u \leq 1, \qquad \sigma \leq 1. \tag{5.34}$$

We retain the setting recommended by Liou [120] and employ the values $K_p = 0.25$, $K_u = 0.75$ and $\sigma = 1.0$.

5.2.3 Gradient Reconstruction

The cell-centered finite volume representation requires that variables stored at cell centroids are extrapolated to cell faces in order to obtain the *left* and *right* states for flux computation. In the most basic form, the variables are considered as constant within each cell and the cell-centered value is employed directly to evaluate the fluxes. However, this zeroth-order extrapolation results into an overly dissipative scheme with only a first order spatial accuracy. A common strategy is to use a first-order accurate linear reconstruction, followed by the application of a limiter to avoid spurious oscillations at discontinuities. This section presents the numerical method employed for gradient reconstruction, while limiters are discussed in Sec. 5.2.4.

Gradients are most commonly approximated using either a Green-Gauss (GG) method, or a least squares minimization (LSQ) [168]. The GG techniques further differ by

the scheme used to interpolate cell-face values, while the least squares employ various stencils and may be either weighted or unweighted. In order to evaluate the fluxes with a second order of accuracy, the gradient approximation needs to be at least first-order accurate [13]. Mavriplis [126] found that unweighted least squares underpredict severely normal gradients on some meshes, which could be remedied by the use of inverse distance weighting or by resorting to a Green-Gauss method. Sozer et al. [168] compared three GG-based approaches with a LSQ minimization and a curvilinear gradient method and demonstrated that the commonly used GG technique with either a simple or an inverse-distance weighted averaging is inconsistent and zeroth order accurate on irregular meshes. They further found gradient operators with compact stencils to exhibit generally lower errors. The unsatisfactory performance of the GG method with simple averaging was confirmed by Mishriky and Walsh [130], who derived analytically that it has a zeroth order of accuracy on meshes with an arbitrary spacing. They also showed that the GG method with a more suitable face-value interpolation achieves a first order of accuracy, similarly to the unweighted LSQ method. Syrakos at al. [175] also concluded that a first order of accuracy can be achieved with a GG method via a suitable choice of face-value interpolation. They found the inverse distance weighted LSQ approach to be at least first order accurate and, with a particular choice of the weighting exponent (-3/2), up to second order accurate on some types of meshes. This setting achieved superior accuracy also in an analysis performed by the author, although of a lesser than second order [2].

The weighted LSQ gradient approximation is implemented in the present solver. Linear approximation of a variable ϕ over a cell Ω_i is given by

$$\phi(\boldsymbol{x})|_i = \overline{\phi}_i + (\nabla\phi)_i \cdot (\boldsymbol{x} - \boldsymbol{x}_i), \tag{5.35}$$

where $(\nabla\phi)_i = [\partial\phi/\partial x,\, \partial\phi/\partial y]_i^T$ denotes the gradient and $\overline{\phi}_i$ the cell-average value stored at the cell centroid with coordinates $\boldsymbol{x}_i = [x_i, y_i]^T$. Substituting for $\boldsymbol{x}$ and $\phi(\boldsymbol{x})$ the centroid coordinates and ϕ averages of neighbouring cells, we obtain the following over-determined system of linear equations

$$\begin{bmatrix} \Delta x_{i1} & \Delta y_{i1} \\ \Delta x_{i2} & \Delta y_{i2} \\ \vdots & \vdots \\ \Delta x_{im} & \Delta y_{im} \end{bmatrix} (\nabla\phi)_i = \begin{bmatrix} \Delta\overline{\phi}_{i1} \\ \Delta\overline{\phi}_{i2} \\ \vdots \\ \Delta\overline{\phi}_{im} \end{bmatrix}, \tag{5.36}$$

where $\Delta(\cdot)_{ij} = (\cdot)_j - (\cdot)_i$ and m is the number of adjacent cells. The stencil may be either face-based or vertex-based, as illustrated in Fig 5.6. In order to increase accuracy of the reconstruction, each equation is multiplied by a weighting factor w_{ij} which takes into account the distance of the neighbouring cell centroid to the centroid of Ω_i:

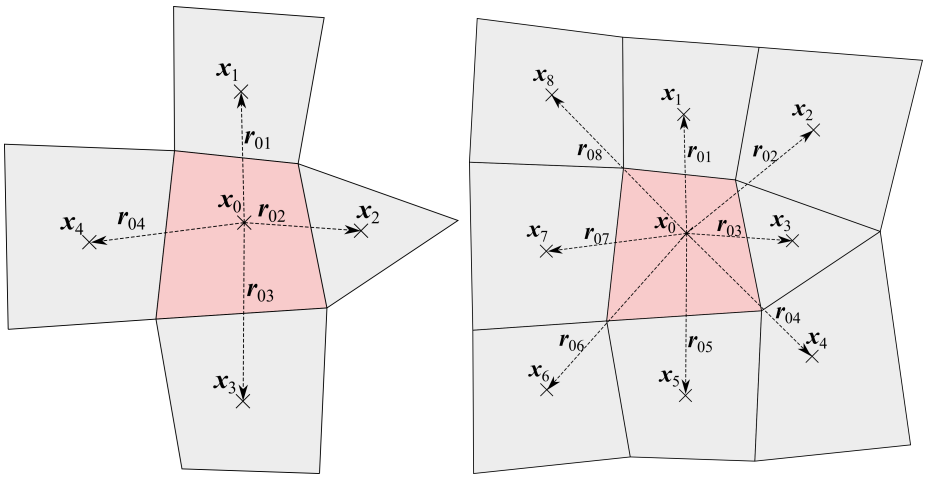

Figure 5.6: Face-based (left) and vertex-based (right) stencils for gradient reconstruction with weighted LSQ.

$$\begin{bmatrix} w_{i1}\Delta x_{i1} & w_{i1}\Delta y_{i1} \\ w_{i2}\Delta x_{i2} & w_{i2}\Delta y_{i2} \\ \vdots & \vdots \\ w_{im}\Delta x_{im} & w_{im}\Delta y_{im} \end{bmatrix} (\nabla\phi)_i = \begin{bmatrix} w_{i1}\Delta\overline{\phi}_{i1} \\ w_{i2}\Delta\overline{\phi}_{i2} \\ \vdots \\ w_{im}\Delta\overline{\phi}_{im} \end{bmatrix}, \tag{5.37}$$

with

$$w_{ij} = \left[\sqrt{(\Delta x_{ij})^2 + (\Delta y_{ij})^2}\right]^{-k}. \tag{5.38}$$

When the inverse-distance exponent k is set to zero, one obtains the unweighted system of equations 5.36. Common choices for the exponent are $k \in \{0, 1, \frac{3}{2}, 2\}$.

The system of linear equations 5.37 may be written as $A(\nabla\phi)_i = \boldsymbol{b}$ and solved in the least squares sense, i.e. to minimize the L_2 norm of the error $\boldsymbol{b} - A(\nabla\phi)_i$. A common approach is to multiply the system of equations by A^T, which yields a system of *normal equations* that has a unique solution, providing that A has independent columns [175]. However, this approach is not suitable, as the system of normal equations may be ill-conditioned on highly stretched grids [78]. Therefore, a QR-decomposition using the Gram-Schmidt method is employed instead. The matrix A is decomposed into a product of an orthogonal matrix $Q \in \mathbb{R}^{m\times 2}$ and an upper triangular matrix $R \in \mathbb{R}^{2\times 2}$:

$$A = QR \tag{5.39}$$

For a derivation of the decomposition see e.g. [78], we shall only give the final formula for the gradient calculation:

$$(\nabla\phi)_i = R^{-1}Q^T b = \sum_{j=1}^{m} \begin{bmatrix} \frac{w_{ij}^2}{r_{11}^2}\Delta x_{ij} - \frac{r_{12}}{r_{11}r_{22}} w_{ij}^2 \left(\Delta y_{ij} - \frac{r_{12}}{r_{11}}\Delta x_{ij} \right) \\ \frac{w_{ij}^2}{r_{22}^2}\Delta y_{ij} - \frac{r_{12}}{r_{11}r_{22}} w_{ij}^2 \Delta x_{ij} \end{bmatrix} \Delta\phi_{ij}, \quad (5.40)$$

where the components of the matrix R are:

$$\begin{aligned} r_{11} &= \sqrt{\sum_{j=1}^{m} w_{ij}^2 (\Delta x_{ij})^2} \\ r_{12} &= \frac{1}{r_{11}} \sum_{j=1}^{m} w_{ij}^2 \Delta x_{ij} \Delta y_{ij}. \\ r_{22} &= \sqrt{\sum_{j=1}^{m} w_{ij}^2 (\Delta y_{ij})^2 - r_{12}^2} \end{aligned} \quad (5.41)$$

An extension of the approach to three dimensions can be found in [14].

5.2.4 Limiter Functions

Higher-order accurate gradient reconstructions may introduce new extrema into the solution, leading to a formation of spurious oscillations near discontinuities such as shockwaves. A gradient limiting strategy needs to be introduced to ensure that the numerical scheme is *monotonicity preserving*, i.e. to guarantee that the local maxima in the flow-field are non-increasing, the local minima non-decreasing and no new extrema are created [14]. According to Godunov's theorem [115], any linear, monotonicity preserving method is at most first order accurate, hence nonlinear limiter functions need to be employed. The fundamental principle of the limiter is to reduce reconstructed slopes in order to constrain solution variations. At strong discontinuities, the gradient is reduced to zero and the numerical scheme becomes locally first order accurate. In smooth flow regions, on the other hand, the limiter remains inactive and the original order of accuracy of the gradient reconstruction is recovered.

Limiting strategies for conservation laws in one dimension are often based on some form of total variation diminishing (TVD) [115]. However, the TVD principle has been found overly restrictive for solutions on multidimensional Cartesian grids and not necessary to prove positivity or convergence to the correct entropy solution [10]. A theorem of Goodman and Leveque [115] states that TVD methods in two space dimensions are at most first order accurate. Moreover, the definition of the total variation on unstructured grids is problematic. The TVD condition for multi-dimensional schemes is often relaxed to a discrete form of the *maximum principle* (MP), requiring that the reconstructed values are bounded by extrema within the

local stencil of neighbouring cells. The simplest method to impose the maximum principle is to multiply the reconstructed gradient by a suitable scalar limiter ζ:

$$\phi(\boldsymbol{x})|_0 = \overline{\phi}_0 + \zeta(\nabla\phi)_0 \cdot (\boldsymbol{x} - \boldsymbol{x}_0). \tag{5.42}$$

This approach was successfully implemented by Barth and Jespersen [8] in creation of a truly multidimensional limiter for unstructured grids. However, their method suffered from problems with convergence because the limiter reacted to a low-amplitude numerical noise in smooth flow regions. Moreover, the strategy of multiplying the gradient by a scalar was found excessively dissipative, as the limiting triggered by one face degrades the gradient in all directions [13]. Numerous approaches have since been introduced with the aim to take into account the full multidimensionality of the problem. For example, Hubbard [100] applied a projection of the gradient to the maximum principle region, Berger and Aftosmis [13] solved directional limiting as a linear programming problem and Delis and Nikolos [36] introduced an edge-based limiter. The remainder of this section gives a brief overview of the limiters implemented in the present solver.

Barth & Jespersen limiter

The limiter of Barth and Jespersen [8] was constructed by an extension of Spekreijse's multidimensional limiter [169] to unstructured grids. The strategy invokes the maximum principle on a faced-based stencil of neighbouring cells to construct a monotonicity preserving scheme. The left part of Fig. 5.7 shows an example of the Barth and Jepsersen stencil, formed by the grey-coloured neighbouring cells together with the concerned cell Ω_0 that is highlighted in red. Let us denote $\overline{\phi}_0^{min}$, $\overline{\phi}_0^{max}$ respectively the minimum and the maximum of the cell-average values $\overline{\phi}_j$ within the stencil. The condition for reconstruction on cell Ω_0 then reads:

$$\overline{\phi}_0^{\min} \leq \phi(\boldsymbol{x})|_0 \leq \overline{\phi}_0^{\max} \tag{5.43}$$

This condition needs to be verified at cell vertices, since that is where extrema occur in the case of a linear reconstruction. By defining

$$\Delta_{\max}^{\mathrm{BJ}} = \overline{\phi}_0^{\max} - \overline{\phi}_0, \qquad \Delta_{\min}^{\mathrm{BJ}} = \overline{\phi}_0^{\min} - \overline{\phi}_0, \qquad \Delta_i = (\nabla\phi)_0 \cdot \boldsymbol{r}_{0i}, \tag{5.44}$$

where $\boldsymbol{r}_{0i}$ denotes a vector from the cell Ω_0 centroid to the vertex V_i, we obtain the following condition for the limiter:

$$\frac{\overline{\phi}_0^{\min} - \overline{\phi}_0}{(\nabla\phi)_0 \cdot \boldsymbol{r}_{0i}} \leq \zeta_0 \leq \frac{\overline{\phi}_0^{\max} - \overline{\phi}_0}{(\nabla\phi)_0 \cdot \boldsymbol{r}_{0i}} \qquad \text{or} \qquad \frac{\Delta_{\min}^{\mathrm{BJ}}}{\Delta_i} \leq \zeta_0 \leq \frac{\Delta_{\max}^{\mathrm{BJ}}}{\Delta_i}. \tag{5.45}$$

The above condition needs to be fulfilled at each vertex, hence the Barth and Jespersen limiter is formulated as follows:

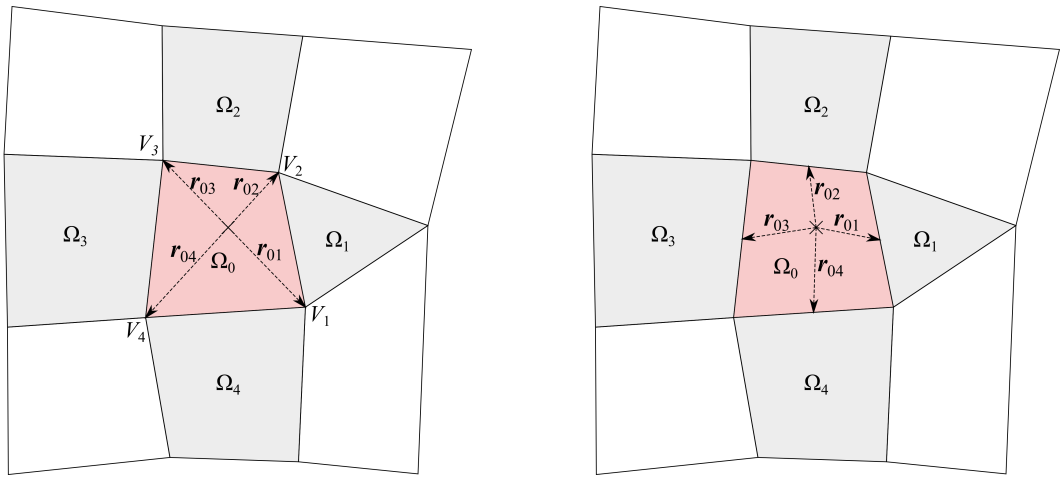

Figure 5.7: Stencil of the Barth & Jespersen limiter with vertex-based (left) and face-based (right) MP conditions

$$\zeta_0^{\mathrm{BJ}} = \min_{\forall V_i \in \Omega_0} \begin{cases} \tilde{\zeta}\left(\frac{\Delta_{\max}^{\mathrm{BJ}}}{\Delta_i}\right)^{\mathrm{BJ}} & \text{if } \Delta_i > 0 \\ \tilde{\zeta}\left(\frac{\Delta_{\min}^{\mathrm{BJ}}}{\Delta_i}\right)^{\mathrm{BJ}} & \text{if } \Delta_i < 0 \\ 1 & \text{if } \Delta_i = 0 \end{cases} \tag{5.46}$$

with

$$\tilde{\zeta}\left(\frac{\Delta_+}{\Delta_-}\right)^{\mathrm{BJ}} = \min\left(1, \frac{\Delta_+}{\Delta_-}\right) \tag{5.47}$$

Once the value of the limiter is determined, it is substituted into Eq. 5.42 to obtain the limited reconstruction within the concerned cell. A less stringent version of the limiter can be constructed by requiring that the condition 5.45 is satisfied at face midpoints instead of vertices (Fig. 5.7-right). Since fluxes are evaluated at face midpoints rather than at vertices, the maximum principle is not violated. This modified version is implemented in the present solver.

Venkatakrishnan limiter

The Barth and Jespersen limiter suffers from poor convergence, because it reacts to machine-level noise in smooth flow regions [78]. Aiming to address this deficiency, Venkatakrishnan [185] modified the formulation by employing a smooth limiter function analogous to the van Albada limiter. The limiter function $\tilde{\zeta}^{\mathrm{BJ}}$ in Eq. 5.46 is replaced with

$$\tilde{\zeta}\left(\frac{\Delta_+}{\Delta_-}\right)^{\mathrm{Venk}} = \frac{1}{\Delta_-}\left[\frac{(\Delta_+^2 + \epsilon^2)\Delta_- + 2\Delta_-^2\Delta_+}{\Delta_+^2 + 2\Delta_-^2 + \Delta_+\Delta_- + \epsilon^2}\right] \tag{5.48}$$

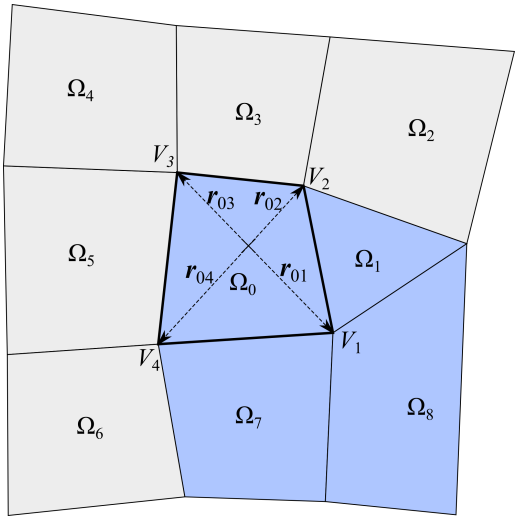

Figure 5.8: Stencil of the MLP. Cells in the local stencil for vertex V_1 highlighted in blue, other cells within the Ω_0 stencil shown in grey.

where $\epsilon^2 = (K\Delta x)^3$, K is a constant and Δx is a measure of the local grid spacing, calculated in two dimensions as a square root of the cell volume. The rest of the procedure remains unaltered. As suggested by Venkatakrishnan in order to avoid division by zero, Δ_i is replaced by $\text{sign}(\Delta_i)(|\Delta_i| + \mu)$ in the implementation, with μ corresponding to the machine accuracy. There is no general recommendation on the value of the constant K. It needs to be tuned for each computational case to achieve the desired balance between the diffusivity of the limiter and its convergence behaviour.

Multidimensional Limiting Process (MLP)

Park et al. [142, 141] devised a limiting strategy for unstructured grids within the MUSCL (Monotone Upstream-centered Schemes for Conservation Laws) framework. The maximum principle is invoked to obtain a monotonic solution, similarly to the limiters of Barth and Jespersen or Venkatakrishnan. The MLP technique is distinguished by considering more profoundly the multi-dimensionality of the flow when constructing the MP region.

Let us consider a cell Ω_0 and denote the reconstructed values at its vertices ϕ_{0i}. The MLP is expressed with the following condition:

$$\overline{\phi}_{0i}^{\min} \leq \phi_{0i} \leq \overline{\phi}_{0i}^{\max}, \tag{5.49}$$

where $(\overline{\phi}_{0i}^{\min}, \overline{\phi}_{0i}^{\max})$ are the minimum and maximum cell-average values within the neighbouring cells sharing the vertex V_i. An example of the local stencil is shown in in Fig. 5.8, where the cells sharing the vertex V_1 are highlighted in blue. This approach yields different bounds for reconstruction at each vertex, in contrast to the Barth and Jespersen limiter where a single set of bounds is considered for the entire cell.

Applying the MLP condition 5.49 to the limited linear reconstruction, Eq. 5.42, we obtain a permissible range for the scalar limiter ζ_0:

$$\frac{\overline{\phi}_{0i}^{\min} - \overline{\phi}_0}{(\nabla\phi)_0 \cdot \boldsymbol{r}_{0i}} \leq \zeta_0 \leq \frac{\overline{\phi}_{0i}^{\max} - \overline{\phi}_0}{(\nabla\phi)_0 \cdot \boldsymbol{r}_{0i}} \qquad \text{or} \qquad \frac{\Delta_{\min}^{\mathrm{MLP}}}{\Delta_i} \leq \zeta_0 \leq \frac{\Delta_{\max}^{\mathrm{MLP}}}{\Delta_i}. \tag{5.50}$$

The definition of the MLP limiter formally resembles the Barth and Jespersen and Venkataktrishnan limiters, with the difference that $(\Delta_{\max}^{\mathrm{MLP}}, \Delta_{\min}^{\mathrm{MLP}})$ is taken instead of $(\Delta_{\max}^{\mathrm{BJ}}, \Delta_{\min}^{\mathrm{BJ}})$:

$$\zeta_0^{\mathrm{MLP}} = \min_{\forall V_i \in \Omega_0} \begin{cases} \tilde{\zeta}\left(\frac{\Delta_{\max}^{\mathrm{MLP}}}{\Delta_i}\right) & \text{if } \Delta_i > 0 \\ \tilde{\zeta}\left(\frac{\Delta_{\min}^{\mathrm{MLP}}}{\Delta_i}\right) & \text{if } \Delta_i < 0 \\ 1 & \text{if } \Delta_i = 0 \end{cases} \tag{5.51}$$

Park, Yoon and Kim [142] proposed two variants of the limiting strategy, distinguished by the formulation of $\tilde{\zeta}$. The first one, denoted MLP-u1, represents the steepest slope in the allowable limiting region:

$$\tilde{\zeta}\left(\frac{\Delta_+}{\Delta_-}\right)^{\mathrm{MLP-u1}} = \tilde{\zeta}\left(\frac{\Delta_+}{\Delta_-}\right)^{\mathrm{BJ}} = \min\left(1, \frac{\Delta_+}{\Delta_-}\right). \tag{5.52}$$

However, due to its non-differentiability, it may suffer from convergence problems similarly to the original Barth and Jespersen approach. Hence the modification devised by Venkataktrishnan for the Barth and Jespersen limiter is employed within the MLP framework, creating the differentiable MLP-u2 version:

$$\tilde{\zeta}\left(\frac{\Delta_+}{\Delta_-}\right)^{\mathrm{MLP-u2}} = \tilde{\zeta}\left(\frac{\Delta_+}{\Delta_-}\right)^{\mathrm{Venk}} = \frac{1}{\Delta_-}\left[\frac{(\Delta_+^2 + \epsilon^2)\Delta_- + 2\Delta_-^2\Delta_+}{\Delta_+^2 + 2\Delta_-^2 + \Delta_+\Delta_- + \epsilon^2}\right] \tag{5.53}$$

It is again required to set the constant K empirically in order to calculate $\epsilon^2 = (K\Delta x)^3$.

Face-based limiter of Delis et al.

The limiters of Barth and Jespersen [8], Venkatakrishnan [185] and Park et al. [142] act by multiplying the reconstructed gradient with a scalar. Limiting required in one direction affects all components of the gradient and the resulting scheme that may be unnecessarily dissipative. Therefore, Delis et al. [35, 34, 36] developed a procedure which performs the limiting individually for each face of the cell. Their strategy effectively applies the concept of one-dimensional MUSCL-type limiters to multidimensional flows on unstructured grids.

Let us consider the limiter application within a cell Ω_0, for a face shared with a neighbouring cell Ω_q (Fig. 5.9). The procedure comprises two steps. First, the

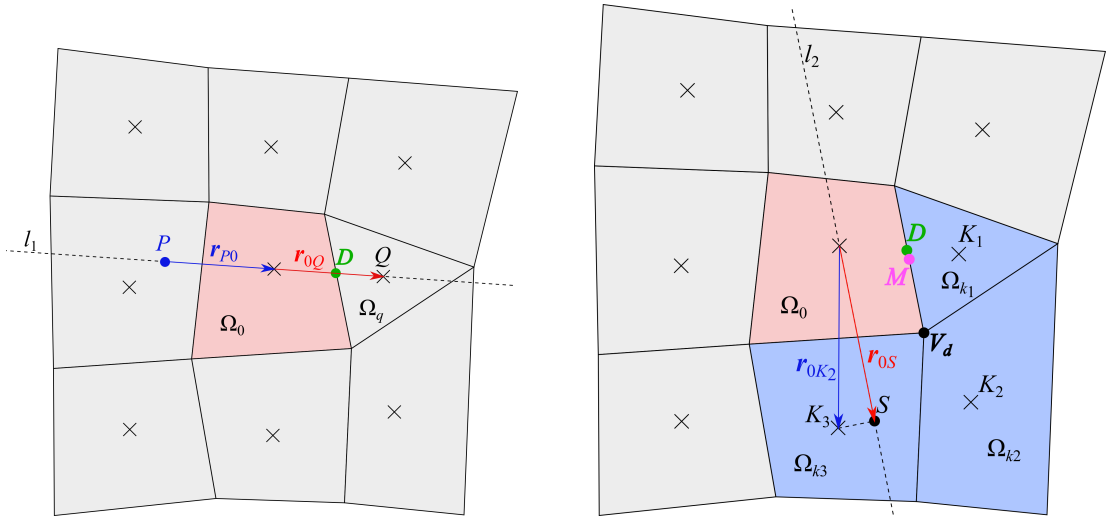

Figure 5.9: The first (left) and the second (right) step of the limiting procedure by Delis et al.

limiting is performed along a line connecting the centroids of Ω_0 and Ω_q with the goal to obtain the value at a point D, i.e. at the intersection between this line and the concerned face. If this point coincided with the face midpoint M, this value could be used directly for the flux computation. However, as this is not true on a general unstructured grid, a second reconstruction and limiting step needs to be executed from D to M in order to achieve a second order accuracy.

1. **Reconstruction at the intersection point D.** The first step of the procedure is performed along a line l_1, connecting the centroids of Ω_0 and Ω_q. In order to apply a one-dimensional limiter function, two consecutive gradient projections to the line l_1 need to be evaluated. Based on the knowledge of the cell-average values in the face-adjacent cells, we can easily define a projection of the gradient $(\nabla\phi)_0^{\text{cnt},1}$ that is central to the point D:

$$(\nabla\phi)_0^{\text{cnt},1} \cdot \boldsymbol{r}_{0Q} = \overline{\phi}_Q - \overline{\phi}_0 \tag{5.54}$$

Next, we construct a virtual node P on the line l_1, such that the centroid of Ω_0 is the midpoint of $\overline{PQ}$. This virtual node then serves to define a projection of the upwind gradient $(\nabla\phi)_0^{\text{upw},1}$:

$$\begin{aligned}(\nabla\phi)_0^{\text{upw},1} \cdot \boldsymbol{r}_{P0} = \overline{\phi}_0 - \phi_P = (\overline{\phi}_0 - \overline{\phi}_Q) + (\overline{\phi}_Q - \phi_P) = \\ = \overline{\phi}_0 - \overline{\phi}_Q + 2(\nabla\phi)_0 \cdot \boldsymbol{r}_{0Q},\end{aligned} \tag{5.55}$$

where $(\nabla\phi)_0$ is the gradient on Ω_0 reconstructed with the weighted least squares method. Once the two gradient projections are determined, the limited value at D can be calculated:

$$\phi_D = \overline{\phi}_0 + \frac{||\boldsymbol{r}_{0D}||}{||\boldsymbol{r}_{0Q}||} L\left((\nabla\phi)_0^{\text{upw},1} \cdot \boldsymbol{r}_{0Q}, (\nabla\phi)_0^{\text{cnt},1} \cdot \boldsymbol{r}_{0Q}\right) \tag{5.56}$$

Here L is a one-dimensional limiter function which will be defined later.

2. **Reconstruction at the face midpoint** M**.** The second step is realized along a line l_2, parallel to DM and intersecting the centroid of Ω_0. In the first step of the limiting procedure, the *downwind* value was known, as it was simply represented by the cell-average of the cell Ω_q, i.e. by $\overline{\phi}_q$. Definition of the downwind value is more complicated in the second step, as it needs to be interpolated between the neighbouring cells. First, out of the two vertices belonging to the face between Ω_0 and Ω_q, we identify a *downwind vertex* V_d as the one that is more distant from D. Let us denote Ω_{k_j} all cells sharing the vertex V_d, other than Ω_0. Note that among them is also the cell previously denoted as Ω_q, which will now be referred to as Ω_{k_1} to simplify the notation (see Fig. 5.9). From the set of Ω_{k_j}, we choose the cell for which the angle between the line l_2 and the centroid-connecting vector $\boldsymbol{r}_{0k_j}$ is the smallest. In the depicted case, this criterion selects the cell Ω_{k_3}. A projection of its centroid, K_3, onto the line l_2 crates a virtual node S. The point S is the sought *downwind node*. We approximate the value of ϕ at S with:

$$\phi_S = \overline{\phi}_{k_3} + \boldsymbol{r}_{K_3S} \cdot (\nabla\phi)_{k_3}. \tag{5.57}$$

The remaining steps follow the procedure employed previously for the reconstruction at the point D, with the definition of the central gradient projection as

$$(\nabla\phi)_0^{\mathrm{cnt},2} \cdot \boldsymbol{r}_{0S} = \overline{\phi}_S - \overline{\phi}_0, \tag{5.58}$$

and of the upwind gradient projection as

$$(\nabla\phi)_0^{\mathrm{upw},2} \cdot \boldsymbol{r}_{0S} = \overline{\phi}_S - \overline{\phi}_0 + 2(\nabla\phi)_0 \cdot \boldsymbol{r}_{0S}, \tag{5.59}$$

to finally determine the limited value at the face-center M:

$$\phi_M = \overline{\phi}_D + \frac{||\boldsymbol{r}_{DM}||}{||\boldsymbol{r}_{0k_2}||} L\left((\nabla\phi)_0^{\mathrm{upw},2} \cdot \boldsymbol{r}_{0S}, (\nabla\phi)_0^{\mathrm{cnt},2} \cdot \boldsymbol{r}_{0S}\right) \tag{5.60}$$

The limiter function L may be chosen arbitrarily from the existing and extensively researched family of 1D limiters. Two limiter functions are implemented in the present solver. The MinMod limiter is defined as:

$$L_{\mathrm{MinMod}}(\Delta_1, \Delta_2) = \begin{cases} \Delta_2 \max\left(0, \min\left(\frac{\Delta_1}{\Delta_2}, 1\right)\right) & \text{if } \Delta_2 \neq 0 \\ 0 & \text{if } \Delta_2 = 0, \end{cases} \tag{5.61}$$

and the van Albada - van Leer limiter reads [34]

$$L_{\mathrm{VAVL}}(\Delta_1, \Delta_2) = \begin{cases} \dfrac{(\Delta_1^2 + \epsilon)\Delta_2 + (\Delta_2^2 + \epsilon)\Delta_1}{\Delta_1^2 + \Delta_2^2 + 2\epsilon} & \text{if } \Delta_1\Delta_2 > 0 \\ 0 & \text{if } \Delta_1\Delta_2 \leq 0. \end{cases} \tag{5.62}$$

Here ϵ, $0 < \epsilon \ll 1$, is a constant preventing indeterminacy of the limiter function in smooth flow regions where the gradients Δ_1, Δ_2 approach zero. In the present implementation, $\epsilon = 10^{-16}$.

5.2.5 Temporal Integration

The method of lines, applied to the governing flow equations, yields a system of coupled ordinary differential equations in the form

$$\frac{d}{dt}\left(\boldsymbol{W}_i|\Omega_i|\right) = -\boldsymbol{R}_i, \qquad i = 1 \ldots N_{cells}. \tag{5.63}$$

The system of equations is integrated in time, either to reach a steady-state solution characterised by the residuals $\boldsymbol{R}_i$ approaching zero, or to capture the temporal evolution of an unsteady flow. Time-marching flutter computations are performed on moving grids, which imposes additional constraints on the integration method to guarantee conservativity. This condition, known as the *Geometric Conservation Law* (GCL), is discussed at the beginning of this section. Next, the implemented explicit and implicit time-integration schemes are presented. The section is concluded by a description of acceleration techniques that serve to reduce the computational time.

Geometric Conservation Law

Computations on moving grids require that some geometric quantities are evaluated in each iteration, such as the positions and velocities of grid vertices and the normals to cell faces. The method for calculating these quantities may not be chosen arbitrarily, as it needs to be defined with respect to the temporal integration scheme. The essential condition to consider is the Geometric Conservation Law (GCL), first formulated by Thomas and Lombard [180]. It requires the geometric parameters of the numerical scheme to be calculated such that a uniform flow state is always exactly preserved, independently of grid deformation.

The implications of the GCL for the stability and accuracy of the ALE method have been widely discussed. Koobus and Farhat [109] performed aeroelastic simulations with several numerical schemes and reported a severe degradation of accuracy in cases where the GCL was violated. On the other hand, some evidence has been shown that if the time-step is sufficiently small, the use of a GCL non-compliant scheme may not affect the solution strongly [15]. Moreover, as demonstrated by Geuzaine et al. [56], GCL is not a necessary condition for achieving the design accuracy of a numerical scheme on moving grids. Nevertheless, respecting the GCL guarantees several desirable properties for the numerical method. It is a necessary and sufficient condition for the numerical scheme to preserve non-linear stability [45], and it further ensures accuracy of at least a first order [65]. Nevertheless, the GCL should not be considered strictly in relation to the order of accuracy. Instead, the concept is similar to the conservativity of numerical schemes for spatial discretisation [127].

It is convenient for the finite volume method to consider the geometric conservation law in integral form. Its derivation can be found e.g. in [46] or [37]. Let us denote Δt the chosen time step and $t^n = n\Delta t$ the time level at the n-th iteration with the solution $\boldsymbol{W}^n = \boldsymbol{W}(t^n)$. Integrating Eq. 4.15 between t^n and t^{n+1} yields

$$\int_{t^n}^{t^{n+1}} \frac{\partial}{\partial t} \int_{\Omega(t)} \boldsymbol{W} d\Omega dt + \int_{t^n}^{t^{n+1}} \oint_{\partial\Omega(t)} \boldsymbol{F}^{ALE} dS dt = 0, \tag{5.64}$$

$$\int_{\Omega(t^{n+1})} \boldsymbol{W}^{n+1} d\Omega - \int_{\Omega(t^n)} \boldsymbol{W}^n d\Omega + \int_{t^n}^{t^{n+1}} \oint_{\partial\Omega(t)} \boldsymbol{F}^{ALE} dS dt = 0, \tag{5.65}$$

Let us denote $\boldsymbol{W}^*$ a given uniform state of flow. The GCL states that such solution needs to be exactly preserved, hence we substitute $\boldsymbol{W}^n = \boldsymbol{W}^{n+1} = \boldsymbol{W}^*$ in Eq. 5.65 and obtain:

$$\boldsymbol{W}^* \left[\int_{\Omega(t^{n+1})} d\Omega - \int_{\Omega(t^n)} d\Omega \right] = - \int_{t^n}^{t^{n+1}} \oint_{\partial\Omega(t)} \boldsymbol{F}^{ALE} dS dt \tag{5.66}$$

Let us recall that the flux $\boldsymbol{F}^{ALE}$ consists of two contributions, where the first one is equal to the convective flux in Eulerian representation and the other accounts for the flux induced by the control volume boundary motion (Eq. 4.16). The former term disappears due to flow uniformity, therefore the flux integral reads:

$$\oint_{\partial\Omega(t)} \boldsymbol{F}^{ALE} dS = - \oint_{\partial\Omega(t)} \boldsymbol{W}^* (\boldsymbol{s} \cdot \boldsymbol{n}) dS \tag{5.67}$$

It should be noted that although we are considering inviscid flow equations, the derivation of the GCL is equivalent for viscous flows, as the viscous flux terms disappear due to flow uniformity. Substituting Eq. 5.67 into Eq. 5.66, we finally obtain the integral form of the geometric conservation law:

$$\Omega^{n+1} - \Omega^n = \int_{t^n}^{t^{n+1}} \oint_{\partial\Omega(t)} (\boldsymbol{s} \cdot \boldsymbol{n}) dS dt \tag{5.68}$$

The geometrical meaning of the law is that the change in volume of each cell between t^n and t^{n+1} must be equal to the volume swept by the cell boundary during Δt [46]. This requirement has the following implications for numerical integration in time [109]:

- Equation 5.68 must hold when the temporal integration on the right side is performed with the same technique as applied to the governing equations (Eq. 5.63)
- The calculation of grid vertex positions and velocities is not as arbitrary as the acronym ALE suggests. It needs to be performed in a fashion that together with the temporal integration method ensures compliance with the GCL.

Explicit Euler Scheme

The temporal derivative in Eq. 5.63 is approximated by the explicit Euler scheme as:

$$\frac{d}{dt}\left(\boldsymbol{W}_i|\Omega_i|\right) \approx \frac{\boldsymbol{W}_i^{n+1}|\Omega_i|^{n+1} - \boldsymbol{W}_i^{n}|\Omega_i|^{n}}{\Delta t}, \tag{5.69}$$

where Δt is a timestep and the superscripts n, $n+1$ denote quantities evaluated at the time-levels $t^n = n\Delta t$, $t^{n+1} = (n+1)\Delta t$ respectively. In order to comply with the GCL, the residual vector needs to be evaluated at a midpoint configuration whose grid coordinates and velocities are calculated as follows [113]:

$$\boldsymbol{x}^{n+1/2} = \frac{\boldsymbol{x}^n + \boldsymbol{x}^{n+1}}{2}, \qquad \boldsymbol{s}^{n+1/2} = \frac{\boldsymbol{x}^{n+1} - \boldsymbol{x}^n}{\Delta t}. \tag{5.70}$$

Substituting Eq. 5.69 in Eq. 5.63 yields a formula for calculating a new iteration:

$$\boldsymbol{W}_i^{n+1} = \frac{1}{|\Omega_i|^{n+1}}\left[\boldsymbol{W}_i^{n}|\Omega_i|^{n} - \Delta t \boldsymbol{R}_i(\boldsymbol{x}^{n+1/2}, \boldsymbol{s}^{n+1/2}, \boldsymbol{W}^n)\right]. \tag{5.71}$$

While the explicit Euler scheme is easily implemented, its practical applicability is limited as it achieves only a first-order accuracy. Another limitation, typically proving itself as even more severe, arises from the conditional stability which puts a constraint on the maximum time-step. The Courant-Friedrichs-Lewy (CFL) condition for a system of linearised Euler equations in 1D reads [14]

$$\Delta t \leq \mathrm{CFL}\frac{\Delta x}{|u| + a}. \tag{5.72}$$

Here $|u| + a$ is the spectral radius of the convective flux Jacobian, i.e. the highest propagation speed. The term $\Delta x/(|u|+a)$ represents convection time over a cell with the dimension Δx for a wave travelling at the velocity $|u| + a$. The generalization of the CFL constraint to computations on unstructured grids in multiple dimensions is not unique. The condition used in the present work bounds the maximum local time-step in a cell Ω as follows:

$$\Delta t \leq \min_{M_j \in \Omega}\left(\mathrm{CFL}\frac{2||\boldsymbol{r}_{SM_j}||}{\left|(\boldsymbol{u} - \boldsymbol{s}) \cdot \frac{\boldsymbol{r}_{SM_j}}{||\boldsymbol{r}_{SM_j}||}\right| + a}\right), \tag{5.73}$$

where $\boldsymbol{r}_{SM_j}$ denotes a vector from the cell centroid S to a face midpoint M_j, $\boldsymbol{u}$ and $\boldsymbol{s}$ are the flow and grid velocities respectively and a is the local speed of sound.

Practical experience has shown that given the second-order spatial discretisation with gradient reconstruction and limiting implemented in the present solver, the upper stability bound for the CFL value on unstructured grids is approximately

0.35. Unsteady computations require the use of a global time-step, obtained by evaluating the condition 5.73 in each cell of the grid and taking the minimum value. Steady-state computations may be accelerated with the use of local time-stepping described in Sec. 5.2.5.

Runge-Kutta Scheme

An explicit low-storage $l-$stage Runge-Kutta method between the time-levels n and $n+1$ can be expressed as

$$\begin{aligned}
\boldsymbol{W}_i^{(0)} =& \boldsymbol{W}_i^n, \\
\boldsymbol{W}_i^{(k)} =& \frac{1}{|\Omega_i|^{(k)}} \left[\boldsymbol{W}_i^{(0)} |\Omega_i|^{(0)} - \alpha_k \Delta t \boldsymbol{R}_i(\boldsymbol{x}^{(k/2)}, \boldsymbol{s}^{(k/2)}, \boldsymbol{W}^{(k-1)}) \right], \\
& k = 1 \dots l, \\
\boldsymbol{W}_i^{n+1} =& \boldsymbol{W}_i^{(l)}.
\end{aligned} \tag{5.74}$$

Similarly to the explicit Euler scheme, the residuals are evaluated on a midpoint grid. However, instead of considering the iterations n and $n+1$, the definition of the midpoint grid is based on the time-levels t^n and $t^{(k)}$:

$$\boldsymbol{x}^{(k)} = \boldsymbol{x}^n + \alpha_k(\boldsymbol{x}^{n+1} - \boldsymbol{x}^n), \qquad \boldsymbol{x}^{(k/2)} = \frac{\boldsymbol{x}^n + \boldsymbol{x}^{(k)}}{2}, \qquad \boldsymbol{s}^{(k/2)} = \frac{\boldsymbol{x}^{(k)} - \boldsymbol{x}^n}{\alpha_k \Delta t} \tag{5.75}$$

In the present work, a four-stage Runge-Kutta scheme (RK4) with the coefficients set to $\alpha_1 = 1/4$, $\alpha_2 = 1/3$, $\alpha_3 = 1/2$ and $\alpha_4 = 1$ is adopted. The scheme is fourth-order time accurate for a system of linear equations [166]. Since the RK4 scheme is conditionally stable, there is a limitation on the maximum time-step similarly to the Euler method. The time-step is again determined by Eq. 5.73, but the CFL number may be increased to 1.0 as opposed to 0.35 used for the Euler scheme. However, as a single iteration of the RK4 scheme requires four evaluations of the residual vector, the overall computational costs are not reduced.

Implicit Integration with Dual Time-Stepping

An implicit discretisation of Euler equations in the semi-discrete form 5.63 may be expressed as [41]:

$$\begin{aligned}
&\frac{\beta_1(\boldsymbol{W}|\Omega|)^{n+1} + \beta_0(\boldsymbol{W}|\Omega|)^n + \beta_{-1}(\boldsymbol{W}|\Omega|)^{n-1}}{\Delta t} \\
&\qquad + \gamma_1 \boldsymbol{R}(\boldsymbol{x}^{n+1}, \boldsymbol{s}^{n+1}, \boldsymbol{W}^{n+1}) + \gamma_0 \boldsymbol{R}(\boldsymbol{x}^n, \boldsymbol{s}^n, \boldsymbol{W}^n) = 0.
\end{aligned} \tag{5.76}$$

Note that we omit the cell-denoting subscript i for $\boldsymbol{W}$ and $\boldsymbol{R}$ to simplify the notation. The coefficients β_{-1}, β_0, β_1, γ_0 and γ_1 are selected in function of the target accuracy and stability. A second order backward difference method is obtained by setting the coefficients to

$$\beta_{-1} = \frac{1}{2}, \quad \beta_0 = -2, \quad \beta_1 = \frac{3}{2}, \quad \gamma_0 = 0, \quad \gamma_1 = 1. \tag{5.77}$$

The method is A-stable and well suited also for large time-steps [40].

Equation 5.76 is solved with a dual time-stepping approach. For each advancement in the physical time t, a loop of inner iterations is performed to solve the steady-state problem

$$|\Omega|^{n+1}\frac{d\boldsymbol{W}^*}{d\tau} + \boldsymbol{R}^*(\boldsymbol{W^*}) = 0, \tag{5.78}$$

by marching in a pseudo-time τ. The residual $\boldsymbol{R}^*$ is defined as

$$\boldsymbol{R}^*(\boldsymbol{W^*}) = \frac{\beta_1|\Omega|^{n+1}}{\Delta t}\boldsymbol{W}^* + \gamma_1\boldsymbol{R}(\boldsymbol{x}^{n+1}, \boldsymbol{s}^{n+1}, \boldsymbol{W}^*) + \boldsymbol{Q}, \tag{5.79}$$

where the terms from iterations $n-1$, n are encompassed in the source term $\boldsymbol{Q}$ that is constant during the inner cycle:

$$\boldsymbol{Q} = \frac{\beta_0\boldsymbol{W}^n|\Omega|^n + \beta_{-1}\boldsymbol{W}^{n-1}|\Omega|^{n-1}}{\Delta t} + \gamma_0\boldsymbol{R}(\boldsymbol{x}^n, \boldsymbol{s}^n, \boldsymbol{W}^n) \tag{5.80}$$

The set of ordinary differential equations 5.78 is solved with the explicit Runge-Kutta method described above. As the residual $\boldsymbol{R}^*$ is diminished, the solution of the steady-state problem converges to $\boldsymbol{W}^{n+1}$:

$$\frac{d\boldsymbol{W}^*}{d\tau} \to 0 \quad \Longrightarrow \quad \boldsymbol{W}^* \to \boldsymbol{W}^{n+1}. \tag{5.81}$$

In order to achieve the desired temporal accuracy of the scheme, convergence needs to be established in each internal loop before advancing to the next physical time level. The drop in the residual $\boldsymbol{R}^*$ during the inner cycle, required to achieve a temporal accuracy of the order m, is a function $(\Delta t)^{m-1}$ [41]. This means that for a second order accuracy, the necessary reduction of the residual scales linearly with the time-step of the outer iterations. Hence there is no general value of the residual that could serve as a termination criterion for the inner loop. The required number of inner iterations is instead determined with respect to convergence of integral parameters of interest, such as work-per-cycle in flutter calculations.

The procedure requires that grid velocities are evaluated at the time-levels n and $n+1$. A second order accurate backward difference is used for that purpose:

$$\boldsymbol{s}^{n+1} = \frac{3\boldsymbol{x}^{n+1} - 4\boldsymbol{x}^{n} + \boldsymbol{x}^{n-1}}{2\Delta t}. \tag{5.82}$$

Acceleration Techniques

The solver features local time-stepping and implicit residual smoothing for accelerating convergence and reducing the computational time. Both techniques are applicable to the explicit integration methods for steady computations and to the inner iteration cycle of the implicit integration method for time-accurate computations.

When local time-stepping is employed, the largest possible time-step is used locally in each cell to integrate the governing equations, instead of adopting a global value for all cells. The transient solution is consequently no longer accurate. However, this is no hindrance, since only the converged solution of a steady-state problem is of interest.

Residual smoothing serves to increase the maximum allowable CFL number of the explicit time-stepping scheme. A central implicit residual smoothing [14, 40] is obtained by applying the Laplacian operator to the residual. The originally computed residual $\boldsymbol{R}_0$ in a cell Ω_0 is replaced with a new smoothed residual $\tilde{\boldsymbol{R}}_0$, defined by

$$(1 + N\epsilon)\tilde{\boldsymbol{R}}_0 - \epsilon \sum_{i=1}^{N} \tilde{\boldsymbol{R}}_i = \boldsymbol{R}_0, \tag{5.83}$$

where the subscript i denotes each of the N cells adjacent to Ω_0. The system of linear equations is solved iteratively by performing five steps of the Jacobi method. Blažek [14] notes that two Jacobi iterations are usually sufficient. However, according to the author's experience, better convergence achieved thanks to the higher number of steps allows for a greater increase of the CFL number without a significant penalty in the overall computational time. The constant ϵ is set to 0.75, which enables raising the CFL by up to a factor of two [40].

5.2.6 Implementation of Non-Reflecting Boundary Conditions

This section provides a step-by-step description of the NRBC implementation in the present solver. Giving an accurate account is especially important for the Spectral NRBC, as the procedure is relatively complex and notable differences between individual implementations may arise.

Note that Fourier transforms, required at multiple steps of the algorithm, are realized by means of the Fastest Fourier Transform in the West (FFTW) library, version 3.3.9 [52].

Exact Steady NRBC

1. **Calculate the average state.** The instantaneous flow-field at the domain boundary is spatially averaged. The cell-face values used in the averaging are extrapolated from the domain interior with the same MUSCL-type procedure as employed to reconstruct the left and right states at inner cell interfaces. The nonlinearity of Euler equations raises the question of a correct method for averaging. Giles [59] suggests a *mixed-out averaging* as the only rigorous procedure. However, as Cumpsty and Horlock [31] demonstrate, the matter is not so trivial and a *work averaging* is preferable for turbomachines. A simple area-averaging procedure is used in the current computational model, as the averaging method is not essential for the non-reflecting behaviour of the boundary conditions. Since a discrete Fourier transform will be applied later in the procedure, the mesh spacing along the boundary needs to be uniform. Hence the area averaging reduces to the arithmetic average

$$\overline{\phi} = \frac{1}{N_y} \sum_j \phi_j, \tag{5.84}$$

   where N_y is the number of cell faces forming the boundary. The averaging is applied to primitive variables, whose mean values are subsequently used to calculate other thermodynamic quantities, such as entropy or total enthalpy.

2. **Calculate perturbations in characteristic variables.** The perturbation $\delta \boldsymbol{q}_j$ at a cell-face j is defined as a local difference from the mean state $\overline{\boldsymbol{q}}$. The perturbation in primitive variables is then transformed to a characteristic perturbation $\boldsymbol{c}_j$:

$$\delta \boldsymbol{q}_j = \begin{bmatrix} \rho_j - \overline{\rho} \\ u_j - \overline{u} \\ v_j - \overline{v} \\ p_j - \overline{p} \end{bmatrix}, \qquad \boldsymbol{c}_j = L_{1d} \delta \boldsymbol{q}_j \tag{5.85}$$

3. **Transform to the frequency domain.** A spatial discrete Fourier transform (DFT) of the characteristic perturbations is performed. For a wave-number $m_l = \frac{2\pi l}{P}$, where P is the domain pitch, the Fourier coefficient $\hat{\boldsymbol{c}}_{m_l}$ is given by

$$\hat{\boldsymbol{c}}_{m_l} = \frac{1}{N_y} \sum_{j=0}^{N_y - 1} \boldsymbol{c}_j \, e^{-\frac{\mathrm{i} 2\pi j l}{N_y}}, \qquad l = 1 ... N_y - 1 \tag{5.86}$$

   The procedure is realized with the FFTW library. The Fourier coefficient for $m_l = 0$, representing the spatial average, is set to zero.

4. **Apply the non-reflecting condition.** The non-reflecting condition, expressed by Eq. 4.69 for inlet and by Eq. 4.70 for outlet, is applied to each Fourier mode of the incoming characteristics, yielding $\hat{\boldsymbol{c}}_{m_l}^{(target)}$. The outgoing characteristics remain unchanged.

5. **Transform back to the physical domain.** The target local perturbations in the spatial domain are obtained by performing an inverse DFT of the Fourier coefficients:

$$\boldsymbol{c}_j^{(target)} = \mathrm{Re}\left(\sum_{l=0}^{N_y-1} \hat{\boldsymbol{c}}_{m_l}^{(target)}\, e^{\frac{\mathrm{i}2\pi jl}{N_y}}\right) \tag{5.87}$$

   The FFTW library is employed also for this step.

6. **Calculate global changes in characteristic variables.** The global change in characteristic variables, $\overline{\delta \boldsymbol{c}^{in}}$, applied to uphold the user-prescribed values at the boundary, is obtained by performing one step of the Newton-Rhapson procedure given by Eq. 4.74.

7. **Calculate the target boundary values.** The local perturbations $\boldsymbol{c}_j^{(target)}$ are summed with the mean change $\overline{\delta \boldsymbol{c}^{in}}$ and transformed to primitive variables:

$$\delta \boldsymbol{q}_j^{(target)} = R_{1d}(\overline{\delta \boldsymbol{c}^{in}} + \boldsymbol{c}_j^{(target)}), \tag{5.88}$$

   Finally, adding the primitive perturbations $\delta \boldsymbol{q}_j$ to the mean flow yields the target boundary values:

$$\boldsymbol{q}_j = \overline{\boldsymbol{q}} + \delta \boldsymbol{q}_j^{(target)} \tag{5.89}$$

   Giles [59] originally proposed to apply under-relaxation in this step to guarantee well-posedness of the mathematical formulation:

$$\boldsymbol{q}_j^{(n+1)} = \sigma(\overline{\boldsymbol{q}} + \delta \boldsymbol{q}_j^{(target)}) + (1-\sigma)\boldsymbol{q}_j^{(n)}, \tag{5.90}$$

   where $\sigma \in (0, 1)$ is an under-relaxation factor. However, the need for under-relaxation has been found unnecessary for the present solver and the newly computed value from Eq. 5.89 is imposed directly.

Spectral NRBC

A crucial aspect regarding the implementation of the Spectral NRBC is the calculation of temporal Fourier coefficients. A straightforward approach would be to store the entire solution history of the boundary flow field over the last period. In order to alleviate computational requirements, Fourier transform may subsequently be performed only for a selected set of most relevant harmonics [163]. Alternatively, the temporal Fourier coefficients may be determined iteratively in a manner similar to He's method for phase-lagged boundary conditions [87]. The latter approach was found superior in terms of convergence and computational demands in [156] and it is implemented in the present solver.

1. **Calculate the average state.** The averaging procedure is analogical to the Exact Steady NRBC, with the difference that the averaging is now performed spatially along the boundary as well as temporally over the last period. The

boundary grid spacing is uniform and the time-marching solver uses a fixed time-step, hence the mean value is given by an arithmetic average:

$$\overline{\phi} = \frac{1}{N_t N_y} \sum_{k=0}^{N_t-1} \sum_{j=0}^{N_y-1} \phi_{kj}, \tag{5.91}$$

where ϕ_{kj} is a the quantity ϕ evaluated at a cell face j and a time level k, N_t denotes the number of time-steps per period and N_y the number of cell faces forming the boundary.

2. **Calculate perturbations in characteristic variables.** The primitive and characteristic perturbations are now defined with respect to the spatially and temporally averaged mean flow. The perturbation at a time-level k and cell face j is defined as:

$$\delta \boldsymbol{q}_{kj} = \begin{bmatrix} \rho_{kj} - \overline{\rho} \\ u_{kj} - \overline{u} \\ v_{kj} - \overline{v} \\ p_{kj} - \overline{p} \end{bmatrix}, \qquad \boldsymbol{c}_{kj} = L_{1d} \delta \boldsymbol{q}_{kj} \tag{5.92}$$

3. **Perform Fourier transform in time.** The temporal Fourier coefficients are initialized to zero and subsequently updated at each time level with an iterative procedure, similar to the phase lag method of He [87]. Since we will now be dealing with 2D Fourier transforms, additional notation needs to be introduced. In order to distinguish between the temporal-only transformation and the space-and-time transformation, the temporal Fourier coefficients will be denoted as $\hat{\boldsymbol{c}}^{\tau}$, whereas the 2D Fourier coefficients will be marked by $\hat{\boldsymbol{c}}^{\tau y}$. Reminding that $m_l = \frac{2\pi l}{P}$ is the wave-number of a spatial harmonic l, analogically $\omega_p = \frac{2\pi p}{T}$ denotes the angular frequency of a temporal harmonic p.

   The updating procedure starts by reconstructing the solution at the current time-step k for each cell-face j, using the latest set of temporal Fourier coefficients $\hat{\boldsymbol{c}}^{\tau(old)}_{\omega_p,j}$:

$$\boldsymbol{c}^{(rec)}_{kj} = \mathrm{Re}\left(\sum_{p=0}^{N_t-1} \hat{\boldsymbol{c}}^{\tau(old)}_{\omega_p,j} \, e^{\frac{\mathrm{i}2\pi kp}{N_t}} \right). \tag{5.93}$$

   Next, an updated set of temporal Fourier coefficients is obtained by taking into account the difference between the reconstructed value and the actual flow state at the current time-step [156]:

$$\hat{\boldsymbol{c}}^{\tau(new)}_{\omega_p,j} = \hat{\boldsymbol{c}}^{\tau(old)}_{\omega_p,j} + \frac{1}{N_t} \left(\boldsymbol{c}_{kj} - \boldsymbol{c}^{(rec)}_{kj} \right) e^{-\frac{\mathrm{i}2\pi kp}{N_t}}. \tag{5.94}$$

4. **Perform Fourier transform in space.** A spatial Fourier transform is applied to the updated temporal coefficients:

$$\hat{\boldsymbol{c}}^{\tau y}_{\omega_p m_l} = \sum_{j=0}^{N_y-1} \hat{\boldsymbol{c}}^{\tau(new)}_{\omega_p,j}\, e^{-\frac{\mathrm{i}2\pi jl}{N_y}} \tag{5.95}$$

The FFTW library is used for this step. The coefficient $\hat{\boldsymbol{c}}^{\tau y}_{0,0}$ is set to zero.

5. **Apply the non-reflecting condition.** The non-reflecting condition, given by Eq. 4.64 for inlet and by Eq. 4.65 for outlet, needs to be applied to every mode, i.e to each combination of ω and m, with the exception of the space-time average mode $\hat{\boldsymbol{c}}^{\tau y}_{0,0}$. In the case of modes with $\omega = 0$, Eqs. 4.64 and 4.65 contain undefined expressions, as $\kappa = \frac{m}{\omega}$ goes to infinity. The limit case for $\kappa \to \infty$ is the Exact Steady NRBC, hence the target perturbations for these modes are calculated from Eqs. 4.69 and 4.70 instead. The non-reflecting treatment is applied to incoming characteristics only, whereas the outgoing ones remain unchanged.

6. **Transform back to the physical domain.** We need to obtain the target perturbations only at the current time-step k, therefore it would be superfluous to perform a complete 2D inverse Fourier transform. An inverse Fourier transform of the 2D Fourier coefficients is first performed in space only, yielding a set of target temporal Fourier coefficients $\hat{\boldsymbol{c}}^{\tau(target)}_{\omega_p,j}$ at each cell-face j. A temporal inverse Fourier transform is then used to calculate the target characteristic perturbations at the current time-level k only:

$$\boldsymbol{c}^{(target)}_{kj} = \mathrm{Re}\left(\sum_{p=0}^{N_t-1} \hat{\boldsymbol{c}}^{\tau(target)}_{\omega_p,j}\, e^{\frac{\mathrm{i}2\pi kp}{N_t}} \right). \tag{5.96}$$

7. **Calculate global changes in characteristic variables, sum with the local changes and determine the target boundary values.** The remainder of the procedure is equivalent to steps 6 and 7 of the Exact Steady NRBC algorithm. The global change in characteristic variables is obtained with one step of a Newton-Rhapson procedure and added to the local target characteristic perturbations. Finally, a transformation to primitive variables (Eq. 5.88) and a superposition of the target primitive perturbations with the spatially and temporally averaged flow (Eq. 5.89) follow.

5.3 Aeroelastic Analysis

Elastic solid bodies, either wings or blades, are represented by two dimensional sections which undergo an oscillatory motion but do not experience any distortion. The motion is either defined a priori in the case of energy method (Sec. 4.3.1), or it becomes a part of the solution if the fully coupled approach is employed (Sec. 4.3.2). This section elaborates on the numerical methods adopted by each approach that concern the solid body motion. In the first case, the prescribed rigid body oscillations are obtained by approximating an eigenmode determined in a structural

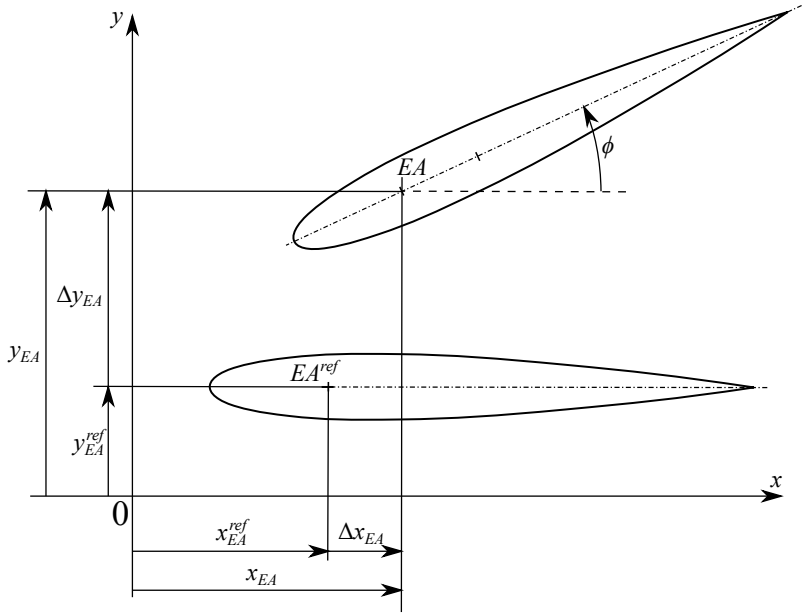

Figure 5.10: Solid body in a reference and displaced configuration

analysis. The fluid-structure coupled methodology, on the other hand, requires that ordinary differential equations describing the motion of an elastically mounted body are integrated simultaneously with the solution of unsteady aerodynamics.

5.3.1 Rigid Body Approximation

The position of a two-dimensional rigid body is defined by the displacement of elastic axis (EA), $\Delta\boldsymbol{x}_{EA} = [\Delta x_{EA}, \Delta y_{EA}]^T$, and by the angle of rotation ϕ about EA, see Fig. 5.10. An aeroelastic analysis using the energy method requires that these parameters are defined a priori as functions of time. The investigation is usually performed either to validate the computational model on an experimental test-case, or to investigate aeroelastic properties of a newly created design. In the former case, the solid body is typically excited by an actuator in a harmonic motion, hence the mode of oscillation is known and it may be readily used in the computational model. In the latter case, a FEM analysis is usually employed to determine eigenmodes and eigenfrequencies of the solid body. The natural modes may also comprise distortion of the two-dimensional section, hence they cannot be used directly in the present computational model which considers the section as a rigid body. The FEM data need to be approximated to obtain the definition of $\Delta\boldsymbol{x}_{EA}(t)$ and $\phi(t)$.

Let us consider the output of FEM analysis in the form of complex displacements $[\Delta\hat{x}_j^{ref}, \Delta\hat{y}_j^{ref}]^T$ for each point j on the solid body surface, such that its instantaneous position at a time t is calculated as

$$\begin{bmatrix} x_j \\ y_j \end{bmatrix} = \begin{bmatrix} x_j^{ref} \\ y_j^{ref} \end{bmatrix} + \begin{bmatrix} \Delta x_j \\ \Delta y_j \end{bmatrix} = \begin{bmatrix} x_j^{ref} \\ y_j^{ref} \end{bmatrix} + \mathrm{Re}\left(\begin{bmatrix} \Delta\hat{x}_j \\ \Delta\hat{y}_j \end{bmatrix} e^{\mathrm{i}\omega t} \right). \tag{5.97}$$

Here $[x_j^{ref}, y_j^{ref}]^T$ are the point coordinates in a reference configuration, $[\Delta x_j, \Delta y_j]^T$

is the instantaneous displacement and ω denotes the angular frequency. At the same time, if the structure is represented by a rigid body, the motion of each points can be defined as

$$\begin{bmatrix} x \\ y \end{bmatrix} = \begin{bmatrix} x^{ref} + \Delta x \\ y^{ref} + \Delta y \end{bmatrix} = \begin{bmatrix} x^{ref}_{EA} + \Delta x_{EA} \\ y^{ref}_{EA} + \Delta y_{EA} \end{bmatrix} + Q \begin{bmatrix} x^{ref} - x^{ref}_{EA} \\ y^{ref} - y^{ref}_{EA} \end{bmatrix}, \tag{5.98}$$

where the rotation matrix reads

$$Q = \begin{bmatrix} \cos\phi & -\sin\phi \\ \sin\phi & \cos\phi \end{bmatrix}. \tag{5.99}$$

Hence for the displacement $[\Delta x, \Delta y]^T$ we obtain

$$\begin{bmatrix} \Delta x \\ \Delta y \end{bmatrix} = \begin{bmatrix} \Delta x_{EA} + (\cos\phi - 1)(x^{ref} - x^{ref}_{EA}) - \sin\phi(y^{ref} - y^{ref}_{EA}) \\ \Delta y_{EA} + (\cos\phi - 1)(y^{ref} - y^{ref}_{EA}) + \sin\phi(x^{ref} - x^{ref}_{EA}) \end{bmatrix}. \tag{5.100}$$

Providing that the angle of rotation is small, the equations may be linearised by setting $\cos\phi \approx 1$ and $\sin\phi \approx \phi$, which yields

$$\begin{bmatrix} \Delta x \\ \Delta y \end{bmatrix} \approx \begin{bmatrix} \Delta x_{EA} - \phi(y^{ref} - y^{ref}_{EA}) \\ \Delta y_{EA} + \phi(x^{ref} - x^{ref}_{EA}) \end{bmatrix}. \tag{5.101}$$

Writing Eq. 5.101 for each point j whose complex displacement $[\Delta\hat{x}^{ref}_j, \Delta\hat{y}^{ref}_j]^T$ is known from FEM, we obtain the following system of linear equations:

$$\begin{bmatrix} 1 & 0 & -(y^{ref}_1 - y^{ref}_{EA}) \\ \vdots & \vdots & \vdots \\ 1 & 0 & -(y^{ref}_N - y^{ref}_{EA}) \\ 0 & 1 & (x^{ref}_1 - x^{ref}_{EA}) \\ \vdots & \vdots & \vdots \\ 0 & 1 & (x^{ref}_N - x^{ref}_{EA}) \end{bmatrix} \begin{bmatrix} \Delta\hat{x}_{EA} \\ \Delta\hat{y}_{EA} \\ \hat{\phi} \end{bmatrix} = \begin{bmatrix} \Delta\hat{x}_1 \\ \vdots \\ \Delta\hat{x}_N \\ \Delta\hat{y}_1 \\ \vdots \\ \Delta\hat{y}_N \end{bmatrix} \tag{5.102}$$

which can be formally written as $A\boldsymbol{q} = \boldsymbol{b}$. Since we have $2N$ equations for the three unknowns $\Delta\hat{x}_{EA}$, $\Delta\hat{y}_{EA}$ and $\hat{\phi}$, and typically $N \gg 1$, the system is overdetermined. A solution in the least squares sense is obtained by multiplying Eq. 5.102 with A^T and solving the following regular system of *normal equations*:

$$\begin{bmatrix} N & 0 & -\sum(y_j^{ref}-y_{EA}^{ref}) \\ 0 & N & \sum(x_j^{ref}-x_{EA}^{ref}) \\ -\sum(y_j^{ref}-y_{EA}^{ref}) & \sum(x_j^{ref}-x_{EA}^{ref}) & \sum[(x_j^{ref}-x_{EA}^{ref})^2+(y_j^{ref}-y_{EA}^{ref})^2] \end{bmatrix}$$
$$\cdot \begin{bmatrix} \Delta\hat{x}_{EA} \\ \Delta\hat{y}_{EA} \\ \hat{\phi} \end{bmatrix} = \begin{bmatrix} \sum \Delta\hat{x}_j \\ \sum \Delta\hat{y}_j \\ \sum[-(y_j^{ref}-y_{EA}^{ref})\Delta\hat{x}_j+(x_j^{ref}-x_{EA}^{ref})\Delta\hat{y}_j] \end{bmatrix}. \quad (5.103)$$

All summations are performed over the index j ranging from 1 to N. Note that due to linearisation, the reference position of elastic axis $[x_{EA}^{ref}, y_{EA}^{ref}]^T$ is not a part of the solution and it needs to be specified a priori.

5.3.2 Fluid-Structure Coupled Computations

The motion of a solid body is described with the set of two second-order ordinary differential equations (ODE) 4.87. They are integrated in time using the same explicit four-stage Runge-Kutta method that is also implemented within the FVM solution of unsteady aerodynamics (Sec. 5.2.5). The second order ODE of motion are first transformed to a set of first-order ODE. Defining a vector of unknowns $\boldsymbol{z}$:

$$\boldsymbol{z} = [\Delta y_{EA}, \phi, \Delta\dot{y}_{EA}, \dot{\phi}]^T, \quad (5.104)$$

we receive a set of four first-order ODE:

$$\dot{z}_1 = z_3, \qquad \dot{z}_2 = z_4,$$
$$\begin{bmatrix} \dot{z}_3 \\ \dot{z}_4 \end{bmatrix} = \begin{bmatrix} m & S_\phi \cos z_2 \\ S_\phi \cos z_2 & I_\phi \end{bmatrix}^{-1} \begin{bmatrix} F_y + S_\phi z_4^2 \sin z_2 - k_y z_1 - b_y z_3 \\ M - k_\phi z_2 - b_\phi z_4 \end{bmatrix} \quad (5.105)$$

.

An explicit Runge-Kutta method may be written as

$$\begin{aligned} \boldsymbol{z}_i^{(0)} &= \boldsymbol{z}_i^n, \\ \boldsymbol{z}_i^{(k)} &= \boldsymbol{z}_i^n + \alpha_k \Delta t f(\boldsymbol{z}^{(k-1)}), \qquad k = 1 \dots l, \\ \boldsymbol{z}^{n+1} &= \boldsymbol{z}^{(l)}, \end{aligned} \quad (5.106)$$

where for the present four-stage scheme $l = 4$, $\alpha_1 = 1/4$, $\alpha_2 = 1/3$, $\alpha_3 = 1/2$ and $\alpha_4 = 1$.

The solution of equations of motion is performed simultaneously with the computation of unsteady aerodynamics in order to obtain a strongly coupled method. The time-marching algorithm is outlined in Fig. 5.11. At the beginning of each iteration, aerodynamic forces acting on the solid bodies are calculated by integrating the surface pressure. The solution of equations of motion yields the position of solid bodies

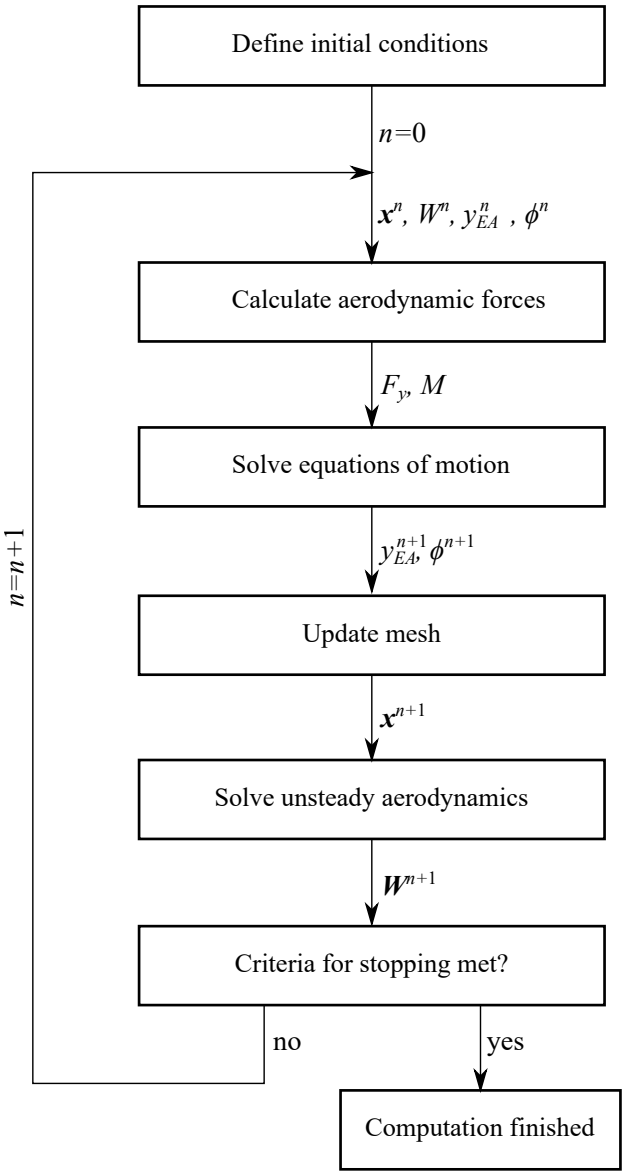

Figure 5.11: Algorithm of fluid-structure coupled computations

at the next time-level and the computational grid is updated accordingly. The position and velocity of solid bodies also represents a boundary condition for the solution of unsteady aerodynamics with the finite volume method. Once the flow-field at the new time-level is obtained, the procedure is repeated. The computation stops upon fulfilling the predefined criteria, such as reaching the target solution time.

Chapter 6

Application and Analysis

6.1 NACA 0012 Airfoil

The computational model is first tested on the case of an isolated airfoil submerged in a freestream flow, before proceeding to the more complex problem of blade cascades. The NACA 0012 airfoil is a suitable test-case for this purpose thanks to a wide availability of experimental data. The results are presented for three configurations. First, a steady-state solution is performed to establish grid convergence and evaluate the solution sensitivity to domain extent for three types of boundary conditions. Solution of unsteady aerodynamics for a harmonically oscillating airfoil follows. The assessment is focused on the unsteady pressure distribution on airfoil surface, as its correct resolution is crucial for the characterisation of aeroelastic stability. And finally, results of fluid-structure coupled computations for an airfoil with two degrees of freedom are shown. Since experimental data are not available for this configuration, a comparison with numerical predictions of other authors is included instead. A part of the results was published by the author in [1], but they are extended and updated in this thesis.

The time-marching solution procedure adopted the dual-time implicit scheme. The acceleration techniques of local time-stepping and implicit residual smoothing were enabled and the CFL number was set to 2.0. The inverse distance weighting exponent of the least squares gradient reconstruction procedure was set to 3/2. The limiting technique of Delis et al. [34] was applied to the reconstructed gradients, utilizing the MinMod limiter function. Other gradient limiting methods implemented in the solver were not tested for this application, as the limiter choice has only a minor effect on the solution due to the subsonic flow conditions.

6.1.1 Steady-State Flow

The computational domain for a steady-state solution is shaped to facilitate generation of a C-type structured grid (Fig. 6.1). The inlet boundary $\partial\Omega_{in}$ is formed by a half-circle centered around the airfoil leading edge (LE) and two tangentially con-

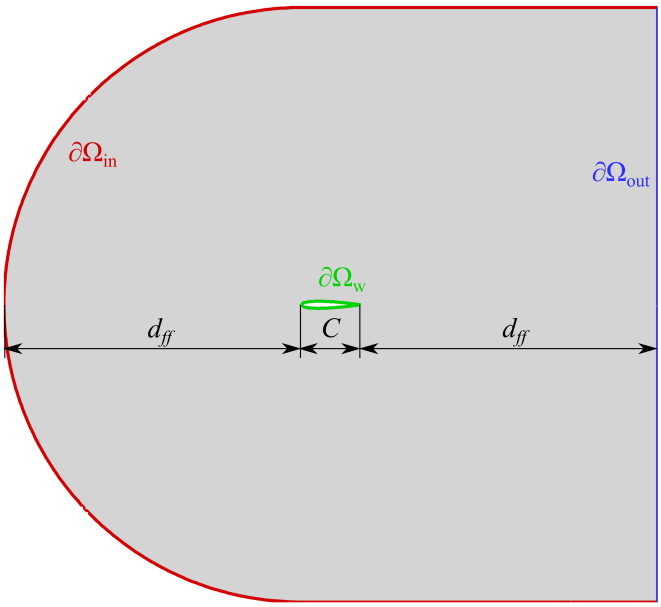

Figure 6.1: NACA 0012 computational domain with farfield boundaries located at the distance of five chords.

Farfield distance	$5C$	$20C$				$100C$
Refinement level	3	1	2	3	4	3
Number of cells	27192	7992	18480	41998	95250	64478

Table 6.1: NACA 0012 grid cell-counts

nected horizontal lines. The outlet boundary $\partial\Omega_{out}$ comprises a single vertical line. Although the inlet and outlet boundaries are referred to individually, an identical boundary condition treatment was used for both. The distinction between inflow and outflow is based on the local flow direction relatively to the boundary, rather than on the geometrical configuration alone. The inlet arc radius and the distance between the airfoil trailing edge (TE) and the outlet boundary are set to an equal dimension, called *farfield distance* (d_{ff}). Its value will be given in multiples of airfoil chord C.

Domain discretisation was performed with quadrilateral C-type structured grids, generated in ANSYS® ICEM 19.1 and converted to an unstructured representation. A grid convergence study was performed on a set of grids with farfield distance $20C$. Starting on level 1 with 7992 cells, the mesh is progressively refined up to level 4 with 95250 cells. In each transition to the next refinement level, the cell size is reduced by 1.5. The computational grid is depicted in Fig. 6.2 with insets showing the refinement levels. Table 6.1 provides an overview of cell counts for all meshes.

The grid convergence study considered a steady-state flow with inlet Mach number 0.15 and airfoil angle of incidence 6°. Ideal gas properties were set to $R = 287\,\mathrm{J\,kg^{-1}\,K^{-1}}$ and $\gamma = 1.4$ in approximation of dry air. An overview of the test-case parameters is given in Tab. 6.2. A farfield boundary condition with vortex correction (FFVC) was imposed at the inlet and outlet boundaries $\partial\Omega_{in}$, $\partial\Omega_{out}$, while a

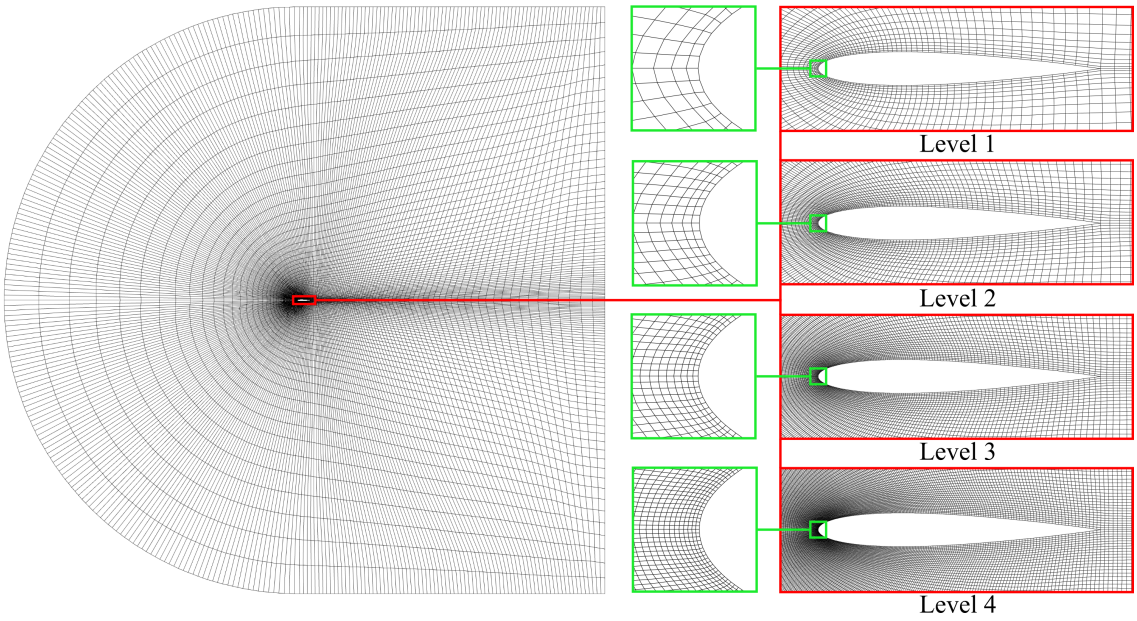

Figure 6.2: NACA 0012 domain discretisation. The overall mesh view on the left is provided for the 20-chord domain and for the level 2 refinement out of the four levels shown in the insets.

Parameter	Symbol	Unit	Value
Airfoil chord	C	[m]	0.3
Angle of incidence	α	[°]	6
Specific heat ratio	γ	[-]	1.4
Specific gas constant	R	$[\mathrm{J\,kg^{-1}\,K^{-1}}]$	287
Freestream density	ρ_{FS}	$[\mathrm{kg\,m^{-3}}]$	1.204
Freestream velocity in x direction	u_{FS}	$[\mathrm{m\,s^{-1}}]$	51.48
Freestream velocity in y direction	v_{FS}	$[\mathrm{m\,s^{-1}}]$	0
Freestream pressure	p_{FS}	[Pa]	101325

Table 6.2: Parameters of NACA 0012 steady-state flow

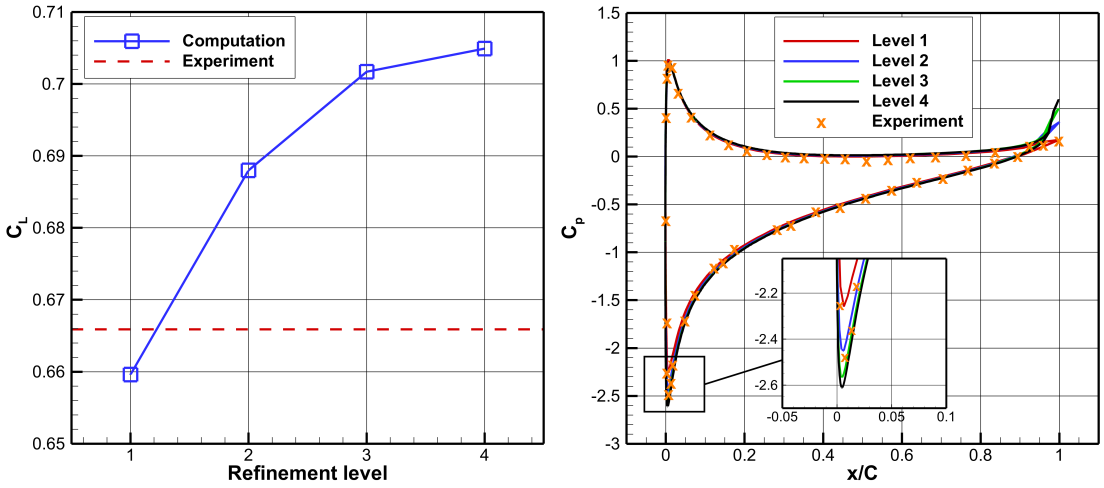

Figure 6.3: Steady-state flow solution in function of grid refinement. Lift coefficient presented on the left and blade surface distribution of pressure coefficient on the right. Experimental data from Gregory and O'Reilly [63].

free-slip condition was applied on the airfoil surface $\partial\Omega_w$.

The assessment of grid convergence was based on the lift coefficient C_L (Eq. 4.34). Figure 6.3-left shows that C_L converges monotonously with grid refinement. Richardson extrapolation performed on the three finest levels yields an estimation of the converged value $C_L = 0.707$. The coarsest grid solution underpredicts lift by 6.76% relatively to the converged value, while on the level 4 mesh the error is reduced to 0.36%. The plot also provides a comparison with the experiment of Gregory and O'Reilly [63]. They measured a value of $C_L = 0.67$, which differs from the numerical prediction by 5.8%.

Pressure distribution on the airfoil surface is plotted in Fig. 6.3-right, using a pressure coefficient C_p with the following definition:

$$C_p = \frac{p - p_1}{p_{01} - p_1}. \tag{6.1}$$

Here the subscript 1 denotes the inlet state defined with the freestream quantities, p_0 is the total pressure and p the static pressure. The pressure distribution is captured consistently on all four refinement levels. Over most of the airfoil surface, the coarsest and finest grid solutions differ only by a small offset in C_p, amounting to less than 0.06 on the suction side and 0.014 on the pressure side. In the vicinity of the leading edge, the grid refinement affects how sharply the suction side pressure minimum is resolved. While the coarsest grid yields a prediction of $C_p = -2.26$, on the finest grid $C_p = -2.61$ is reached. A notable effect of grid refinement is observed also in the aft 5% of both pressure and suction side. A nearly constant distribution is obtained with the level 1 discretisation, whereas on the finer grids a local pressure rise culminating at the TE is captured.

The calculated C_p distribution is in a very good agreement with the measurements of Gregory and O'Reilly [63]. The only significant discrepancy is observed at the

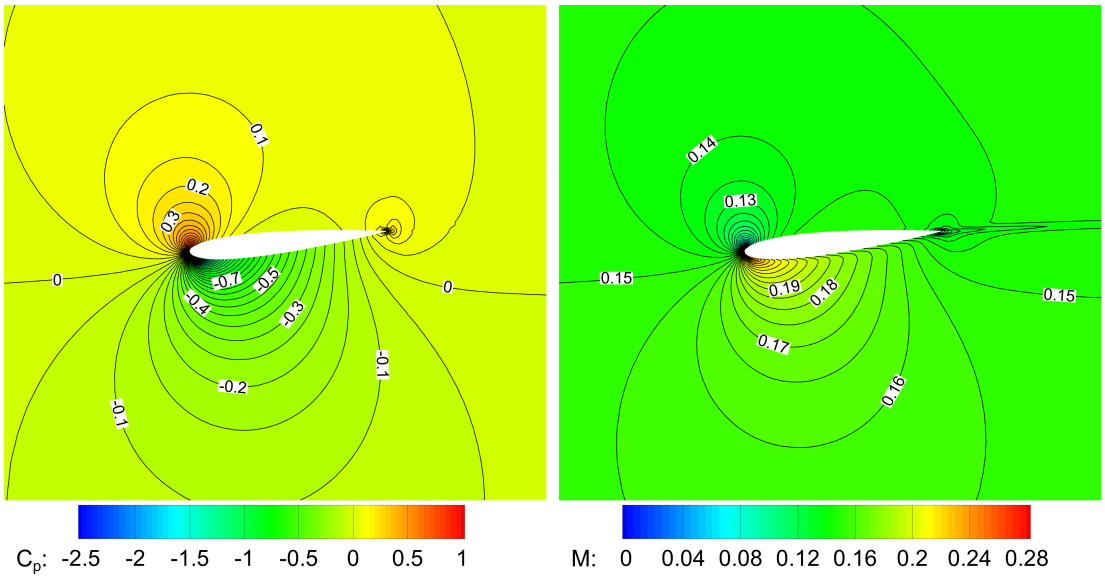

Figure 6.4: Contours of pressure coefficient (left) and Mach number (right) from a steady-state solution on the 20-chord domain.

aft-most experimental data-point, located directly at the TE. The experiment does not indicate the presence of a pressure rise predicted here by the numerical solution.

Based on the grid convergence study, the level 3 discretisation was concluded to offer sufficient accuracy. The lift coefficient is predicted within 0.81% of the converged value and a further cell-size reduction does not alter qualitatively the airfoil pressure distribution.

The near-airfoil flow solution obtained on the level 3 grid is visualised in Fig. 6.4. Contours of pressure coefficient are shown on the left and contours of Mach number on the right. The solution was obtained with 600 steps of the implicit integration scheme, using 180 iterations in the inner cycle. Convergence history of average residuals during the computation run is shown in Fig. 6.5. Convergence does not stall and the residuals continue decreasing until the last iteration. A drop of over 5 orders of magnitude is observed for both momentum components, while the density and energy residuals are reduced by approximately 7 orders of magnitude. Together with the drop of residuals, an important criterion for terminating the simulation is the convergence of global aerodynamic parameters. The lift force arrives within 0.1% of the converged value after 250 time-steps.

A numerical solution performed on a truncated domain approximates a theoretical case with an infinitely large domain. Positioning the farfield boundary at a finite distance from the airfoil contaminates the solution with a perturbation, whose magnitude depends on the farfield distance and on the boundary condition formulation. While a larger domain reduces the effect of the perturbation, it also increases computational demands due to a higher cell-count and slower convergence. An investigation was performed to determine a suitable domain size and boundary condition treatment. Farfield distances of $5C$, $20C$ and $100C$ were considered, in combination with three boundary condition formulations: farfield (FF), farfield with vortex cor-

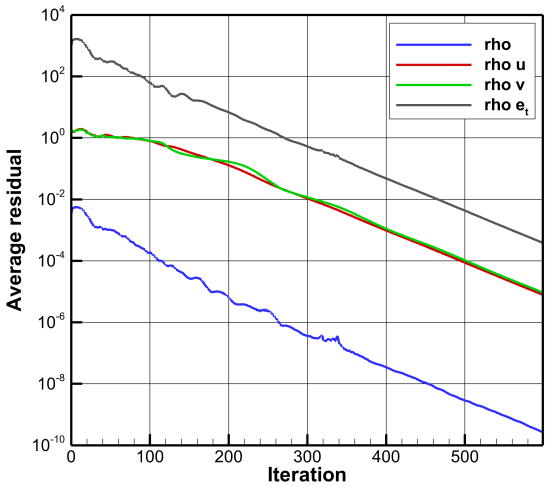

Figure 6.5: Convergence history of a steady-state solution on the 20-chord domain with $\alpha = 6°$ and $M = 0.15$

rection (FFVC) and freestream (FS). The FF and FFVC definitions are described in Sec. 4.2.3. The FS condition is imposed by prescribing directly the full set of four primitive variables defining the freestream state, regardless of the relative flow direction.

Figure 6.6 shows the farfield distance effect on C_L variation for the three boundary conditions. The FS and FF boundary conditions performed similarly, underestimating the aerodynamic lift when the boundary is positioned closer to the airfoil. On the most truncated domain, the discrepancy with the largest domain solution amounted to 4.2% and 5.4% respectively, while on the $20C$ domain it reduced to 1.8% and 2%.

The underestimation of the lift force is to a large extent remedied by employing a vortex correction for the farfield boundary condition. On the $5C$ domain, C_L was overpredicted by 0.4%, whereas a $20C$ domain yielded an underprediction of 0.7%. The vortex correction thus enables the use of more severely truncated domains without compromising the solution accuracy. However, it may not be employed for unsteady computations, as it uses the instantaneous lift force to calculate the correction terms applied at the boundary. An unsteady perturbation in the pressure field surrounding the airfoil thus immediately affects the flow at the boundary, implying an infinite speed of propagation in contradiction with physics. The farfield boundary condition without vortex correction was therefore adopted in unsteady computations.

Computational time increased approximately linearly with the farfield distance, as shown in Fig. 6.7. The plot displays CPU time needed to arrive within 0.1% of the converged lift coefficient value. The $20C$ domain was found to offer the best compromise between accurate lift quantification and computational demands.

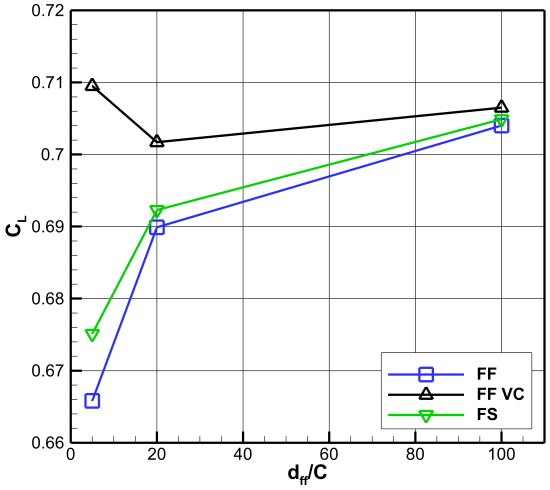

Figure 6.6: Lift coefficient variation with farfield distance for three boundary conditions: farfield (FF), farfield with vortex correction (FFVC) and freestream (FS).

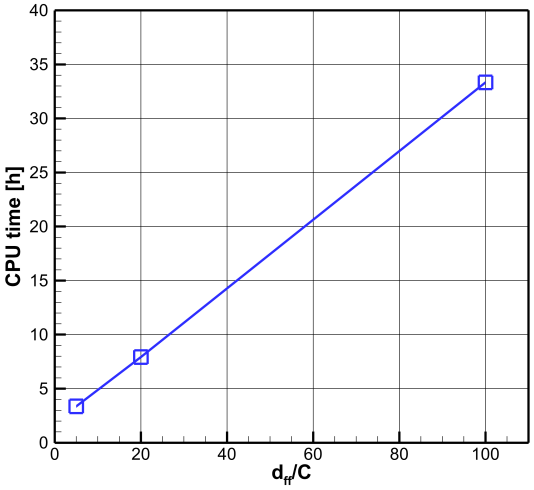

Figure 6.7: CPU time in function of farfield distance (FFVC boundary condition).

6.1.2 Harmonic Airfoil Oscillations

Simulations of a harmonically oscillating NACA 0012 airfoil were performed to validate the solution of unsteady aerodynamics, crucial for an accurate aeroelastic analysis. The test-case configuration was selected to match the experimental setup reported by Benetka [12]. An airfoil with a chord length $C = 0.1322\,\mathrm{m}$ is placed in a rectangular $0.9 \times 0.6\,\mathrm{m}$ test-section and subjected to a pitching motion. The angle of attack is varied harmonically in time according to the formula

$$\alpha(t) = \Delta\alpha sin(2\pi f) \tag{6.2}$$

with a pitching amplitude $\Delta\alpha = 1.25°$ and frequency $f = 43\,\mathrm{Hz}$. The pivoting point

Parameter	Symbol	Unit	Value
Domain height	H	[m]	0.6
Domain length	L	[m]	0.9
Airfoil chord	C	[m]	0.1322
Elastic axis chordwise position	ξ_{EA}	[m]	$0.3C$
Pitching amplitude	$\Delta\alpha$	[°]	1.25
Pitching frequency	f	[Hz]	43
Freestream density	ρ_{FS}	$[\mathrm{kg\,m^{-3}}]$	1.081
Freestream velocity in x direction	u_{FS}	$[\mathrm{m\,s^{-1}}]$	136.1
Freestream velocity in y direction	v_{FS}	$[\mathrm{m\,s^{-1}}]$	0
Freestream pressure	p_{FS}	[Pa]	89410

Table 6.3: Parameters of NACA 0012 harmonic oscillations

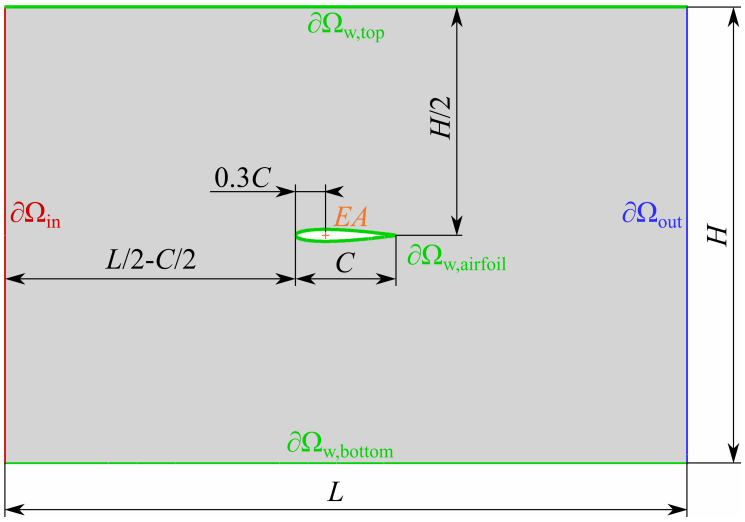

Figure 6.8: Computational domain for simulations of a harmonically oscillating NACA 0012 airfoil.

of oscillations is placed on the profile chord at $0.3C$ from the leading edge (LE). Flow conditions are subsonic, characterised by a freestream Mach number $M_{FS} = 0.4$. A summary of the test-case parameters is provided in Tab. 6.3.

The computational domain shown in Fig. 6.8 has a rectangular shape with the airfoil placed in its center, in approximation of the experimental setup. The left and right boundaries $\partial\Omega_{in}$, $\partial\Omega_{out}$ represent inflow and outflow respectively, and a farfield boundary condition without vortex correction is applied at both. The bottom and top boundaries $\partial\Omega_{w,botom}$, $\partial\Omega_{w,top}$ are modelled as solid walls, same as the airfoil surface $\partial\Omega_{w,airfoil}$.

The domain was discretised with a triangular unstructured grid. Rather than performing a separate grid convergence study, the cell sizing was selected according to the findings obtained for the structured grid (Sec. 6.1.1). The number of elements on the airfoil surface was set to 268, matching the level 3 refinement. As the cells are triangular, the resulting discretisation is in fact finer than an equivalent level 3 structured quadrilateral grid with the same face size. The total cell-count is 35288 and a view of the mesh is presented in Fig. 6.9.

Unsteady computations require that a sufficiently fine discretisation is used not only for the spatial domain, but also for the time-marching procedure. Two physical time-step sizes were considered, corresponding to 100 and 200 steps per period of profile oscillation T. In both cases, the number of inner iterations in the dual time-stepping procedure was varied to establish convergence of the inner cycle. Results were quantified in terms of the aerodynamic damping coefficient Ξ for pitching mode (Eq. 4.78), plotted in Fig. 6.10. With 100 time-steps per period, sufficient inner cycle convergence was reached after 640 inner iterations. Reducing the time-step to half brought a corresponding drop in the number of required inner iterations, hence the overall computational time was nearly unaffected by the time-step choice. The aerodynamic damping coefficient changed only by 0.09% in reducing the time-step from $T/100$ to $T/200$, showing that further temporal refinement is not needed. The

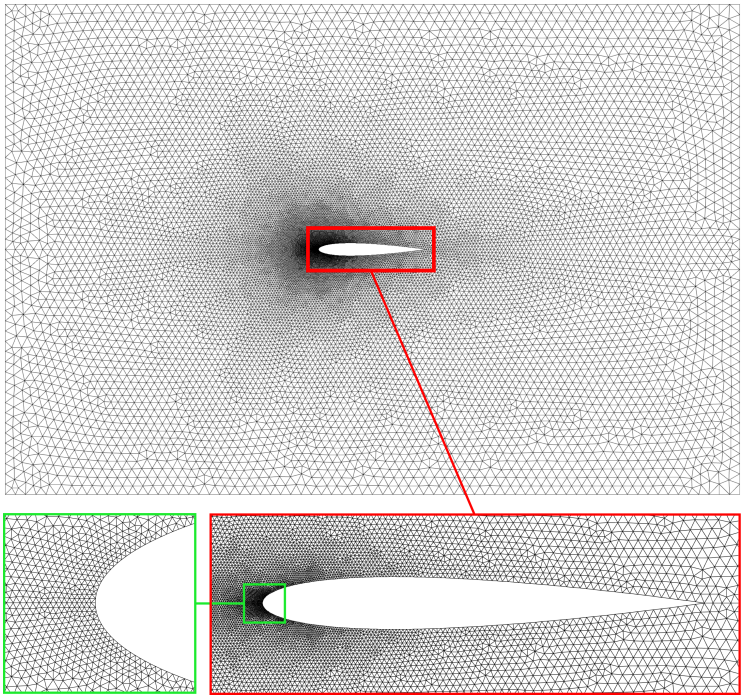

Figure 6.9: Grid for simulations of a harmonically oscillating NACA 0012 airfoil, insets showing in detail the airfoil and the LE region.

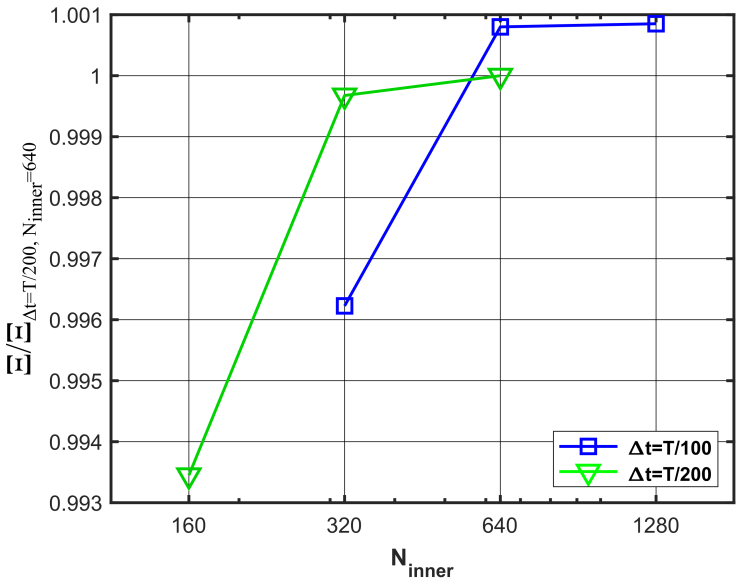

Figure 6.10: Convergence of the aerodynamic damping coefficient Ξ with physical time-step Δt and with the number of inner iterations. Values normalised by Ξ obtained with 200 time-steps per period and 640 inner iterations.

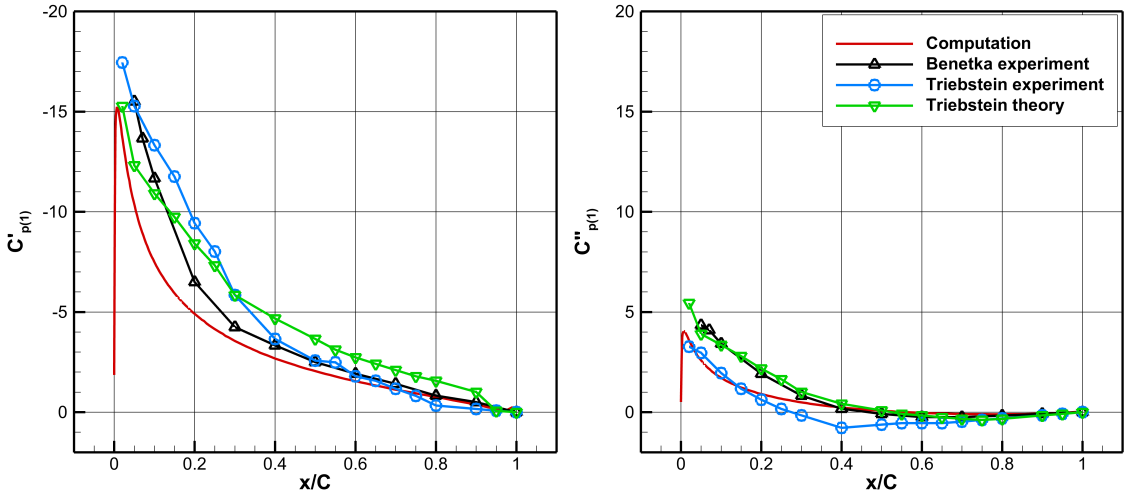

Figure 6.11: Distribution of the real ($C'_{p(1)}$, left) and imaginary ($C''_{p(1)}$, right) parts of the 1^{st} unsteady pressure harmonic on airfoil surface. Comparison of the present computation with experimental data reported by Benetka [12] and with Triebstein's theory and measurements [182].

results presented in the remainder of this section were obtained with $\Delta t = T/200$ and $N_{inner} = 640$. The predicted damping coefficient value was $\Xi = 0.198$, which means that the investigated configuration is aeroelastically stable.

The unsteady pressure distribution on airfoil surface is characterised in Fig. 6.11. The left and right plots show respectively the real ($C'_{p(1)}$) and imaginary ($C''_{p(1)}$) parts of the 1^{st} unsteady pressure harmonic coefficient, defined as:

$$C'_{p(1)} = \mathrm{Re}\left(\frac{\hat{p}_{(1)}}{\Delta\alpha(p_{01} - p_1)}\right), \qquad C''_{p(1)} = \mathrm{Im}\left(\frac{\hat{p}_{(1)}}{\Delta\alpha(p_{01} - p_1)}\right), \tag{6.3}$$

where $\hat{p}_{(1)}$ is the 1^{st} harmonic of unsteady pressure. For the purpose of validation, the measurements of Benetka [12] and the theoretical and experimental data of Triebstein [182] are included. Note that the test-case considered by Triebstein does not exactly correspond to the present one, as he assumed a freestream Mach number 0.7, an oscillation frequency 30 Hz and a pitching axis position at 25 % chord. The plot therefore shows an altered dataset available in [12], scaled to the present $M_{FS} = 0.4$ using the Prandtl-Glauert formula.

The distributions of both the real and the imaginary part are characterised by a peak in the vicinity of the leading edge. Further downstream, they nearly monotonously drop towards zero at the trailing edge. All datasets capture this trend in agreement, although some differences arise locally in the magnitude. The present results match the measurements satisfactorily, deviating in general by less than is the discrepancy between the two experimental datasets.

Parameter	Symbol	Unit	Value
Airfoil chord	C	[m]	0.3
Elastic axis chordwise position	ξ_{EA}	[m]	$0.4C$
Wing span	b	[m]	1
Wing weight	m	[kg]	1.7324
Static moment about EA	S_ϕ	[kg m]	-0.01559
Moment of inertia about EA	I_ϕ	[kg m^2]	0.009746
Bending stiffness	k_y	[N m^{-1}]	2102.18
Torsional stiffness	k_ϕ	[N m rad^{-1}]	73.9116
Structural damping in bending	b_y	[kg s^{-1}]	2.1022
Structural damping in torsion	b_ϕ	[kg m^2 s^{-1} rad^{-1}]	0.07391
Initial vertical displacement	$\Delta y_{EA,0}$	[m]	0.05
Initial angle of incidence	ϕ_0	[°]	6
Initial vertical displacement velocity	$\dot{\Delta y}_{EA,0}$	[m s^{-1}]	0
Initial angular velocity	$\dot{\phi}_0$	[° s^{-1}]	0
Freestream temperature	T_{FS}	[K]	293.15
Freestream velocity in x direction	u_{FS}	[m s^{-1}]	30–45
Freestream velocity in y direction	v_{FS}	[m s^{-1}]	0
Freestream density	ρ_{FS}	[kg m^{-3}]	1.2043

Table 6.4: Parameters of NACA 0012 oscillations with two degrees of freedom

6.1.3 Airfoil Motion with Two Degrees of Freedom

The investigation of the NACA 0012 airfoil is concluded by modelling the unsteady fluid-structure interaction for a system with two degrees of freedom. The fully coupled aeroelastic model considers the airfoil as a rigid body, flexibly supported by springs allowing for a vertical translation and for a pitching motion about the elastic axis (EA). The set of ordinary differential equations describing the behaviour of the system is given in Sec. 4.3.2. The numerical solution procedure for the equations of motion and its coupling with the flow solver is discussed in Sec. 5.3.2.

The considered test-case was adopted from the works of Honzátko [95] and Sváček [174]. The airfoil with a chord length 0.3 m and EA located at 40% chord is vertically displaced by 0.05 m and rotated by 6°. A steady-state flow solution is computed for this configuration and used as initial condition for a transient solution, starting at the time $t = 0$ by releasing the airfoil from the displaced position. Based on the temporal development of the vertical displacement and rotation angle, whose amplitudes may be either increasing, constant, or converging to an equilibrium position, the aeroelastic stability of the system can be assessed. The considered freestream flow velocities were in the range from 30 to 45 m s^{-1}. The mechanical properties of the elastically mounted airfoil are given in Tab. 6.4, together with other relevant parameters.

The computational domain and mesh ware adopted from the steady-state analysis. The farfield boundary was positioned to $20C$ from the airfoil and the level 3 mesh with 41998 cells was employed. A farfield boundary condition without vortex cor-

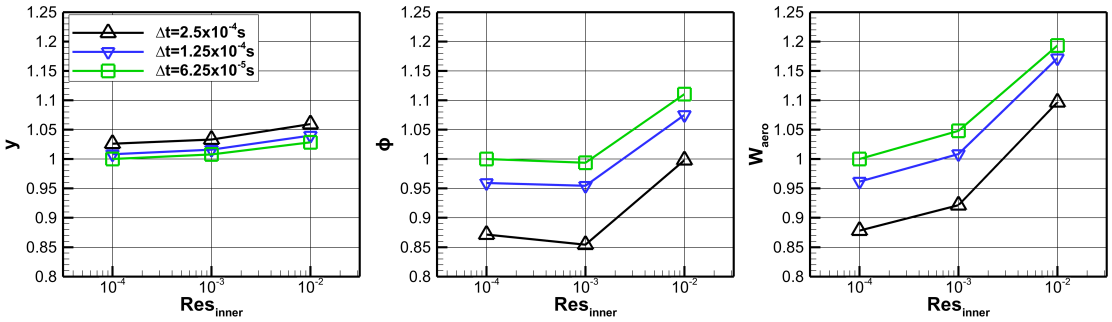

Figure 6.12: Convergence of the two-degree-of-freedom computations with the physical time-step Δt and with the inner cycle residuum Res_{inner}. From left to right, the plots show the instantaneous displacement y and rotation angle ϕ at $t = 0.5\,\mathrm{s}$ and the integral aerodynamic work W_{aero}. All values are normalized by the results obtained with $\Delta t = 6.25 \times 10^{-5}\,\mathrm{s}$, $Res_{inner} = 10^{-4}$.

rection was used at the inlet and outlet boundaries, as the vortex correction given by Eq. 4.36 is not applicable to unsteady flows.

A sufficiently fine temporal discretisation is essential for the accuracy of fluid-structure coupled computations. In contrast to the harmonically oscillating airfoil, the solid body motion is not prescribed a priori. Instead, it is obtained by solving the equations of motion, using aerodynamic forces as a source term. Inaccurately resolved unsteady aerodynamics therefore introduces an error into their solution, that is further combined with the error of the temporal integration method. The predicted solid body position at the next time-level in turn affects the solution of unsteady aerodynamics. The fully coupled solution procedure can thus be expected to manifest high sensitivity to time-step size.

The analysis of temporal refinement was performed with a freestream velocity $u_{FS} = 40\,\mathrm{ms}^{-1}$, considering physical time-steps $2.5 \times 10^{-4}\,\mathrm{s}$, $1.25 \times 10^{-4}\,\mathrm{s}$ and $6.25 \times 10^{-5}\,\mathrm{s}$. The criterion for terminating the inner iteration cycle was based on the value of residuals of momentum, as opposed to the fixed number iterations employed in the case of prescribed harmonic airfoil oscillations. This choice was motivated by the variable rate of flow unsteadiness experienced in the coupled computations. Depending on the aeroelastic stability of the particular configuration, the amplitude of airfoil oscillations may converge to zero or grow exponentially in time, hence the number of iterations required for the convergence of inner cycle changes accordingly.

The effect of temporal discretisation on the prediction of airfoil motion is shown in Fig. 6.12. The plots on the left and in the middle display respectively the instantaneous airfoil displacement and rotation angle at the time $t_1 = 0.5\,\mathrm{s}$, when the airfoil has undergone approximately 4.5 oscillation cycles. The right-most plot shows the work of aerodynamic forces integrated between $t_0 = 0\,\mathrm{s}$ and t_1. The results are displayed for a matrix of nine configurations, obtained by varying the time-step size and the target inner cycle residual of momentum.

The instantaneous vertical displacement manifests the lowest sensitivity out of the three parameters. Its value changes by less than 3% when altering either of the settings within the considered intervals, whereas variations in the instantaneous

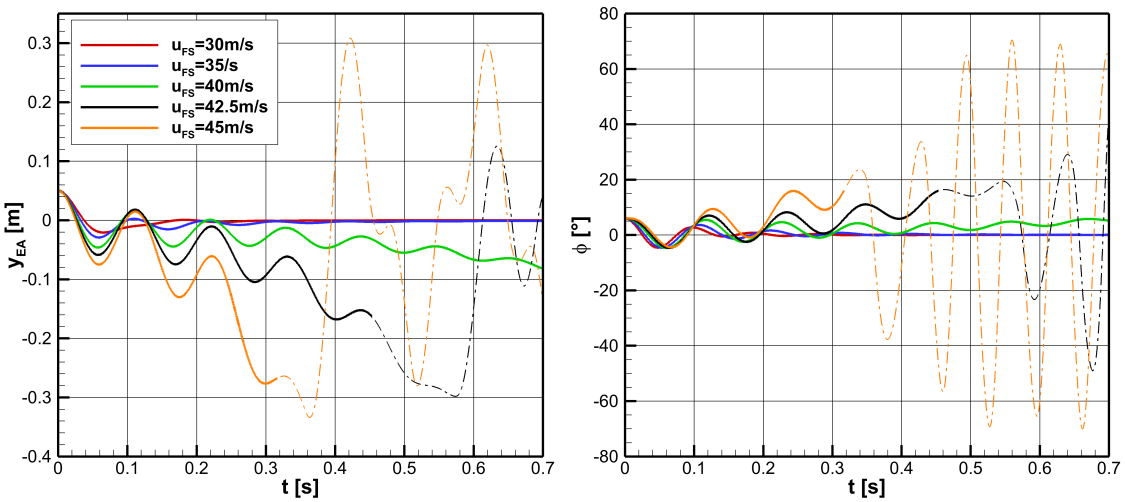

Figure 6.13: Temporal evolutions of the vertical displacement of elastic axis (left) and of the pitching angle (right) for different freestream velocities.

rotation angle and in the integral aerodynamic work amount to 14% and 19% respectively. Considering only the two finest settings of both parameters, i.e. target residuals 10^{-3} and 10^{-4} and time-step sizes 1.25×10^{-4} s and 6.25×10^{-5} s, the variations in each of the observed quantities are less than 5%. As the analysis is focused on evaluating aeroelastic stability and an exact resolution of the transient behaviour of the system is of a secondary interest, this variation is considered as sufficiently small and a further temporal refinement is not performed. The results presented below were obtained with $\Delta t = 1.25 \times 10^{-4}$ s and a terminating inner-cycle residual 10^{-4}.

Let us consider the temporal refinement study in view of the results obtained for the harmonically oscillating airfoil. As shown in Sec. 6.1.2, a change of temporal refinement from 100 to 200 time-steps per period alters the prediction of aerodynamic work per cycle by less than 0.09%. In the case of the fluid-structure coupled computations, the change of aerodynamic work with Δt reduced from 1.25×10^{-4} s ($\approx$ 900 time-steps per period) to 6.25×10^{-5} s ($\approx$ 1800 time-steps per period) is 3.8%. Hence the variation is approximately 40 times higher, in spite of employing a nearly 10 times finer temporal discretisation.

Figure 6.13 shows the temporal evolution of the aeroelastic system for different freestream velocities. The vertical displacement of elastic axis is shown on the left and the pitching angle on the right. The motion is monitored for a duration of 0.7 s, commencing at $t = 0$ s by releasing the airfoil from the fixed position defined by $y_{EA} = 0.05$ m and $\phi = 6°$. With the lowest setting of the freestream velocity, $u_{FS} = 30\,\mathrm{m\,s^{-1}}$, the system is damped and the amplitudes of vertical displacement and pitching angle both converge quickly to zero. A similar behaviour is observed when the freestream velocity rises to $35\,\mathrm{m\,s^{-1}}$, with the difference that the system becomes less damped and converges to the equilibrium position less rapidly.

The damping is sufficient to attenuate oscillations also for $u_{FS} = 40\,\mathrm{m\,s^{-1}}$, yet the vertical displacement and the pitching angle grow in time. This is a manifestation of

a static aeroelastic phenomenon called torsional divergence. Torsional stiffness of the structure is overcome by aerodynamic loading generated with the increment in angle of attack. Naturally, torsional divergence occurs also in the other two cases with even higher freestream velocities. The exponential departure from equilibrium position is accelerated with increased flow velocity. Moreover, the oscillations become less damped, indicating that flutter conditions are approached. As the effect is combined with torsional divergence, it is not clear whether the oscillations have already become unstable at $42.5\,\mathrm{m\,s^{-1}}$ or $45\,\mathrm{m\,s^{-1}}$.

Note that for the two highest freestream velocities, the pitching angle travels past the stall angle, reported experimentally at approximately 16° for a steady state flow [160]. When stall occurs, the flow no longer remains attached to the airfoil surface and separates, inducing a significant drop of lift force. The inviscid flow model is incapable of capturing such effects accurately, hence the temporal evolutions may no longer be regarded as physically correct once the stall angle is exceeded. Therefore, they are marked with a dash-dotted line in the figure.

The present predictions of aeroelastic stability with varying freestream velocity agree well with the numerical results reported by Sváček et al. [174] and by Honzátko [95]. A NASTRAN prediction is also given in both publications, stating that torsional divergence should occur at $u_{FS} = 37.7\,\mathrm{m\,s^{-1}}$ and flutter at $u_{FS} = 42.4\,\mathrm{m\,s^{-1}}$, which is consistent with the present results.

6.2 Tenth Standard Configuration

One of the key aspects of aeroelastic modelling in turbomachinery applications is the implementation of boundary conditions that prevent wave reflections from the artificial inlet and outlet boundaries. In the present work, the Spectral NRBC of Schlüß et al. [158] is employed. Due to the complexity of its formulation, it is vital to verify that it is implemented correctly. A convenient test-case for this purpose is the Tenth Standard Configuration (STCF10) from the collection of turbomachinery flutter experiments formed in the 1980's at École Polytechnique Fédérale de Lausanne. The Tenth Standard Configuration represents a two-dimensional compressor cascade operating at subsonic inlet and outlet conditions. The geometries and experimental data were made public in [49] and they are partly available in a digitized form at [47]. Although there are no experimental data available in the open literature, numerical results of other authors can be used as a reference (e.g. [186, 146, 157]).

There are several reasons that render STCF10 as a particularly suitable application for testing the boundary condition implementation. Most importantly, Schlüß and Frey, the authors of the Spectral NRBC, have recently applied it to this test case and published the results in [157]. A direct comparison with the present implementation can thus be performed. Schlüß and Frey considered subsonic operating conditions, which reduces the complexity of flow field solution in comparison with transonic applications and highlights the role of boundary condition treatment. More over, this test-case is prone to artificial wave reflections from boundaries [146] and reveals

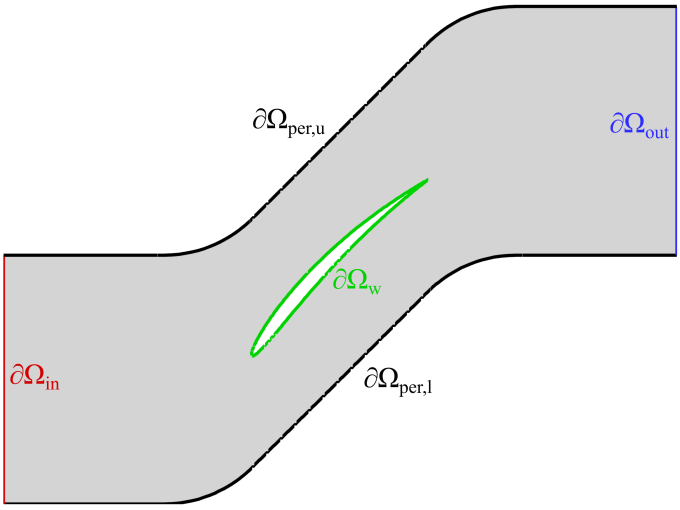

Figure 6.14: Single-blade computational domain of STCF10

thus any deficiency in the reflection properties of boundary conditions. Any major discrepancy between the present results and [157] would most likely indicate an error in the Spectral NRBC implementation, whereas a good agreement would give a high level of confidence in its correctness.

The compressor cascade is formed by modified NACA 0006 profiles whose definition is together with operating conditions provided in [49]. The blades are positioned at a stagger angle $\delta = 45°$ with a spacing equal to their chord. A single blade is included in the computational domain for steady-state simulations. In flutter computations, the number of blades is varied in function of the interblade phase angle (IBPA) so as to achieve direct periodicity between the $\partial\Omega_{per,l}$ and $\partial\Omega_{per,u}$ boundaries (Fig. 6.14). In order to maintain consistency with the work of Schlüß and Frey [157], the inlet and outlet boundaries $\partial\Omega_{in}$, $\partial\Omega_{out}$ are located at a distance of one chord from the blades.

The operating conditions in [49] are specified for two configurations with inlet Mach numbers 0.7 and 0.8. The present analysis adopts the lower setting, for which the flow conditions remain subsonic in the entire domain. Only the inlet Mach number and flow angle are specified [49], whereas the numerical solution requires the definition of total conditions and flow angle at the inlet and static pressure at the outlet. The inlet total conditions were set to $T_{01} = 293.15\,\text{K}$, $p_{01} = 101\,325\,\text{Pa}$, while the outlet static pressure $p_2 = 88\,499\,\text{Pa}$ was determined iteratively so as to achieve the target inlet Mach number. The working medium is an ideal gas approximating dry air with $R = 287\,\text{J}\,\text{kg}^{-1}\,\text{K}^{-1}$ and $\gamma = 1.4$. An overview of relevant test-case parameters is provided in Tab. 6.5.

The solver setup was adopted from the NACA 0012 simulations, employing the implicit integration scheme with local time-stepping and implicit residual smoothing and the limiting procedure of Delis et al. with the MinMod limiter. A notable alteration was made in the weighted least squares reconstruction of gradients. The initial setting of the inverse distance weighting exponent $k = \frac{3}{2}$ caused solver divergence in the blade trailing edge area, which was resolved by reducing the value to $k = 1.0$.

Parameter	Symbol	Unit	Value
Blade chord	C	[m]	0.1
Blade spacing (pitch)	P	[m]	0.1
Stagger angle	δ	[°]	45
Inlet Mach number	M_1	[-]	0.7
Inlet flow angle	β_1	[°]	55
Inlet total pressure	p_{01}	[Pa]	101325
Inlet total temperature	T_{01}	[K]	293.15
Outlet static pressure	p_2	[Pa]	88499
Specific heat ratio	γ	[-]	1.4
Specific gas constant	R	$[\mathrm{J\,kg^{-1}\,K^{-1}}]$	287
EA position (chordwise coord.)	ξ_{EA}	[m]	$0.5C$
EA position (chord-normal coord.)	η_{EA}	[m]	$0.05C$
Pitching amplitude	$\Delta\alpha$	[°]	1
Reduced frequency	$\tilde{\omega}$	[-]	0.5
Frequency	f	[Hz]	382.356

Table 6.5: Overview of STCF10 parameters

Although this modification may in some cases decrease the accuracy of gradient reconstruction, it is still sufficient to provide the target second-order accurate flux evaluation [175]. The CFL number was set to 3.0.

6.2.1 Steady-State Flow

The domain was discretised with unstructured triangular grids, generated in ANSYS® ICEM 19.1. Three discretisation levels were considered, reducing the cell size by a factor of 1.3 with each refinement. The cell-count per blade channel starts at 10477 on the coarsest level 1 mesh and increases to 16878 and 28585 with the level 2 and level 3 refinements respectively. All three mesh levels are shown in Fig. 6.15.

The suitable grid refinement level was determined by evaluating the variation of blade forces. The study employed the Exact Steady NRBC at the inlet and outlet boundaries. Convergence of the axial (F_x) and circumferential (F_y) aerodynamic forces with grid refinement is shown in Fig. 6.16. According to a Richardson extrapolation, both forces are quantified within 0.2% of converged value on the finest mesh. Moreover, the alteration in blade pressure distribution between the level 2 and level 3 solutions is virtually indiscernible. The finest grid was thus concluded to achieve a sufficient resolution and it was employed in further presented steady-state computations.

A comparison of the present simulation with numerical results reported by Petrie-Repar et al. [146] is provided in Fig. 6.17. The figure shows isentropic Mach number distribution on blade surface in function of normalized chord distance. The Tenth Standard Configuration was originally conceived as a two-dimensional test-case, but an extension to three dimensions was devised later. The present 2D inviscid solution

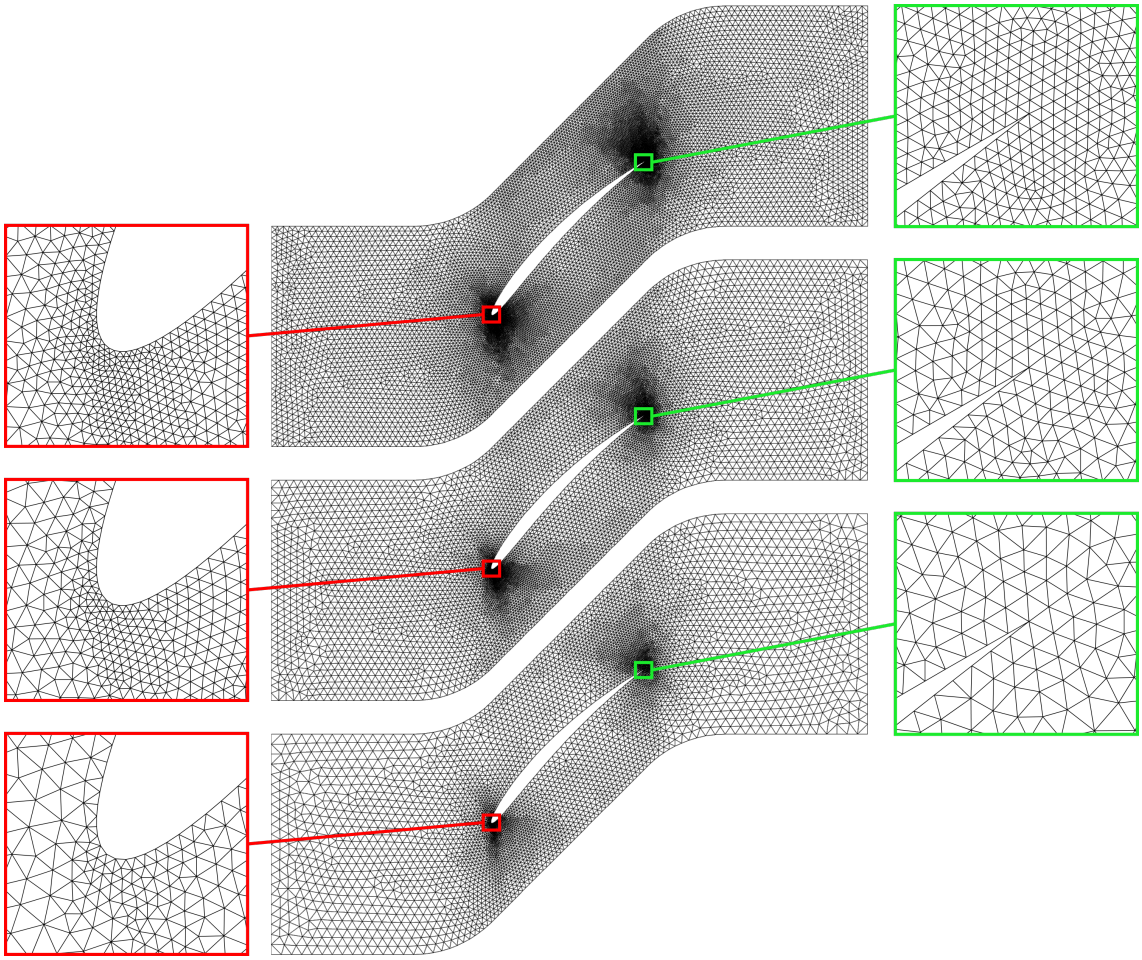

Figure 6.15: STCF10 single-blade domain discretisation with refinement levels 1, 2 and 3 from bottom to top

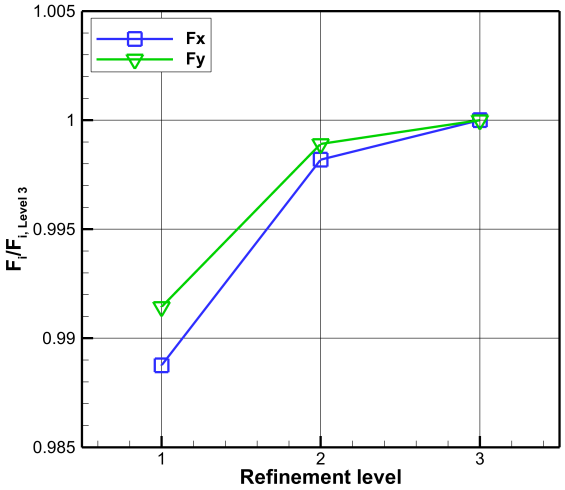

Figure 6.16: Axial (F_x) and circumferential (F_y) aerodynamic blade forces in function of grid refinement. Values normalized by the finest grid results.

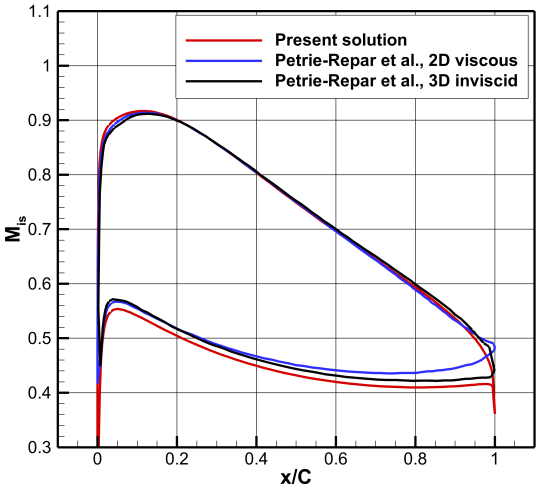

Figure 6.17: Isentropic Mach number distribution on blade surface. Present solution compared with numerical results of Petrie-Repar et al. [146].

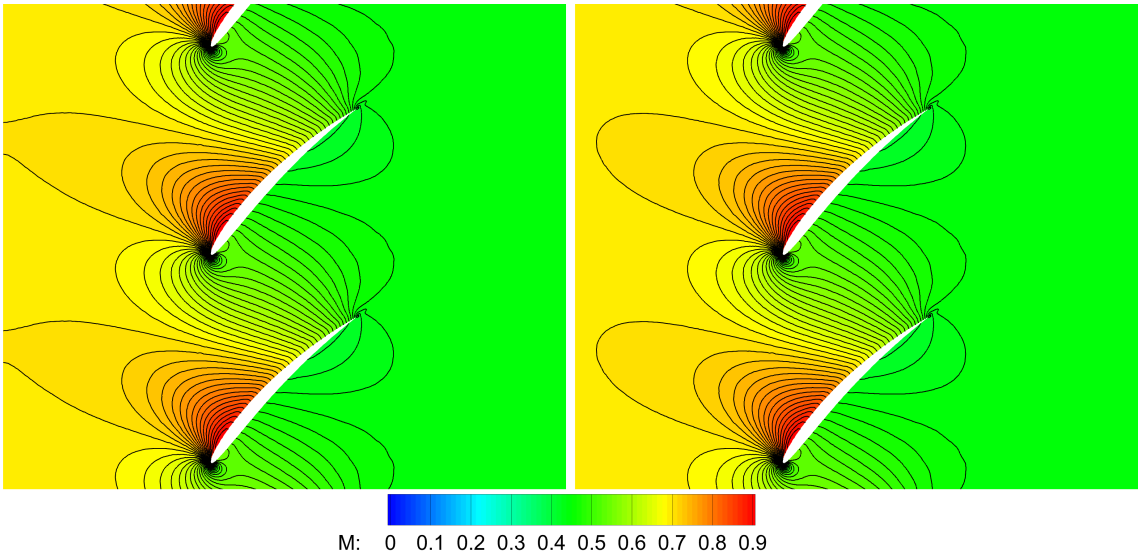

Figure 6.18: Mach number contours from a steady-state solution, obtained with the Simple Turbomachinery BC (left) and the Exact Steady NRBC (right).

is plotted together with the results of 2D viscous and 3D inviscid computations published by Petrie-Repar et al. There is a close agreement between the present results and the reported 3D inviscid solution. The only notable discrepancy is found in the nearly constant offset of $\Delta M_{is} \approx 0.012$ along the pressure side. This can be accounted to a slight difference in the pressure ratio adopted here and in the reference.

While the 2D and 3D inviscid simulations match closely, a more profound difference is observed with the inclusion of viscous flow effects. The isentropic Mach number distribution obtained by Petrie-Repar et al. with the 2D viscous model rises in the aft part of the blade pressure side, whereas both inviscid predictions yield a plateau in this region. The discrepancy between the viscous and inviscid predictions culminates at the trailing edge where it amounts to $\Delta M_{is} \approx 0.05$.

The solution plotted in Fig. 6.17 was obtained with the Exact Steady NRBC imposed at the inlet and outlet boundaries. Changing the boundary condition definition to the Simple Turbomachinery BC brings virtually no difference to the blade surface M_{is} distribution, hence the result is not included in the figure. The nearly perfect match between the two solutions is confirmed by plotting Mach number contours in Fig. 6.18. The only discrepancy is observed at the inlet boundary, where the Simple Turbomachinery BC distorts slightly the Mach number contours. The flow remains subsonic in the whole domain, reaching a peak Mach number 0.907 on the blade suction side at 12.5% chord.

6.2.2 Torsion Mode Oscillations

The Tenth Standard Configuration provides a set of flutter test-cases either in a torsion mode or in a chord-normal bending mode, each at four different reduced frequencies. The present analysis is performed for pitching oscillations at a reduced

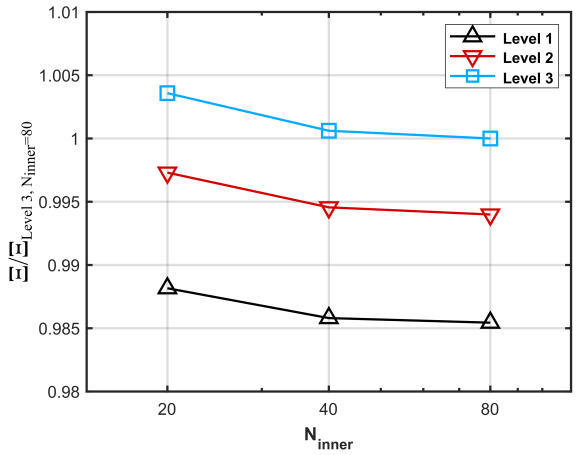

Figure 6.19: Convergence of the aerodynamic damping coefficient with grid refinement level and with the number of inner iterations for $\sigma = 0°$

frequency $\tilde{\omega} = 0.5$, referred to as cases 2 and 3 in the literature [49]. These two cases are characterised by interblade phase angles of 0° and 90° respectively, whereas the present simulations are conducted for the whole IBPA range with a step of 30°. The pitching axis is located at $[0.5C, 0.05C]$ in profile coordinates. The amplitude of the pitching motion is set to $\Delta\alpha = 1\,\text{deg}$ to be consistent with the setup adopted by Schlüß and Frey [157], in contrast to $\Delta\alpha = 2\,\text{deg}$ given in the original STCF10 definition [49]. Operating conditions are retained from the steady-state test case. For an overview of relevant parameters see Tab. 6.5.

The grid independence study shown in the previous section yielded the conclusion that the level 3 discretisation is sufficiently refined to resolve a steady-state flow. It remains to be verified whether this refinement is also sufficient for an accurate aeroelastic analysis. Additionally, a suitable time-step needs to selected. The temporal discretisation is refined consistently with the spatial one, increasing the number of time-steps per period also by the ratio of ≈ 1.3. Starting with 100 time-steps per period on the level 1 grid, this number is raised to 132 and 172 on the level 2 and 3 grids respectively. The variation of the aerodynamic damping coefficient Ξ with discretisation level is used as a measure for the required spatial and temporal refinement. The definition of Ξ for pitching oscillations from Eq. 4.78 is employed. The interblade phase angle of 0° is imposed and the Spectral NRBC is prescribed at the inlet and outlet boundaries.

Figure 6.19 shows convergence of Ξ with refinement level and with the number of inner-cycle iterations. On all three discretisation levels, 40 iterations are sufficient to achieve inner cycle convergence, as further doubling their number alters the predicted aerodynamic damping by less than 0.07%. According to a Richardson extrapolation, computation on the finest discretisation level yields aerodynamic damping prediction with an error of $\approx 0.5\,\%$, which is sufficient for the present investigation. All results presented further in this section were obtained on the level 3 grid.

The predicted aerodynamic damping is plotted in Fig. 6.20 in function of the interblade phase angle. Due to the lack of available experimental data for this test-case, two sets of numerical results of other authors are included instead as a reference.

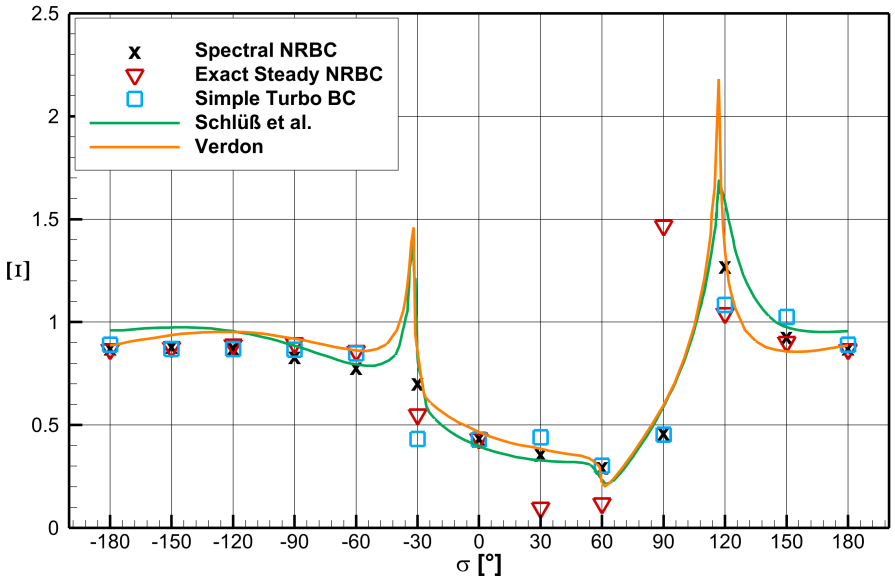

Figure 6.20: Aerodynamic damping curve, present computations with different boundary conditions and results of Schlüß et al.[157] and Verdon [186].

The data reported by Verdon [186] were obtained by solving linearised unsteady aerodynamic theory which considers the unsteady flow as a small perturbation to a fully nonuniform isentropic and irrotational background steady flow. More recently, Schlüß et al.[157] published results from a nonlinear unsteady solver based on RANS equations with a laminar to turbulent transition model. Importantly, they applied the Spectral NRBC at the inlet and outlet boundaries, providing thus a reference for the validation of its present implementation. Both datasets match well and predict two distinct peaks in aerodynamic damping at $\sigma \approx -30°$ and $\sigma \approx 120°$, ascribed to acoustic resonance [157]. The close agreement between the reference numerical predictions provides confidence in their correctness, especially considering that it was achieved in spite of employing two substantially different models.

The present computations were performed with three different boundary condition formulations for inflow and outflow. The Simple Turbomachinery BC imposes uniform total conditions at the inlet and average static pressure at the outlet, without applying any non-reflecting treatment. The other two boundary conditions aim to suppress reflections of perturbations, using the theory of Giles [58] based on linearised Euler equations. Only spatial flow perturbations are considered in the Exact Steady NRBC, whereas the Spectral NRBC treats also the temporal ones. Flow linearisation should not represent a severe limitation for the performance of non-reflecting boundary conditions in this case, as the flow is subsonic and the blade vibration amplitude is small.

The aerodynamic damping curve obtained with the Spectral NRBC matches very well the reference results. For some IBPAs, the predictions are closer to those of Schlüß et al., while for others a better match with Verdon's results is achieved. This can be accounted to the fact that the present computational model shares some features with either of the references. Fully nonlinear unsteady flow equations, a time-marching solution procedure and the Spectral NRBC are employed similarly to

Schlüß et al., whereas an inviscid flow assumption is shared with Verdon. Crucially, the agreement between the present and the reference results holds also in the vicinity of acoustic resonance peaks in aerodynamic damping, found at $\sigma \approx -30°$ and $\sigma \approx 120°$. Here the correct suppression of wave reflections is especially important, as manifested by the poor performance of the Simple Turbomachinery BC and the Exact Steady NRBC. In contrast, it plays a less significant role in the case that both the inlet and outlet pressure waves are cut-off. This is observed in the IBPA range $\sigma \approx -180°$ to $\sigma \approx -60°$ where all three boundary conditions give consistent results. Overall, the Simple Turbomachinery BC deviates less from the Spectral NRBC predictions (up to 39 %) than the Exact Steady NRBC (up to 215 %). Both of them fail to capture the acoustic resonance peaks.

A representative set of IBPAs $-90°$, $0°$ and $120°$ was selected for a closer examination of the results. Figure 6.21 shows snapshots of instantaneous pressure fluctuations for the three IBPAs and the three boundary condition formulations. The fluctuations are expressed in terms of a coefficient

$$\tilde{C}_p(\boldsymbol{x}, t) = \frac{p(\boldsymbol{x}, t) - \overline{p}(\boldsymbol{x})}{\Delta\alpha(p_{01} - p_2)}, \tag{6.4}$$

where $\overline{p}(\boldsymbol{x})$ is the local time-average of pressure over a period of oscillation. The instantaneous pressure contours are supplemented with Fig. 6.22 showing the unsteady pressure distribution on blade surface, in terms of the amplitude (left) and phase (right) of the first harmonic coefficient.

The case of $\sigma = -90°$ falls in the IBPA range where both the upstream and downstream pressure waves are cut-off and all three boundary conditions yield consistent values of the aerodynamic damping coefficient. With this particular IBPA, the predictions agree within 7%. Also the first pressure harmonic distributions in Fig. 6.22a match closely, showing the same trends and only a minor offset. Examination of the pressure fluctuation contours in Fig. 6.21a, however, reveals the performance of the Exact Steady NRBC and the Simple Turbomachinery BC to be unsatisfactory. Pronounced pressure wave reflections are formed at the outlet boundary, and to a lesser extent also at the inlet boundary. In contrast, no distinctive wave reflections are observed with the Spectral NRBC.

When all blades oscillate in phase, i.e. $\sigma = 0°$, both the upstream and downstream pressure waves are cut-on and travel perpendicularly to the inlet and outlet boundaries [157]. The Exact Steady NRBC and the Simple Turbomachinery BC yield a virtually identical flow solution, as evidenced by the pressure distribution on the blade as well as in the whole domain. The agreement is so close that the first pressure harmonic plots in Fig. 6.22b overlap and the aerodynamic damping coefficient is evaluated within 1%. The difference in damping quantification between these two boundary conditions and the Spectral NRBC is relatively minor at 2.7%, but the agreement is limited to the integral value. There is an offset of $40°$ to $60°$ in resolving the phase on the blade pressure side (Fig. 6.22b) and the contours of instantaneous pressure fluctuations are qualitatively different (Fig. 6.21b).

Acoustic resonance conditions occur near the $\sigma = 120°$, producing a peak in the

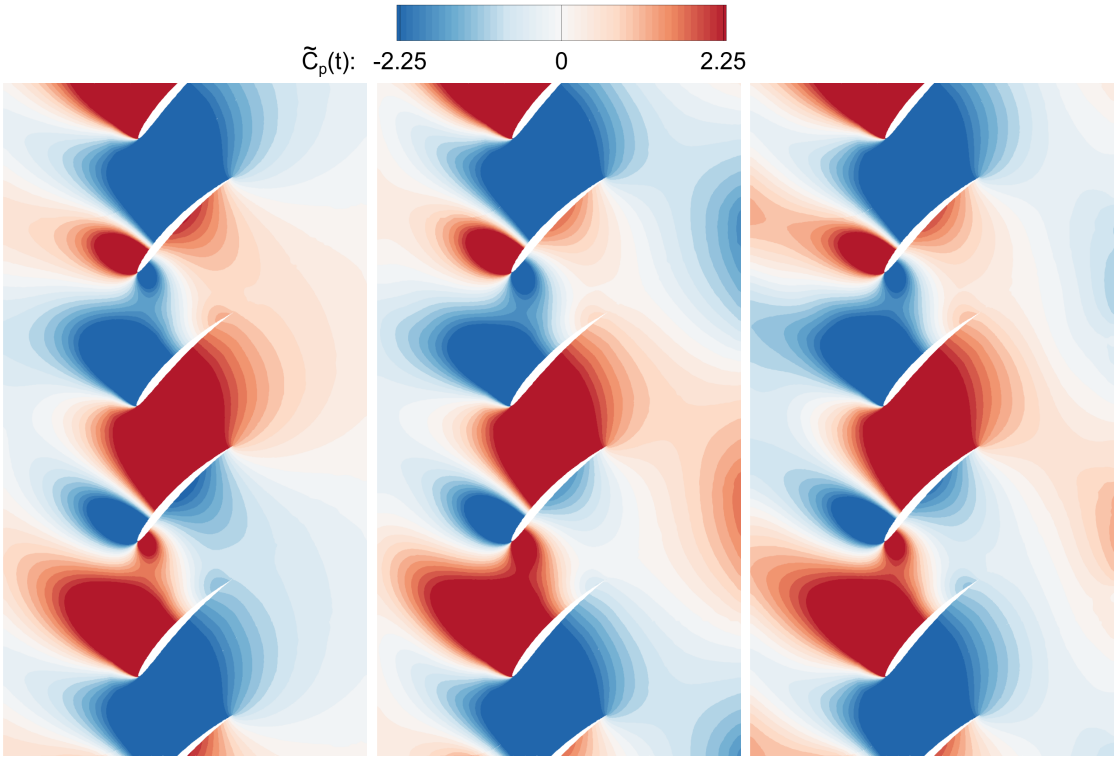

(a) $\sigma = -90°$

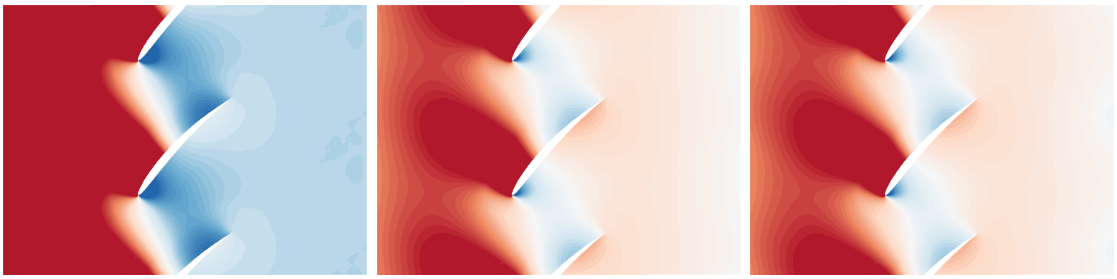

(b) $\sigma = 0°$

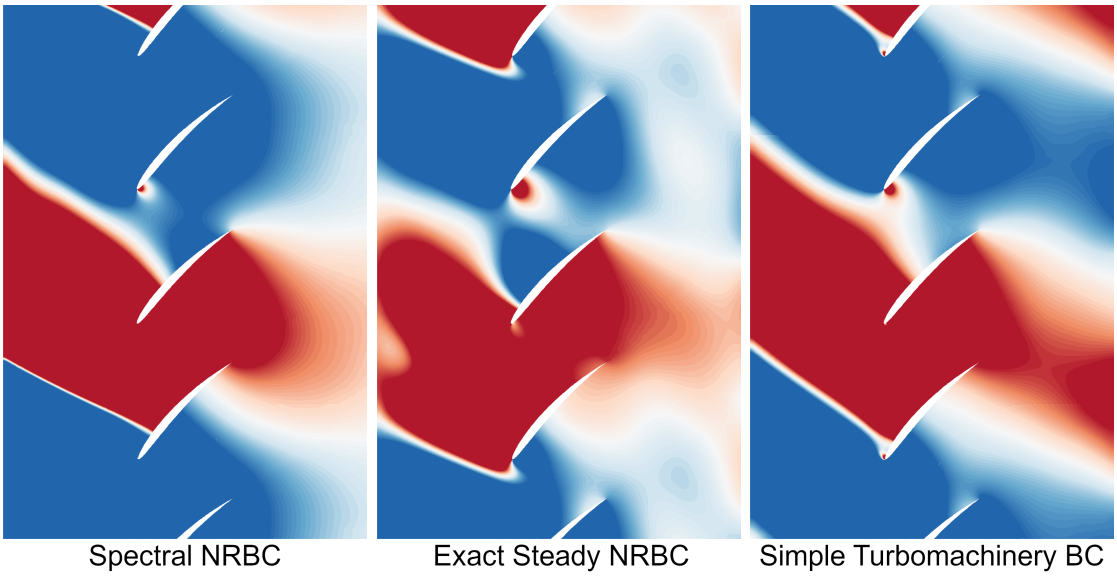

(c) $\sigma = 120°$

Figure 6.21: Contours of instantaneous unsteady pressure fluctuations.

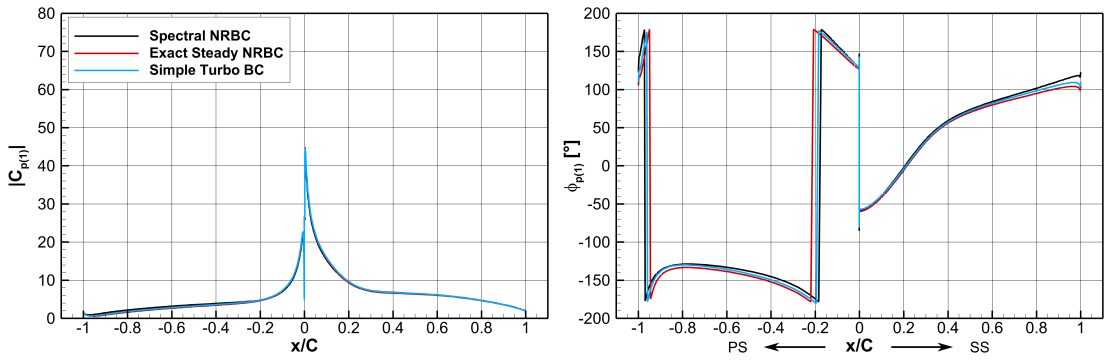

(a) $\sigma = -90°$

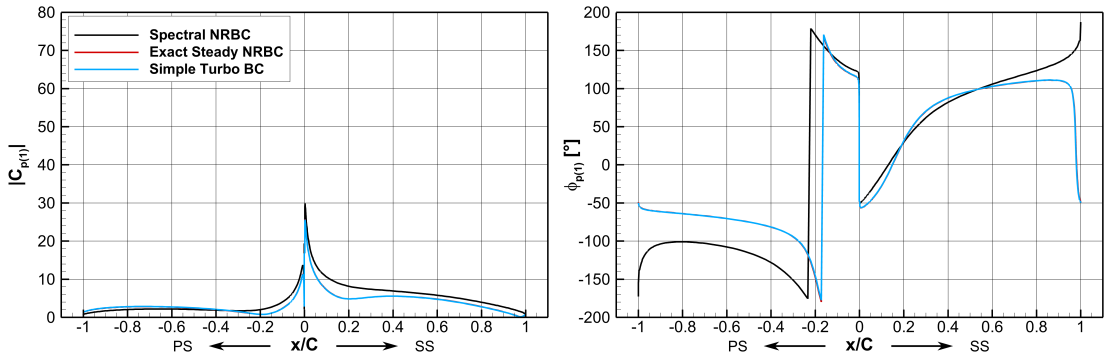

(b) $\sigma = 0°$

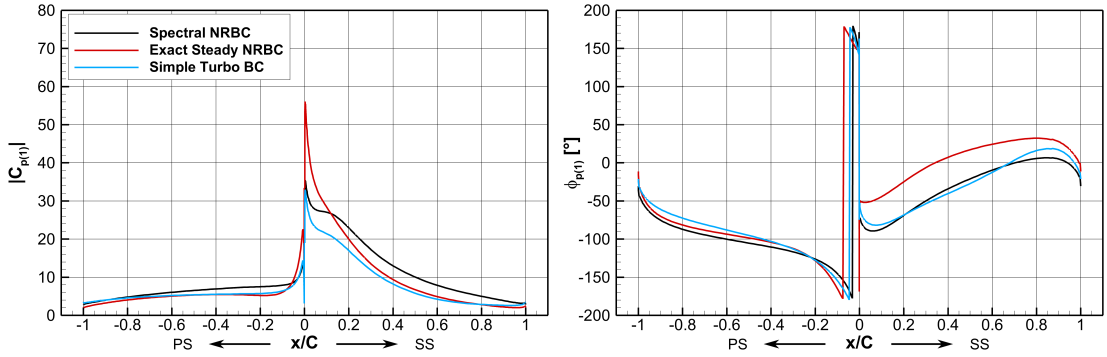

(c) $\sigma = 120°$

Figure 6.22: Distribution of amplitude ($|C_{p(1)}|$, left) and phase ($\phi_{p(1)}$, right) of the 1^{st} unsteady pressure harmonic on blade surface.

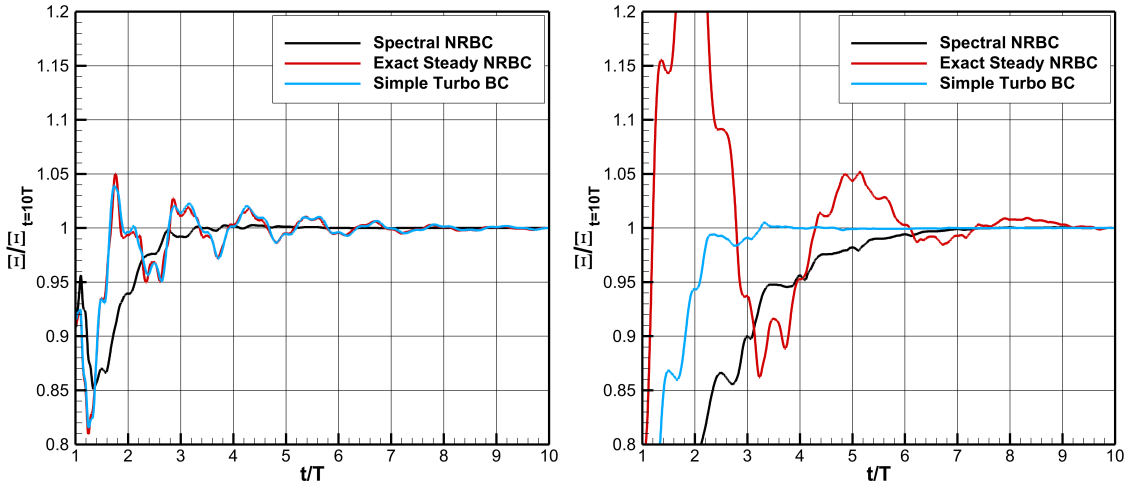

(a) $\sigma = 0°$ (b) $\sigma = 120°$

Figure 6.23: Convergence of the aerodynamic damping coefficient

aerodynamic damping curve. The downstream pressure wave is cut-off, whereas the upstream wave is on the verge of propagating. This is evidenced by the contours of pressure fluctuations obtained with the Spectral NRBC (Fig. 6.21c). The perturbation propagating towards the inlet has a nearly straight wave-front, whereas the downstream wave is curved and dissipates quickly. The other two boundary conditions perform poorly in suppressing the wave reflections and introduce a significant distortion into the pressure field, contaminating thus the solution far into the interblade channels. Both the amplitude and the phase of unsteady blade pressure distribution are affected to a greater extent on the suction side than on the pressure side (Fig. 6.22c).

The Spectral NRBC has been reported to exhibit slower convergence in comparison with other approaches, such as one-dimensional and approximate non-reflecting boundary conditions [156]. However, this behaviour wasn't observed in the present test-case. Two examples of a temporal evolution of the aerodynamic damping coefficient Ξ are provided in Fig. 6.23 for IBPAs 0° and 120°. The damping coefficient is normalised by the value reached after 10 periods of oscillation T. In the case that all blades oscillate in phase, the Spectral NRBC achieves the fastest convergence, with Ξ arriving within 0.1% of the converged value after 5 periods of oscillation (Fig. 6.23a). In contrast, the temporal evolutions obtained with the other two boundary conditions are characterised by fluctuations with a slowly diminishing amplitude. In the case of $\sigma = 120°$ (Fig. 6.23b), the fastest convergence is observed for the Simple Turbomachinery BC, requiring 5 periods for the 0.1% convergence, whereas 7 periods are needed for the Spectral NRBC. The Exact Steady NRBC manifests strong fluctuations in the temporal development of the damping coefficient, similarly to the previous case.

The two examples shown in Fig. 6.23 are illustrative of the convergence behaviour experienced generally in this application. The Spectral NRBC performs consistently for all IBPAs and exhibits no stability issues. Although the two other boundary conditions provide faster convergence in a few cases, they suffer from slowly vanishing

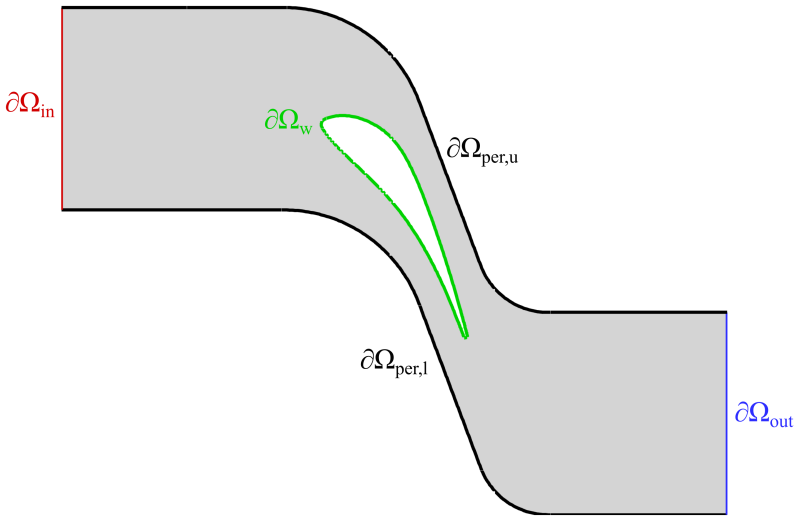

Figure 6.24: STCF4 single-blade computational domain

fluctuations in others. This can be accounted to the poor suppression of reflections inhibiting the convergence.

6.3 Fourth Standard Configuration

The Fourth Standard Configuration (STCF4) is another turbomachinery flutter test-case from the collection of EPFL [49]. Experimental data are publicly available at [47], providing thus a reference for the validation of the present computational model. The experimental rig featured a non-rotating annular low-pressure turbine cascade with 20 blades. The inflow remained subsonic in all tested operating conditions, while the exit flow ranged from subsonic to supersonic. The following analysis focuses on Test Case 628 with a supersonic outflow. Due to the presence of shockwaves in the transonic flow field, this is a challenging test-case for the non-reflecting boundary conditions as well as for the whole computational model. The present results are an updated and extended version of the findings published by the author in [3, 2].

The computations were performed on a 2D domain, obtained from the 3D experimental geometry by performing a circumferential section at blade midspan. The resulting computational domain with the inlet and outlet boundaries positioned at the distance of one chord from the blade is shown in Fig. 6.24. Its axial extent was varied in the present investigation to assess the effect on the flow solution. The domains will be further denoted according to the inflow and outflow boundary positions, such that e.g. 0.5C1C refers to a domain with the inlet located at $0.5C$ upstream of the blade leading edge (LE) and the outlet at $1C$ downstream of the trailing edge (TE).

Operating conditions reported in the documentation of the measurements [47] comprise the inlet total pressure p_{01}, the inlet flow angle β_1 and the outlet static pressure p_2. However, the inlet total temperature T_{01} is not specified. This study uses the setting $T_{01} = 330\,\mathrm{K}$ as adopted by Waite [191]. He notes that although the actual

Parameter	Symbol	Unit	Value
Blade chord	C	[m]	0.072
Blade spacing (pitch)	P	[m]	0.05625
Stagger angle	δ	[°]	-56.6
Inlet total pressure	p_{01}	[Pa]	217100
Inlet total temperature	T_{01}	[K]	330
Inlet flow angle	β_1	[°]	-28
Outlet static pressure, steady	$p_{2,st}$	[Pa]	69200
Outlet static pressure, oscillations	$p_{2,oscil}$	[Pa]	66200
Specific heat ratio	γ	[-]	1.4
Specific gas constant	R	$[\mathrm{J\,kg^{-1}\,K^{-1}}]$	287

Table 6.6: Overview of STCF4 parameters

experimental value was probably closer to $T_{01} = 360\,\mathrm{K}$, the effect of this discrepancy on the resolution of Mach number and flow angle seems to be negligible. The flow solution is more sensitive to the inlet flow angle, whose value $\beta_1 = 12°$ is provided, but it was found to yield a rather poor agreement with the measurements in subsequent computational studies according to Waite. This discrepancy was ascribed to the upstream pressure probe being placed too close to the blade LE (5 mm) in the experimental rig, causing the measurements to be obtained with an error. Waite reports that imposing $\beta_1 = 28°$ produces a better match with the experiments, hence this value was adopted in the present work. The ideal gas model with $R = 287\,\mathrm{J\,kg^{-1}\,K^{-1}}$ and $\gamma = 1.4$ was employed for the working fluid. Relevant test-case parameters are listed in Tab. 6.6.

In contrast to the NACA 0012 (Sec. 6.1) and STCF10 (Sec. 6.2) test-cases, the flow field of the Test Case 628 of STCF4 is transonic and features distinct shock-waves. The presence of steep gradients implies that the choice of a limiting strategy in the gradient reconstructing procedure plays an important role. The sharpness of shockwave resolution as well as the rate of convergence are affected. A set of different limiters was therefore tested on a steady flow solution and the most favourably performing one was subsequently adopted in unsteady simulations. The study also concentrates on the behaviour of different boundary condition formulations, comparing the Simple Turbomachinery BC, the Exact Steady NRBC, and for the unsteady analysis also the Spectral NRBC. The time-marching procedure employed the implicit integration scheme with local time-stepping and implicit residual smoothing and the least-squares gradient reconstruction adopted the setting of inverse distance weighting exponent $k = 1.0$. The CFL number 3.0 was used throughout in the computations.

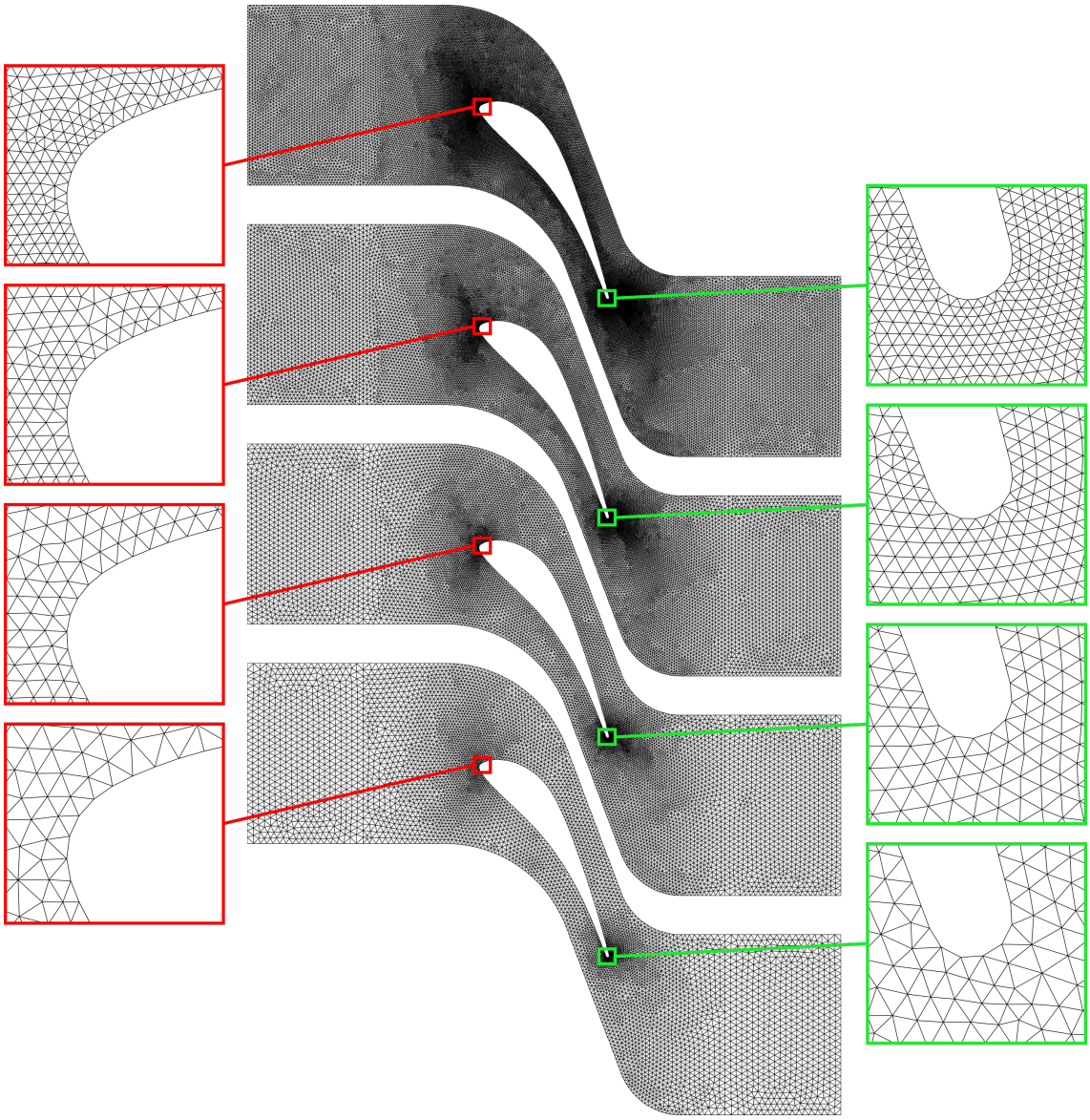

Figure 6.25: STCF4 single-blade domain discretisation with refinement levels 1 to 4 from bottom to top. Inlet and outlet boundaries positioned at 1 chord from blades.

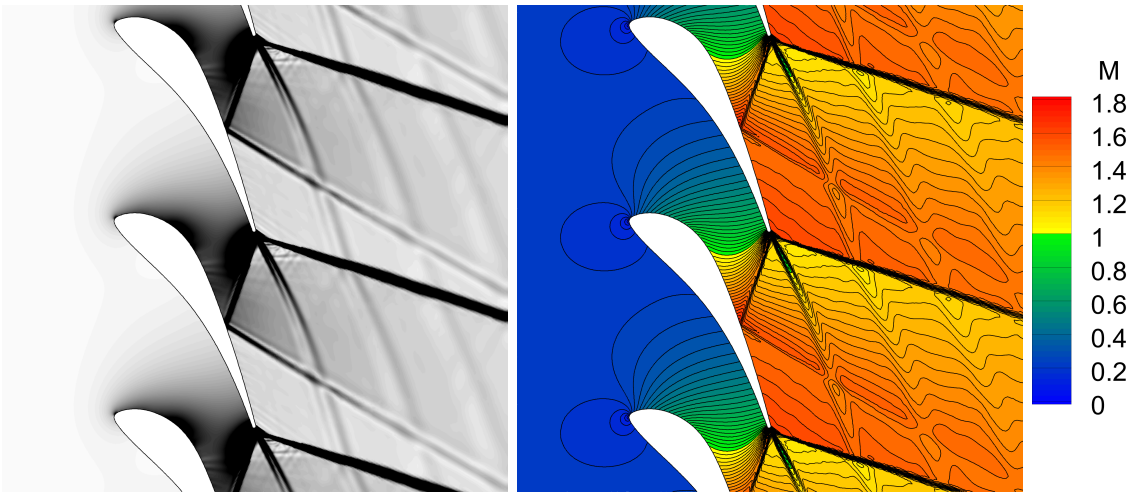

Figure 6.26: Pseudo-schlieren image (left) and Mach number contours (right) on the level 4 grid.

6.3.1 Steady-State Flow

Grid Independence Study

The commercial grid generator ANSYS® ICEM 19.1 was employed to discretise the domain with unstructured triangular grids. The grid independence study was performed on four refinement levels of the 1C1C domain, imposing the Exact Steady NRBC at the inlet and outlet boundaries. In each transition to the next refinement level, the cell dimension was reduced by a factor of 1.3. The cell-counts amount to 12340, 20119, 33415 and 58892 when listed from the coarsest (level 1) to the finest (level 4) discretisation. The meshes are shown in Fig. 6.25 with insets zooming on the LE and TE regions.

Flow solution on the finest grid is presented in Fig. 6.26. On the left, contours of density gradient mimicking a schlieren photography highlight the presence of shockwaves in the flow field. On the right, Mach number contours are plotted in a colormap discerning between subsonic and supersonic regions. The inlet flow field is subsonic at $M \approx 0.21$ and highly uniform. The flow is accelerated in the blade passage and reaches a peak Mach number 1.7 before encountering a right-running shockwave that emanates from the upper blade TE. The shockwave impinges on the suction side (SS) of the lower blade at $\approx 60\%$ chord and its reflection propagates towards the outlet at an angle of $-32°$ from axial direction. A left-running shockwave also forms at the TE and propagates downstream at $-18°$. Another non-uniformity represent blade wakes, constituting a perturbation in density and temperature, but not in pressure. Only very slight shockwave reflections from the outlet boundary can be discerned in the pseudo-schlieren plot. This indicates that the Exact Steady NRBC formulation is effective, although unable to suppress all reflections completely.

Figure 6.27 shows that the effect of grid refinement on the flow solution is limited to the sharpness of shockwave resolution. Pressure coefficient on blade surface is plotted in function of chord and exhibits negligible variation with refinement everywhere but

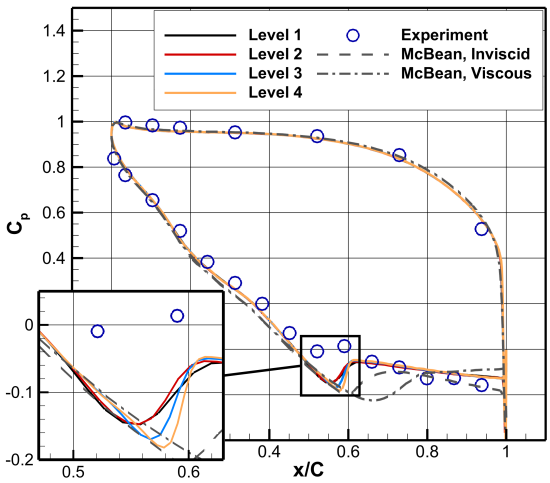

Figure 6.27: Distribution of pressure coefficient on blade surface with different grid refinement levels. Experimental data from [47], McBean's results from [128].

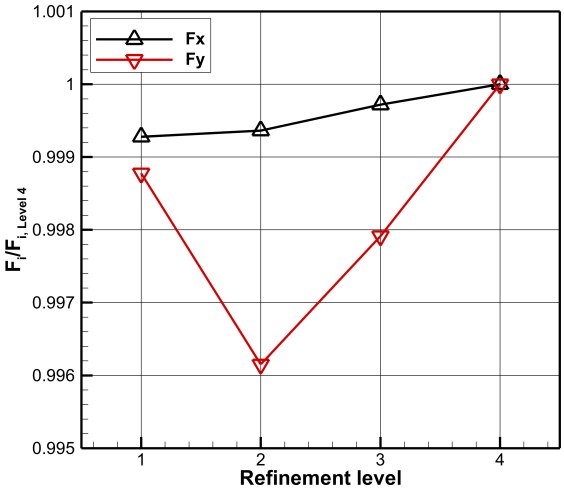

Figure 6.28: Axial (F_x) and circumferential (F_y) aerodynamic blade forces in function of grid refinement. Values normalized by the finest grid results.

in the vicinity of shockwave impingement at $\approx 60\,\%$ SS. Here the distribution reaches a local minimum, followed by a pressure rise and a plateau that extends until the trailing edge. On the coarser grids, the pressure distribution becomes smeared and the minimum less distinct. A mild variation can be observed even between the two finest mesh levels, indicating that a further refinement might be needed to obtain a fully converged solution.

The computed blade pressure distribution is compared with the results of inviscid and viscous simulations published by McBean et al. [128] and with measurements from [47]. All datasets are in a close agreement on the whole pressure side and on a portion of the suction side upstream of the shockwave impingement. The present solution matches the experimental data also in terms of the shock position at $\approx 0.6C$, but the pressure levels immediately before and after the shock are underpredicted. Further downstream, the agreement with experimental data is renewed. Both numerical solutions published by Waite et al. also exhibit this local pressure underprediction, but they additionally deviate in the shock impingement position. It is predicted to occur at different positions by the inviscid and viscous models, but in both cases further downstream captured by the measurements.

The sharpness of shock resolution affects the evaluation of integral aerodynamic forces acting on the blade. However, as shown in Fig. 6.28, the influence is only minor. The variation of axial and circumferential forces on the four mesh levels amounts respectively to $0.07\,\%$ and $0.39\,\%$ overall and to $0.03\,\%$ and $0.21\,\%$ in the final refinement. Even on the coarsest grid, the flow-field prediction is qualitatively consistent with the finest one.

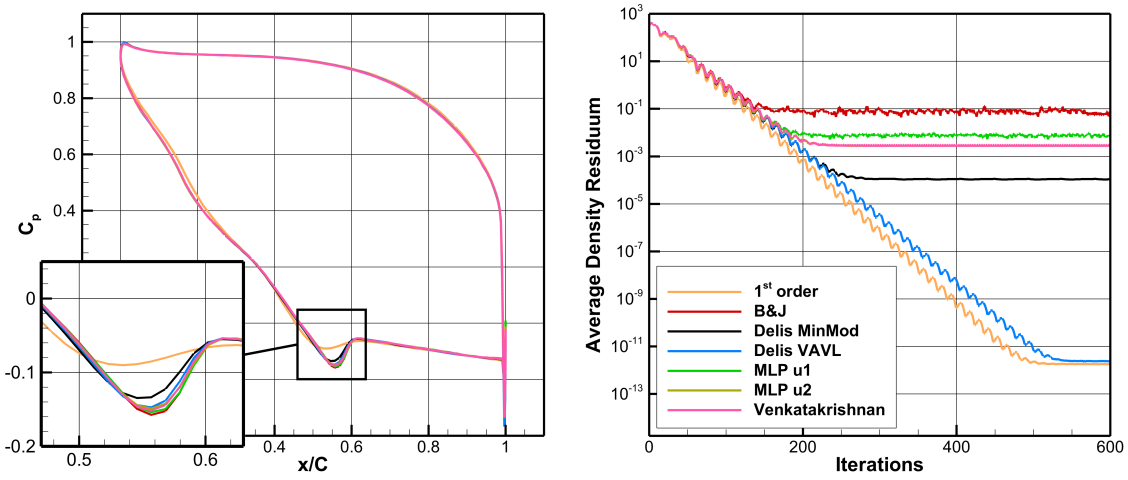

Figure 6.29: Blade surface pressure coefficient distributions (left) and convergence histories (right) obtained with different limiters.

Flux Limiter Comparison

The resolution of discontinuities, such as shockwaves, is affected by the gradient limiting strategy employed in the evaluation of inviscid fluxes. The method of Barth and Jespersen [8], its modification by Venkatakrishnan [185], two variants of the face-based approach of Delis et al. [35] and two variants of the Multidimensional Limiting Process by Park et al. [142, 141] are implemented in the solver. Their comparison is presented in this section, focusing on the sharpness of shockwave resolution and on convergence behaviour. All computations were performed on the level 2 mesh.

Figure 6.29-left show pressure coefficient distributions on blade surface, obtained with the six different limiters. Additionally, the result of a first order solution is shown, in which the gradient reconstruction step is omitted and the cell-center values are used directly in flux evaluation. The highly dissipative first order method nearly failed to register the local pressure minimum induced by the impingement of the right running TE shockwave on the SS. The sharpness of the shockwave signature also highlights the differences between the individual gradient limiting methods, negligible elsewhere on the blade. Although the location of the pressure minimum is captured consistently, its magnitude varies depending on the employed limiter. The sharpest resolution was obtained with the Barth and Jespersen technique, whereas the MinMod variation of the method devised by Delis et al. is shown to be the most dissipative. The other limiters are found in between of those two in terms of dissipativeness, but rather closer to the method of Barth and Jespersen.

While the Barth and Jespersen limiter achieved the sharpest resolution of discontinuities, it suffered from a poor convergence behaviour. As shown in Fig. 6.29-right, the average density residuum decreased by less than four orders of magnitude before its convergence stalled. This well-known shortcoming of the limiter is caused by its activity in smooth flow regions triggered by numerical noise, as described for example by Haselbacher [78]. Venkatakrishnan's modification addresses this issue to some extent and achieves a further reduction of the residuum by one and a half orders of magnitude with the setting $K = 10$. The value of this constant was varied,

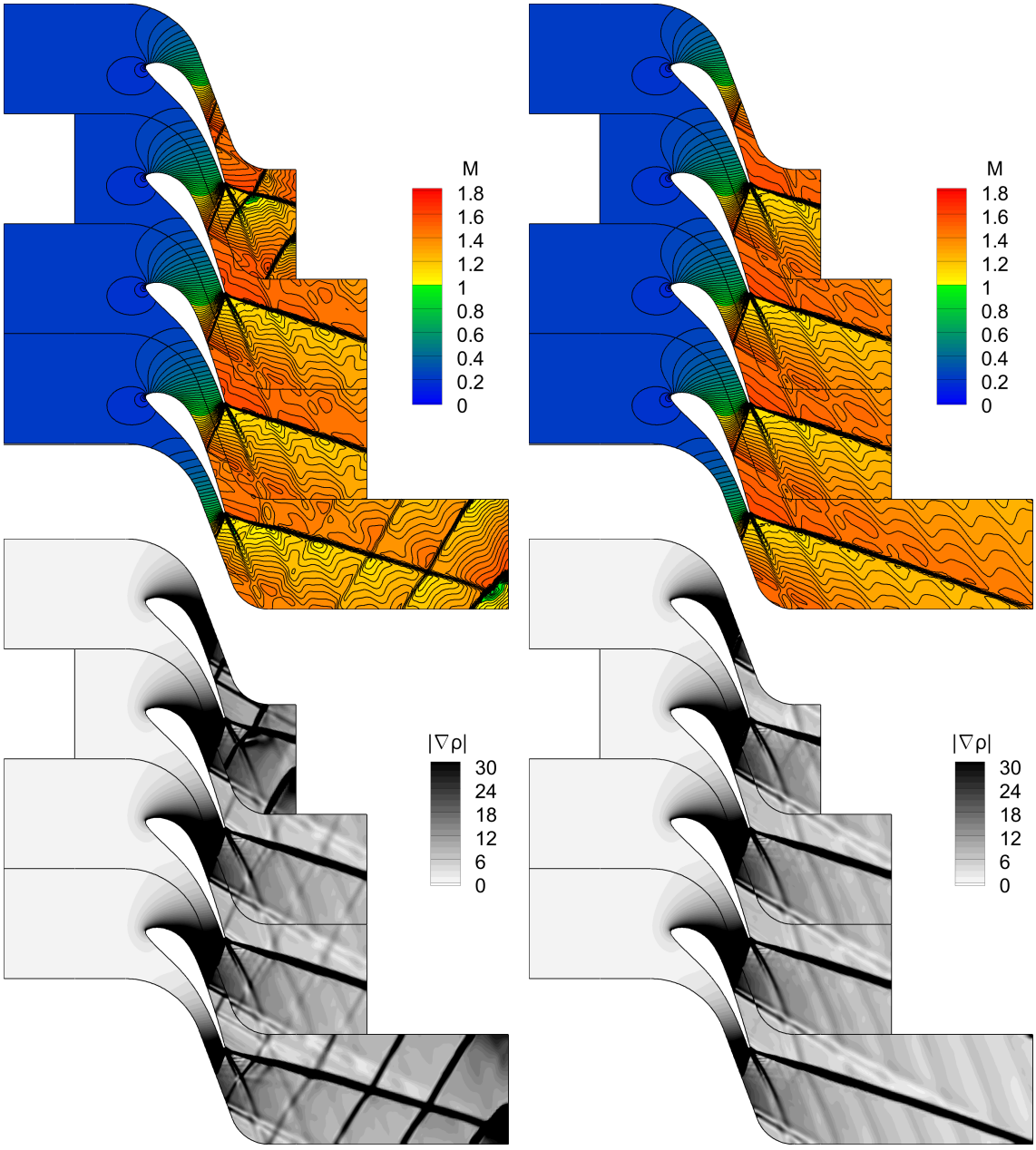

(a) Simple Turbomachinery BC (b) Exact Steady NRBC

Figure 6.30: Contours of Mach number (top) and density gradient (bottom) on domains with different axial extents. Domains from top to bottom: 1C0.5C, 0.5C1C, 1C1C and 1C2C.

but no major improvement of convergence was observed. Since the need for tuning K in each test-case individually is impractical, the effect of its variation was not investigated further. The MLP derives from the limiters of Barth and Jespersen and of Venkatakrishnan in its $u1$ and $u2$ variants respectively. In both cases, the convergence behaviour was similar to that of the original limiters. A notably improved performance was achieved with the approach of Delis et al. When combining it with the dissipative MinMod limiter, the residuum dropped by seven orders of magnitude, while a decrease of fourteen orders of magnitude was accomplished in conjunction with the van Albada-van Leer (VAVL) limiter. The reduction of residuals thus nearly matched that of the first order method. The combination of a sharp shockwave resolution and a superior convergence behaviour renders the technique of Delis et al. in combination with the VAVL limiter as the most advantageous for the present application.

Sensitivity to Domain Extent

Turbomachinery computations are often performed on truncated domains with the inlet and outlet boundaries positioned close to the internal components. This arrangement approximates the tight packaging typical for the real machines and helps to alleviate computational requirements by reducing the mesh cell-count. The inlet and outlet boundary conditions should thus ideally be formulated such that the flow solution is not affected by the axial position of the boundary, even if it is moved to a close vicinity of the blade-row.

Figure 6.30 shows the effect of boundary position on flow field predictions obtained with the Simple Turbomachinery BC and with the Exact Steady NRBC. The top plots of Mach number contours are supplemented by the density gradient contours on the bottom to highlight the shockwave pattern. The axial location of each boundary was varied individually in order to view its influence in isolation. The boundary condition values were not imposed directly as listed in Tab. 6.6, instead they were altered so as to maintain the operating point regardless of the domain extent. The values to be prescribed were determined by performing an iterative procedure, targeting to match the circumferential averages of total pressure, total temperature and flow angle at $0.5C$ upstream of the blade, and of static pressure at $0.5C$ downstream of the blade.

The inlet flow field is highly uniform in terms of both the stagnation quantities and the flow angle and the solutions obtained with the two boundary conditions match closely upstream of the blades. Moving the inflow boundary between $1C$ and $0.5C$ upstream of the blade LE has a negligible effect in both cases. The outlet flow field, in contrast, features strong non-uniformities due to the downstream propagation of the left-running TE shockwave, the reflected right-running TE shockwave and the blade wake. The Simple Turbomachinery BC produces spurious shockwave reflections that are particularly pronounced on the 1C0.5C and 1C2C domains, but distinctly present in all cases. The perturbations propagate upstream towards the blades and distort the pressure distribution on the aft portion of the SS. In contrast, the Exact Steady NRBC produces consistent flow field predictions with all tested outlet positions.

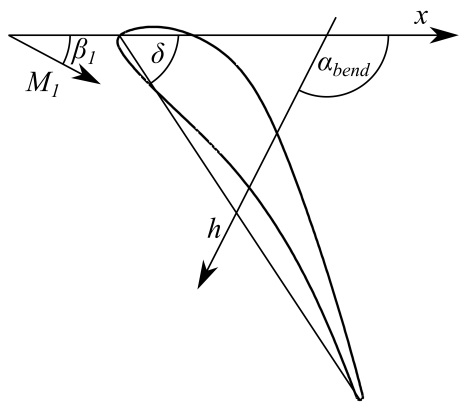

Figure 6.31: Sketch of STCF4 bending mode oscillations.

Parameter	Symbol	Unit	Value
Oscillation angle from axis	α_{bend}	[°]	-117
Oscillation amplitude	h	[mm]	0.292
Reduced frequency	$\tilde{\omega}$	[-]	0.082
Frequency	f	[Hz]	152

Table 6.7: Parameters of STCF4 bending mode oscillations.

Although the reflections of the left-running TE shockwaves from the outlet boundary are not suppressed entirely, their intensity is low and they have a very limited effect on the near-blade flow field. A physically valid solution can thus be obtained with the Exact Steady NRBC even on highly truncated domains.

6.3.2 Bending Mode Oscillations

The Test Case 628 of the Fourth Standard Configuration represents bending mode oscillations at an angle of $-117°$ from the machine axis and with a reduced frequency $\tilde{\omega} = 0.082$. A sketch of the configuration is shown in Fig. 6.31 and parameters of the oscillations are summarised in Tab. 6.7. The experimental rig comprises 20 blades, hence the IBPA can be varied with an increment of 18°. Note that the operating point differs from the steady-state case, as the outlet static pressure is decreased by 3 kPa to 66 200 Pa.

Grid Independence Study

The grid independence study performed for the unsteady solution targeted convergence of the aerodynamic damping coefficient Ξ. All four mesh levels were considered in the assessment and the temporal discretisation was refined consistently with the spatial one, adopting a ratio of ≈ 1.3 between the time-steps on each two consecutive mesh levels. The number of time-steps per period was thus progressively increased from 100 to 132, 172 and 220. The analysis was performed for $\sigma = 180°$, employing the 1C1C domain with the Spectral NRBC imposed at the inlet and outlet

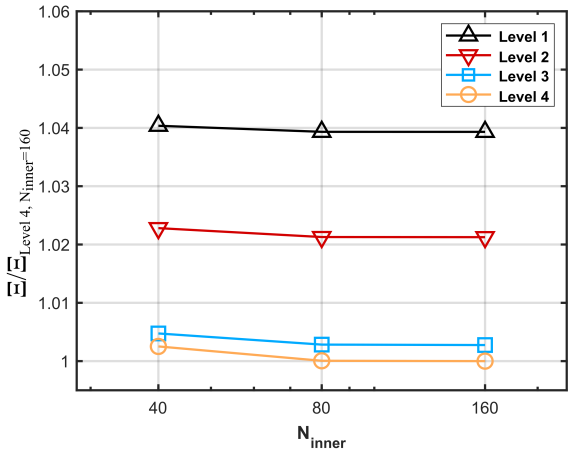

Figure 6.32: Convergence of the aerodynamic damping coefficient with refinement level and with the number of inner iterations for $\sigma = 180°$.

boundaries.

The aerodynamic damping coefficient was evaluated with Eq. 4.79 where the maximum displacement is given by the oscillation amplitude h. Convergence of Ξ with grid refinement is plotted in Fig. 6.32 for computations adopting 40, 80 and 160 inner-cycle iterations in the implicit integration scheme. It was found that the inner cycle may be terminated after 80 iterations, as executing additional 80 iterations altered the quantification of Ξ by less than 0.08 % in all cases. The aeroelastic assessment exhibited a higher sensitivity to grid refinement than found in the STCF10 test-case. The three coarsest mesh levels feature similar cell-counts on both geometries and they produce a variation of Ξ by 3.7 % in the present case as opposed to 1.5 % in the case of STCF10. This variation is also notably higher than that of the static aerodynamic blade forces which amounts to 0.4 %.

A more detailed insight into the effect of grid refinement onto the unsteady flow solution is provided by plotting distributions of unsteady pressure fluctuations on blade surface. The unsteady pressure coefficient for bending-mode oscillations is defined as:

$$\tilde{C}_p(\boldsymbol{x}, t) = \frac{p(\boldsymbol{x}, t) - \overline{p}(\boldsymbol{x})}{\dfrac{h}{C}\left(p_{01} - p_2\right)}. \tag{6.5}$$

Figure 6.33 shows the amplitude (left) and phase (right) of the first harmonic of $\tilde{C}_p(t)$ on blade surface in function of chord. Differences between the solutions on the four meshes are negligible on the whole PS and on the SS portion upstream of $0.55C$. Further downstream, the right-running TE shockwave of the neighbouring blade impinges on the SS and produces a distinct peak in the unsteady pressure amplitude. The sharpness of the peak resolution is notably affected by grid refinement, but the discrepancy is locally bounded and the pressure amplitude is captured consistently further downstream. In contrast, phase is affected on the whole aft portion of the SS. The distributions feature strong fluctuations whose pattern changes in function

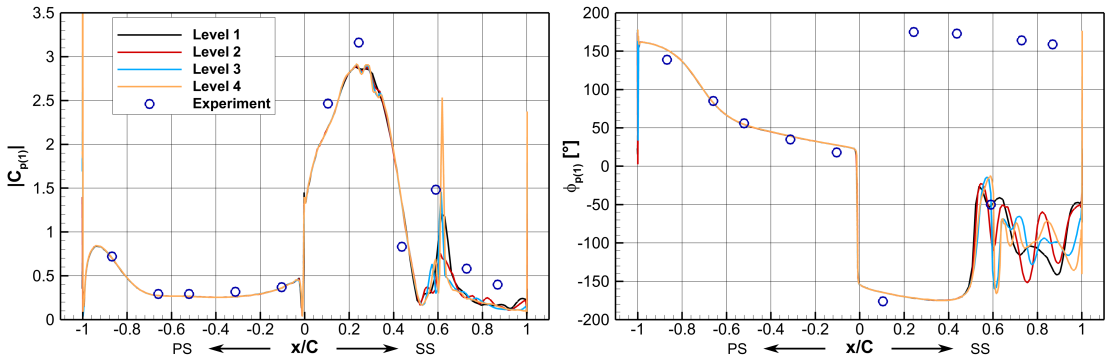

Figure 6.33: Distributions of amplitude ($|C_{p(1)}|$, left) and phase ($\phi_{p(1)}$, right) of the 1^{st} unsteady pressure harmonic on blade surface for $\sigma = 180°$. Experimental data from [47].

of the discretisation level. However, as the local unsteady pressure amplitude is relatively low, the resulting effect on the prediction of Ξ is only minor. It varies by less than 0.3 % between the two finest meshes, which proves the level 3 discretisation to be sufficiently refined for the purpose of this study.

Experimental data from [47] are included in the plots as a reference. The computation achieves close agreement with the measurements on the whole PS and on the portion of SS upstream of the shockwave impingement, i.e. in the same areas where the solution exhibits low sensitivity to mesh refinement. On the aft part of SS, the numerical prediction of amplitude also matches the experimental data well, but the discrepancy in phase amounts locally up to 120°. McBean et al. [128] showed that phase of pressure fluctuations is influenced by viscous effects in this region. In their comparison of inviscid and viscous computations, the inclusion of viscous effects in the model brought a closer match of phase prediction with experimental data, but at the same time the disagreement in amplitude increased. Based on these findings, it can be concluded that enhancing the present solver with turbulence modelling has the potential to alleviate the discrepancy observed in phase prediction.

Sensitivity to Domain Extent

The influence of axial domain extent on the unsteady flow solution is investigated in this section, comparing results obtained with the Spectral NRBC, the Exact Steady NRBC and the Simple Turbomachinery BC. The study was performed independently for the inlet and outlet boundaries, such that the position of one boundary was varied while the other remained fixed at the distance of one chord from the blade. The case of $\sigma = 180°$ was considered and the domain was discretised with the level 3 mesh. The sensitivity of aeroelastic predictions to domain extent was quantified in terms of the aerodynamic damping coefficient Ξ.

The variation of Ξ with the inlet and outlet positions is shown respectively on the left and on the right of Fig. 6.34. The subsonic incoming flow-field is characterised by very mild gradients, which contributes to the relatively low sensitivity of damping predictions to the inlet boundary position. For the considered upstream domain

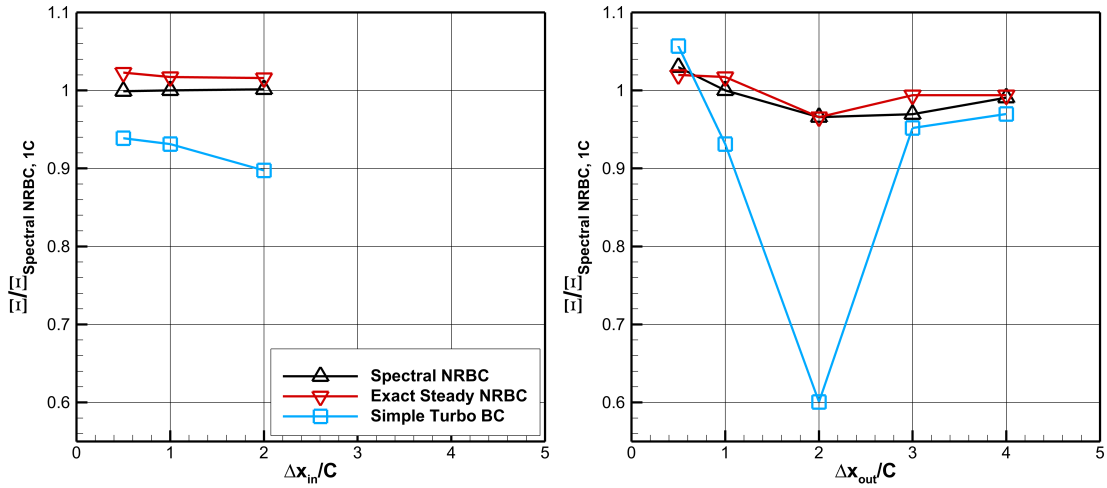

Figure 6.34: Variation of the aerodynamic damping coefficient in function of the inlet (left) and outlet (right) boundary distance from blades for $\sigma = 180°$.

extents of $2C$, $1C$ and $0.5C$, the predictions obtained with the Spectral NRBC vary by 0.25 %. The Exact Steady NRBC exhibits only a slightly higher sensitivity at $\Delta\Xi = 0.7\,\%$, while the Simple Turbomachinery BC produces by far the highest variation of $\Delta\Xi = 4.6\,\%$.

The outlet flow field features distinct perturbations in the form of shockwaves and blade wakes. In case that the boundary condition fails to suppress spurious reflections of the perturbations, these propagate upstream and contaminate the flow solution in blade passages. The quantification of aerodynamic damping coefficient is thus significantly affected. Moving the outlet boundary modifies the pattern of these reflections, resulting in a changed damping prediction. This phenomenon can also be observed in the steady-state flow field in Fig. 6.30 where the Simple Turbomachinery BC produces reflected shockwave patterns of different structure and intensity in function of the outlet boundary position. In contrast, an effective non-reflecting boundary condition treatment should minimize the influence of domain extent on the aeroelastic assessment.

As can be expected due to the outflow non-uniformity, the solutions with all three boundary conditions exhibit a notably higher sensitivity to the boundary position than in the case of inlet. The downstream distance of the outlet boundary from the blade TE is varied between $0.5C$ and $4C$. The Spectral NRBC and the Exact Steady NRBC perform consistently also in this case, although the respective damping variations of 6.2 % and 5.3 % are higher in absolute values. The Simple Turbomachinery BC fails to suppress the wave reflections, which causes the damping predictions to vary by 43.2 %.

Figure 6.35 shows how the boundary position affects unsteady pressure fluctuations on blade surface. Distributions of amplitude and phase of the first pressure harmonic are plotted for each of the three boundary conditions on the 1C1C, 0.5C1C, 1C0.5C and 1C4C domains. Whether the inlet or the outlet boundary is moved, and regardless of the boundary condition, the influence of axial domain extent is confined to the aft portion of the SS, downstream of the shockwave impingement.

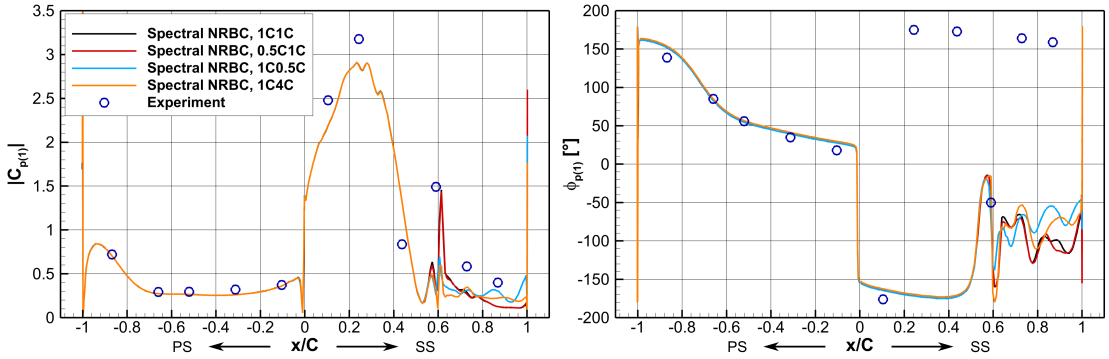

(a) Spectral NRBC

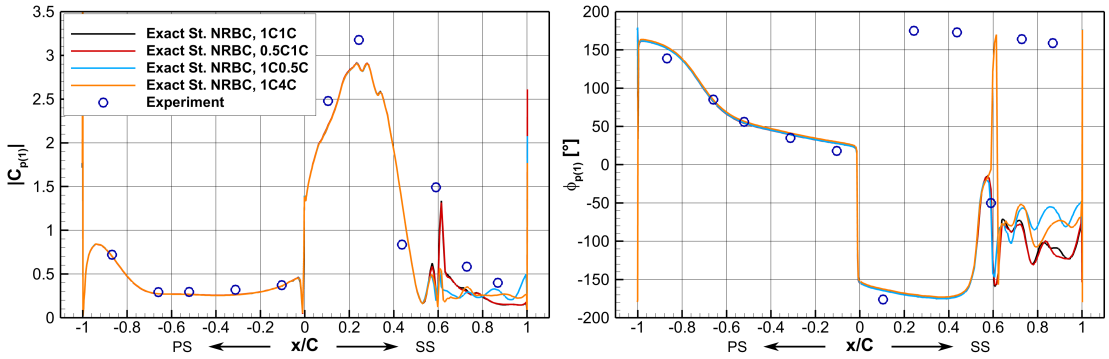

(b) Exact Steady NRBC

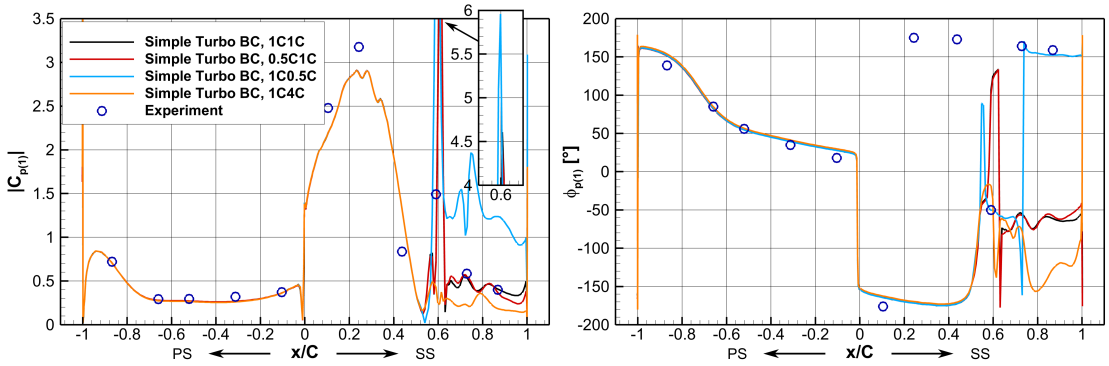

(c) Simple Turbomachinery BC

Figure 6.35: Distributions of amplitude ($|C_{p(1)}|$, left) and phase ($\phi_{p(1)}$, right) of the 1^{st} unsteady pressure harmonic on blade surface for $\sigma = 180°$, using different domain sizes and boundary conditions.

The Spectral NRBC and the Exact Steady NRBC yield nearly identical results, which indicates a predominance of modes with a high ratio of circumferential to temporal wave number. With either of the non-reflecting boundary conditions, the inlet position induces only a very small and locally bounded variation of phase around $0.9C$ of the blade SS. Amplitude remains virtually unaffected. In contrast, changing the downstream domain extent produces greater variations of both amplitude (max. $\Delta|C_{p(1)}| = 0.3$ outside of the shock impingement peak) and phase (max. $\Delta\Phi_{p(1)} = 45°$). The Simple Turbomachinery BC exhibits higher sensitivity in both cases, but especially for the outflow, whose position alters the predictions by up to $\Delta|C_{p(1)}| = 1.5$ and $\Delta\Phi_{p(1)} = 150°$.

Analysis of Aeroelastic Stability

The experimental annular turbine cascade features 20 blades, therefore the travelling-wave oscillations can occur only in a discrete set of IBPAs spaced by 18°. In the present analysis, every other vibration mode is considered and the IBPA range is covered with increments of 36°. Aerodynamic damping curve predictions obtained with the three boundary condition formulations are shown in Fig. 6.36a together with experimental data from [47]. Computations using the Simple Turbomachinery BC diverged in all cases but $\sigma = 0°$ and $\sigma = 180°$, hence only these two data-points are plotted. The results shown here were obtained on the 1C2C domain.

The Spectral NRBC and the Exact Steady NRBC yield a closely matching quantification of the aerodynamic damping coefficient, with a discrepancy of $\Delta\Xi < 0.03$ in all cases but $\sigma = 0°$ where $\Delta\Xi = 0.07$. Here the blades vibrate in phase and the waves propagate perpendicularly to the boundaries. As the Exact Steady NRBC considers only circumferential modes, it cannot suppress reflections of such waves, in contrast with the Spectral NRBC which accounts for all modes. The close match observed at all other IBPAs indicates a predominance of circumferential wave-modes in these cases.

The aerodynamic damping curve obtained with either of the non-reflecting boundary conditions is qualitatively consistent with experimental data. The agreement is achieved in terms of its nearly sinusoidal shape, free of any distinct local peaks, as well as in the extent of negative damping range from $-140°$ to $-18°$. The evaluation of aeroelastic stability yields the same conclusion, i.e. the blade cascade is unstable, whether it is based on the measurements or on the numerical results. Quantitatively, the simulations yield positively offset values relatively to the measurements. The discrepancy falls in the range $\Delta\Xi \in [0.04, 0.19]$ in most cases, but it rises to $\Delta\Xi \approx 0.3$ for $\sigma \in [72°, 144°]$.

In order to determine why the mismatch increases in this range, it is useful to examine the unsteady blade pressure distributions plotted in Fig. 6.37. For each investigated IBPA, the calculated amplitude and phase of the first harmonic are shown, together with experimental data from [47]. The conclusions regarding the comparison of numerical and experimental results drawn above for $\sigma = 180°$ are to a large extent valid generally. Namely, numerical predictions agree closely with measurements on the whole pressure side and on the front portion of the suction

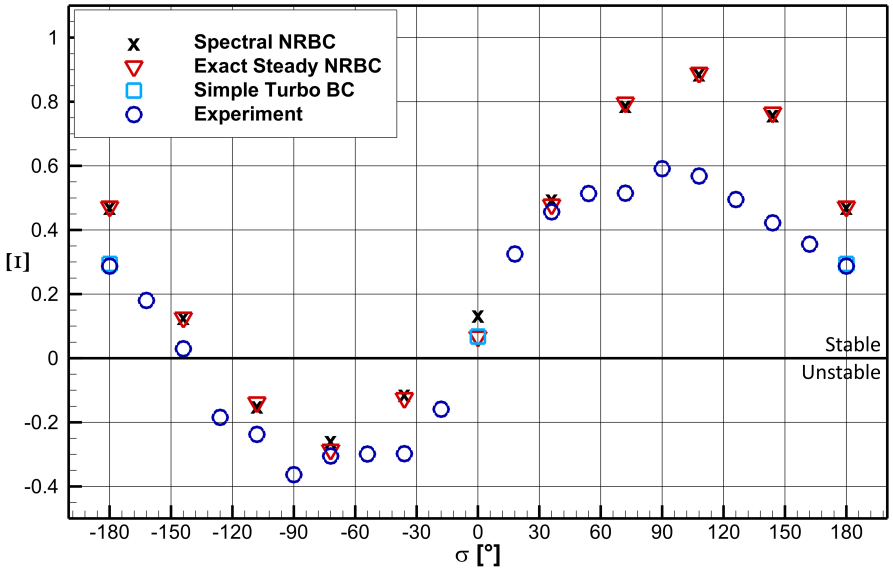

(a) Aerodynamic damping curve obtained on the 1C2C domain, experimental data from [47].

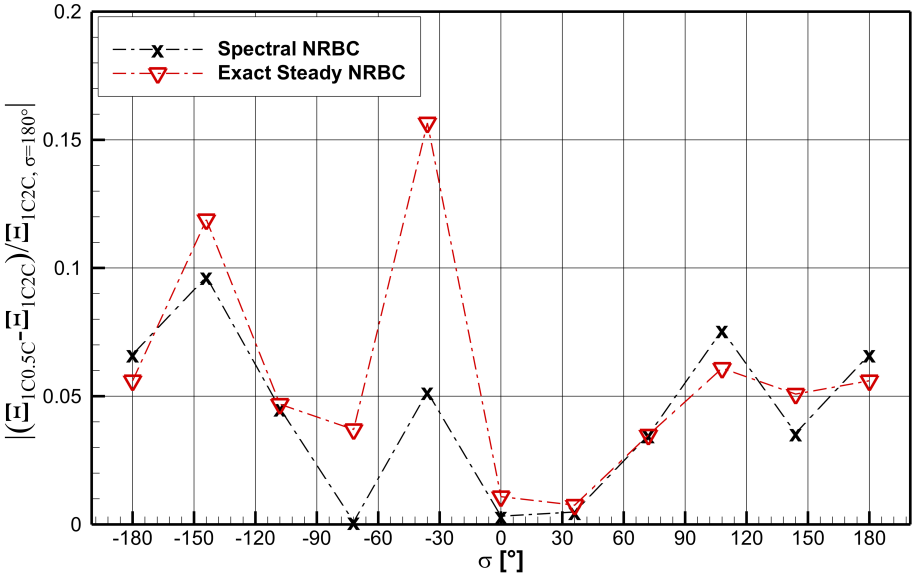

(b) Discrepancy between results on short-outlet (1C0.5C) and long-outlet (1C2C) domains.

Figure 6.36: Aerodynamic damping versus IBPA.

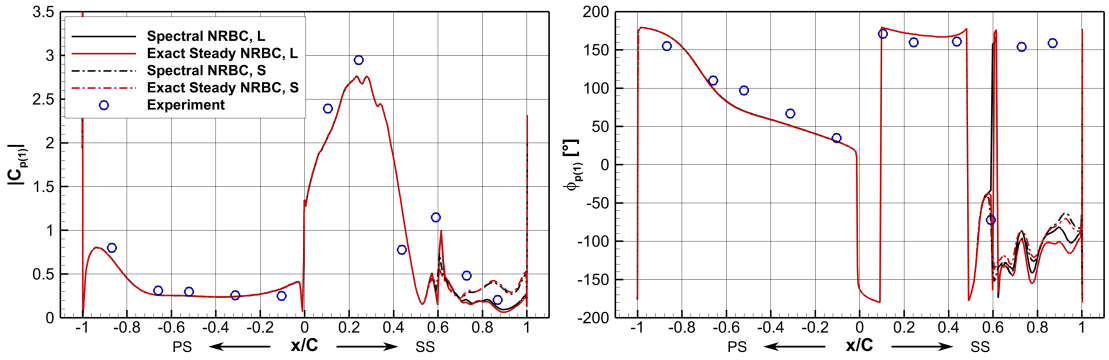

(a) $\sigma = -144°$

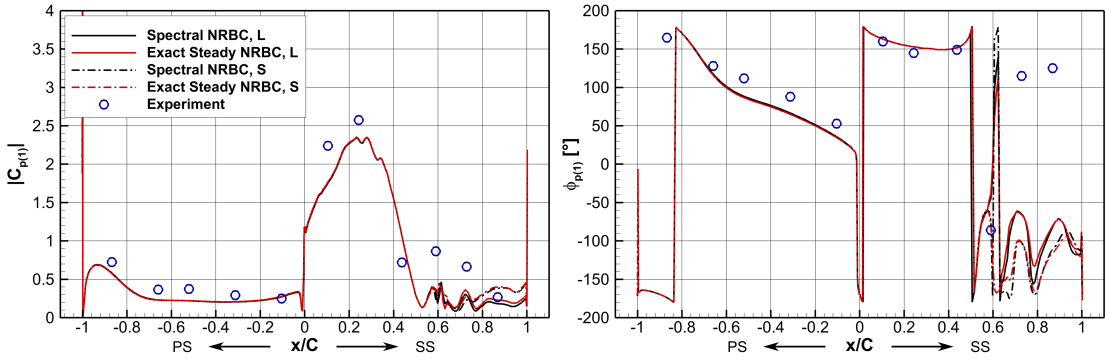

(b) $\sigma = -108°$

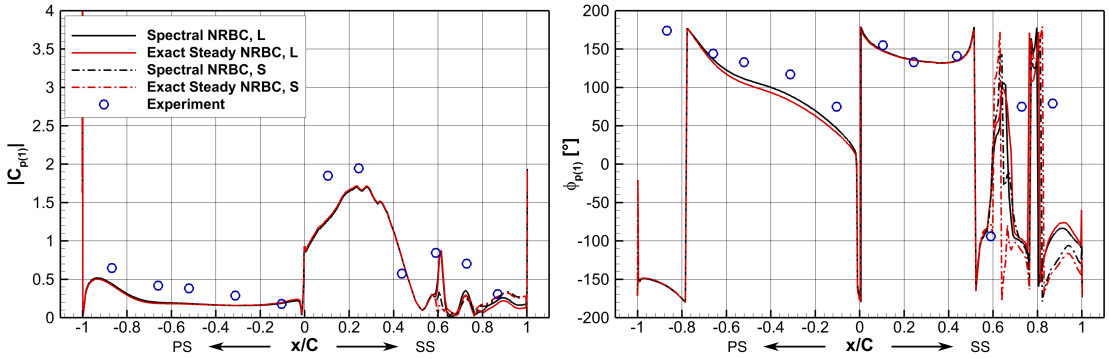

(c) $\sigma = -72°$

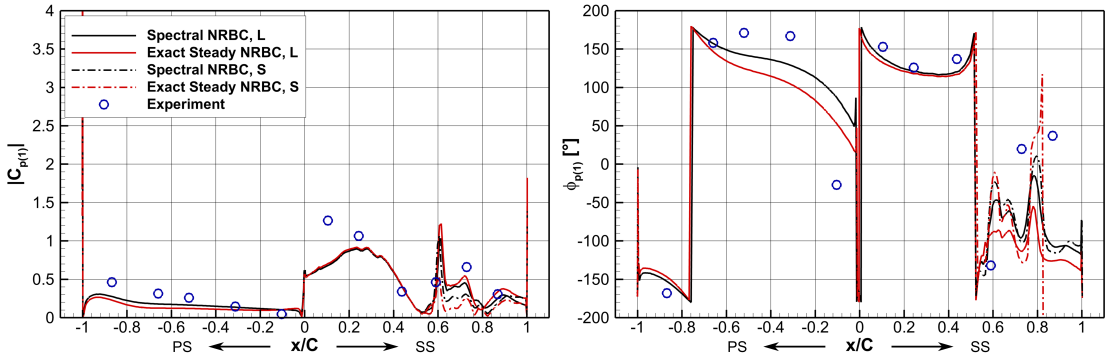

(d) $\sigma = -36°$

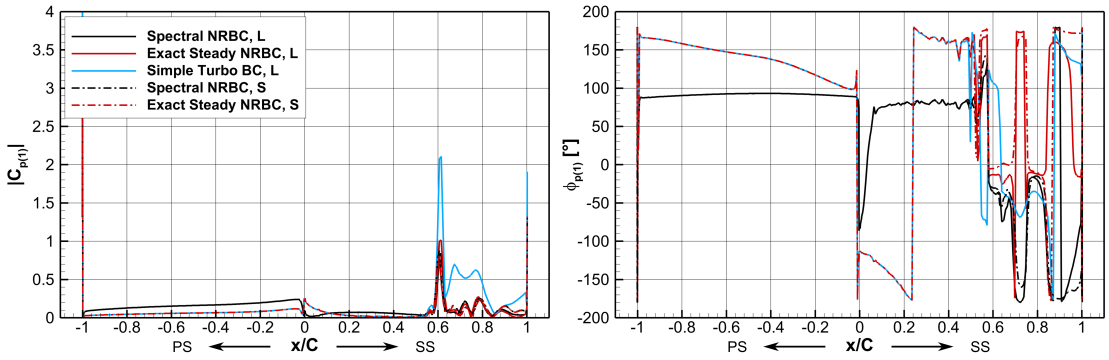

(e) $\sigma = 0°$

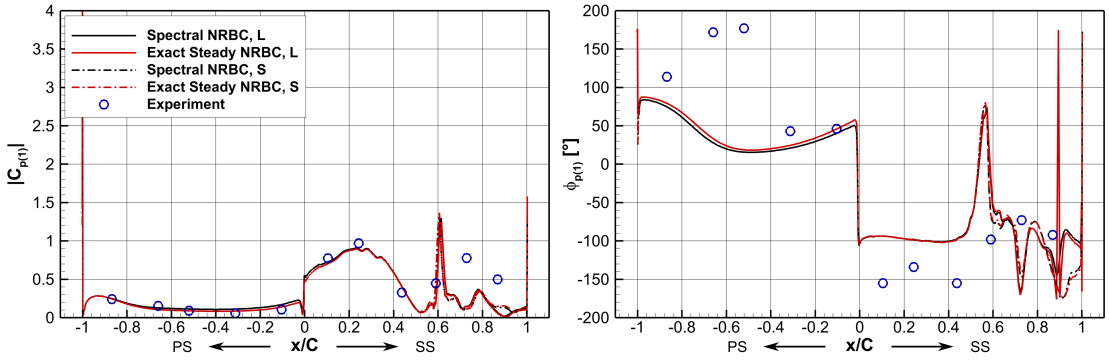

(f) $\sigma = 36°$

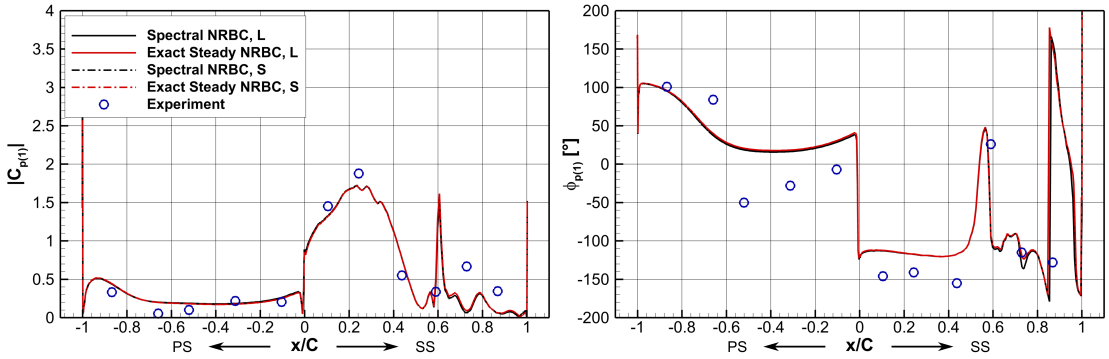

(g) $\sigma = 72°$

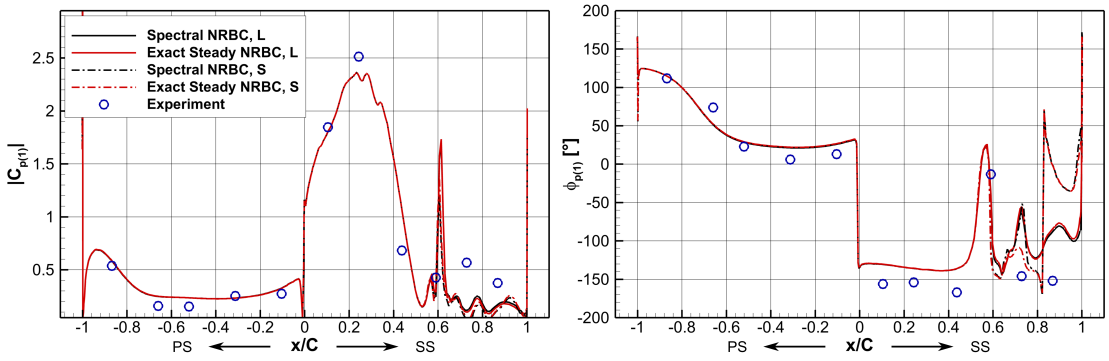

(h) $\sigma = 108°$

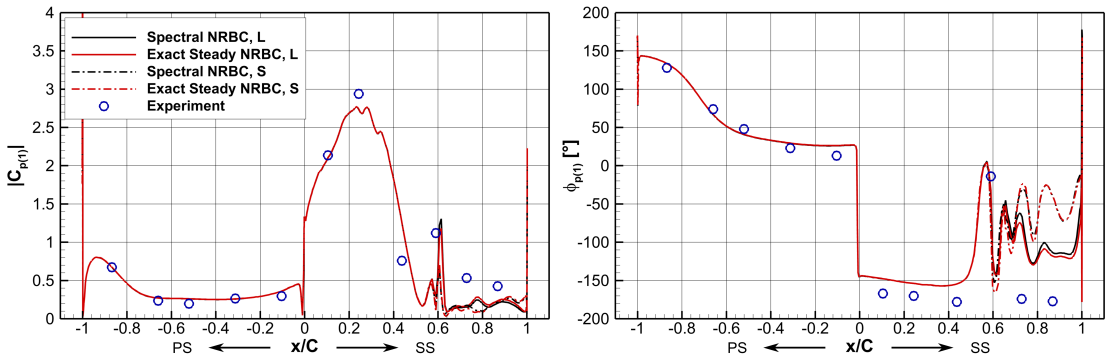

(i) $\sigma = 144°$

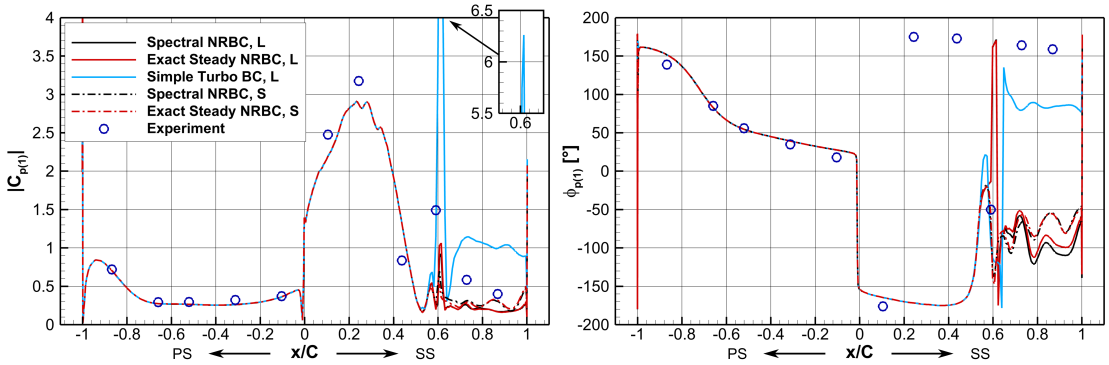

(j) $\sigma = 180°$

Figure 6.37: Distributions of amplitude ($|C_{p(1)}|$, left) and phase ($\phi_{p(1)}$, right) of the 1^{st} unsteady blade pressure harmonic on a long-outlet ("L", 1C2C) and a short-outlet ("S", 1C0.5C) domain.

side, whereas greater differences are found downstream of the shock impingement on the suction side. A partial exception from this trend is observed in the cases $\sigma = -36°$, $\sigma = 36°$ and $\sigma = 72°$. Experimental data show an abrupt change in phase on the PS, occurring in the three cases respectively at $0.2C$, $0.4C$ and $0.6C$, in contrast to the smooth distributions predicted numerically. This discrepancy is limited only to the phase of pressure fluctuations, whereas amplitude predictions are consistent with the measurements. It is unclear what mechanism could cause such a sudden phase-only alteration, considering that the PS surface is smoothly curved and faces a subsonic flow field. Possibly, the measurements could be affected by the presence of an external perturbation.

The highest discrepancy between numerical and experimental results in terms of the unsteady pressure distribution occurs at different IBPAs than in terms of the aerodynamic damping coefficient. Since the latter is an integral evaluation of the former, the lack of correlation indicates that there is a considerable error in calculating Ξ from the measured unsteady pressure distributions. Neglecting higher harmonics, the aerodynamic damping coefficient of a blade oscillating in a bending mode can be approximated with the following formula:

$$\Xi = -\sum_{i=1}^{N} \frac{\left|C_{p(1),i}\right| sin\left(\phi_{p(1),i}\right) (\boldsymbol{e}_i \cdot \boldsymbol{n}_i) \Delta S_i}{h(p_{01} - p_2)}, \tag{6.6}$$

where N is the number of data points (i.e. pressure probes), $\boldsymbol{e}_i$ denotes a unit vector in the bending direction, $\boldsymbol{n}_i$ a unit surface normal vector and ΔS_i the area element of a data point i. The accuracy of this approximation is highly dependent on the number of data points, which there were in the experimental campaign only 5 on the blade pressure side and 6 on the suction side. Considering further that the unsteady pressure distributions are highly non-uniform and feature sharp peaks, the experimental evaluation of Ξ is bound to suffer from a substantial numerical error. To a large extent, the disagreement between the numerical and experimental quantification of the aerodynamic damping coefficient can be attributed to this error.

The sensitivity of aerodynamic damping prediction to the domain extent was discussed above for the case $\sigma = 180°$. In order to verify whether the conclusions are valid generally for the STCF4 cascade, the aerodynamic damping curve was computed on a 1C2C domain as well as on a truncated 1C0.5C domain. The alteration of Ξ due to the downstream domain extent is plotted in Fig. 6.36b for computations using the Spectral NRBC and the Exact Steady NRBC. The damping coefficient for $\sigma = 180°$ on the 1C2C domain is used as a reference value for normalisation. The analysis was not extended to the inlet position effect, as the previous results showed it to be insignificant.

In most cases, the change in aerodynamic damping with the outlet position is similar for both boundary conditions. A notable exception occurs for $\sigma = -36°$ where the Exact NRBC produces a variation of 15.7 % as opposed to 5.2 % yielded by the Spectral NRBC. Also the overall maximum variation of Ξ is lower when using the Spectral NRBC (9.7 %) than the Exact Steady NRBC (15.7 %). Figure 6.37 shows that the unsteady blade pressure distributions are altered only on the aft portion of

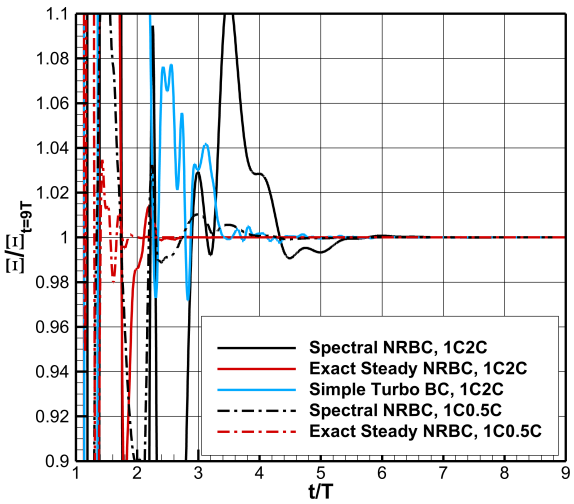

Figure 6.38: Convergence of the aerodynamic damping coefficient for $\sigma = 180°$.

the SS, downstream of the shockwave impingement.

The Spectral NRBC exhibited in general slower convergence than the Exact Steady NRBC. An illustrative example of the convergence behaviour is provided in Fig. 6.38 for $\sigma = 180°$. Let us consider the computation as converged when increasing the simulated time by a factor of two would alter the aerodynamic damping coefficient by less than 0.1 %. Computations employing the Spectral NRBC converged after 2.5 to 5.3 oscillation cycles, about twice as many as needed with the Exact Steady NRBC. The Simple Turbomachinery BC failed to converge in all but two cases.

Convergence can potentially be accelerated by moving the inlet and outlet boundaries closer to the blades. In the present case, using the shorter 1C0.5C domain allowed the number of time-steps to be reduced by up to 28 % for some IBPAs, but brought negligible benefit for others. This effect was similar with either of the two non-reflecting boundary conditions.

6.4 Turbine Cascade M8

The investigated blade cascade represents a near-tip section of a Doosan Škoda Power steam turbine rotor M8. Typically for a low-pressure turbine stage, the blade length is considerable at 1.4 m. High peripheral velocities are therefore reached at a higher span, causing the relative inflow conditions to be supersonic. Additionally to the shockwaves originating in the blade passage and propagating downstream, as found in transonic blade cascades, a detached bow shock can be expected to form upstream of the blade leading edge and propagate towards the inlet boundary. This configuration thus places high demands on the formulation of non-reflecting boundary conditions for both inflow and outflow. The flow analysis presented in this section considers only the Exact Steady NRBC and the Spectral NRBC, as the Simple Turbomachinery BC diverged even in a steady-state solution. Aeroelastic stability of the cascade was investigated for a coupled bending-torsion mode of blade

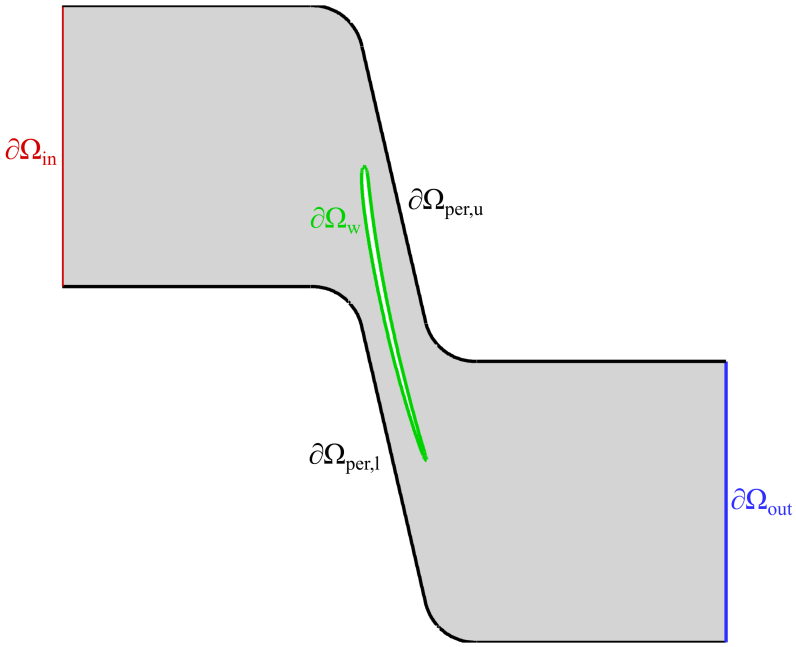

Figure 6.39: M8 single-blade computational domain.

oscillation.

An aeroelastic analysis of the M8 blade cascade was published by the author in [2]. The inlet and outlet boundaries were not treated with non-reflecting boundary conditions, therefore only a lower-span section with subsonic inlet conditions could be investigated. The results shown in this work consider a supersonic 93 % span section and they were partially presented at [3].

Figure 6.39 shows a single-blade domain with the inlet and outlet boundaries placed at the distance of one chord from the blade. In accordance with the notation introduced for STCF4, this domain is referred to as 1C1C. Basic dimensions, operating conditions and fluid parameters are listed in Tab. 6.8. The working medium was modelled as an ideal gas with $R = 438.4\,\mathrm{J\,kg^{-1}\,K^{-1}}$ and $\gamma = 1.0707$. Solver settings were based on the analysis performed for the STCF4 test-case. Evaluation of inviscid

Parameter	Symbol	Unit	Value
Blade chord	C	[m]	0.2945
Blade spacing (pitch)	P	[m]	0.2764
Stagger angle	δ	[°]	-78.135
Inlet total pressure	p_{01}	[Pa]	55013
Inlet total temperature	T_{01}	[K]	356.87
Inlet flow angle	β_1	[°]	-80.58
Outlet static pressure	p_2	[Pa]	10272
Specific heat ratio	γ	[-]	1.0707
Specific gas constant	R	$[\mathrm{J\,kg^{-1}\,K^{-1}}]$	438.4

Table 6.8: Overview of M8 parameters

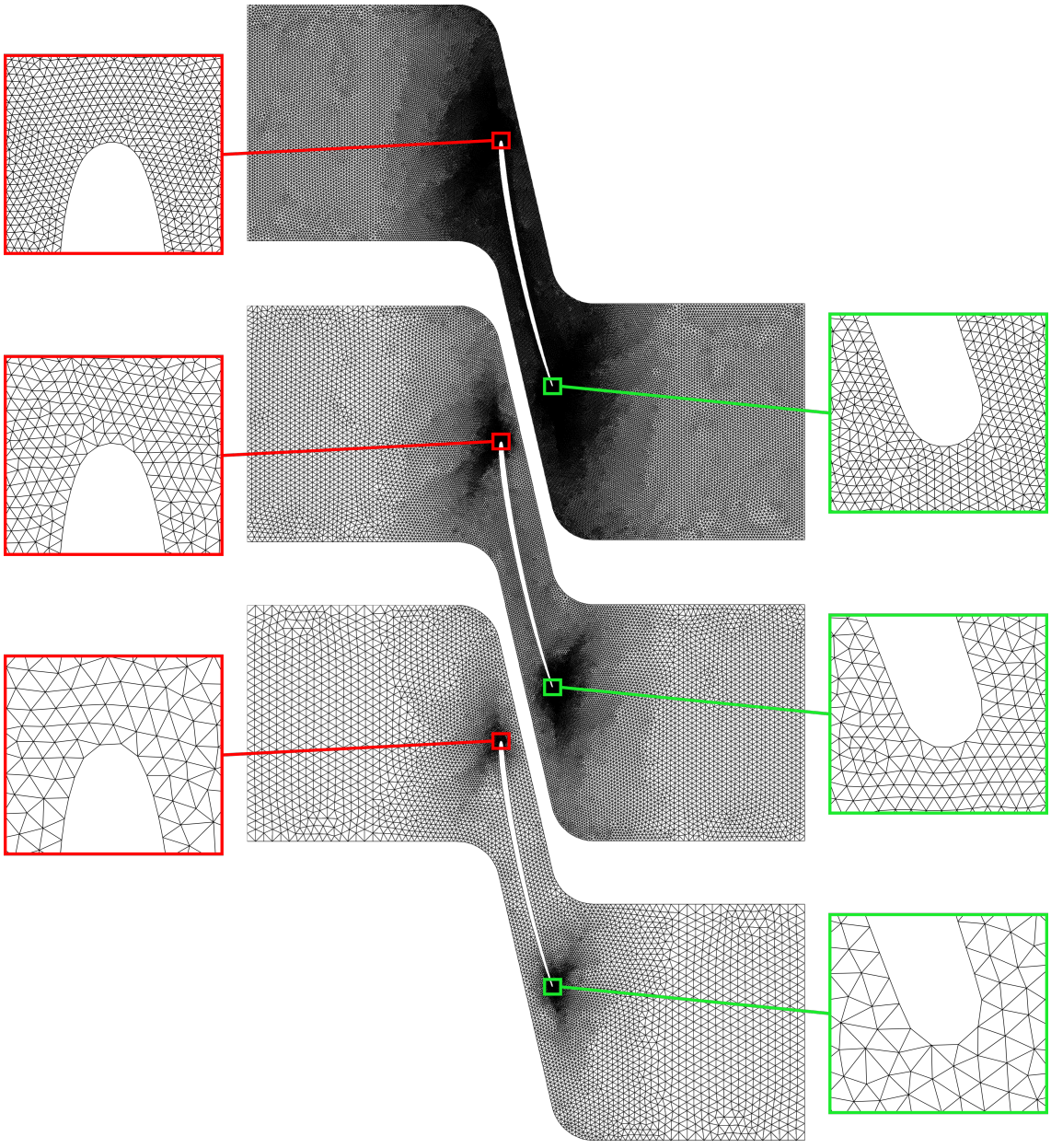

Figure 6.40: M8 single-blade domain discretisation with refinement levels 1 to 3 from bottom to top. Inlet and outlet boundaries positioned at 1 chord from the blades.

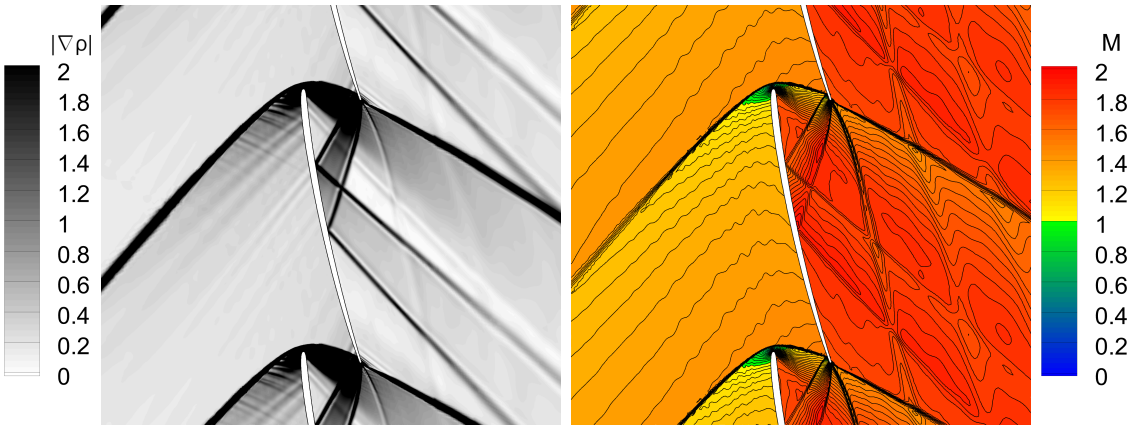

Figure 6.41: Pseudo-schlieren image (left) and Mach number contours (right) on the level 3 grid.

fluxes was preceded by a least squares gradient reconstruction procedure, using the inverse distance weighting exponent $k = 1.0$ and the van Albada-van Leer variant of the Delis et al. limiter. The time-marching solution procedure employed the implicit integration scheme with local time-stepping and implicit residual smoothing and the CFL number was set to 3.0.

6.4.1 Steady-State Flow

Grid Independence Study

Convergence of the steady-state solution with grid refinement was investigated on three levels of unstructured triangular discretisation generated in ANSYS® ICEM 19.1. The cell dimension was reduced by a factor of 1.69 in each refinement, producing cell counts of 13897, 39820 and 114952 per blade passage on the 1C1C domain. Figure 6.40 presents the three mesh levels with insets focusing on the LE and TE regions. The grid independence study was performed with the Exact Steady NRBC imposed at the inflow and outflow boundaries.

The complex flow field topology is illustrated in Fig. 6.41 by plotting contours of density gradient (left) and Mach number (right) on the finest, level 3 mesh. The flow is accelerated in the blade cascade from an average inlet Mach number 1.34 to an average outlet Mach number 1.73. Similarly to the transonic blade cascade STCF4, a pair of shockwaves emanates from the blade TE. The right-running one impinges on the suction side surface of the neighbouring blade near 50 % chord, while the other propagates directly towards the outlet boundary. The inlet flow field features a detached bow shock, formed upstream of the blade LE. One branch of the shockwave propagates directly towards the inflow boundary, whereas the other reaches the outflow boundary after a couple of reflections, occurring at $\approx$ 95 % chord on the upper blade PS and at $\approx$ 27 % chord on the lower blade SS. The flow is supersonic everywhere but in three small patches. One is found near the blade LE immediately downstream of the bow shock, another near the blade TE

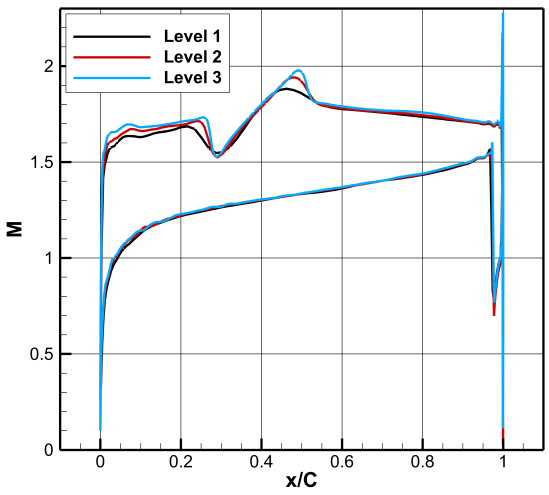

Figure 6.42: Blade surface Mach number distribution with different grid refinement levels.

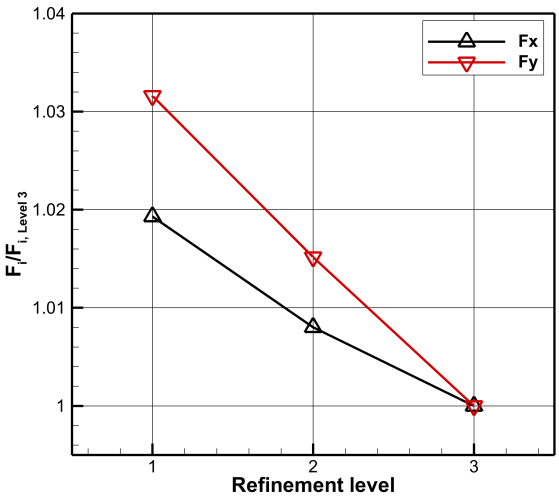

Figure 6.43: Axial (F_x) and circumferential (F_y) aerodynamic blade force in function of grid refinement. Forces normalized by the finest grid results.

downstream of the bow shock impingement on the PS, and the last in a small portion of the blade wake. The Exact Steady NRBC is based on linearised Euler equations, whereas the present flow field is strongly nonlinear. In spite of this limitation, the boundary condition works highly effectively in preventing the formation of spurious wave reflections and only minor perturbations appear in the contour plots.

Figure 6.42 provides a comparison of blade surface Mach number distributions on the three mesh levels. There is very little difference in resolving the pressure side distribution, including the shockwave impingement at $0.98C$. On the suction side, the effect of grid refinement is more pronounced. The Mach number predictions exhibit an offset on the front portion of the surface, upstream of the reflected bow-shock impingement at $0.27C$. The finer the mesh resolution, the higher Mach level is reached, with the difference between the level 1 and level 3 meshes amounting to $\Delta M \approx 0.07$. The sharpness of the Mach number peak that precedes the right running TE shockwave impingement at $0.5C$ is also notably affected. The coarsest grid yields a Mach number maximum 1.88 at this location, while values of 1.94 and 1.98 are obtained on the level 2 and level 3 grids respectively. Elsewhere on the suction side, all three predictions match closely. Crucially, the Mach number distribution is in the second refinement step altered less than in the first one, evidencing that the flow solution has a converging trend.

The variation of blade forces with refinement is plotted in Fig. 6.43. Due to the increased complexity of the flow field, the sensitivity to cell-size is higher than in the STCF4 test-case. Between the level 2 and level 3 meshes, the axial and circumferential aerodynamic loads change by 0.8 % and 1.5 % respectively. The forces vary nearly linearly with grid refinement and do not exhibit a converging trend. However, flow features are captured consistently on all three meshes and the blade Mach number distributions converge locally, as shown in Fig 6.42. The level 2 refinement provides a sufficient resolution of the steady-state flow for the purpose of this study.

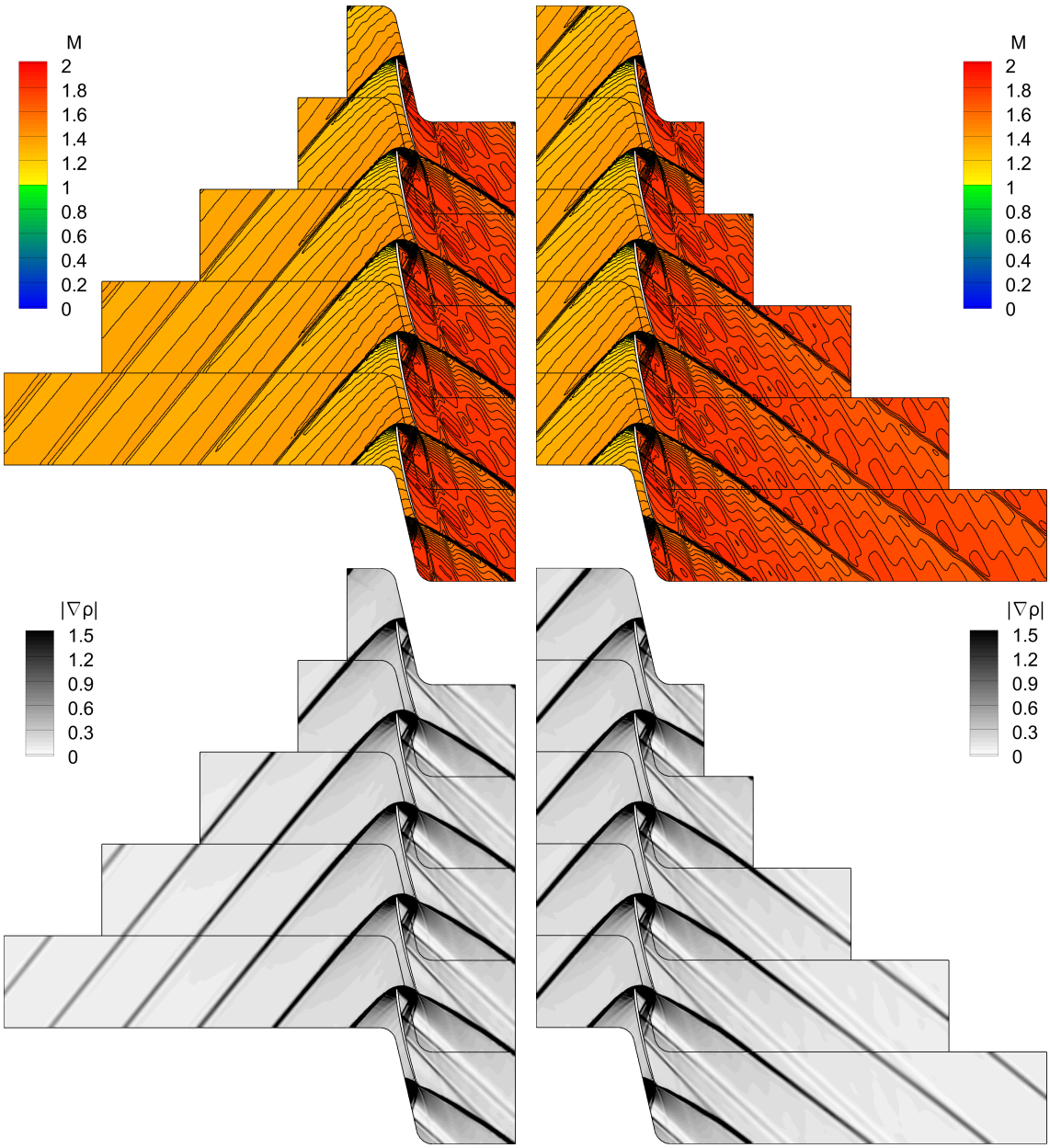

(a) Varying inlet position, from top to bottom domains 0.5C1C, 1C1C, 2C1C, 3C1C, 4C1C.

(b) Varying outlet position, from top to bottom domains 1C0.5C, 1C1C, 1C2C, 1C3C, 1C4C.

Figure 6.44: Contours of Mach number (top) and density gradient (bottom) with different domain extents.

Sensitivity to Domain Extent

The inlet flow field of subsonic and transonic blade cascades, such as STCF10 in Sec. 6.2 and STCF4 in Sec. 6.3, is nearly uniform when viewed at a sufficient distance upstream of the blades. In contrast, the supersonic cascade M8 features an upstream propagating bow-shock, which places increased demands on the inlet boundary condition treatment. The Simple Turbomachinery BC failed to converge in such demanding flow conditions, hence the analysis of the steady-state solution sensitivity to domain extent was performed only with the Exact Steady NRBC.

Figure 6.44 shows contours of Mach number (top) and density gradient (bottom) on domains with different axial extents, discretised with the level 2 mesh. In order to isolate the effect of inflow and outflow positions, each of the boundaries is moved individually while the other one remains fixed at a distance of one chord from the blades. In both cases, the range considered for the boundary-to-blade distance is from $0.5C$ to $4C$.

The outlet flow field resembles qualitatively the transonic STCF4 cascade, on which the Exact Steady NRBC has been shown to exhibit little sensitivity to the boundary position (Sec. 6.3). A similar behaviour is observed also in the present case, as evidenced by the contour plots in Fig. 6.44b. Even with the outlet boundary placed at a half-chord distance from the blades, no significant wave reflections are observed and the density gradient and Mach number distributions match closely the long-domain solutions.

Results obtained with different upstream domain extents are also consistent and show little variation in either the Mach number or the density gradient pattern (Fig. 6.44a). However, the spurious reflections of upstream propagating bow-shocks are more pronounced than the perturbations observed at the outlet boundary. They are most evident on the shortest domain 0.5C1C and lose on intensity as the inlet boundary moves further away from the blades. Similarly as in the case of the outlet boundary, these perturbations have little effect on the prediction of the blade-channel flow field. Using the Exact Steady NRBC thus enables truncating the domain extent both upstream and downstream of the blade cascade without compromising notably the accuracy of the solution.

6.4.2 Coupled Mode Oscillations

The investigation of aeroelastic stability was performed for a coupled mode of oscillation, provided by a three-dimensional finite element model. The evaluation of natural modes and frequencies was performed in vacuo, i.e. without the consideration of aerodynamic forces. The output of the finite element analysis in the form of complex displacements for points forming the three-dimensional blade surface was interpolated onto the 93 % span section. Neglecting the profile deformation, a general two-dimensional eigenmode can be approximated with a rigid body motion, using the procedure described in Sec. 5.3.1. The blade vibrates in a coupled mode, such that it undergoes a pitching motion while its elastic axis (EA) follows a trajectory in

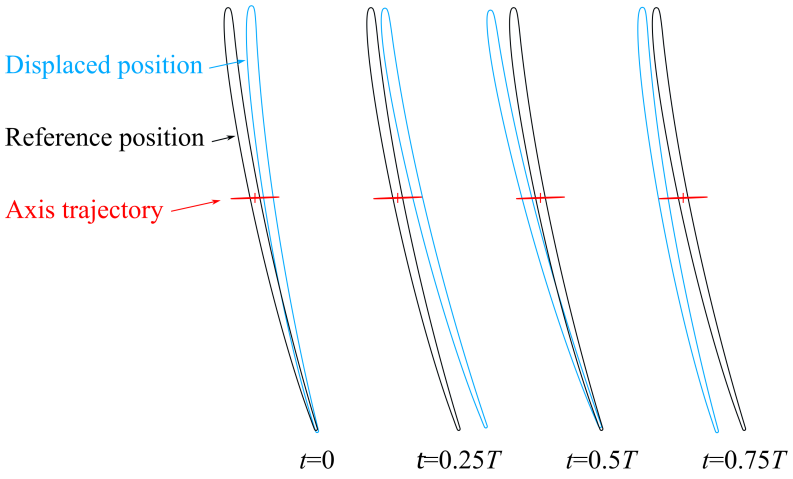

Figure 6.45: Sketch of coupled-mode oscillations of M8. Displacement scaled by a factor of two.

Parameter	Symbol	Unit	Value
Horizontal EA displacement amplitude	Δx_{EA}	[mm]	8.168
Horizontal EA displacement phase	$\phi_{x_{EA}}$	[°]	-56.13
Vertical EA displacement amplitude	Δy_{EA}	[mm]	0.307
Vertical EA displacement phase	$\phi_{y_{EA}}$	[°]	-29.74
Pitching amplitude	$\Delta\alpha$	[°]	1.75
Pitching phase	ϕ_α	[°]	-149.09
Reduced frequency	$\tilde{\omega}$	[-]	0.194
Frequency	f	[Hz]	141.312

Table 6.9: Parameters of M8 coupled-mode oscillations.

the shape of an ellipse. Figure 6.45 shows snapshots of the displaced and reference blade positions at four time instants during an oscillation cycle. The elastic axis is placed at the midpoint of camberline and the harmonic vibrations are characterised by a reduced frequency $\tilde{\omega} = 0.194$. The amplitude and phase of the horizontal and vertical EA displacements and of the pitching angle are listed in Tab. 6.9.

Grid Independence Study

Independence of the unsteady flow solution on domain discretisation was investigated on the same set of meshes as used for the steady-state flow in Sec. 6.4.1. The number of time-steps per period of oscillation was varied in accordance with mesh refinement, starting with 100 on the coarsest grid and proceeding via 172 to 288. The study was performed for the configuration of in-phase oscillating blades, i.e. $\sigma = 0°$, and adopted the 1C1C domain with the Spectral NRBC imposed at inflow and outflow.

The key parameter for assessing aeroelastic stability is the aerodynamic damping coefficient Ξ. Its convergence with grid refinement and with the number of inner-

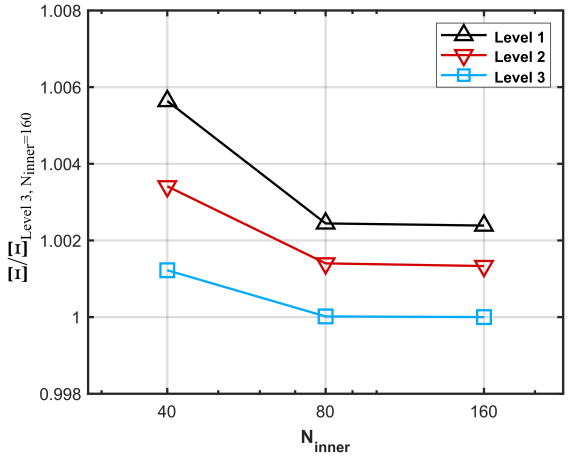

Figure 6.46: Convergence of the aerodynamic damping coefficient with grid refinement level and with the number of inner iterations for $\sigma = 0°$.

cycle iterations is plotted in Fig. 6.46. The implicit integration scheme was found to converge after 80 inner iterations, as performing an additional set of 80 altered the quantification of Ξ by less than 0.01 % in all cases. The change in aerodynamic damping with grid refinement amounts to 0.11 % between levels 1 and 2 and to 0.14 % between levels 2 and 3. These variations are lower than on the STCF4 and STCF10 blade cascades with comparably refined meshes, but they do not exhibit a converging trend. It needs to be established whether the flow solution converges locally in spite of the trend in integral quantification.

Figure 6.47 shows amplitude (left) and phase (right) of the first harmonic of unsteady pressure coefficient (Eq. 6.5) in function of chord. The solutions on all three mesh levels are in a close agreement. The predictions of amplitude differ mainly in the peaks at $0.4C$ and $0.52C$, whose resolution is smeared on the coarsest grid, but nearly unchanged between levels 2 and 3. The distribution of phase varies predominantly on the aft portion of the suction side, where more pronounced fluctuations appear with grid refinement. Their pattern is a signature of unsuppressed wave reflections emanating from the outlet boundary. On the coarsest grid, the perturbations dissipate before reaching the blade channel. As the cell-size is reduced, they

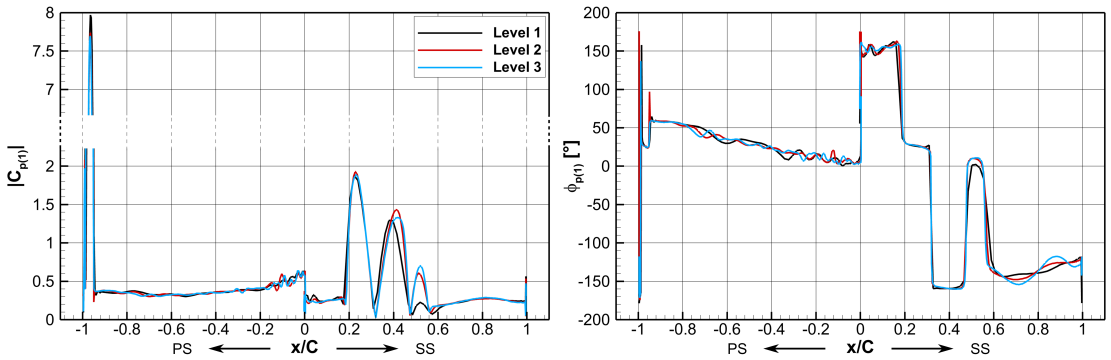

Figure 6.47: Distributions of amplitude ($|C_{p(1)}|$, left) and phase ($\phi_{p(1)}$, right) of the 1^{st} unsteady pressure harmonic on blade surface for $\sigma = 0°$.

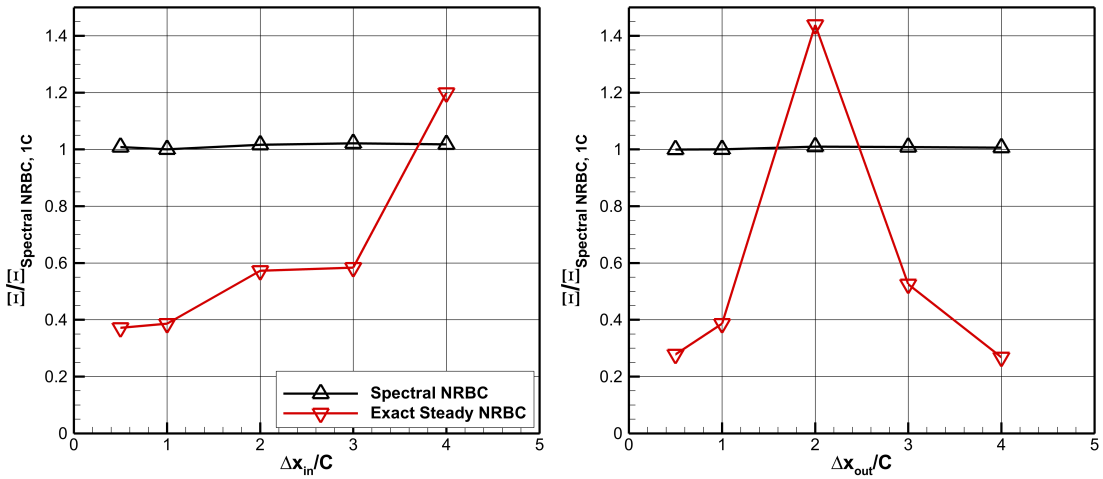

Figure 6.48: Variation of the aerodynamic damping coefficient in function of the inlet (left) and outlet (right) boundary distances from blades for $\sigma = 0°$.

become more sharply resolved and prevent the phase distribution from converging in this region. The effect of the spurious wave reflections on the unsteady blade pressure prediction is only mild, as amplitude remains nearly unchanged and phase is altered by less than $\approx 8°$ between two consecutive grid levels.

The second grid refinement step brings negligible alterations of the unsteady blade pressure distribution everywhere but in phase on the aft part of the SS. Considering additionally that the change in the aerodynamic damping coefficient is insignificant at 0.14 %, the level 2 mesh is found to provide a sufficiently fine discretisation for an accurate aeroelastic analysis.

Sensitivity to Domain Extent

The influence of domain size on the unsteady flow solution was investigated on the same set of domains as in the steady-state case in Sec. 6.4.1. The analysis could thus be performed individually for the inflow and outflow boundaries. Only the Exact Steady NRBC and the Spectral NRBC were tested, as computations using the Simple Turbomachinery BC failed to converge. The discretisation was performed with the level 2 refinement and the IBPA of 0° was imposed for the blade oscillations.

Figure 6.48 shows how the inlet (left) and outlet (right) boundary positions affect the quantification of the aerodynamic damping coefficient Ξ. The distance of either boundary from the blades is varied between $0.5C$ and $4C$. The Spectral NRBC exhibits little sensitivity to domain extent, with the changes in Ξ amounting to 2.1 % and 1 % in the case of inflow and outflow respectively. These results show that the boundary condition is highly effective in suppressing spurious wave reflections even in the presence of shockwaves propagating both upstream and downstream. In contrast, the Exact Steady NRBC yields inconsistent results on the different domains. There is over a threefold difference between the lowest and highest damping prediction when moving the inlet boundary, and more than a fivefold difference in the case of outlet.

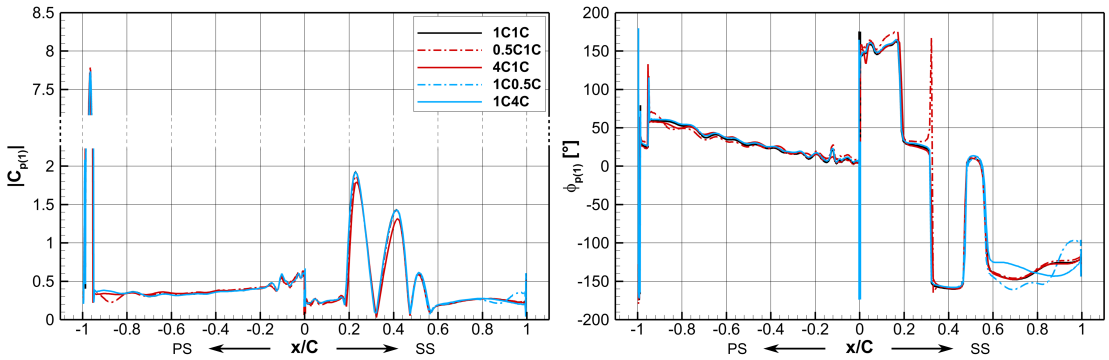

(a) Spectral NRBC

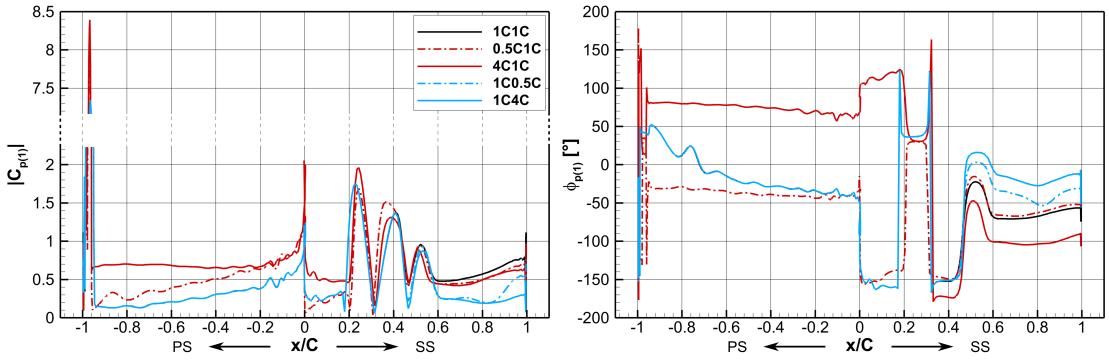

(b) Exact Steady NRBC

Figure 6.49: Distributions of amplitude ($|C_{p(1)}|$, left) and phase ($\phi_{p(1)}$, right) of the 1^{st} unsteady pressure harmonic on blade surface with different domain sizes and boundary conditions for $\sigma = 0°$.

Results obtained with the Spectral NRBC exhibit low sensitivity to domain extent also in terms of the unsteady blade pressure distribution in Fig. 6.49a. Amplitude and phase of the first harmonic are plotted on the left and right of the figure respectively. Solutions on five domains are shown, selected such that the nearest ($0.5C$) and furthest ($4C$) positions of each boundary are included, together with the 1C1C domain. There are only locally bounded differences of a small magnitude between the solutions. A truncation of either the upstream or the downstream domain extent to $0.5C$ amplifies the spurious wave reflections and induces a fluctuation in amplitude by $\Delta|C_{p(1)}| \approx 0.15$ near $0.9C$. Phase is affected mainly on the aft 40 % of the SS, by up to 38°.

The sensitivity of unsteady solution to domain extent increases notably with the use of the Exact Steady NRBC (Fig. 6.49b). The outlet boundary position affects mainly the aft 55 % of the SS, where it induces an offset of $\Delta|C_{p(1)}| \approx 0.4$ and $\Delta|\phi_{p(1)}| \approx 50°$. The changes caused by moving the inlet boundary are even more profound, in terms of both magnitude and spatial extent. The unsteady pressure distribution is altered almost on the entire blade surface by up to $\Delta|C_{p(1)}| = 0.57$ and $\Delta|\phi_{p(1)}| = 115°$. An entirely different solution is thus obtained by changing the position of either boundary. This behaviour highlights the importance of employing a boundary condition with good reflecting properties for the accuracy of aeroelastic predictions.

Analysis of Aeroelastic Stability

The investigation of aeroelastic stability was performed with an IBPA resolution of 30°. Either the Exact Steady NRBC or the Spectral NRBC were imposed, the former only in combination with a 2C2C domain and the latter also with truncated 0.5C2C and 2C0.5C domains. The selection of these configurations was motivated by two main targets of the analysis. Firstly, to establish how the lack of temporal wave-modes in the formulation of NRBC impacts the assessment of aeroelastic stability over a range of IBPAs. And secondly, to investigate the influence of domain truncation on the accuracy of damping curve prediction with the Spectral NRBC.

The results are plotted in Fig. 6.50, whose part (a) shows damping coefficient predictions and part (b) relative differences to a reference computation, performed on the 2C2C domain with the Spectral NRBC. All results are consistent in characterising the aeroelastic behaviour as unstable over the whole IBPA range. The reference damping curve exhibits an approximately sinusoidal shape that is, however, disrupted for $\sigma \in [-90°, -30°]$. The three cases within this range are found in the vicinity of acoustic resonance conditions that have a stabilizing effect and shift the damping coefficient towards zero. A notable discrepancy of up to 26 % appears here between the results obtained with the Spectral NRBC and the Exact Steady NRBC. A similar behaviour was observed also on the STCF10 blade cascade (Sec. 6.2) where the Exact Steady NRBC likewise failed to predict the acoustic resonance peaks. An even higher discrepancy of 38 % appears at $\sigma = 0°$, similarly to the STCF4 cascade (Sec. 6.3). The in-phase blade vibrations excite waves that propagate perpendicularly to the inlet and outlet boundaries and as such are not accounted for by the Exact Steady NRBC. Apart from these four IBPAs, the two boundary conditions differ by less than 10 % in the prediction of Ξ.

Figure 6.51 presents blade surface distributions of the first unsteady pressure coefficient harmonic for all investigated IBPAs. The results obtained with the two different boundary conditions on the 2C2C domain match closely for $\sigma \in [30°, 180°]$, but substantial differences arise outside of this range. Typically, an offset in amplitude and phase is found either on the entire PS ($\sigma \in [-150°, -90°]$), on the aft half of the SS ($\sigma \in [-60°, -30°]$), or in both of these areas ($\sigma = 0°$). The discrepancy is especially significant in the latter case, not only as it encompasses most of the blade surface, but also due to its magnitude. The two solutions differ by up to $\Delta C_{p(1)} = 0.75$ and $\Delta\phi_{p(1)} = 120°$. This case thus highlights that a substantial error can be introduced by considering only spatial wave modes in the formulation of non-reflecting boundary conditions.

The Spectral NRBC produces consistent results on all three domains. Figure 6.50b shows that changing the outlet boundary position alters the quantification of Ξ by less than 6 % in all cases. Truncating analogically the domain inflow brings a similarly low alteration $\Delta\Xi < 7\,\%$ for all IBPAs but $\sigma = -120°$. Here it rises to 20 % and forms thus a singular exception from the overall trend which will be discussed further.

The unsteady blade pressure distributions exhibit low sensitivity to the position of either boundary (Figure 6.51). A change of the upstream domain extent from

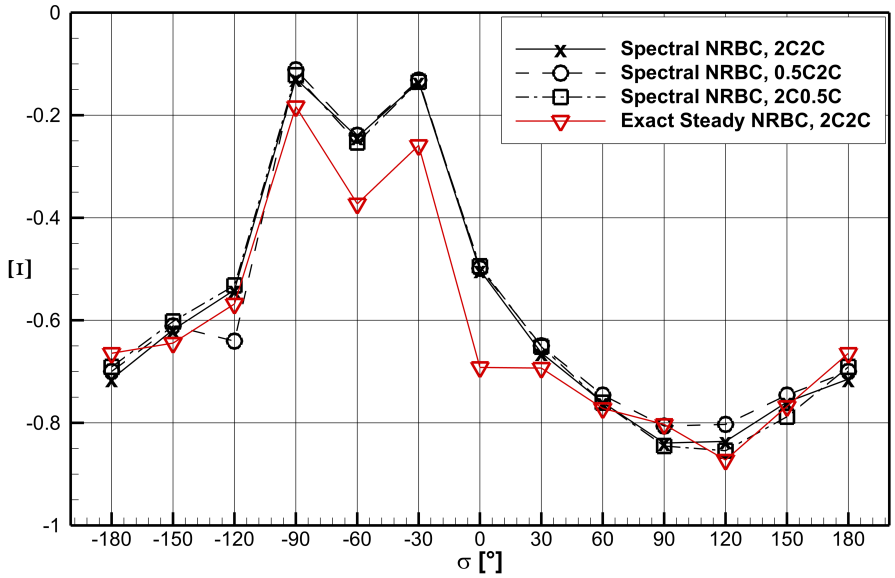

(a) Aerodynamic damping curve predictions using different domain extents and boundary conditions.

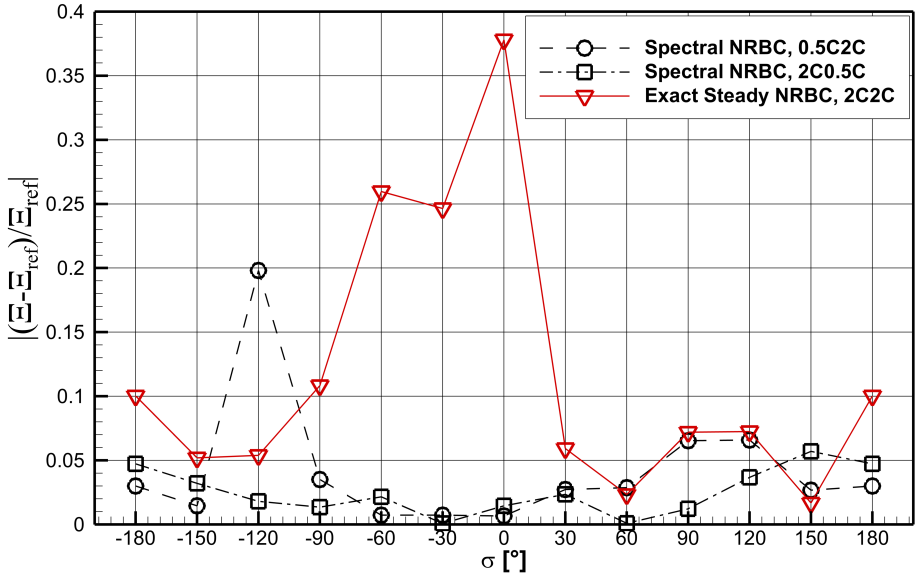

(b) Relative difference to a reference computation performed on the 2C2C domain with the Spectral NRBC.

Figure 6.50: Aerodynamic damping versus IBPA.

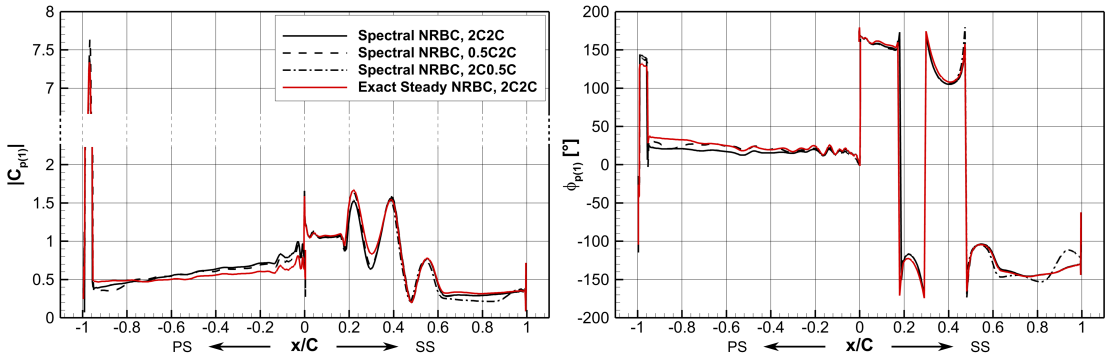

(a) $\sigma = -150°$

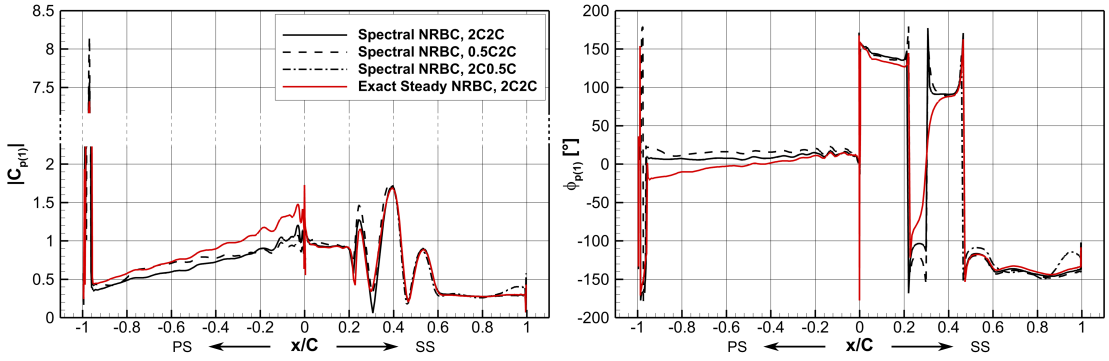

(b) $\sigma = -120°$

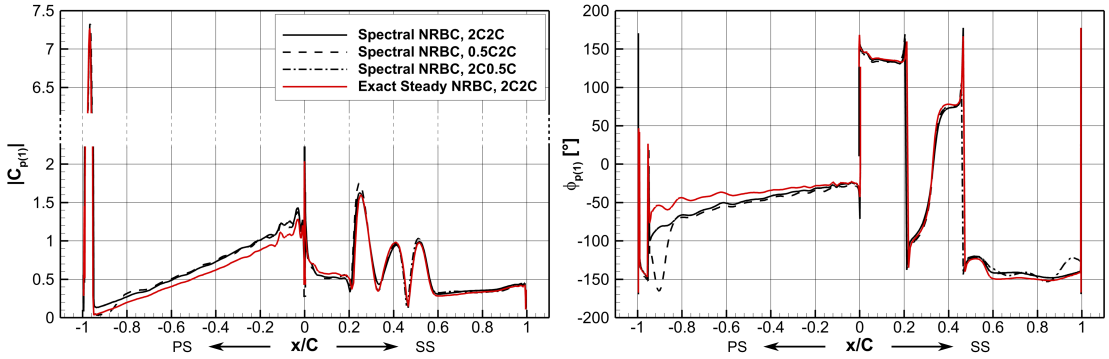

(c) $\sigma = -90°$

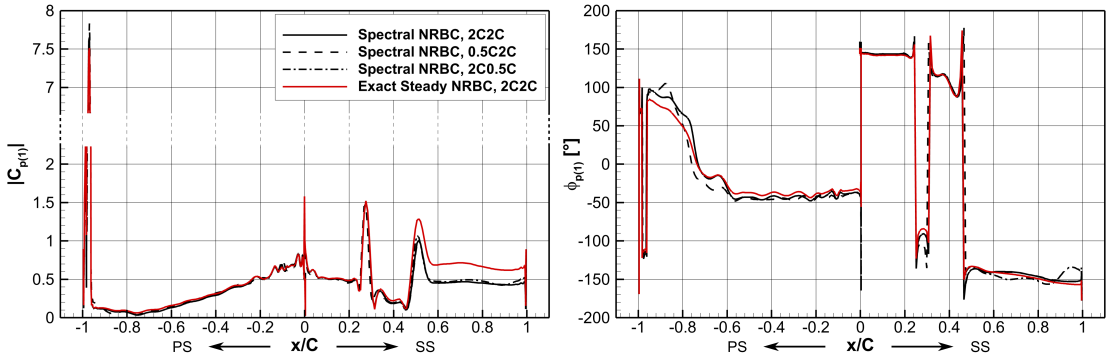

(d) $\sigma = -60°$

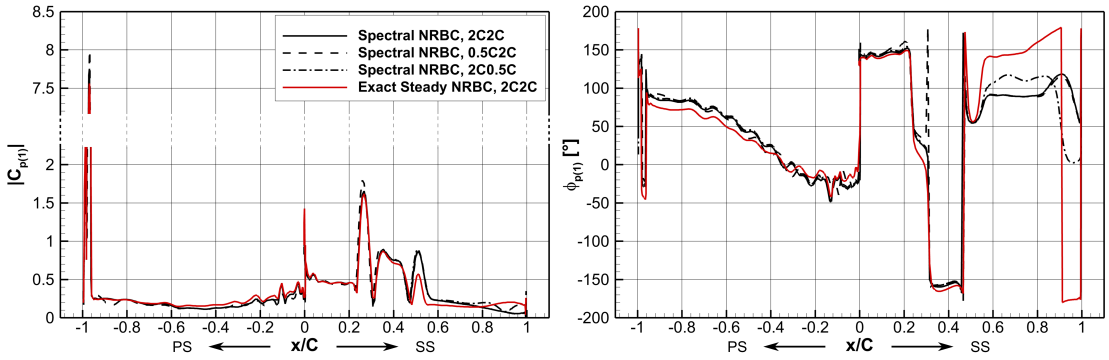

(e) $\sigma = -30°$

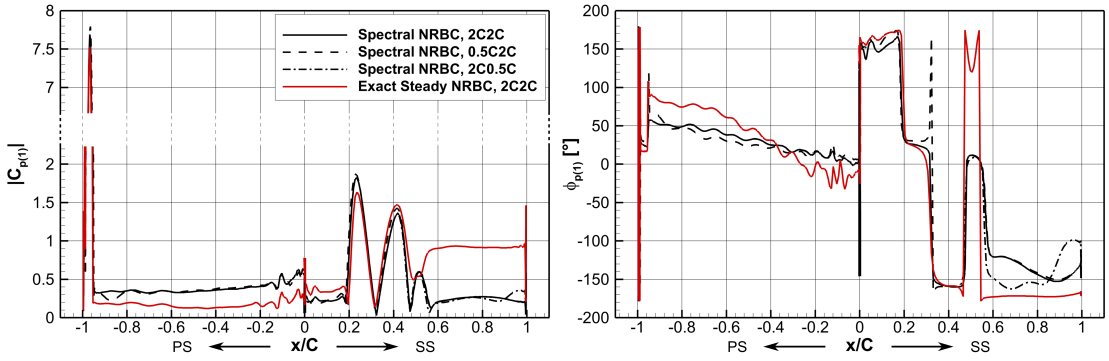

(f) $\sigma = 0°$

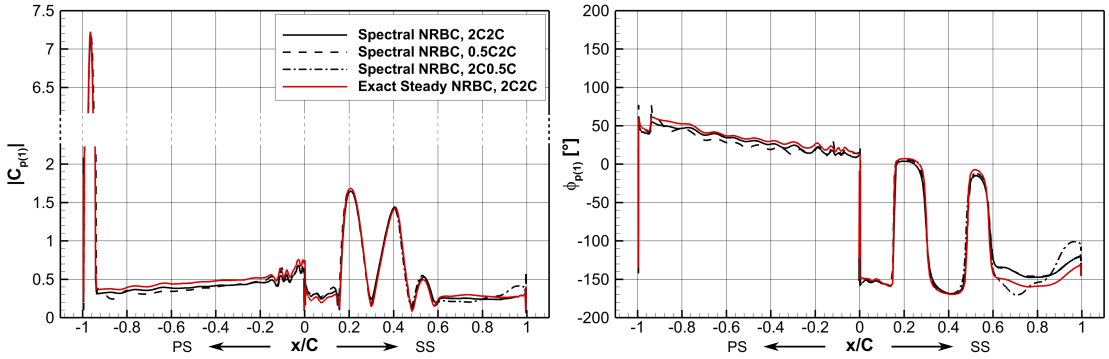

(g) $\sigma = 30°$

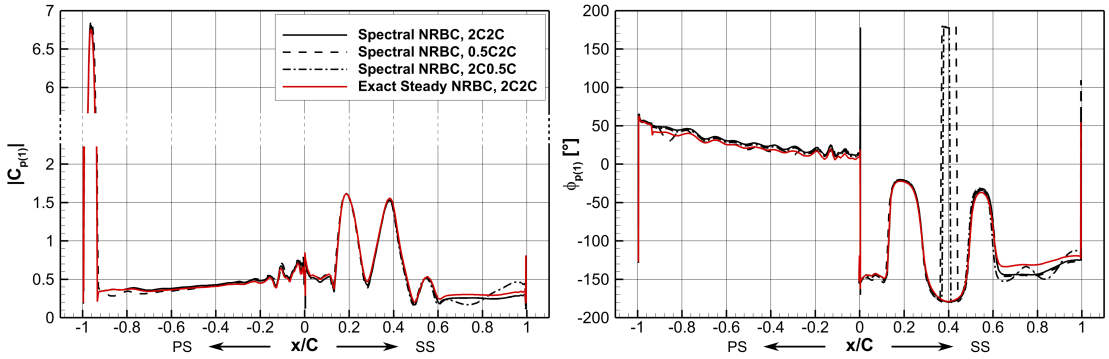

(h) $\sigma = 60°$

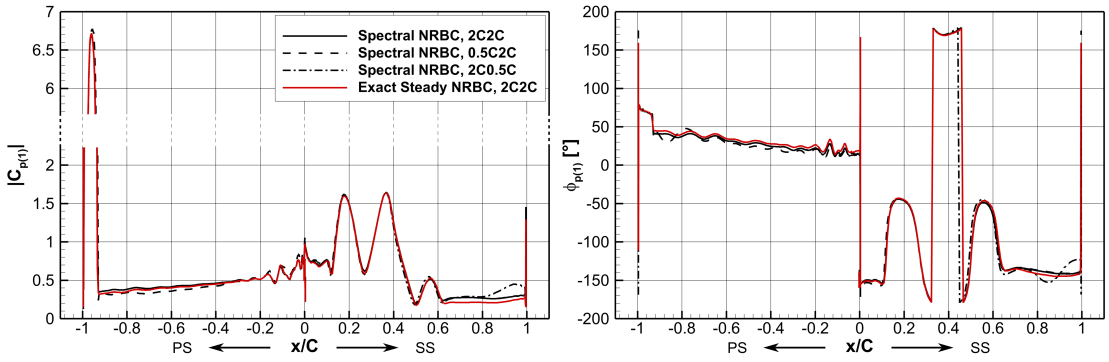

(i) $\sigma = 90°$

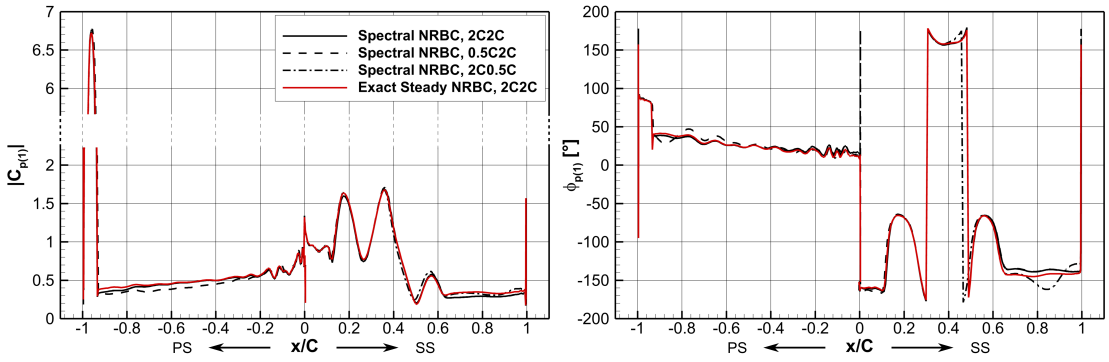

(j) $\sigma = 120°$

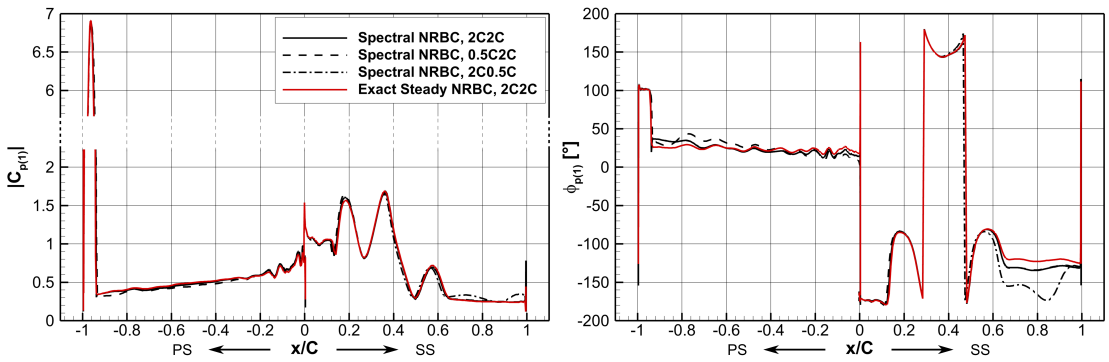

(k) $\sigma = 150°$

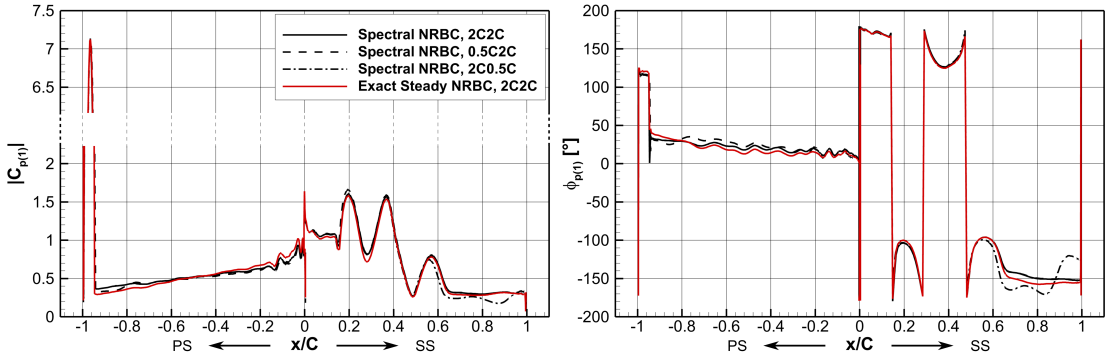

(l) $\sigma = 180°$

Figure 6.51: Distributions of amplitude ($|C_{p(1)}|$, left) and phase ($\phi_{p(1)}$, right) of the 1^{st} unsteady blade pressure harmonic.

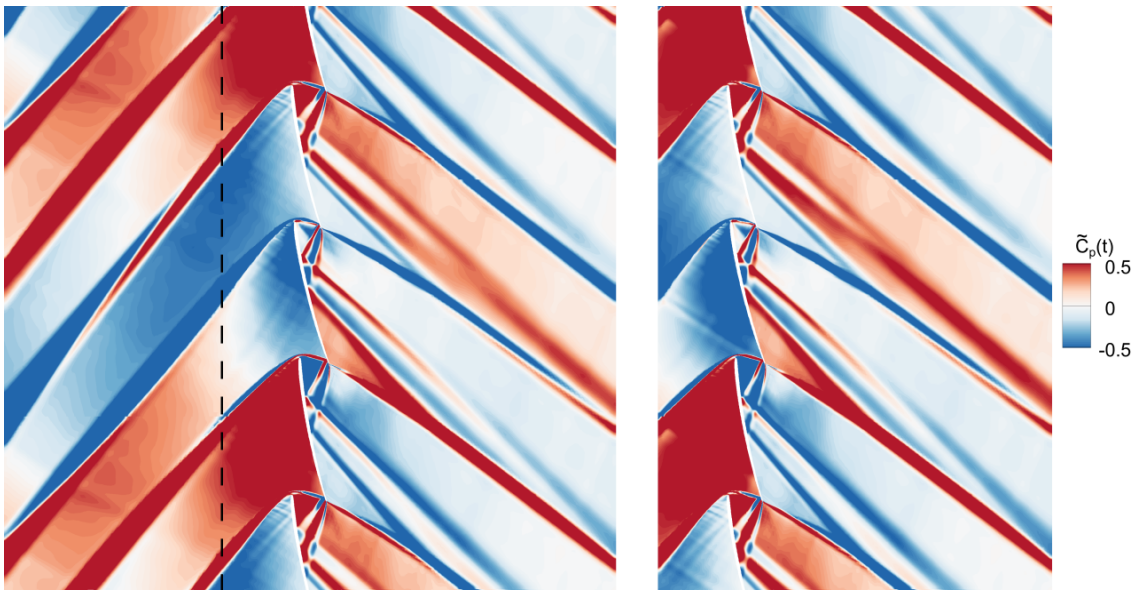

Figure 6.52: Contours of instantaneous pressure fluctuations on the 2C2C (left) and 0.5C2C (right) domains for $\sigma = -120°$ with the Spectral NRBC. Dashed line indicates the position of the 0.5C2C domain inlet.

$2C$ to $0.5C$ induces only a minor offset in the PS distributions ($\Delta C_{p(1)} < 0.1$, $\Delta\phi_{p(1)} < 10°$), while the SS predictions remain virtually unaffected. An analogical outflow truncation produces fluctuations in the aft SS distributions on account of stronger reflections of the downstream propagating shockwaves. The peak discrepancy between the long and short outflow solutions amounts to $\Delta C_{p(1)} \approx 0.2$ and $\Delta\phi_{p(1)} \approx 90°$, but only locally on a very small extent of the blade surface. Its effect on the integral damping quantification is therefore limited.

The case of $\sigma = -120°$ stands out from the overall trend by yielding a nearly three times higher sensitivity of Ξ to the inflow extent than in any other case. However, the plots of unsteady blade pressure distribution in Fig. 6.51b do not show any qualitative difference to other IBPAs. The change of inlet boundary position produces an offset in both phase and amplitude over most of the PS while having nearly no effect on the SS distribution. At $\Delta C_{p(1)} \approx 0.1$ and $\Delta\phi_{p(1)} \approx 9°$, neither offset is larger than at other IBPAs. The difference is that both of the offsets are present and they cover a larger portion of the blade surface, which results in a higher alteration of the aerodynamic damping coefficient.

The absence of a major qualitative change with upstream domain truncation is further documented in Fig. 6.52. Solutions on the reference 2C2C (left) and truncated 0.5C2C (right) domains are compared in terms of instantaneous pressure fluctuation contours. The following definition of pressure coefficient is used:

$$\tilde{C}_p(t) = \frac{p(t) - \overline{p(t)}}{\frac{h}{C}(p_{01} - p_2)}. \tag{6.7}$$

The upstream domain extent affects mainly the amplitude of pressure fluctuations

and not their pattern. They are more pronounced on the 0.5C2C domain, as already shown in the plots of unsteady blade surface pressure distribution (Fig. 6.51b). Qualitative differences are limited to the topology of bow-shock reflections emanating from the inlet boundary. As a result, they impact the blade surface in a different spot.

The variation in aerodynamic damping with inflow position is partly caused by a mismatched operating point. The values of total pressure, total temperature and flow angle, prescribed at the inlet of the truncated domain, are based on corresponding circumferential averages extracted from a steady-state computation on the 2C2C domain. Due to the nonlinearity of the flow field, there is a small difference between the circumferential averages extracted from a steady-state computation and from a time-averaged unsteady computation. In the case of $\sigma = -120°$, this difference amounts to $\Delta p_{01} = 17\,\mathrm{Pa}$, $\Delta T_{01} = 0.03\,\mathrm{K}$ and $\Delta\beta_1 = 0.04°$. Although the discrepancy may seem small enough to be insignificant, it affects notably the quantification of aerodynamic damping. An additional short-inlet computation was performed for this IBPA, using the corrected boundary conditions based on the unsteady long-inlet solution. The difference between the 2C2C and 0.5C2C damping predictions, amounting originally to 19.8 %, decreased to 12.9 %. Such impact of a slight modification of the inlet boundary conditions manifests how extremely sensitive the unsteady flow solution of a supersonic blade cascade is to the prescribed inflow state.

The supersonic turbine cascade manifested a markedly slower convergence than the subsonic and transonic test-cases STCF10 and STCF4. The temporal evolution of the aerodynamic damping coefficient exhibited strong fluctuations with a slowly diminishing amplitude, although a one-period moving average typically converged within several oscillation cycles. The solution was considered as converged when Ξ varied by less than 0.1 % during the last oscillation cycle and when its moving average changed by less than 0.1 % in the last 5 oscillation cycles. Depending on the IBPA, convergence on the 2C2C domain was reached after 7 to 30 cycles with the Spectral NRBC and after 8 to 35 cycles with the Exact Steady NRBC. The Spectral NRBC thus did not exhibit a worse convergence rate, in contrast to what has been reported for some applications in the past and attributed to the phase-lagged calculation of temporal harmonics [156].

A representative example of the convergence behaviour is provided in Fig. 6.53 for $\sigma = 0°$. Temporal evolution of the aerodynamic damping coefficient is shown for both boundary conditions on the reference domain and for the Spectral NRBC additionally on the two truncated domains. On the 2C2C domain, the damping coefficient arrives within 1 % of the converged value already after 4 oscillation cycles with the Spectral NRBC and after 6 cycles with the Exact Steady NRBC. However, in order to obtain a convergence within 0.1 %, the number of simulated cycles needs to be significantly higher at 15 and 13 respectively.

One might expect that faster convergence would be achieved by reducing the domain extent, but the results of this action are ambivalent on the M8 cascade. In the example shown in Fig. 6.53, moving the inlet closer to the blade accelerates the 0.1 % convergence from 15 to 10 cycles, but changing analogically the outlet position

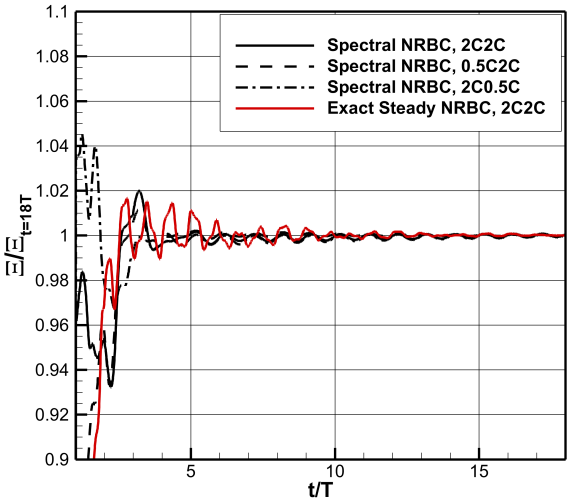

Figure 6.53: Convergence of the aerodynamic damping coefficient for $\sigma = 0°$

stretches it to 16 cycles. At other investigated IBPAs, the effect of truncating the domain on either end was sometimes beneficial and sometimes detrimental. The 0.1 % convergence was always reached at the latest after 30 cycles.

Chapter 7

Conclusions and Future Work

7.1 Conclusions

This thesis deals with a numerical prediction of flutter in turbomachinery blade cascades. A bespoke unsteady flow solver for computations on deforming domains has been developed and implemented in C++ by the author. After testing the computational model on the case of an isolated airfoil, it was applied to the assessment of aeroelastic stability for three blade cascades with a subsonic, transonic and supersonic flow regime. The analysis focused primarily on the performance of non-reflecting boundary conditions, motivated by the high sensitivity of flutter predictions to perturbations emanating from the inflow and outflow boundaries. The Spectral NRBC was shown to be highly successful in preventing the formation of spurious wave reflections, providing thus an accurate prediction of aerodynamic damping even for complex flow-fields. Although the wave reflections are not always completely suppressed on account of the underlying linearised model, their magnitude is low enough to have only a minor effect on the near-blade flow field. The solution exhibits only a very mild sensitivity to the inflow and outflow positions, which enables employing highly truncated domains without compromising accuracy. The study has further demonstrated that using a boundary condition that fails to suppress the spurious wave reflections can result in a fundamentally incorrect aeroelastic assessment.

Numerical solution methods. The finite volume discretisation employs Liou's AUSM$^+$-up scheme [120] for the evaluation of inviscid fluxes. This approach was selected for its applicability to a wide range of flow regimes, as the investigated test cases comprise a low subsonic airfoil with a freestream $M = 0.15$ as well as a supersonic blade cascade with a maximum $M = 1.95$. In both of these cases, the scheme contributed to a satisfactory convergence behaviour and did not produce spurious pressure oscillations in low-speed regions, known to afflict the original AUSM$^+$ version [121]. A gradient reconstruction and limiting procedure was applied to increase the spatial order of accuracy. A least squares approximation of gradients with a vertex-based stencil was used, employing initially an inverse distance weighting exponent $k = \frac{3}{2}$. However, this value was found to cause the solution to diverge in some cases, which was resolved by modifying the setting to $k = 1$. Although this

modification may on some meshes decrease the accuracy of gradient reconstruction, it is still sufficient to provide a second-order accurate flux evaluation. Gradient reconstruction is followed by imposing a limiter to prevent the formation of oscillations near discontinuities. Based on a comparison of six gradient limiting strategies, the face-based technique of Delis and Nikolos [36] in combination with the van Albada-van Leer limiter was adopted. It was shown to produce a sharp shockwave resolution and achieve fast convergence, absent of residual stall.

Aeroelastic analysis of an isolated airfoil. The computational model was first tested on the case of an isolated NACA 0012 airfoil, before proceeding to the more complex problem of blade cascades. The analysis included a steady-state case, prescribed torsion-mode vibrations and fully coupled oscillations with two degrees of freedom. In the first two cases, the numerical solution was validated by comparison with experimental data. The predictions of blade pressure distribution achieved a close agreement with the measurements, in terms of both the steady-state flow and the unsteady fluctuations. It was shown that adding a vortex correction to the far-field boundary condition improves the accuracy of aerodynamic force prediction on truncated domains. However, this method is not applicable to unsteady flows. The fully coupled simulations of airfoil oscillations with two degrees of freedom predicted that as the freestream velocity is increases, the system undergoes a transition from damped oscillations through torsional divergence to flutter instability. The trends as well as the onset velocities were consistent with numerical results of other authors.

Non-reflecting boundary conditions in steady-state flows. A steady-state solution was first performed for each of the blade cascades investigated on aeroelastic stability, i.e. for a subsonic compressor cascade STCF10, a transonic turbine cascade STCF4 and a supersonic turbine cascade M8. The steady-state predictions obtained with the Exact Steady NRBC and with the Simple Turbomachinery BC were nearly identical in subsonic flow conditions, found at both boundaries of STCF10 and at the inlet of STCF4. However, profound differences occurred in the presence of shockwaves, characterising the outlet of STCF4 and both boundaries of M8. The solution produced by the Exact Steady NRBC was nearly free of spurious wave reflections and exhibited little sensitivity to the boundary position. Although the perturbations gained slightly on intensity as the boundaries were moved closer to the blades, the near-blade flow field remained largely unaffected. The axial domain extent could thus be reduced to half a chord upstream and downstream of the blades without compromising accuracy of the solution, even in the case of the M8 cascade with a supersonic inflow. In contrast, the Simple Turbomachinery BC produced strong shockwave reflections at the STCF4 outlet, with an intensity and topology varying in function of the domain extent. These perturbations propagated upstream and modified the near-blade flow-field, introducing a substantial error into the aerodynamic characterisation of the cascade. On the M8 cascade, the Simple Turbomachinery BC failed to produce a converged solution.

Non-reflecting boundary conditions in flutter predictions. The Spectral NRBC exhibited good reflection properties in unsteady flow solutions on all three blade cascades. On the subsonic cascade STCF10, the predicted aerodynamic damping curve matched closely numerical results of other authors even in the vicinity of

acoustic resonance peaks. An examination of the unsteady flow field did not show any evidence of reflected waves. A satisfactory agreement of calculated aerodynamic damping with experimental data was achieved on the transonic STCF4 cascade. Although weak shockwave reflections were found to emanate from the outlet boundary and propagate upstream, they did not affect the quantification of aerodynamic damping significantly. Similar observations were made also for the M8 cascade. This test case is challenging due to the supersonic inflow conditions, inducing the formation of a detached bow shock that propagates towards the inlet boundary. The Spectral NRBC, being based on the linearised form of Euler equations, did not achieve a full suppression of spurious shockwave reflections in the highly nonlinear flow field. However, the weak perturbations formed at the boundaries had only a very limited impact on the unsteady flow solution in blade vicinity.

A comparison of the Spectral NRBC with the Exact Steady NRBC and the Simple Turbomachinery BC demonstrated that the use of boundary conditions with good reflection properties is vital for the accuracy of aeroelastic evaluations. Importantly, this conclusion applies also to blade cascades with a subsonic flow regime. There the spurious wave reflections may not be imminently obvious, in contrast to flows featuring shockwaves, yet they can have a profound effect on the unsteady flow solution. The Exact Steady NRBC predicted the damping coefficient in a reasonable agreement with the Spectral NRBC only in cases with predominant circumferential wave-modes, such as at most IBPAs of the transonic STCF4 cascade. However, even if the integral damping value was similar, clear evidence of unsuppressed wave reflections could be found in the flow-field obtained with the Exact Steady NRBC. The damping predictions deviated from the Spectral NRBC solution the furthest near acoustic resonance conditions and in the case of in-phase blade vibrations, characterised by a boundary-normal wave propagation. The discrepancy amounted up to 215 % on the subsonic cascade STCF10, 51 % on the transonic cascade STCF4 and 38 % on the supersonic cascade M8. The Simple Turbomachinery BC provided on the STCF10 cascade a similarly unsatisfactory performance as the Exact Steady NRBC and mostly failed to converge in the other two test-cases.

Solution sensitivity to domain extent. The sensitivity of aeroelastic assessments to axial domain extent is highly dependent on the presence of strong gradients and discontinuities in the flow-field. Results obtained with the Spectral NRBC were virtually unaffected by the inlet boundary position of STCF4 thanks to the highly uniform subsonic inflow. In supersonic flows featuring shockwaves, such as at the outlet of STCF4 and at both boundaries of M8, the effect of domain truncation gained on significance. Maximum variations of the aerodynamic damping coefficient amounted to 9.7 % (STCF4 outlet), 5.7 % (M8 outlet) and 12.9 % (M8 inlet). In spite of the quantitative change in damping, the unsteady flow-field remained qualitatively consistent. Although the shockwave reflections became more pronounced with the boundaries moved closer to the blades, they remained relatively weak even with a half-chord boundary distance. The Exact Steady NRBC exhibited similar sensitivity to domain extent on STCF4, but in case of the supersonic cascade M8, the position of either boundary affected the damping quantification by more than 300 %.

Effect of boundary conditions on convergence. It has been reported in the

past that the Spectral NRBC suffers from slower convergence on account of the phase-lagged updating procedure of temporal Fourier coefficients [158]. This issue did not appear in the present applications where the number of oscillation cycles to reach convergence was comparable to the other two boundary conditions. Overall, the slowest convergence of the aerodynamic damping coefficient was experienced on the supersonic cascade M8, where up to 35 oscillation cycles needed to be simulated. Domain truncation helped to accelerate convergence in some cases, but it had an adverse effect in others.

7.2 Review of Objectives

Objectives related to the implementation of the computational model:

- **Devise a mesh motion strategy for flow solution on deforming domains.** A computationally inexpensive analytical method for grid motion on domains with oscillating blades was implemented. The technique managed to maintain high mesh quality even with large blade displacements.
- **Analyse techniques for gradient reconstruction and limiting.** A weighted least squares method was employed for the reconstruction of gradients. The inverse distance weighting exponent set to $k = 1$ achieved an optimal combination of accuracy and stability. Six techniques were investigated for the subsequent gradient limiting step. The approach of Delis and Nikolos [36] adopting the van Albada-van Leer limiter was found as the most advantageous for the considered applications.
- **Implement non-reflecting boundary conditions.** Two non-reflecting boundary condition formulations were successfully implemented, namely the Exact Steady NRBC of Giles [58] for steady flows and the Spectral NRBC of Schlüß for periodic unsteady flows.
- **Validate the computational model.** The solver was extensively validated by comparing the present predictions with experimental data and with numerical results of other authors. Overall, a very good agreement was achieved, although some discrepancy appeared in predicting the phase of unsteady pressure fluctuations downstream of a shockwave. This mismatch was ascribed to the inviscid flow model.

Objectives related to solver validation and analysis of non-reflecting boundary conditions for aeroelastic assessment:

- **Analyse the performance of Spectral NRBC in nonlinear flows.** The Spectral NRBC was shown to have good reflection properties even in applications with a highly nonlinear flow-field, including a blade cascade with a supersonic inflow. Although weak shockwave reflections were discernible in some cases, their effect on the near-blade flow solution and on the aeroelastic assessment was insignificant.

- **Quantify the impact of unsuppressed wave reflections on aeroelastic assessments.** A comparison of the Spectral NRBC with two other boundary conditions demonstrated that an effective suppression of wave reflections is essential for the accurate prediction of aerodynamic damping. Perturbations emanating from the inlet and outlet boundaries may produce a fundamentally unphysical solution or cause the solver to diverge.
- **Analyse sensitivity of flutter predictions to domain extent.** The influence of boundary position was analysed by comparing solutions on domains with different axial lengths. The quantification of aerodynamic damping varied significantly when using boundary conditions with inferior reflection properties. In contrast, the Spectral NRBC yielded consistent predictions without a qualitative alteration of the unsteady flow field. Thus it enables the adoption of highly truncated domains without compromising the solution accuracy.

7.3 Future Work Recommendations

The outcomes of this thesis can serve as a basis for future research, targeted primarily to improve the fidelity of the present unsteady flow solver and to enhance further the applicability of non-reflecting boundary conditions.

- The present computational model describes an inviscid two-dimensional flow. The inclusion of turbulence modelling could further improve the fidelity of aeroelastic assessments. In particular, according to findings presented in Sec. 6.3, a more accurate prediction of unsteady pressure phase downstream of a shock impingement on the blade surface could be achieved. Extending the model to three dimensions would open up the possibility to study a wide range of intriguing aeroelastic problems, such as for example the effect of tip leakage flows on turbine blade flutter.
- A part of this study is the assessment of solution sensitivity to domain extent. When the position of either the inlet or the outlet boundary is changed, the imposed average values of total pressure, total temperature, flow angle and static pressure need to be slightly altered in order to maintain a constant operating point. As finding the target modified values is a lengthy iterative procedure, it is not feasible to perform it individually for each investigated IBPA. Instead, the matching of operating point was performed only once for the steady-state solution and the outcome was then employed in all unsteady flow simulations. Due to the strong nonlinearity of transonic and supersonic turbomachinery flows, this can cause a slight alteration of the operating point across the IBPA range and affect the aerodynamic damping prediction. A particularly sensitive to the exact operating point setting is the turbine cascade M8 with a supersonic inflow, for which altering the inlet boundary condition by $\Delta p_{01} = 17\,\mathrm{Pa}$, $\Delta T_{01} = 0.03\,\mathrm{K}$ and $\Delta\beta_1 = 0.04°$ modified the damping prediction by nearly 7 %. Therefore, it would be desirable to devise a more

elaborate matching procedure that would reduce the variation of operating point with IBPA.

- The Spectral NRBC was shown to exhibit good reflection properties even in strongly nonlinear unsteady flows. Nevertheless, reflections of shockwaves were not eliminated completely and generated weak perturbations, discernible in the density gradient field and in unsteady pressure distributions on the aft portion of blade suction side. A mild variation of aerodynamic damping predictions with domain extent was also observed. These deficiencies were ascribed to the inherent limitation of the Spectral NRBC, resulting from its derivation using linearised Euler equations. In order to improve further the suppression of wave reflections, development of a higher order extension could be beneficial. However, it needs to be considered that even in the present form the Spectral NRBC is highly complex and intricate to implement.

- A second limitation of the Spectral NRBC arises from the requirement that the flow is periodic in both space and time. This restricts its applicability in aeroelastic analysis exclusively to the uncoupled energy method, prescribing harmonic blade oscillations based on an a priori structural analysis. While the uncoupled approach is known to yield sufficiently accurate predictions for conventional blades, novel designs may require the use of fully coupled fluid-structure interaction simulations. Moreover, the transient behaviour of the system may also be of interest. The Spectral NRBC cannot be used in these cases and the available alternatives, such as temporally local approximate boundary conditions, may produce unphysical wave reflections leading to an inaccurate aeroelastic assessment [157]. The development of an improved non-reflecting boundary condition formulation for aperiodic flows therefore remains an open challenge.

References

Author's publications

[1] M. Pátý and J. Halama. "Numerical Simulation of Aeroelastic Effects for an Airfoil with Two Degrees of Freedom". In: *ACC Journal* 25.1 (2019).

[2] M. Pátý and J. Halama. "On the Use of a Flux-Splitting Scheme in the Numerical Flutter Analysis of a Low-Pressure Turbine Stage". In: *Acta Polytecnica* 61.SI (2021).

[3] M. Pátý and J. Halama. "On the Application of Non-Reflecting Boundary Conditions to a Turbine Flutter Simulation with a Supersonic Inlet". In: *ESCO 2020*. 2020.

Bibliography

[4] J. J. Adamczyk. "Model Equation for Simulating Flows in Multistage Turbomachinery". In: *ASME Paper No. 85-GT-226* (1985).

[5] T. J. Akai and H. Atassi. "Aerodynamic and Aeroelastic Characteristics of Oscillating Loaded Cascades at Low Mach Number—Part II: Stability and Flutter Boundaries". In: *Journal of Engineering for Power* 102.2 (Apr. 1980), pp. 352–356. ISSN: 0022-0825.

[6] S. Allmaras, V. Venkatakrishnan and F. Johnson. "Farfield Boundary Conditions for 2-D Airfoils". In: 17th AIAA Computational Fluid Dynamics Conference. 2005.

[7] H. Atassi and T. J. Akai. "Aerodynamic and Aeroelastic Characteristics of Oscillating Loaded Cascades at Low Mach Number—Part I: Pressure Distribution, Forces, and Moments". In: *Journal of Engineering for Power* 102.2 (Apr. 1980), pp. 344–351. ISSN: 0022-0825.

[8] T. Barth and D. Jespersen. "The Design and Application of Upwind Schemes on Unstructured Meshes". In: 27th Aerospace Sciences Meeting. 1989.

[9] J. T. Batina. "Unsteady Euler Algorithm with Unstructured Dynamic Mesh for Complex-Aircraft Aerodynamic Analysis". In: *AIAA Journal* 29.3 (1991), pp. 327–333.

[10] P. Batten, C. Lambert and D. Causon. "Positively Conservative High-Resolution Convection Schemes for Unstructured Elements". In: *International Journal for Numerical Methods in Engineering* 39.11 (1996), pp. 1821–1838.

[11] O. Bendiksen. "Aeroelastic Problems in Turbomachines". In: *31st structures, structural dynamics and materials conference*. 1990, p. 1157.

[12] J. Benetka. *Měření kmitajícího profilu v různě vysokých měřících prostorech, Technical report Z-2610/81*. cz. Technical Report. Aeronautical Research and Test Institute, Prague, Letňany, 1981.

[13] M. Berger, M. Aftosmis and S. Muman. "Analysis of Slope Limiters on Irregular Grids". In: *43rd AIAA Aerospace Sciences Meeting and Exhibit*. 2012.

[14] J. Blazek. *Computational Fluid Dynamics: Principles and Applications*. Elsevier, 2015.

[15] D. Boffi and L. Gastaldi. "Stability and Geometric Conservation Laws for ALE Formulations". In: *Computer Methods in Applied Mechanics and Engineering* 193.42 (2004), pp. 4717–4739. ISSN: 0045-7825.

[16] A. Bölcs and T. Fransson. *Aeroelasticity in Turbomachines: Comparison of Theoretical and Experimental Cascade Results + Appendix A5*. EPFL Lausanne, 1986.

[17] W. Campbell. *Protection of Steam Turbine Disk Wheels from Axial Vibration*. eng. Schenectady, N.Y.: General electric company, 1924.

[18] M. S. Campobasso and M. B. Giles. "Stabilization of a Linear Flow Solver for Turbomachinery Aeroelasticity Using Recursive Projection Method". In: *AIAA Journal* 42.9 (2004), pp. 1765–1774.

[19] M. S. Campobasso and M. B. Giles. "Effects of Flow Instabilities on the Linear Analysis of Turbomachinery Aeroelasticity". In: *Journal of Propulsion and Power* 19.2 (2003), pp. 250–259.

[20] M. Campobasso and M. Giles. "Computing Linear Harmonic Unsteady Flows in Turbomachines with Complex Iterative Solvers". In: *17th AIAA Computational Fluid Dynamics Conference*. 2005.

[21] F. O. Carta and A. O. St. Hilaire. "Effect of Interblade Phase Angle and Incidence Angle on Cascade Pitching Stability". In: *Journal of Engineering for Power* 102.2 (Apr. 1980), pp. 391–396. ISSN: 0022-0825.

[22] C. Chahine, T. Verstraete and L. He. "A Comparative Study of Coupled and Decoupled Fan Flutter Prediction Methods Under Variation of Mass Ratio and Blade Stiffness". In: *Journal of Fluids and Structures* 85 (2019), pp. 110–125. ISSN: 0889-9746.

[23] J. Chassaing and G. Gerolymos. "Time-domain Implementation of Nonreflecting Boundary-Conditions for the Nonlinear Euler Equations". In: *Applied Mathematical Modelling* 31.10 (2007), pp. 2172–2188. ISSN: 0307-904X.

[24] T. Chen, P. Vasanthakumar and L. He. "Analysis of Unsteady Blade Row Interaction Using Nonlinear Harmonic Approach". In: *Journal of Propulsion and Power* 17.3 (2001), pp. 651–658.

[25] J. P. Clark et al. "The Effect of Airfoil Scaling on the Predicted Unsteady Loading on the Blade of a 1 and 1/2 Stage Transonic Turbine and a Comparison With Experimental Results". In: *Turbo Expo: Power for Land, Sea, and Air*. Vol. Volume 1: Aircraft Engine; Marine; Turbomachinery; Microturbines and Small Turbomachinery. V001T03A020. May 2000.

[26] W. S. Clark and K. C. Hall. "A Time-Linearized Navier–Stokes Analysis of Stall Flutter". In: *Journal of Turbomachinery* 122.3 (Feb. 1999), pp. 467–476. ISSN: 0889-504X.

[27] A. R. Collar. "The Expanding Domain of Aeroelasticity". In: *The Journal of the Royal Aeronautical Society* 50.428 (1946), pp. 613–636.

[28] H. R. Cox and A. G. Pugsley. *Theory of Loss of Lateral Control due to Wing Twisting*. London, Great Britain: Air Ministry. Aeronautical Research Committee. Reports and memoranda, no. 1506, 1933.

[29] E. F. Crawley and K. C. Hall. "Optimization and Mechanisms of Mistuning in Cascades". In: *Journal of Engineering for Gas Turbines and Power* 107.2 (Apr. 1985), pp. 418–426. ISSN: 0742-4795.

[30] P. I. Crumpton and M. B. Giles. "Implicit Time–Accurate Solutions on Unstructured Dynamic Grids". In: *International Journal for Numerical Methods in Fluids* 25.11 (1997), pp. 1285–1300.

[31] N. A. Cumpsty and J. H. Horlock. "Averaging Nonuniform Flow for a Purpose". In: *Journal of Turbomachinery* 128.1 (Feb. 2005), pp. 120–129. ISSN: 0889-504X.

[32] C. H. Custer et al. "Unsteady Simulation of a 1.5 Stage Turbine Using an Implicitly Coupled Nonlinear Harmonic Balance Method". In: *Turbo Expo: Power for Land, Sea, and Air*. Vol. Volume 8: Turbomachinery, Parts A, B, and C. June 2012, pp. 2303–2317.

[33] C. Degand and C. Farhat. "A Three-Dimensional Torsional Spring Analogy Method for Unstructured Dynamic Meshes". In: *Computers & Structures* 80.3 (2002), pp. 305–316. ISSN: 0045-7949.

[34] A. I. Delis and I. K. Nikolos. "A Novel Multidimensional Solution Reconstruction and Edge-Based Limiting Procedure for Unstructured Cell-Centered Finite Volumes with Application to Shallow Water Dynamics". In: *International Journal for Numerical Methods in Fluids* 71.5 (2013), pp. 584–633.

[35] A. I. Delis, I. Nikolos and M. Kazolea. "Performance and Comparison of Cell-Centered and Node-Centered Unstructured Finite Volume Discretizations for Shallow Water Free Surface Flows". In: *Archives of Computational Methods in Engineering* 18.1 (2011), pp. 57–118.

[36] A. Delis and I. Nikolos. "On a Solution Reconstruction and Limiting Procedure for Unstructured Finite Volumes". In: vol. American Institute of Mathematical Sciences (AIMS) Journal Vol 8. Proceedings of HYP2012 Conference. May 2014, pp. 491–499.

[37] H. Doi. "Fluid/Structure Coupled Aeroelastic Computations for Transonic Flows in Turbomachinery". PhD thesis. Stanford University, 2002.

[38] H. Doi and J. J. Alonso. "Fluid/Structure Coupled Aeroelastic Computations for Transonic Flows in Turbomachinery". In: *Turbo Expo: Power for Land, Sea, and Air*. Vol. Volume 4: Turbo Expo 2002, Parts A and B. June 2002, pp. 787–794.

[39] N. Donini. "Aeroelasticity of Turbomachines. Linearized Flutter Analysis". PhD thesis. Politecnicno di Milano, 2012.

[40] *Edge: Theoretical Formulation*. ISSN-1650-1942. FOI - Swedish Defense Research Agency, Stockholm. 2007.

[41] P. Eliasson et al. “Computations and Measurements of Unsteady Pressure on a Delta Wing with an Oscillating Flap”. In: *Proc. 3rd ECCOMAS CFD Conf., Paris, Wiley*. 1996, pp. 478–484.

[42] B. Engquist and A. Majda. “Absorbing Boundary Conditions for Numerical Simulation of Waves”. In: *Proceedings of the National Academy of Sciences* 74.5 (1977), pp. 1765–1766. ISSN: 0027-8424.

[43] J. I. Erdos, E. Alzner and W. McNally. “Numerical Solution of Periodic Transonic Flow through a Fan Stage”. In: *AIAA Journal* 15.11 (1977), pp. 1559–1568.

[44] L. E. Eriksson. “Generation of Boundary-Conforming Grids around Wing-Body Configurations Using Transfinite Interpolation”. In: *AIAA Journal* 20.10 (1982), pp. 1313–1320.

[45] C. Farhat, P. Geuzaine and C. Grandmont. “The Discrete Geometric Conservation Law and the Nonlinear Stability of ALE Schemes for the Solution of Flow Problems on Moving Grids”. In: *Journal of Computational Physics* 174.2 (2001), pp. 669–694. ISSN: 0021-9991.

[46] C. Farhat, M. Lesoinne and N. Maman. “Mixed Explicit/Implicit Time Integration of Coupled Aeroelastic Problems: Three-Field Formulation, Geometric Conservation and Distributed Solution”. In: *International Journal for Numerical Methods in Fluids* 21.10 (1995), pp. 807–835.

[47] *Fourth Standard Configuration Experimental Data*. `https://www.rpmturbo.com/testcases/STCF/STCF4_update/stcf4_update.htm`. Accessed: 2020-05-27.

[48] T. H. Fransson and M. Pandolfi. “Numerical Investigation of Unsteady Subsonic Compressible Flows Through an Oscillating Cascade”. In: *Turbo Expo: Power for Land, Sea, and Air*. Vol. Volume 1: Turbomachinery. V001T01A119. June 1986.

[49] T. Fransson and J. Verdon. “Updated Report on Standard Configurations for Unsteady Flow Through Vibrating Axial-Flow Turbomachine Cascades: Status as of July 1991”. In: *Royal Institute of Technology, Stockholm, Sweden and United Technologies Research Center, East Hartford, CT, Report* (1992).

[50] R. A. Frazer and W. J. Duncan. *The Flutter of Monoplanes, Biplanes and Tail Units*. London, Great Britain: Air Ministry. Aeronautical Research Committee. Reports and memoranda, no. 1255, 1931.

[51] K. K. Frey and S. Fleeter. “Combined-Simultaneous Gust and Oscillating Compressor Blade Unsteady Aerodynamics”. In: *ASME 1999 International Gas Turbine and Aeroengine Congress and Exhibition. Volume 4. Indianapolis, Indiana, USA*. June 1999.

[52] M. Frigo and S. G. Johnson. “FFTW: Fastest Fourier Transform in the West”. In: *Astrophysics Source Code Library* (2012).

[53] J. Garcia and G. Guruswamy. "Aeroelastic Analysis of Transonic Wings Using Navier-Stokes Equations and a Nonlinear Beam Finite Element Model". In: *40th Structures, Structural Dynamics, and Materials Conference and Exhibit*. 1999.

[54] G. A. Gerolymos. "Advances in the Numerical Integration of the Three-Dimensional Euler Equations in Vibrating Cascades". In: *Journal of Turbomachinery* 115.4 (Oct. 1993), pp. 781–790. ISSN: 0889-504X.

[55] G. A. Gerolymos. "Numerical Integration of the Blade-to-Blade Surface Euler Equations in Vibrating Cascades". In: *AIAA Journal* 26.12 (1988), pp. 1483–1492.

[56] P. Geuzaine, C. Grandmont and C. Farhat. "Design and Analysis of ALE Schemes with Provable Second-Order Time-Accuracy for Inviscid and Viscous Flow Simulations". In: *Journal of Computational Physics* 191.1 (2003), pp. 206–227. ISSN: 0021-9991.

[57] M. Giles. "An Approach for Multi-Stage Calculations Incorporating Unsteadiness". In: *Turbo Expo: Power for Land, Sea, and Air*. Vol. Volume 1: Turbomachinery. V001T01A092. June 1992.

[58] M. Giles. *Non-Reflecting Boundary Conditions for the Euler Equations*. Technical Report. Computational Fluid Dynamics Laboratory, Dept. of Aeronautics & Astronautics, MIT. CFDL-TR-88-1, 1988.

[59] M. Giles. *UNSFLO: A Numerical Method for the Calculation of Unsteady Flow in Turbomachinery*. Technical Report. Massachusetts Institute of Technology. Gas Turbine Laboratory Report Nr. 205, 1991.

[60] M. B. Giles. "Calculation of Unsteady Wake/Rotor Interaction". In: *Journal of Propulsion and Power* 4.4 (1988), pp. 356–362.

[61] M. B. Giles. "Nonreflecting Boundary Conditions for Euler Equation Calculations". In: *AIAA Journal* 28.12 (1990), pp. 2050–2058.

[62] M. E. Goldstein, W. Braun and J. J. Adamczyk. "Unsteady Flow in a Supersonic Cascade with Strong In-Passage Shocks". In: *Journal of Fluid Mechanics* 83.3 (1977), pp. 569–604.

[63] N. Gregory and C. O'Reilly. *Low-Speed Aerodynamic Characteristics of NACA 0012 Aerofoil Section, Including the Effects of Upper-Surface Roughness Simulating Hoar Frost*. London, Great Britain: Aeronautical Research Council, Reports and Memoranda no. 3726, 1970.

[64] B. Grüber and V. Carstens. "The Impact of Viscous Effects on the Aerodynamic Damping of Vibrating Transonic Compressor Blades—A Numerical Study ". In: *Journal of Turbomachinery* 123.2 (Feb. 2000), pp. 409–417. ISSN: 0889-504X.

[65] H. Guillard and C. Farhat. "On the Significance of the Geometric Conservation Law for Flow Computations on Moving Meshes". In: *Computer Methods in Applied Mechanics and Engineering* 190.11 (2000), pp. 1467–1482. ISSN: 0045-7825.

[66] G. P. Guruswamy and C. Byun. "Direct Coupling of Euler Flow Equations with Plate Finite Element Structures". In: *AIAA Journal* 33.2 (1995), pp. 375–377.

[67] T. Hagstrom. *On High-Order Radiation Boundary Conditions*. Springer, New York, 1997, pp. 1–21.

[68] J. Halama. "Numerical Solution of Single- and Two-Phase Internal Flow Problems". Habilitation. Czech Technical University in Prague, 2012.

[69] K. C. Hall, W. S. Clark and C. B. Lorence. "A Linearized Euler Analysis of Unsteady Transonic Flows in Turbomachinery". In: *Journal of Turbomachinery* 116.3 (July 1994), pp. 477–488. ISSN: 0889-504X.

[70] K. C. Hall and C. B. Lorence. "Calculation of Three-Dimensional Unsteady Flows in Turbomachinery Using the Linearized Harmonic Euler Equations". In: *Journal of Turbomachinery* 115.4 (Oct. 1993), pp. 800–809. ISSN: 0889-504X.

[71] K. C. Hall and P. D. Silkowski. "The Influence of Neighboring Blade Rows on the Unsteady Aerodynamic Response of Cascades". In: *Journal of Turbomachinery* 119.1 (Jan. 1997), pp. 85–93. ISSN: 0889-504X.

[72] K. Hall et al. "Frequency Domain Techniques for Complex and Nonlinear Flows in Turbomachinery". In: *33rd AIAA Fluid Dynamics Conference and Exhibit*. June 2003.

[73] K. C. Hall and E. F. Crawley. "Calculation of Unsteady Flows in Turbomachinery Using the Linearized Euler Equations". In: *AIAA Journal* 27.6 (1989), pp. 777–787.

[74] K. C. Hall and K. Ekici. "Multistage Coupling for Unsteady Flows in Turbomachinery". In: *AIAA Journal* 43.3 (2005), pp. 624–632.

[75] K. C. Hall, J. P. Thomas and W. S. Clark. "Computation of Unsteady Nonlinear Flows in Cascades Using a Harmonic Balance Technique". In: *AIAA Journal* 40.5 (2002), pp. 879–886.

[76] K. C. Hall and J. M. Verdon. "Gust Response Analysis for Cascades Operating in Nonuniform Mean Flows". In: *AIAA Journal* 29.9 (1991), pp. 1463–1471.

[77] P. Hartwich and S. Agrawal. "Method for Perturbing Multiblock Patched Grids in Aeroelastic and Design Optimization Applications". In: *13th Computational Fluid Dynamics Conference*. 1997.

[78] A. C. Haselbacher. "A Grid-Transparent Numerical Method for Compressible Viscous Flows on Mixed Unstructured Grids". PhD thesis. Loughborough University, Sept. 1999.

[79] M. E. Hayder, F. Q. Hu and M. Y. Hussaini. "Toward Perfectly Absorbing Boundary Conditions for Euler Equations". In: *AIAA Journal* 37.8 (1999), pp. 912–918.

[80] L. He. "An Euler Solution for Unsteady Flows Around Oscillating Blades". In: *Journal of Turbomachinery* 112.4 (Oct. 1990), pp. 714–722. ISSN: 0889-504X.

[81] L. He. "New Two-Grid Acceleration Method for Unsteady Navier Stokes Calculations". In: *Journal of Propulsion and Power* 9.2 (1993), pp. 272–280.

[82] L. He. "Unsteady Flow in Oscillating Turbine Cascades: Part 1—Linear Cascade Experiment". In: *Journal of Turbomachinery* 120.2 (Apr. 1998), pp. 262–268. ISSN: 0889-504X.

[83] L. He and J. D. Denton. "Inviscid-Viscous Coupled Solution for Unsteady Flows Through Vibrating Blades: Part 1—Description of the Method". In: *Journal of Turbomachinery* 115.1 (Jan. 1993), pp. 94–100. ISSN: 0889-504X.

[84] L. He and J. D. Denton. "Inviscid-Viscous Coupled Solution for Unsteady Flows Through Vibrating Blades: Part 2—Computational Results". In: *Journal of Turbomachinery* 115.1 (Jan. 1993), pp. 101–109. ISSN: 0889-504X.

[85] L. He and J. D. Denton. "Three Dimensional Time-Marching Inviscid and Viscous Solutions for Unsteady Flows Around Vibrating Blades". In: *Turbo Expo: Power for Land, Sea, and Air*. Vol. Volume 1: Aircraft Engine; Marine; Turbomachinery; Microturbines and Small Turbomachinery. V001T03A033. May 1993.

[86] L. He et al. "Analysis of Rotor-Rotor and Stator-Stator Interferences in Multi-Stage Turbomachines ". In: *Journal of Turbomachinery* 124.4 (Nov. 2002), pp. 564–571. ISSN: 0889-504X.

[87] L. He. "Method of Simulating Unsteady Turbomachinery Flows with Multiple Perturbations". In: *AIAA Journal* 30.11 (1992), pp. 2730–2735.

[88] S. Henninger et al. "Time-Domain Implementation of Higher-Order Non-Reflecting Boundary Conditions for Turbomachinery Applications". In: *Turbo Expo: Power for Land, Sea, and Air*. Vol. Volume 2B: Turbomachinery. June 2015.

[89] R. L. Higdon. "Initial-Boundary Value Problems for Linear Hyperbolic System". In: *SIAM Review* 28.2 (1986), pp. 177–217.

[90] C. Hirsch. *Numerical Computation of Internal and External Flows: The Fundamentals of Computational Fluid Dynamics*. Elsevier, 2007.

[91] E. H. Hirschel, H. Prem and G. Madelung. *Aeronautical Research in Germany: From Lilienthal until Today*. Berlin, Germany: Springer Science & Business Media, 2012.

[92] C. Hirt, A. Amsden and J. Cook. "An Arbitrary Lagrangian-Eulerian Computing Method for all Flow Speeds". In: *Journal of Computational Physics* 14.3 (1974), pp. 227–253. ISSN: 0021-9991.

[93] W. Höhn. "Numerical Investigation of Blade Flutter at or Near Stall in Axial Turbomachines". PhD thesis. Royal Institute of Technology, Stockholm, Sweden, 2000.

[94] D. Holmes and H. Chuang. "2D Linearized Harmonic Euler Flow Analysis for Flutter and Forced Response". In: *Unsteady Aerodynamics, Aeroacoustics, and Aeroelasticity of Turbomachines and Propellers*. Springer, New York, NY, 1993, pp. 213–230.

[95] R. Honzátko. “Numerical Simulations of Incompressible Flows with Dynamical and Aeroelastic Effects”. PhD thesis. Czech Technical University in Prague, Prague, Czech Republic, 2007.

[96] D. Hoyniak and S. Fleeter. “The Effect of Circumferential Aerodynamic Detuning on Coupled Bending-Torsion Unstalled Supersonic Flutter”. In: *Journal of Turbomachinery* 108.2 (Oct. 1986), pp. 253–260. ISSN: 0889-504X.

[97] M. von Hoyningen-Huene and A. R. Jung. “Comparison of Different Acceleration Techniques and Methods for Periodic Boundary Treatment in Unsteady Turbine Stage Flow Simulations ”. In: *Journal of Turbomachinery* 122.2 (Feb. 1999), pp. 234–246. ISSN: 0889-504X.

[98] W. Huang. “Practical Aspects of Formulation and Solution of Moving Mesh Partial Differential Equations”. In: *Journal of Computational Physics* 171.2 (2001), pp. 753–775. ISSN: 0021-9991.

[99] X. Huang. “Three-Dimensional Unsteady Flow in the Oscillating Turbine Blade Row”. PhD thesis. Durham University, 2006.

[100] M. Hubbard. “Multidimensional Slope Limiters for MUSCL-Type Finite Volume Schemes on Unstructured Grids”. In: *Journal of Computational Physics* 155.1 (1999), pp. 54–74. ISSN: 0021-9991.

[101] D. Huff. “Numerical Simulations of Unsteady, Viscous, Transonic Flow over Isolated and Cascaded Airfoils Using a Deforming Grid”. In: *19th AIAA, Fluid Dynamics, Plasma Dynamics, and Lasers Conference*. 1987, p. 1316.

[102] M. Imregun. “Prediction of Flutter Stability Using Aeroelastic Frequency Response Functions”. In: *Journal of Fluids and Structures* 9.4 (1995), pp. 419–434. ISSN: 0889-9746.

[103] A. Jameson. “Time Dependent Calculations Using Multigrid, with Applications to Unsteady Flows past Airfoils and Wings”. In: *10th Computational Fluid Dynamics Conference*. 1991.

[104] R. L. Jay and S. Fleeter. “Unsteady Aerodynamic Measurements in Forced Vibration Research”. In: *AGARD Manual on Aeroelasticity in Axial Flow Turbomachines, AGARD-AG-298*. Ed. by M. F. Platzer and F. O. Carta. Advisory group for aerospace research and development Neuilly-Sur-Seine (France), 1988.

[105] M. Jöcker. “Numerical Investigation of the Aerodynamic Vibration Excitation of High-Pressure Turbine Rotors”. PhD thesis. Royal Institute of Technology, Stockholm, Sweden, 2002.

[106] J. John Siegel et al. “Application of a Multi-Disciplinary Computing Environment (MDICE) for loosely coupled fluid-structural analysis”. In: *7th AIAA/USAF/NASA/ISSMO Symposium on Multidisciplinary Analysis and Optimization*. 1998.

[107] R. Kamakoti and W. Shyy. “Fluid-Structure Interaction for Aeroelastic Applications”. en. In: *Progress in Aerospace Sciences* 40 (2005), pp. 535–558. ISSN: 8.

[108] R. E. Kielb and K. R. V. Kaza. "Aeroelastic Characteristics of a Cascade of Mistuned Blades in Subsonic and Supersonic Flows". In: *Journal of Vibration, Acoustics, Stress, and Reliability in Design* 105.4 (Oct. 1983), pp. 425–433. ISSN: 0739-3717.

[109] B. Koobus and C. Farhat. "Second-Order Time-Accurate and Geometrically Conservative Implicit Schemes for flow Computations on Unstructured Dynamic Meshes". In: *Computer Methods in Applied Mechanics and Engineering* 170.1 (1999), pp. 103–129. ISSN: 0045-7825.

[110] H.-O. Kreiss. "Initial Boundary Value Problems for Hyperbolic Systems". In: *Communications on Pure and Applied Mathematics* 23.3 (1970), pp. 277–298.

[111] F. Lane. "System Mode Shapes in the Flutter of Compressor Blade Rows". In: *Journal of the Aeronautical Sciences* 23.1 (1956), pp. 54–66.

[112] C. B. Laney. *Computational Gasdynamics*. Cambridge university press, 1998.

[113] M. Lesoinne and C. Farhat. "Geometric Conservation Laws for Flow Problems with Moving Boundaries and Deformable Meshes, and their Impact on Aeroelastic Computations". In: *Computer Methods in Applied Mechanics and Engineering* 134.1 (1996), pp. 71–90. ISSN: 0045-7825.

[114] R. J. LeVeque. *Finite Volume Methods for Hyperbolic Problems*. Cambridge university press, 2002.

[115] R. J. LeVeque. *Numerical Methods for Conservation Laws*. Birkhäuser Verlag, Basel, Switzerland, 1992.

[116] H. D. Li and L. He. "Blade Aerodynamic Damping Variation With Rotor-Stator Gap: A Computational Study Using Single-Passage Approach". In: *ASME Turbo Expo 2003, collocated with the 2003 International Joint Power Generation Conference. Volume 4. Atlanta, Georgia, USA*. June 2003.

[117] H. D. Li and L. He. "Toward Intra-Row Gap Optimization for One and Half Stage Transonic Compressor". In: *Journal of Turbomachinery* 127.3 (Jan. 2005), pp. 589–598. ISSN: 0889-504X.

[118] H. Li and Z. Sheng. "A Check on the Energy Method of Predicting Blade Transonic Stall Flutter". In: *Turbo Expo: Power for Land, Sea, and Air*. Vol. Volume 4: Manufacturing Materials and Metallurgy; Ceramics; Structures and Dynamics; Controls, Diagnostics and Instrumentation; Process Industries; Technology Resources; General. V004T09A010. Sept. 1985.

[119] D. R. Lindquist and M. B. Giles. "Validity of Linearized Unsteady Euler Equations with Shock Capturing". In: *AIAA Journal* 32.1 (1994), pp. 46–53.

[120] M.-S. Liou. "A Sequel to AUSM, Part II: AUSM+-up for All Speeds". In: *Journal of Computational Physics* 214.1 (2006), pp. 137–170. ISSN: 0021-9991.

[121] M.-S. Liou. "A Sequel to AUSM: AUSM+". In: *Journal of Computational Physics* 129.2 (1996), pp. 364–382. ISSN: 0021-9991.

[122] M.-S. Liou and C. J. Steffen. "A New Flux Splitting Scheme". In: *Journal of Computational Physics* 107.1 (1993), pp. 23–39. ISSN: 0021-9991.

[123] J. F. Lubomski. “Status of NASA Full-Scale Engine Aeroelasticity Research”. In: *21st Struct., Structural Dyn., and Mater. Conf.* May 1980.

[124] J. Marshall and M. Giles. “Some Applications of a Time-Linearized Euler Method to Flutter & Forced Response in Turbomachinery”. In: *Unsteady Aerodynamics and Aeroelasticity of Turbomachines*. Springer, 1998, pp. 225–240.

[125] P.-A. Masserey, I. McBean and H. Lorini. “Analysis and Improvement of Vibrational Behaviour on the ND37 A Last Stage Blade”. In: *VGB PowerTech* 92 (8 July 2012).

[126] D. Mavriplis. “Revisiting the Least-Squares Procedure for Gradient Reconstruction on Unstructured Meshes”. In: *16th AIAA Computational Fluid Dynamics Conference*. 2003.

[127] D. J. Mavriplis and Z. Yang. “Construction of the Discrete Geometric Conservation Law for High-Order Time-Accurate Simulations on Dynamic Meshes”. In: *Journal of Computational Physics* 213.2 (2006), pp. 557–573. ISSN: 0021-9991.

[128] I. McBean et al. “Prediction of Flutter of Turbine Blades in a Transonic Annular Cascade”. In: *Journal of Fluids Engineering* 127.6 (May 2005), pp. 1053–1058. ISSN: 0098-2202.

[129] D. Micallef et al. “Three-Dimensional Viscous Flutter Analyses of a Turbine Cascade in Subsonic and Transonic Flows”. In: *ASME Turbo Expo 2012: Turbine Technical Conference and Exposition, Volume 7. Copenhagen, Denmark.* June 2012.

[130] F. Mishriky and P. Walsh. “Towards Understanding the Influence of Gradient Reconstruction Methods on Unstructured Flow Simulations”. In: *Transactions of the Canadian Society for Mechanical Engineering* 41.2 (2017), pp. 169–179.

[131] T. Miyakozawa. “Flutter and Forced Response of Turbomachinery with Frequency Mistuning and Aerodynamic Asymmetry”. PhD thesis. Duke University, Durham, North Carolina, 2008.

[132] F. Moyroud, G. Jacquet-Richardet and T. H. Fransson. “Aeroelasticity in Turbomachines: Some Aspects of the Effect of Coupling Modeling and Blade Material Changes”. In: *International Journal of Rotating Machinery* 6.4 (2000).

[133] T. Nagashim and D. Whitehead. *Linearized Supersonic Unsteady Flow in Cascades*. London, Great Britain: Aeronautical Research Council, Reports and Memoranda no. 3811, 19677.

[134] K. Namba M.and Nanba. “Unsteady Aerodynamic Work on Oscillating Annulat Cascades in Counter Rotation”. In: *Unsteady Aerodynamics, Aeroacoustics and Aeroelasticity of Turbomachines*. Ed. by K. C. Hall, R. E. Kielb and J. P. Thomas. Dordrecht: Springer Netherlands, 2006, pp. 177–188. ISBN: 978-1-4020-4605-6.

[135] M. Namba and A. Ishikawa. "Three-Dimensional Aerodynamic Characteristics of Oscillating Supersonic and Transonic Annular Cascades". In: *Journal of Engineering for Power* 105.1 (Jan. 1983), pp. 138–146. ISSN: 0022-0825.

[136] M. Namba. "Subsonic Cascade Flutter with Finite Mean Lift". In: *AIAA Journal* 13.5 (1975), pp. 586–593.

[137] R. H. Ni and F. Sisto. "Numerical Computation of Nonstationary Aerodynamics of Flat Plate Cascades in Compressible Flow". In: *Journal of Engineering for Power* 98.2 (Apr. 1976), pp. 165–170. ISSN: 0022-0825.

[138] W. Ning and L. He. "Computation of Unsteady Flows Around Oscillating Blades Using Linear and Nonlinear Harmonic Euler Methods". In: *Journal of Turbomachinery* 120.3 (July 1998), pp. 508–514. ISSN: 0889-504X.

[139] M. Nowinski and J. Panovsky. "Flutter Mechanisms in Low Pressure Turbine Blades". In: *Journal of Engineering for Gas Turbines and Power* 122.1 (Oct. 2000), pp. 82–88. ISSN: 0742-4795.

[140] J. Panovsky and R. E. Kielb. "A Design Method to Prevent Low Pressure Turbine Blade Flutter ". In: *Journal of Engineering for Gas Turbines and Power* 122.1 (200), pp. 89–98. ISSN: 0742-4795.

[141] J. S. Park and C. Kim. "Multi-Dimensional Limiting Process for Finite Volume Methods on Unstructured Grids". In: *Computers & Fluids* 65 (2012). Sixth International Conference on Computational Fluid Dynamics (ICCFD6), pp. 8–24. ISSN: 0045-7930.

[142] J. S. Park, S.-H. Yoon and C. Kim. "Multi-Dimensional Limiting Process for Hyperbolic Conservation Laws on Unstructured Grids". In: *Journal of Computational Physics* 229.3 (2010), pp. 788–812. ISSN: 0021-9991.

[143] *Tip Running Clearances Effects on Tip Vortices Induced Axial Compressor Rotor Flutter*. Vol. Volume 6: Structures and Dynamics, Parts A and B. June 2011, pp. 1243–1252.

[144] B. Perry. *Re-Computation of Numerical Results Contained in NACA Report No. 496*. Technical Report. NASA. Langley Research Center, Hampton, Virginia, United States, 2015.

[145] P. Petrie-Repar et al. "Advanced Flutter Analysis of a Long Shrouded Steam Turbine Blade". In: *Turbo Expo: Power for Land, Sea, and Air*. Vol. Volume 7B: Structures and Dynamics. V07BT35A022. June 2014.

[146] P. J. Petrie-Repar, A. McGhee and P. A. Jacobs. "Three-Dimensional Viscous Flutter Analysis of Standard Configuration 10". In: vol. Volume 5: Turbo Expo 2007. Turbo Expo: Power for Land, Sea, and Air. May 2007, pp. 665–674.

[147] C. L. Rumsey et al. *A User's Guide to CGNS*. Technical Memorandum. National Aeronautics and Space Administration. Langley Research Center Hampton, Virginia, United States, 2001.

[148] M. Sadeghi and F. Liu. "Coupled Fluid-Structure Simulation for Turbomachinery Blade Rows". In: *43rd AIAA Aerospace Sciences Meeting and Exhibit*. 2005.

[149] M. Sadeghi and F. Liu. "Computation of Cascade Flutter by Uncoupled and Coupled Methods". In: *International Journal of Computational Fluid Dynamics* 19.8 (2005), pp. 559–569.

[150] G. Saiz. "Turbomachinery Aeroelasticity Using a Time-Linearised Multi Blade-row Approach". PhD thesis. University of London, Imperial College of Science, Technology and Medicine, 2008.

[151] P. H. Saksono, W. G. Dettmer and D. Perić. "An Adaptive Remeshing Strategy for Flows with Moving Boundaries and Fluid–Structure Interaction". In: *International Journal for Numerical Methods in Engineering* 71.9 (2007), pp. 1009–1050.

[152] L. Salles and M. Vahdati. "Comparison of Two Numerical Algorithms for Computing the Effects of Mistuning of Fan Flutter". In: *Turbo Expo: Power for Land, Sea, and Air*. Vol. Volume 7B: Structures and Dynamics. V07BT34A018. June 2016.

[153] R. A. K. Sanches and H. B. Coda. "On Fluid–Shell Coupling Using an Arbitrary Lagrangian–Eulerian Fluid Solver Coupled to a Positional Lagrangian Shell Solver". In: *Applied Mathematical Modelling* 38.14 (2014), pp. 3401–3418. ISSN: 0307-904X.

[154] A. J. Sanders, K. K. Hassan and D. C. Rabe. "Experimental and Numerical Study of Stall Flutter in a Transonic Low-Aspect Ratio Fan Blisk ". In: *Journal of Turbomachinery* 126.1 (Mar. 2004), pp. 166–174. ISSN: 0889-504X.

[155] L. Sbardella and M. Imregun. "Linearized Unsteady Viscous Turbomachinery Flows Using Hybrid Grids ". In: *Journal of Turbomachinery* 123.3 (Feb. 2001), pp. 568–582. ISSN: 0889-504X.

[156] D. Schlüß and C. Frey. "Time Domain Flutter Simulations of a Steam Turbine Stage Using Sptectral 2D Non-Reflecting Boundary Conditions". In: *15th International Symposium on Unsteady Aerodynamics, Aeroacoustics & Aeroelasticity of Turbomachines (ISUAAAT15)*. June 2018.

[157] D. Schlüß and C. Frey. "Time Domain Implementation of a Spectral Non-Reflecting Boundary Condition for Unsteady Turbomachinery Flows". In: *24th ISABE Conference*. Proceedings of the 24th ISABE Conference. May 2019.

[158] D. Schlüß, C. Frey and G. Ashcroft. "Consistent Non-Reflecting Boundary Conditions for Both Steady and Unsteady Flow Simulations in Turbomachinery Applications". In: *ECCOMAS Congresses, Greece*. 2016.

[159] M. Schmitz et al. "Axial Turbine Blade Vibrations Induced by the Stator Flow". In: *Unsteady Aerodynamics, Aeroacoustics and Aeroelasticity of Turbomachines*. Springer, 2006, pp. 107–118.

[160] R. E. Sheldahl and P. C. Klimas. *Aerodynamic Characteristics of Seven Symmetrical Airfoil Sections Through 180-Degree Angle of Attack for Use in Aerodynamic Analysis of Vertical Axis Wind Turbines*. Tech. rep. Sandia National Labs., Albuquerque, NM (USA), Mar. 1981.

[161] S. Sieg. “High Cycle Fatigue and the War Fighter”. In: *Proceedings 5th National Turbine Engine High Cycle Fatigue Conference, Chandler, Arizona, USA*. 2000.

[162] P. D. Silkowski et al. “Computational-Fluid-Dynamics Investigation of Aeromechanics”. In: *Journal of Propulsion and Power* 18.4 (2002), pp. 788–796.

[163] P. Sivel. “Analysis of Spectral Non-Reflecting Boundary Conditions for Unsteady Simulations of Turbomachinery Flows in Terms of Predictive Quality and Computational Effort”. MA thesis. RWTH Aachen University, Oct. 2018.

[164] A. Slone, C. Bailey and M. Cross. “Dynamic Solid Mechanics Using Finite Volume Methods”. In: *Applied Mathematical Modelling* 27.2 (2003), pp. 69–87. ISSN: 0307-904X.

[165] A. Slone et al. “Dynamic Fluid–Structure Interaction Using Finite Volume Unstructured Mesh Procedures”. In: *Computers & Structures* 80.5 (2002), pp. 371–390. ISSN: 0045-7949.

[166] R. W. Smith. “AUSM(ALE): A Geometrically Conservative Arbitrary Lagrangian–Eulerian Flux Splitting Scheme”. In: *Journal of Computational Physics* 150.1 (1999), pp. 268–286. ISSN: 0021-9991.

[167] S. N. Smith. *Discrete Frequency Sound Generation in Axial Flow Turbomachines*. London, Great Britain: Aeronautical Research Council, Reports and Memoranda no. 3709, 1972.

[168] E. Sozer, C. Brehm and C. C. Kiris. “Gradient Calculation Methods on Arbitrary Polyhedral Unstructured Meshes for Cell-Centered CFD Solvers”. In: *52nd Aerospace Sciences Meeting*. 2014.

[169] S. Spekreijse. “Multigrid Solution of Monotone Second-Order Discretizations of Hyperbolic Conservation Laws”. In: *Mathematics of Computation* 49.179 (1987), pp. 135–155. ISSN: 00255718, 10886842.

[170] A. Srinivasan. “Flutter and Resonant Vibration Characteristics of Engine Blades: An IGTI Scholar Paper”. In: vol. Volume 4: Manufacturing Materials and Metallurgy; Ceramics; Structures and Dynamics; Controls, Diagnostics and Instrumentation; Education; IGTI Scholar Award. Turbo Expo: Power for Land, Sea, and Air. V004T17A001. June 1997.

[171] R. Srivastava and T. G. Keith. “Influence of Shock Wave on Turbomachinery Blade Row Flutter”. In: *Journal of Propulsion and Power* 21.1 (2005), pp. 167–174.

[172] R. Srivastava and T. S. R. Reddy. “Comparative Study of Coupled-Mode Flutter-Analysis Methods for Fan Configurations”. In: *Journal of Propulsion and Power* 15.3 (1999), pp. 447–453.

[173] K. Stein, T. Tezduyar and R. Benney. “Mesh Moving Techniques for Fluid-Structure Interactions With Large Displacements”. In: *Journal of Applied Mechanics* 70.1 (Jan. 2003), pp. 58–63. ISSN: 0021-8936.

[174] P. Sváček, M. Feistauer and J. Horáček. “Numerical Simulation of Flow Induced airfoil Vibrations with Large Amplitudes”. In: *Journal of Fluids and Structures* 23.3 (2007), pp. 391–411. ISSN: 0889-9746.

[175] A. Syrakos et al. “A cCritical Analysis of Some Popular Methods for the Discretisation of the Gradient Operator in Finite Volume Methods”. In: *Physics of Fluids* 29.12 (2017), p. 127103.

[176] E. Széchényi. “Fan Blade Flutter: Single Blade Instability or Blade to Blade Coupling?” In: *Turbo Expo: Power for Land, Sea, and Air*. Vol. Volume 1: Aircraft Engine; Marine; Turbomachinery; Microturbines and Small Turbomachinery. V001T03A055. Mar. 1985.

[177] T. Theodorsen. *Report No. 496: General Theory of Aerodynamic Instability and the Mechanism of Flutter*. Technical Report. National Advisory Committee for Aeronautics. Langley Aeronautical Lab.; Langley Field, VA, USA, 1935.

[178] T. Theodorsen. *Report No. 685: Mechanism of Flutter A Theoretical and Experimental Investigation of the Flutter Problem*. Technical Report. National Advisory Committee for Aeronautics. Langley Aeronautical Lab.; Langley Field, VA, USA, 1940.

[179] J. P. Thomas, E. H. Dowell and K. C. Hall. “Nonlinear Inviscid Aerodynamic Effects on Transonic Divergence, Flutter, and Limit-Cycle Oscillations”. In: *AIAA Journal* 40.4 (2002), pp. 638–646.

[180] P. D. Thomas and C. K. Lombard. “Geometric Conservation Law and Its Application to Flow Computations on Moving Grids”. In: *AIAA Journal* 17.10 (1979), pp. 1030–1037.

[181] A. Torkaman et al. “Gas Turbine Cycle Upgrade and Validation for Heavy Duty Industrial Machines”. In: *Turbo Expo: Power for Land, Sea, and Air*. Vol. Volume 3: Coal, Biomass and Alternative Fuels; Cycle Innovations; Electric Power; Industrial and Cogeneration Applications; Organic Rankine Cycle Power Systems. V003T06A021. June 2017.

[182] H. Triebstein. “Steady and Unsteady Transonic Pressure Distributions on NACA 0012”. In: *Journal of Aircraft* 23.3 (1986), pp. 213–219.

[183] M. Vahdati and M. Imregun. “A Non-Linear Aeroelasticity Analysis of a Fan Blade Using Unstructured Dynamic Meshes”. In: *Proceedings of the Institution of Mechanical Engineers, Part C: Journal of Mechanical Engineering Science* 210.6 (1996), pp. 549–564.

[184] M. Vahdati, G. Simpson and M. Imregun. “Mechanisms for Wide-Chord Fan Blade Flutter”. In: *Journal of Turbomachinery* 133.4 (Apr. 2011). 041029. ISSN: 0889-504X.

[185] V. Venkatakrishnan. “On the Accuracy of Limiters and Convergence to Steady State Solutions”. In: 31st Aerospace Sciences Meeting, Reno, Nevada, USA. 1993.

[186] J. Verdon. “Linearized Unsteady Aerodynamics for Turbomachinery Aeroelastic Applications”. In: 26th Joint Propulsion Conference. 1990.

[187] J. M. Verdon and J. R. Caspar. “A Linearized Unsteady Aerodynamic Analysis for Transonic Cascades”. In: *Journal of Fluid Mechanics* 149 (1984), pp. 403–429.

[188] J. M. Verdon and J. E. McCune. "Unsteady Supersonic Cascade in Subsonic Axial Flow". In: *AIAA Journal* 13.2 (1975), pp. 193–201.

[189] S. Vilmin et al. "Unsteady Flow Modeling Across the Rotor/Stator Interface Using the Nonlinear Harmonic Method". In: *Turbo Expo: Power for Land, Sea, and Air*. Vol. Volume 6: Turbomachinery, Parts A and B. May 2006, pp. 1227–1237.

[190] D. Vogt. "Experimental Investigation of Three-Dimensional Mechanisms in Low-Pressure Turbine Flutter". PhD thesis. Royal Institute of Technology, Stockholm, Sweden, 2005.

[191] J. J. Waite. "Physical Insights, Steady Aerodynamic Effects, and a Design Tool for Low-Pressure Turbine Flutter". PhD thesis. Duke University, Durham, North Carolina, 2016.

[192] L. Wang et al. "Unsteady Simulation of a Counter–Rotating Research Compressor Using the Nonlinear Harmonic Method". In: *Proceedings of the Institution of Mechanical Engineers, Part G: Journal of Aerospace Engineering* 227.3 (2013), pp. 415–424.

[193] D. S. Whitehead. "A Finite Element Solution of Unsteady Two-Dimensional Flow in Cascades". In: *International Journal for Numerical Methods in Fluids* 10.1 (1990), pp. 13–34.

[194] D. Whitehead. *Bending Flutter of Unstalled Cascade Blades at Finite Deflection*. London, Great Britain: Aeronautical Research Council, Reports and Memoranda no. 3386, 1962.

[195] D. Whitehead. *Force and Moment Coefficients for Aerofoils in Cascade*. London, Great Britain: Aeronautical Research Council, Reports and Memoranda no. 3254, 1960.

[196] D. Whitehead. *The Effect of Compressibility on Unstalled Torsional Flutter*. London, Great Britain: University Engineering Dept., Cambridge. Reports and memoranda, no. 3754, 1973.

[197] J. William Usab and E. Murman. "Embedded Mesh Solutions Of The Euler Equation Using a Muitiple-grid Method". In: *6th Computational Fluid Dynamics Conference Danvers*. 1983.

[198] D. Wisler. *Blade Row Interaction and Unsteady Effects in Axial Flow Compressors and Fans*. VKI Lecture Series 1998-02: Blade Row Interference Effects in Axial Turbomachinery Stages. 1998.

[199] X. Wu et al. "A Numerical Investigation of Aeroacoustic Fan Blade Flutter". In: *ASME Turbo Expo, Volume 4. Atlanta, Georgia, USA*. June 2003.

[200] M. Zhang et al. "Analysis on Flutter Characteristics of Transonic Compressor Blade Row by a Fluid-Structure Coupled Method". In: *Turbo Expo: Power for Land, Sea, and Air*. Vol. Volume 7: Structures and Dynamics, Parts A and B. June 2012, pp. 1519–1528.

[201] X. Zhang et al. "Computation of Fan Noise Radiation through A Realistic Engine Exhaust Geometry with Flow". In: *9th AIAA/CEAS Aeroacoustics Conference and Exhibit*. 2003.

[202] Y. Zheng and H. Yang. “Coupled Fluid-structure Flutter Analysis of a Transonic Fan”. In: *Chinese Journal of Aeronautics* 24.3 (2011), pp. 258–264. ISSN: 1000-9361.